



Title	Study on the Energy Transfer Processes in Polynuclear Lanthanide Complexes
Author(s)	大曲, 駿
Citation	北海道大学. 博士(工学) 甲第13242号
Issue Date	2018-03-22
DOI	10.14943/doctoral.k13242
Doc URL	http://hdl.handle.net/2115/70107
Type	theses (doctoral)
File Information	Shun_Omagari.pdf



[Instructions for use](#)

Study on the Energy Transfer Processes in Polynuclear Lanthanide Complexes

多核希土類錯体における
エネルギー移動過程に関する研究

Shun Omagari

Graduate School of Chemical Sciences and Engineering
Hokkaido University

I. List of Publications

For Thesis

- 1. Spin-orbit Coupling Dependent Energy Transfer in Luminescent Nonanuclear Yb-Gd / Yb-Lu Clusters** (Chapter 4)

S. Omagari, T. Nakanishi, Y. Kitagawa, T. Seki, K. Fushimi, H. Ito, A. Meijerink, Y. Hasegawa, *J. Lumin.* **2017**, *submitted*.

- 2. Origin of Concentration Quenching in Ytterbium Coordination Polymers: Phonon-Assisted Energy Transfer** (Chapter 3)

S. Omagari, T. Nakanishi, Y. Hirai, Y. Kitagawa, T. Seki, K. Fushimi, H. Ito, Y. Hasegawa, *Eur. J. Inorg. Chem.* **2017**, *in publication*.

- 3. Critical Role of Energy Transfer Between Terbium Ions for Suppression of Back Energy Transfer in Nonanuclear Terbium Clusters** (Chapter 6)

S. Omagari, T. Nakanishi, Y. Kitagawa, T. Seki, K. Fushimi, H. Ito, A. Meijerink, Y. Hasegawa, *Sci. Rep.* **2016**, *6*, 37008.

- 4. Effective Photosensitized Energy Transfer of Nonanuclear Terbium Clusters Using Methyl Salicylate Derivatives** (Chapter 5)

S. Omagari, T. Nakanishi, T. Seki, Y. Kitagawa, Y. Takahata, K. Fushimi, H. Ito, Y. Hasegawa, *J. Phys. Chem. A* **2015**, *119*, 1943-1947.

- 5. Synthesis and Photoluminescence Properties of Nonanuclear Tb(III) Clusters with Long Alkyl Chain Group** (Chapter 5)

S. Omagari, T. Nakanishi, Y. Kitagawa, K. Fushimi, Y. Hasegawa, *e-J. Surf. Sci. Nanotech.* **2015**, *13*, 27-30.

Other Publications

1. Temperature dependence of $4f^n-15d^1 \rightarrow 4f^n$ luminescence of Ce^{3+} and Pr^{3+} ions in Sr_2GeO_4 host

K. Fiaczyk, S. Omagari, A. Meijerink, E. Zych, *J. Lumin.* **2018**, *198*, 163-170.

2. A Luminescent Mechanochromic 9-Anthryl Gold(I) Isocyanide Complex with an Emission Maximum at 900 nm after Mechanical Stimulation

T. Seki, N. Tokodai, S. Omagari, T. Nakanishi, Y. Hasegawa, T. Iwasa, T. Taketsugu, H. Ito, *J. Am. Chem. Soc.* **2017**, *139*, 6514-6517.

3. Development of Ion-Conductive and Vapoluminescent Porous Coordination Polymers Composed of Ruthenium(II) Metalloligand

A. Watanabe, A. Kobayashi, E. Satoh, Y. Nagao, S. Omagari, T. Nakanishi, Y. Hasegawa, W. M. C. Sameera, M. Yoshida, M. Kato, *Inorg. Chem.* **2017**, *56*, 3005-3013.

4. Synthesis of Dipyridinogermole-Copper Complex as Soluble Phosphorescent Material

K. Murakami, Y. Ooyama, S. Watase, K. Matsukawa, S. Omagari, T. Nakanishi, Y. Hasegawa, K. Inumaru, J. Ohshita, *Chem. Lett.* **2016**, *45*, 502-504.

5. Drastically Improved Durability and Efficiency of Silicon Solar Cells Using Hyper-Stable Lanthanide Coordination Polymer Beads

H. Kataoka, T. Nakanishi, S. Omagari, Y. Takabatake, Y. Kitagawa, Y. Hasegawa, *Bull. Chem. Soc. Jpn.* **2016**, *89*, 103-109.

6. Photo-Degradation Analysis of Luminescent Polymers with Lanthanide Complexes

H. Kataoka, S. Omagari, T. Nakanishi, Y. Hasegawa, *J. Photopolym. Sci. Technol.* **2015**, *28*, 247-254.

7. EVA Thin Film with Thermo- and Moisture-stable Luminescent Copolymer Beads Composed of Eu(III) Complexes for Improvement of Energy Conversion Efficiency on Silicon Solar Cell

H. Kataoka, S. Omagari, T. Nakanishi, Y. Hasegawa, *Opt. Mater.* **2015**, *42*, 411-416.

II. List of Presentations

1. Concentration quenching mechanism of Ytterbium(III) coordination polymer

○S. Omagari, T. Nakanishi, Y. Hirai, Y. Kitagawa, K. Fushimi, Y. Hasegawa, 錯体化学会第 67 回討論会, 2Fa-05, 北海道大学札幌キャンパス, 札幌, 2017 年 9 月 18 日. (Oral Presentation)

2. 九核希土類クラスターにおけるエネルギー移動と発光特性に関する研究

○大曲駿, 中西貴之, 北川裕一, 伏見公志, 長谷川靖哉, 第 78 回応用物理学会秋季学術講演会, 7p-A414-1, 福岡国際会議場, 福岡, 2017 年 9 月 7 日. (Invited Oral Presentation)

3. テルビウムクラスターにおけるエネルギー移動と発光特性

○大曲駿, 中西貴之, 北川裕一, 伏見公志, 長谷川靖哉, 錯体化学若手の会夏の学校 2017, 西浦温泉ホテルたつき, 蒲郡, 2017 年 8 月 2 日. (Invited Oral Presentation)

4. Mechanism Elucidation and Suppression of Back Energy Transfer in Nonanuclear Tb³⁺ Clusters

○S. Omagari, T. Nakanishi, Y. Kitagawa, K. Fushimi, Y. Hasegawa, Nagoya Univ.-Tsinghua Univ.-Toyota Motor Corp.-Hokkaido Univ. Joint Symposium, P02, Takayama Municipal Cultural Hall, Takayama, September 13, 2017. (Poster)

5. Energy Transfer and Luminescence Properties of Nonanuclear Rare-Earth Clusters including Terbium and Gadolinium

○S. Omagari, T. Nakanishi, Y. Kitagawa, K. Fushimi, Y. Hasegawa, 第 64 回応用物理学会春季学術講演会, 14p-411-10, パシフィコ横浜, 横浜, 2017 年 3 月 13 日. (Oral Presentation)

6. Molecular Design for Improving Photoluminescence Efficiency in Lanthanide Complexes

○S. Omagari, Y. Hasegawa, 9th HOPE meeting, JP1601, Tokyo International Forum, Tokyo, February 26, 2017. (Poster)

7. Dependency of Spin of Lanthanide Electrons on Ligand Emission in Lanthanide Clusters

○S. Omagari, T. Nakanishi, Y. Kitagawa, K. Fushimi, Y. Hasegawa, 2016 年光化学討論会, 1C03, 東京大学駒場第一キャンパス, 東京, 2016 年 9 月 6 日. (Oral Presentation)

8. Excited State Dynamics of Nonanuclear Tb(III) Clusters

○S. Omagari, T. Nakanishi, Y. Kitagawa, K. Fushimi, Y. Hasegawa, Rare Earths 2016, C09-23, 北海道大学札幌キャンパス, 札幌, 2016 年 6 月 10 日. (Oral Presentation)

9. Effective photosensitized energy transfer of nonanuclear terbium clusters using methyl salicylate derivatives

○S. Omagari, T. Nakanishi, T. Seki, Y. Kitagawa, Y. Takahata, K. Fushimi, H. Ito, Y. Hasegawa, The International Chemical Congress of Pacific Basin Societies 2015 (Pacifichem 2015), 55 (1074), Honolulu (HI, USA), December 15, 2015. (Poster)

10. テルビウムクラスターにおける配位子の電子構造と光増感エネルギー移動の関係

○大曲駿, 中西貴之, 北川裕一, 伏見公志, 長谷川靖哉, 日本化学会北海道支部 2015 年夏季研究発表会, E15, 北海道教育大学函館キャンパス, 函館, 2015 年 7 月 18 日. (Oral Presentation)

11. エネルギー移動のループを利用した希土類クラスターの発光増強

○大曲駿, 中西貴之, 北川裕一, 関朋宏, 伏見公志, 伊藤肇, 長谷川靖哉, 化学系学協会北海道支部 2015 年冬季研究発表会, 1B15, 北海道大学札幌キャンパス, 札幌, 2015 年 1 月 26 日. (Oral Presentation)

12. Ln-O 格子を有する九核ランタニドクラスターの合成とその光物性

○大曲駿, 中西貴之, 北川裕一, 伏見公志, 長谷川靖哉, 第 4 回 CSJ 化学フェスタ 2014, 4P061, タワーホール船堀, 東京, 2014 年 10 月 15 日. (Poster)

13. 九核ランタニドクラスターにおける発光メカニズムの解明

○大曲駿, 中西貴之, 伏見公志, 長谷川靖哉, 2014 年光化学討論会, 1P087, 北海道大学札幌キャンパス, 札幌, 2014 年 10 月 11 日. (Poster)

14. Synthesis and Photoluminescence Properties of Nonanuclear Tb(III) Clusters with Long Alkyl Chain

○S. Omagari, T. Nakanishi, Y. Kitagawa, K. Fushimi, Y. Hasegawa, 15th Chitose International Forum on Photonics & Technology, P9, Chitose Institute of Science and Technology, Chitose, October 2, 2014. (Poster)

15. テルビウムとガドリニウムで構成された九核ランタニドクラスターの発光メカニズム

○大曲駿, 中西貴之, 伏見公志, 長谷川靖哉, 第 26 回配位化合物の光化学討論会, P30, 首都大東京南大沢キャンパス, 東京, 2014 年 8 月 7 日. (Poster)

16. Photophysical Properties of Nonanuclear Tb(III) Clusters with Intramolecular Interactions

○S. Omagari, T. Nakanishi, Y. Kitagawa, K. Fushimi, Y. Hasegawa, 10th International Workshop on Supramolecular Nanoscience of Chemically Programmed Pigments, P19, Ritsumeikan University Biwako-Kusatsu Campus, Kusatsu, May 31, 2014. (Poster)

17. 長鎖アルキル基を導入した九核 Tb(III)クラスタの合成と光機能評価

○大曲駿, 中西貴之, 伏見公志, 長谷川靖哉, 日本化学会第 94 期春季年会, 2F3-08, 名古屋大学東山キャンパス, 名古屋, 2014 年 3 月 28 日. (Oral Presentation)

III. Achievements

1. 「学生講演賞」, 2017 年錯体化学会第 67 回討論会.
2. 「講演奨励賞」, 2017 年第 64 回応用物理学会春季学術講演会.
3. 「優秀学生発表賞 (口頭)」, 2016 年光化学討論会.
4. “Student Poster Award”, The International Chemical Congress of Pacific Basin Societies 2015 (Pacifichem 2015).
5. Featured in the Chem-station’s “Spotlight Research” in response to the Student Poster Award in Pacifichem 2015.
6. 「優秀講演賞 (口頭部門)」, 日本化学会北海道支部 2015 年夏季研究発表会.
7. 「優秀講演賞 (口頭部門)」, 化学系学協会北海道支部 2015 年冬季研究発表会.
8. 「優秀ポスター発表賞」, 2014 年度錯体化学若手の会北海道支部第 3 回勉強会.
9. 「優秀学生発表賞 (ポスター)」, 2014 年光化学討論会.
10. 「優秀ポスター賞」, 第 26 回配位化合物の光化学討論会.

Table of Contents

I. List of Publications	i
II. List of Presentations	iii
III. Achievements	v

Chapter 1: *General Introduction*

1.1. Introduction	2
1.1.1. Descriptions of Light	
1.1.2. Photoluminescence	
1.2. Lanthanides	8
1.2.1. Electron Configuration and Chemistry	
1.2.2. Luminescence	
1.3. Lanthanide Complexes	14
1.3.1. Luminescence Mechanism	
1.3.2. Polynuclear Lanthanide Complexes	
1.4. Outline	20
1.5. References	23
1.6. Abbreviations	28

Chapter 2: *Theory*

2.1. Introduction	30
2.2. Lanthanides	30
2.1.1. Energy Levels and Wavefunctions	
2.1.2. Radiative Rate Constants	
2.1.3. Energy Transfer Rate Constants	
2.3. Kinetic Analysis of Excited State	39
2.2.1. Rate Equation for Impulse Excitation	
2.2.2. Rate Equation for Constant Excitation	
2.2.3. Simple Mononuclear Case	
2.4. References	46

Chapter 3: Concentration Quenching in Ytterbium Coordination

Polymers

3.1. Introduction	48
3.2. Experimental Section	50
3.2.1. Material	
3.2.2. Apparatus	
3.2.3. Synthesis	
3.2.4. Spectroscopy	
3.2.5. Crystallography	
3.3. Theoretical Methods	54
3.3.1. Rate Constants	
3.3.2. Rate Equations	
3.4. Results and Discussion	60
3.4.1. Structure	
3.4.2. Photophysical Properties	
3.4.3. Theoretical Lifetimes	
3.5. Conclusion	68
3.6. Appendix	70
3.6.1. Absorption Spectra of Yb(III) Ions	
3.6.2. MATLAB Script for Calculation of Theoretical Lifetimes	
3.6.3. Quantitative Considerations of Theoretical Lifetimes	
3.7. References	76

Chapter 4: Spin-Orbit Coupling and Energy Transfer in Nonanuclear

Lanthanide Clusters

4.1. Introduction	80
4.2. Experimental Section	81
4.2.1. Material	
4.2.2. Apparatus	
4.2.3. Synthesis	
4.2.4. Spectroscopy	
4.2.5. Crystallography	

4.3. Results and Discussion	84
4.3.1. Structure and Identification	
4.3.2. Photophysical Properties	
4.4. Conclusion	94
4.5. Appendix	94
4.5.1. Notes on Spin-Orbit Coupling	
4.5.2. Continuous Shape Measure and Shape Measure	
4.6. References	96

Chapter 5: *Back Energy Transfer in Terbium Clusters*

5.1. Introduction	100
5.2. Experimental Section	101
5.2.1. Material	
5.2.2. Apparatus	
5.2.3. Synthesis	
5.2.4. Spectroscopy	
5.2.5. Computational Details	
5.3. Results and Discussion	104
5.3.1. Structure	
5.3.2. Intramolecular Interactions and Photophysical Properties	
5.3.3. Mechanism of Back Energy Transfer	
5.4. Conclusion	116
5.5. Appendix	117
5.5.1. Intrinsic Quantum Yield Measurements	
5.5.2. BET Rate Constant	
5.5.3. BET and T_1 Decay	
5.6. References	120

Chapter 6: *Suppression of Back Energy Transfer by Energy Transfer between Terbium Ions*

6.1. Introduction	124
6.2. Theoretical Motivation	125
6.2.1. Theoretical Method	

6.2.2. Results	
6.3. Experimental Section	132
6.3.1. Material	
6.3.2. Apparatus	
6.3.3. Synthesis	
6.3.4. Spectroscopy	
6.4. Results and Discussion	134
6.4.1. Structure and Identification	
6.4.2. Photophysical Properties	
6.5. Conclusion	141
6.6. Appendix	142
6.6.1. Dependence of TbTbET in Absence of BET	
6.6.2. MATLAB Script for Theoretical Calculation of Tb ₉ -Bu	
6.7. References	146

Chapter 7: *Summary and Outlook*

7.1. Summary and Conclusion	150
7.2. Outlook	151

Acknowledgements

Chapter 1

GENERAL INTRODUCTION

1.1. Introduction

“Light brings us the news of the Universe,” said W. H. Bragg in *The Universe of Light* in 1933.^[1] He was indeed right that it does. Production, manipulation, and utilization of light have been one of the most extensively studied areas in science, and also one of the most practical. Humanity has become increasingly reliant on technology utilizing light throughout the history, and it is now difficult to find a society that does not rely on light. Plants (and even some bacteria) also absorb sunlight for photosynthesis, which is vital to the ecosystem including our existence. Utilization of light has also lead to other scientific discoveries, with one of the most recent (2017) Nobel Prize in Physics going to R. Weiss, K. Throne, and B. Barish for the observation of gravitational waves using laser interferometer gravitational-wave observatory (LIGO).

The history of science and technology based on light is quite long and in a sense could date all the way back to the Stone Age when human had used fire for heat and light. However, modern (commercialized) lighting was only available since the early 20th century with incandescent light bulbs. Today, fluorescent lamps and light-emitting diode (LED) lamps are



Figure 1.1 Examples of application of light. Images taken from ref [2] (top left), ref [3] (top right), ref [4] (bottom left), and ref [5] (bottom right).

usually used for general lighting, but high-pressure sodium lamps are commonly used for street lights. Cathode ray tube (CRT) based displays are rarely produced now and are replaced by liquid crystal (LCD) and (briefly) plasma displays. More recently, organic light-emitting diode (OLED) displays have emerged as another type of displays. Lasers (light amplification by stimulated emission of radiation) are also one of the most important technologies that use light, being invented by T. H. Maiman in 1960. Applications include, but not limited to, telecommunication, quantum computing, optical memory, medicine, military weapons, and cutting/welding in industry. As a tool for the further development in science, lasers are used in time-resolved spectroscopy, Fourier-transform infrared spectroscopy (FTIR), Raman spectroscopy, fluorescence microscopy, dynamic light scattering (DLS), laser fusion, laser cooling, and ion trapping (Figure 1.1).^[2-5]

1.1.1. Descriptions of Light

There are several quantitative descriptions of light (or more precisely, electromagnetic radiation), but the two main descriptions are *intensity* and *energy* of the light. Some other descriptions are coherence and polarity, but it is not the focus of this thesis. The difference between the *intensity* and *energy* of light can be visually explained by particle-like interpretation of light called “photon” (Figure 1.2). The *energy* of light refers to photon energy, meaning the energy carried by a single photon. The unit used can be wavenumber [cm^{-1}], electronvolt [eV], or wavelength [nm], all of which can be easily converted. As shown in the photon energy spectrum in Figure 1.2a, light is classified into radio waves, (microwaves), infrared light, visible light, ultraviolet light, X-rays, and gamma rays depending on the energy carried by a photon. The visible region and the regions below and above the energy of this region (near-infrared and ultraviolet) is of particular importance in this thesis. As the name implies, the visible region of light is the region that the human eyes can detect. A color of light could be composed of light of single energy (color) or combination of light of different energies. The primary colors (Figure 1.3) are the (minimum number of) pure colors to be able to express any color by a combination of them. To express a certain color, one can use additive or subtractive mixing of primary colors. In additive mixing, one combines light of different energies. For example, a total mixture of the conventional red, green, and blue (RGB) primary colors yields white (Figure 1.3a). In subtractive mixing, one combines pigments that absorb light of different energies. For example, a total mixture of yellow, magenta, and cyan pigments yields black by absorbing all colors of light, rendering it unable for the human eyes to receive

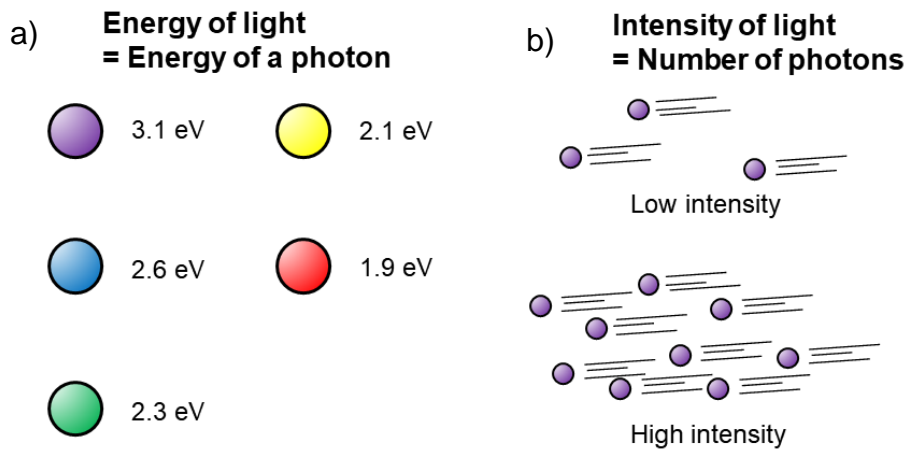


Figure 1.2 a) *Energy* and b) *intensity* of the light in the particle (rough) description.

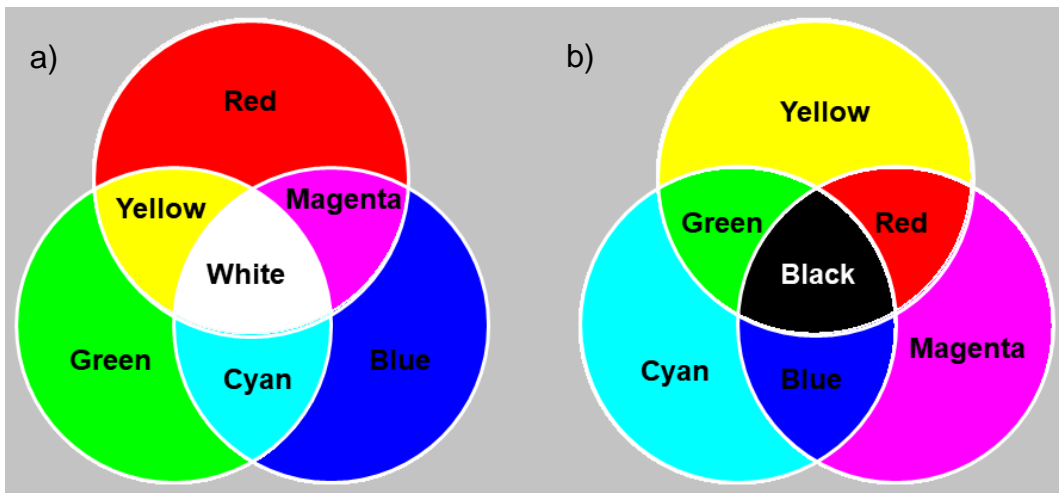


Figure 1.3 a) Additive mixing (primary colors: blue, green, and red) and b) subtractive mixing (primary colors: cyan, yellow, and magenta).

any light (Figure 1.3b). Near-infrared (NIR) and ultraviolet (UV) lights are not visible to human eyes, but there are many applications. NIR light is used for bioimaging for their high transmission in biological tissues, and opto-telecommunication for their low loss in optical fibers. Most compounds absorb light of UV region. Therefore, they can be used for forensic analysis and drug detection. High energy UV is potentially hazardous to organisms as it can disrupt DNA molecules, and can be used as disinfectants.

The *intensity* of light roughly refers to the number of photons that are detected by the observer (Figure 1.2b). However, most units used to describe the *intensity* of light do *not* count the number of photons due to the instrumental difficulty in precisely detecting the number of photons (of single energy). Most detectors measure the total energy resulting from the photons that enter the detector instead. The most common unit used to describe the intensity of light is irradiance (also known as flux density) expressed in W m^{-2} (watts per meter squared), which is radiant flux received by a surface of unit area. Radiant flux, expressed in W (or J s^{-1}), refers to the total energy of light (photons) emitted per unit time. As can be inferred from the definition of radiant flux, irradiance includes information on the *energy* of light and not just the *intensity* of light. In general, a light may be composed of photons with various energy. In spectroscopy, where one measures the intensity of each photon energy, it is often a poor practice to judge the *intensity* of light based on the irradiance without the information of the photon *energy* that the light is composed of.

1.1.2. Photoluminescence

A material that can emit photons is called luminescent material. Emission of photons requires that the material is electronically excited by some excitation source. Depending on the excitation source, a prefix is added to the word “luminescence”. For example, if a material is excited by light, the resulting luminescence is termed “photoluminescence”. Let it be an applied voltage, and it is termed “electroluminescence”. Likewise, if the excitation source is chemical reactions, mechanical stimulation, or applied heat, the corresponding luminescence is called chemiluminescence, mechanoluminescence, or thermoluminescence, respectively.

The quantum mechanical description of photoluminescence is provided by quantum field theory. In this theory, the electromagnetic field is quantized and the interaction of this field with the compound in question is calculated. Nonetheless, they can be roughly approximated to quantum mechanics in the non-relativistic Schrödinger equation for one photon process, as will be treated in this thesis. In any compounds there are multiple electronic states, vibrational states, and spin states. The lowest state is called the “ground state”, and any of the higher energy states are called “excited state”. Any processes that goes between such states are called “transition”. Photoluminescence in this case is the transition between two electronic states involving an absorption or emission photon corresponding to the energy gap between the states. Under adiabatic approximation (such as Born-Huang, Born-Oppenheimer, or crude adiabatic), the movement of electrons is assumed to move much faster than the nuclei so that vibrational

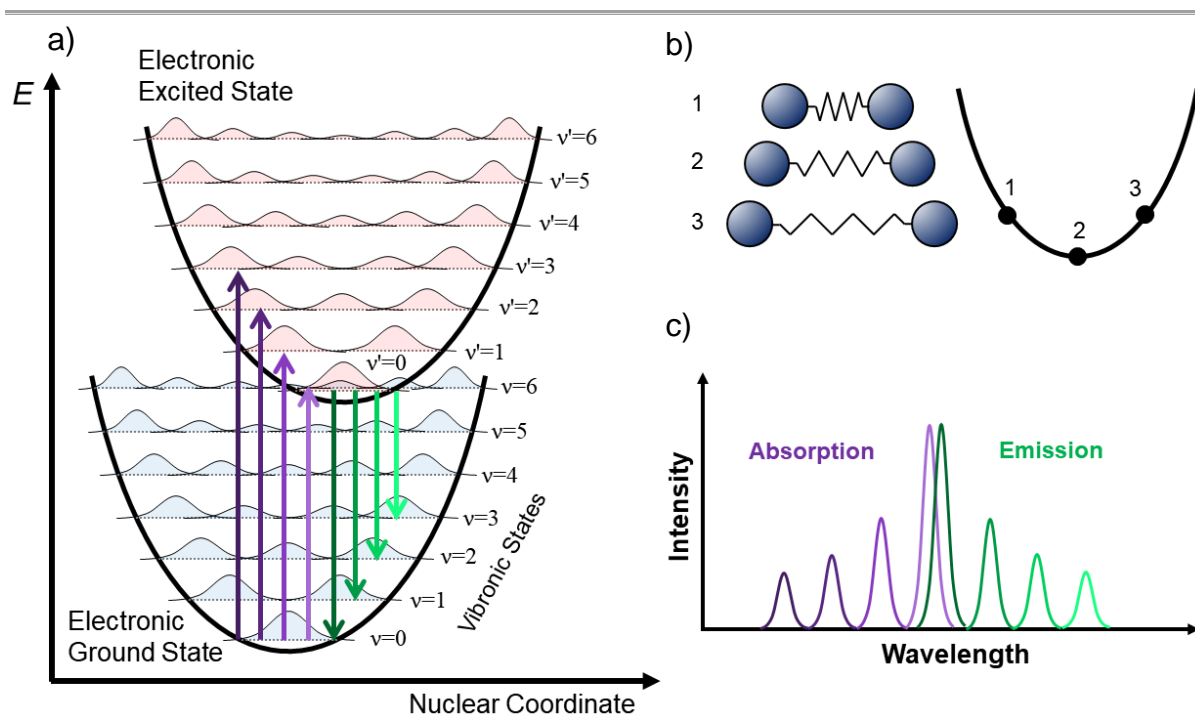


Figure 1.4 a) Potential energy curve for a diatomic compound and photoluminescence. Up arrow represents absorption and down arrow represents emission. The waves on each of the potential depicts the probability density of the vibronic modes. v represents the quantum number of the vibronic mode. b) Classical depiction of the vibration of a two-atom molecule and their corresponding energies on the potential curve. c) Absorption and emission spectra resulting from a). Wavelength is the inverse of energy. Longer wavelength means lower energy photon and shorter wavelength means larger energy photon.

states are determined once an electronic state for a given configuration of the nuclei of the compound is solved. This produces a potential energy surface, and for diatomic molecules a potential energy curve (Figure 1.4a). Both the potential energy of ground and excited states are depicted as quadratic curves. This is because for a diatomic compound, two atoms can be considered to be bonded together like a spring, classically speaking. By the Hooke's law, this produces a quadratic potential curve (Figure 1.4b). The x -axis (nuclear coordinate) position of the minimum of the potential energy curves is called the "equilibrium position". The equilibrium position of the two potential curves is depicted as being different because generally the different electronic states usually involve changes to the bonding length and strength, and thus the energetically stable point as well. Quantum mechanically, vibrations of the molecules

are quantized (quantum harmonic oscillator) and thus there are equal gaps in energy between the vibrational states. In reality, a compound is comprised of much more than two atoms, which increases the degree of freedom in the movement of the nuclei, resulting in multiple vibrational modes. Moreover, the potential energy surface is not quadratic, especially in higher energy limit because bonds can significantly change (anharmonic).

Electronic transition (or luminescence) typically proceeds from the lowest vibrational states of an electronic state (higher vibrational states can still be populated by thermal excitation). Under Franck-Condon approximation (which assumes Born-Oppenheimer approximation) an electronic transition is fully vertical as shown in the arrows of Figure 1.4a because the slow moving nuclei cannot change its configuration faster than the electrons. In practice, absorption and emission spectra, which show the dependence of photon energy on the intensity of the transition, are in the form of that shown in Figure 1.4c. The vibrational bands are observed because the electromagnetic field couples vibrational states of an electronic state with another electronic state, and the emission intensity depends on the amplitude of the overlap of vibrational states. The degree of coupling depends on the displacement of the equilibrium position of the ground and excited state.

All photophysical processes are kinetic. This means that luminescence can be expressed in terms of how “fast” they emit a photon from an excited state. The rate constant of this process is called “radiative rate constant” and is in the unit of emission of photon per second [s^{-1}]. Many of the light sources seem like they are continuously emitting. Microscopically, if only one single emitting center is considered, blinking of an emitting center at a rate mentioned above is observed.^[6] Macroscopically, numerous emitting centers blink that make the material looks as if it is continuously emitting. The efficiency of photoluminescence of a material is expressed by “quantum yield” Φ defined by the number of emitted photons per number of absorbed photons:

$$\Phi = \frac{\text{(Number of emitted photons)}}{\text{(Number of absorbed photons)}} \quad [1.1]$$

In practice, the quantum yield of a photoluminescent material is rarely unity (100%). This is because excited material can deactivate to a ground state without photon emission in the form of heat through vibration of the compound and/or the surrounding matrix. This phenomenon is called internal conversion (but often confusing called “vibrational relaxation”).^[7]

Internal conversion is a nonadiabatic process. This means that the adiabatic approximation used in the case of luminescence cannot be directly applied. Quantum mechanically, the off-diagonal matrix elements resulting from the nuclear kinetic energy operator cause coupling of

vibrational and electronic states even without electromagnetic field. The nonradiative rate constant of this process is exponentially dependent on the energy gap between two electronic states. This is the “energy gap law”, and it is also the basis of Kasha’s rule.^[8] Kasha’s rule states that an emission will occur from the lowest vibrational state of the lowest excited electronic state. In many molecules, the energy gap between two electronically excited states is too small that internal conversion between these two states proceed much faster than luminescence from the second excited state. In contrast, energy gap between the first excited and ground states are usually larger allowing luminescence. The implication of this rule is that NIR luminescence (emission of a photon of small energy) is typically more inefficient than UV-visible luminescence (emission of a photon of large energy).

Spin multiplicity is another factor that greatly affects the emission process. A transition between two electronic states of the same spin multiplicity is an allowed process and is called “fluorescence.” On the other hand, a transition between those of different multiplicity is a forbidden process and is called “phosphorescence.” Typically, fluorescence have a large radiative rate constant ranging from $10^7 - 10^{11} \text{ s}^{-1}$ while phosphorescence has a small radiative rate constant ranging from $10^1 - 10^4 \text{ s}^{-1}$. Consequently, phosphorescence is usually not observed in room temperature as internal conversion dominates.

There are numerous types of photoluminescent materials available today, but the common (and commercially available) ones used today include Ce:YPO₄ (blue), Tb:YPO₄ (green), Eu:Y₂O₃ (red) (these three are used for fluorescent lamps), and Ce:Y₃Al₅O₁₂ (green-yellow, used for white LED). These materials can be considered as spectral converters, which convert light of certain wavelength (or *energy*) into the light of different wavelength. Other potential applications of spectral converters are films to produce an optimal wavelength of light for solar panels and crops. Some photoluminescent materials are used as solid-state laser medium such as Ti-sapphire lasers, ruby lasers, and Nd:YAG lasers.

1.2. Lanthanides

Lanthanides (Ln) are 15 metallic elements in the periodic table with atom number 57 to 71 (Figure 1.5, blue elements). They are also called “rare-earth” along with scandium (Sc) and yttrium (Y) for their similar chemical properties (Figure 1.5, yellow and blue elements). The name rare-earth originated from their low availability at the time they were discovered (1787) due to the difficulty in purification. Lanthanides could also be classified as “f-elements” along

earth as a whole is estimated to be up to 242 ppm in the Earth's crust, more than the amount of carbon (200 ppm).^[9]

The filling of seven 4f-orbitals^[10] (Figure 1.6a) in the lanthanides gives rise to many unique physical properties. The chemical properties of lanthanides have also been considered significant in synthetic chemistry as a catalyst. General chemical properties of lanthanides include similar ionic radii, reduction potentials, oxidation states, and electronegativity. Physical properties of lanthanides include luminescence and magnetism, which both are intrinsic and usually remain rather unaffected by outer environment. Lanthanides have been playing an important role in the current technologies such as lasers, radars, telecommunication, lighting equipment, and MRIs.^[11] This section will mainly describe the basic properties of lanthanide ions (Ln(III) ions) with greater emphasis on the photophysical properties.

1.2.1. Electron Configuration and Chemistry

The electron configuration of lanthanide is the main reason for their chemical and physical properties. The electron configuration of lanthanides (as well as Sc and Y) is shown in Table 1.1. In its metallic state (0 valence state), the 6s-orbital is fully occupied, and sometimes a single electron occupies the 5d-orbital as well. However, lanthanides in its metallic state are quite reactive (their reactivity is similar to alkali earth metal) and quickly oxidize to a trivalent state. In the trivalent state, lanthanide (Ln(III)) loses three electrons: two from the 6s-orbital and one from either the 4f-orbital or 5d-orbital if it was occupied. This results in a Ln(III) ion with 4f-orbitals that is not completely filled (except lanthanum (La), which do not have any 4f electrons, and lutetium (Lu), which is filled). As shown in Figure 1.6b, 4f-orbitals are narrowly distributed closer to the nucleus than the 5s, 5p, 5d, and 6s-orbitals.^[9] Therefore, 4f-orbitals are “protected” by the outer orbitals and do not contribute to bonding. As a result, the chemical and physical properties are similar throughout the lanthanide series.

Lanthanides are commonly in their trivalent state, but under some conditions, divalent and quadrivalent states are also possible. La and Lu have none and fully occupied 4f-orbitals, respectively, and thus are stable electron configurations. Gadolinium (Gd) has seven 4f-electrons making all of the 4f-orbitals half filled, and is in a relatively stable electron configuration as well. Ce and terbium (Tb) take the relatively stable quadrivalent state by taking the same electron configuration as La and Gd, respectively. Similarly, europium (Eu) and ytterbium (Yb) also reduce into a divalent state by possessing the electron configuration of Gd

Table 1.1 Electron configuration, ionic radii, and electronegativity of lanthanides.

Element		Atomic Number	Configuration of atom	Configuration of trivalent ion	Ionic radii / Å ^a	Electronegativity ^b
Scandium	Sc	21	[Ar]3d ¹ 4s ²	[Ar]	0.87	1.20
Yttrium	Y	39	[Kr]4d ¹ 5s ²	[Kr]	1.019	1.11
Lanthanum	La	57	[Xe]5d ¹ 6s ²	[Xe]	1.16	1.08
Cerium	Ce	58	[Xe]4f ¹ 5d ¹ 6s ²	[Xe]4f ¹	1.143	1.08
Praseodymium	Pr	59	[Xe]4f ³ 6s ²	[Xe]4f ²	1.126	1.07
Neodymium	Nd	60	[Xe]4f ⁴ 6s ²	[Xe]4f ³	1.109	1.07
Promethium	Pm	61	[Xe]4f ⁵ 6s ²	[Xe]4f ⁴	1.093	1.07
Samarium	Sm	62	[Xe]4f ⁶ 6s ²	[Xe]4f ⁵	1.079	1.07
Europium	Eu	63	[Xe]4f ⁷ 6s ²	[Xe]4f ⁶	1.066	1.01
Gadolinium	Gd	64	[Xe]4f ⁷ 5d ¹ 6s ²	[Xe]4f ⁷	1.053	1.11
Terbium	Tb	65	[Xe]4f ⁹ 6s ²	[Xe]4f ⁸	1.04	1.10
Dysprosium	Dy	66	[Xe]4f ¹⁰ 6s ²	[Xe]4f ⁹	1.027	1.10
Holmium	Ho	67	[Xe]4f ¹¹ 6s ²	[Xe]4f ¹⁰	1.015	1.10
Erbium	Er	68	[Xe]4f ¹² 6s ²	[Xe]4f ¹¹	1.004	1.11
Thulium	Tm	69	[Xe]4f ¹³ 6s ²	[Xe]4f ¹²	0.994	1.11
Ytterbium	Yb	70	[Xe]4f ¹⁴ 6s ²	[Xe]4f ¹³	0.985	1.06
Lutetium	Lu	71	[Xe]4f ¹⁴ 5d ¹ 6s ²	[Xe]4f ¹⁴	0.977	1.14

a) Shannon Radii of 8-coordinate Ln(III) ion. b) Value of Ln(III) ion with Pauling scale.

and Lu, respectively. These divalent and quadrivalent states are not stable and require synthesis in a controlled condition.

Relatively large ionic radii of Ln(III) ions compared to other metal ions give rise to variable coordination number of ligating atoms ranging from 3 to 12. Ionic radii of Ln(III) ions

gradually contract from 1.16 Å of La to 0.977 Å of Lu, known as the “lanthanide contraction.” This phenomenon occurs due to the increase in the number of electrons in the inner orbitals that cannot adequately shield the increasing positive charge of nuclei, causing the outer orbitals to be drawn closer to the nuclei. The slight difference in ionic radii is important in purification and extraction of each Ln(III) ions from oxides. However, the effect of lanthanide contraction is small enough to maintain their similarity in chemical properties and thus considered to have similar ionic radii.^[10,12]

1.2.2. Luminescence

Ln(III) ions show distinctive luminescence properties mainly deriving from the 4f-orbitals. This includes spectrally sharp absorption and emission bands (similar to atomic spectra), long emission lifetimes, and small absorption coefficients. This subsection covers basic luminescence properties of Ln(III) ions, namely the energy levels, the spectral width of the emission bands, and emission lifetimes. Further details of what is explained below are provided in Chapter 2.

Energy of 4f-states in Ln(III) ions in its free ion state is fixed for each Ln(III) ions, and thus the absorption and emission wavelength of Ln(III) ions are fixed.^[13–16] The electronic states are determined by electrostatic coupling and spin-orbit coupling of 4f-electrons to the first-order. As stated before, 4f-orbitals are shielded by 5s-, 5p-, 5d-, and 6s-orbitals, and do not contribute to bonding. Therefore, unlike the d-orbitals in transition metals, the crystal-field is a minor perturbation in the determination of the 4f-states. The energy level of 4f-states is shown in the “Dieke diagram” in Figure 1.7a.^[17] Each energy level can be labeled by a Russell-Saunders term symbol: $^{2S+1}L_J$, where S , L , and J are the total spin quantum number ($2S+1$ represents spin multiplicity), total orbital quantum number, and total angular quantum number, respectively. Combination of S , L , and J gives a level, and each level contains $2J+1$ possible microstates. These intrinsic energy levels are advantageous for designing a luminescent material as one can easily expect what wavelength the material is excited and emits.

The absorption and emission of Ln(III) ions are spectrally sharp, similar to an atomic spectrum.^[18,19] Figure 1.7b shows the potential energy of two 4f-states in comparison with a typical luminescent center. Since the 4f-orbitals do not contribute to bonding, the shape of the potential curve, which is determined by bonding and position of the atoms, is unaffected for all 4f-states. Furthermore, the lack of involvement in the bonding keeps the vibrational coupling (a.k.a. electron-phonon coupling) of 4f-states very weak.^[9,20] As a result, absorption

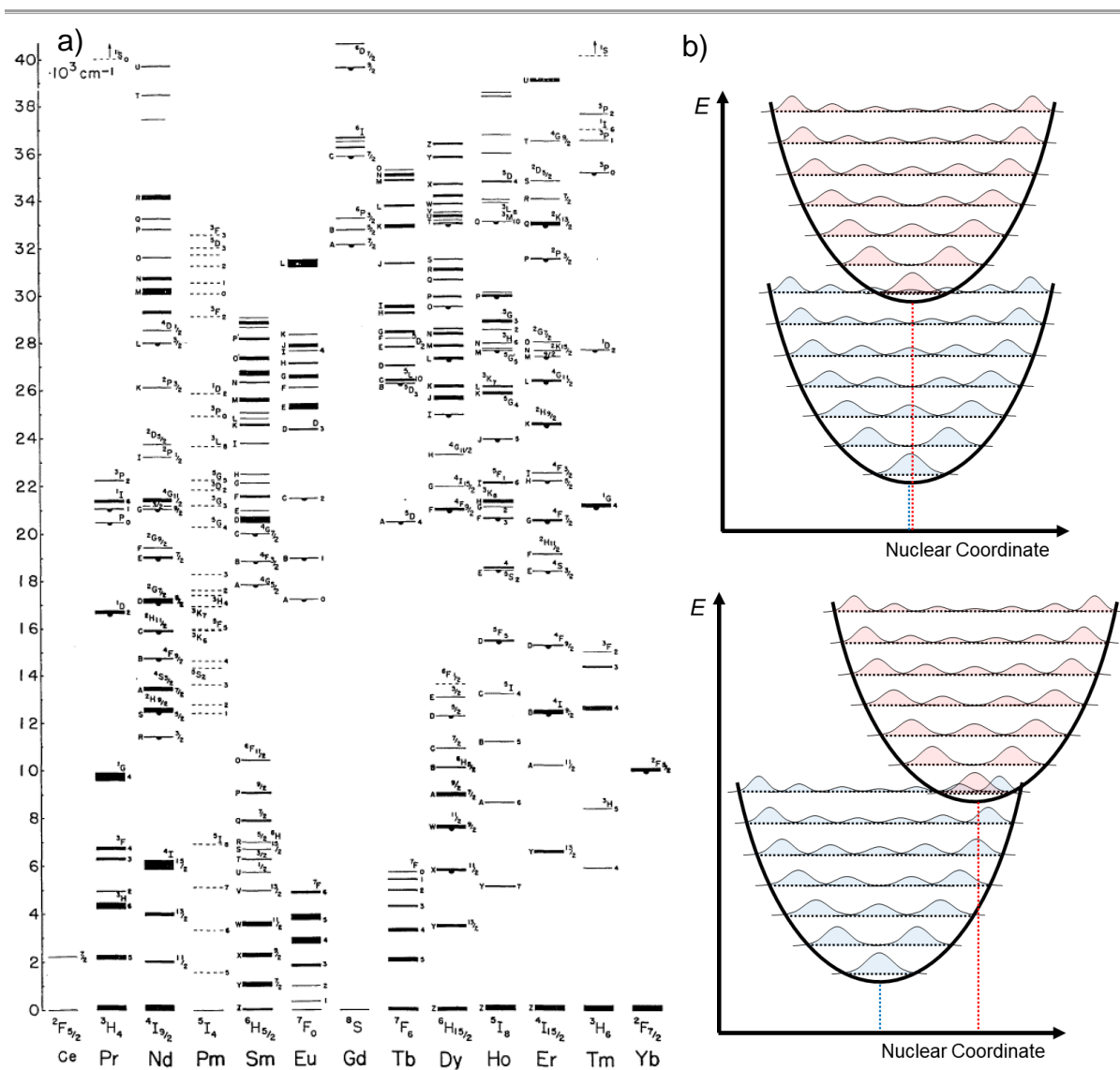


Figure 1.7 a) Dieke diagram representing 4f-state energy levels. Reprinted from ref [17]. b) Schematic image of the potential energy curve of the ground and excited 4f-states (top) and typical luminescent center (bottom).

and emission between two 4f-states are sharp. The splitting usually observed in a single band of Ln(III) ions is called Stark splitting, caused by a crystal-field that lifts some of the degeneracy of $2J+1$ microstates. Thus, a different spectral shape is observed for different coordination environment. Sometimes, the vibronic structure is observed in Ln(III) absorption and emission, called phonon-sidebands.^[21–23] Nonetheless, these bands are very low in intensity.

The emission lifetimes of Ln(III) ions are typically long; they are in the order of microseconds to milliseconds. Emission lifetime τ_{obs} in its simplest form is given by the following equation:

$$\tau_{\text{obs}} = \frac{1}{kr + knr} \quad [1.2]$$

where kr and knr are radiative and nonradiative rate constants, respectively. In lanthanides, both of these rate constants are small in the order of $10^2 - 10^3 \text{ s}^{-1}$. The kr of Ln(III) ions is small, meaning the electronic transitions are weak (small oscillator strength), due to the 4f-4f transitions being Laporte forbidden.^[10,24] Absorption and emission can still be observed in practice because crystal-field causes a mixture of 4f5d-states into 4f-states, leading to partially allowed 4f-4f transitions. Absorption coefficient is no more than $10 \text{ M}^{-1} \text{ cm}^{-1}$ and in most cases smaller than $1 \text{ M}^{-1} \text{ cm}^{-1}$. Qualitatively, the oscillator strength can be made stronger by distorting the symmetry of ligand field (coordination geometry).^[25,26] The oscillator strength of dipole transitions in a Ln(III) ion can be quantitatively calculated using semi-empirical Judd-Ofelt theory.^[27,28] The knr (relaxation via vibrational states) is also small in 4f-4f transitions. As mentioned in the paragraph above, the shape and the nuclear configurational position of the potential curves between 4f-states are nearly identical and the vibrational coupling is thus very weak. This means that relaxation from the crossing point between potentials is low in probability and relaxation through overlap with the vibrational modes is very small as well. Additionally, the wavefunction of the vibrational mode of the ground and excited states tends to be smaller for higher vibrational states of the ground state, further reducing the overlap.

The small absorption coefficient of Ln(III) ions makes it impractical to use the 4f-4f transition for exciting the ions directly. Only few Ln(III) ions such as Tb(III) and Eu(III) ions have, respectively, 4f-4f5d and charge transfer transition in the UV-violet region with relatively large absorption coefficient that can be used to excite 4f-states.^[10,29] Ln(III) ions have many intrinsic properties that distinguish themselves from other elements, making them a necessity for current and future technology. If the absorption band can be fully tuned with very large absorption coefficient, Ln(III) ions can be used efficiently and would be necessary for long-term technological advances.

1.3. Lanthanide Complexes

Lanthanides, as with other metal elements, form chemical bonds with nonmetal elements. Since the 4f-orbitals do not contribute to chemical bonding and the ionic radii is large, the

chemical bonds with lanthanides are mainly ionic. Such property leads to Ln(III) complexes (Figure 1.8a) forming a variety of coordination number and structure and is heavily dependent on the steric effect. Coordination number of Ln(III) complexes is primarily eight (and less commonly nine), but complexes with other coordination numbers (3 to 12) are reported although rare. Due to lanthanide contraction, coordination number is sometimes smaller in the heavier lanthanides even when using the same ligand. Some of the common ligands used are shown in Figure 1.8b, namely, β -diketonate, bipyridine, DOTA (1,4,7,10-tetraaza-cyclododecane-1,4,7,10-tetraacetic acid), and PyBOX (pyridine-2,6-bisoxazoline).^[9,10,30–36] From the perspective of photoluminescence, one of the most important features of Ln(III) complexes is the photosensitization by organic ligands. The absorption coefficient of Ln(III) complexes is usually in the order of 10^3 to 10^4 M⁻¹ cm⁻¹ due to multiple organic ligands.^[31] Energy transfer (ET) from the organic ligands to Ln(III) ions efficiently produces Ln(III) excited states, leading to strong luminescence of Ln(III) ions. Additionally, functionalization

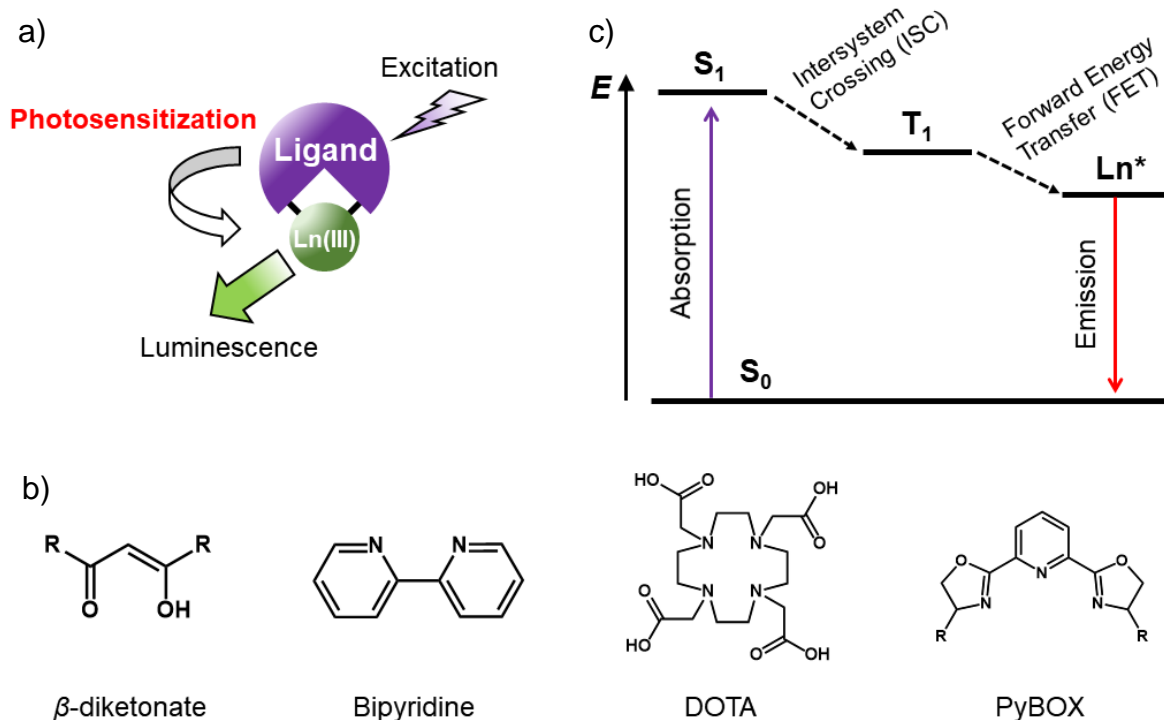


Figure 1.8 a) Schematic depiction of Ln(III) complex. b) Common ligands used for Ln(III) complexes. c) Luminescence mechanism of Ln(III) complexes. Ln^* means excited Ln(III) ion.

is possible by the design of the ligands. For example, target-specific organic ligands can be used as Ln(III) complex for bioimaging agents.^[32,37–40] Other potential applications include lasers, lighting, OLEDs, sensors, and spectral converters.^[39,41–48]

Despite the advantages of Ln(III) complexes, the quantum yield of Ln(III) complexes tends to be lower than the ceramic counterpart. This is due to the additional processes before the Ln(III) ions are excited as well as the use of organic ligands that induce vibrational relaxation.^[49] In this section, the mechanism of photoluminescence of Ln(III) complexes is described first, and then the strategies to improve the quantum yield.

1.3.1. Luminescence Mechanism

Mechanism of luminescence in a typical Ln(III) complex is shown in Figure 1.8c. First, the π -conjugated organic ligands absorb a photon to be electronically excited from the singlet ground state (S_0) to the singlet excited state (S_1). Strong spin-orbit coupling of Ln(III) ion promotes intersystem crossing (ISC) to the triplet excited state (T_1). This process is often said to be caused primarily by the “heavy atom effect”. ET usually occurs from the T_1 state to an excited level of Ln(III) ion. For the convenience of the discussion throughout this thesis, $T_1 \rightarrow$ Ln ET will be denoted as “FET” (“forward energy transfer”), although this is not the usual convention in this area of study. With this mechanism, quantum yield of Ln(III) complexes by ligand excitation Φ_{ligand} can be calculated from the following equation:

$$\Phi_{\text{ligand}} = \eta_{\text{sens}} \times \Phi_{\text{Ln}} , \quad [1.3]$$

where η_{sens} is the overall sensitization efficiency of the Ln(III) ion by the organic ligands, and Φ_{Ln} is the quantum yield of Ln(III) complexes by direct excitation of Ln(III) ion. Φ_{Ln} is given by the following equation:

$$\Phi_{\text{Ln}} = \frac{kr}{kr + knr} . \quad [1.4]$$

Finally, using the equation of emission lifetime τ_{obs} (Equation [1.2]) and “intrinsic” emission lifetime τ_{rad} ($= 1/kr$, emission lifetime of Ln(III) in the ideal state where there are no quenching), Equation [1.3] can be rewritten as follows:

$$\Phi_{\text{ligand}} = \eta_{\text{sens}} \times \frac{\tau_{\text{obs}}}{\tau_{\text{rad}}} . \quad [1.5]$$

As can be interpreted from Equations [1.3] and [1.4], improving the sensitization efficiency and raising the radiative rate constant, while reducing the nonradiative rate constant would increase the quantum yield. The strategy to enhance radiative rate constant was already

explained in paragraph four of 1.2.2. Below explains the reported method to suppress nonradiative process and improve sensitization efficiency.

Nonradiative relaxation to the ground state of Ln(III) ions occurs through vibrational states. Suppressing nonradiative relaxation requires the elimination of the contributing vibrational mode(s). In the case of organic ligands, high energy vibrational modes like C-H (stretching $3000 - 3300 \text{ cm}^{-1}$) and O-H (stretching $3200 - 3700 \text{ cm}^{-1}$) can lead to a high nonradiative rate constant.^[25,50] This is especially prominent for Ln(III) ions with a small energy gap between 4f-states. To reduce nonradiative rate constant, high energy vibrational modes like C-H and O-H needs to be eliminated as much as possible. An example of the reduction by elimination of C-H vibronic mode were provided by Y. Hasegawa et al. for Nd(III) complex^[51,52] and by C. Doffek et al. for Nd(III), Er(III), and Yb(III) complexes.^[53] They showed that replacing C-H bonds with C-D (deuterated) bonds leads to smaller nonradiative rate constants. The suppression of nonradiative relaxation has been extensively studied.

The improvement of sensitization efficiency is complicated compared to the reduction of the nonradiative rate constant because of the multiple factors that affect the efficiency. Breaking down the sensitization efficiency, and also considering the radiative and nonradiative rate constant for S_1 and T_1 states, leads to:

$$\begin{aligned} \eta_{\text{sens}} &= \eta_{\text{ISC}} \times \eta_{\text{FET}} \\ &= \frac{k_{\text{ISC}}}{kr_{S_1} + knr_{S_1} + k_{\text{ISC}}} \times \frac{k_{\text{FET}}}{kr_{T_1} + knr_{T_1} + k_{\text{FET}}} \end{aligned} \quad [1.6]$$

where k_{ISC} , k_{FET} , are $S_1 \rightarrow T_1$ ISC, FET rate constants, respectively. Once again, kr and knr are radiative and nonradiative rate constants and the subscript denotes the states in which they apply to. All of these constants influence the sensitization efficiency. Further complication here is that these rate constants are not fully independent variables, although some of them can be approximated as so. For example, spin-orbit coupling mixes states of different multiplicity, and causes k_{ISC} , kr_{T_1} , and knr_{T_1} to increase while kr_{S_1} and knr_{S_1} to decrease.

In order to promote fast FET, an optimum level of the T_1 state energy in relative to the excited state of the Ln(III) ion is required. From a survey of the available reports on T_1 energy, the T_1 energy of 2000 cm^{-1} above the excited state of a Ln(III) ion is optimal.^[54-58] Below this, the reverse process of FET called “back energy transfer” (BET) occurs and reduces the sensitization efficiency. BET is known to be particularly prominent in Tb(III) complexes, where T_1 state energy lower than 1850 cm^{-1} significantly reduces the quantum yield (Figure 1.9).^[59] The factors that affect the BET rate constant other than the T_1 state energy are not yet

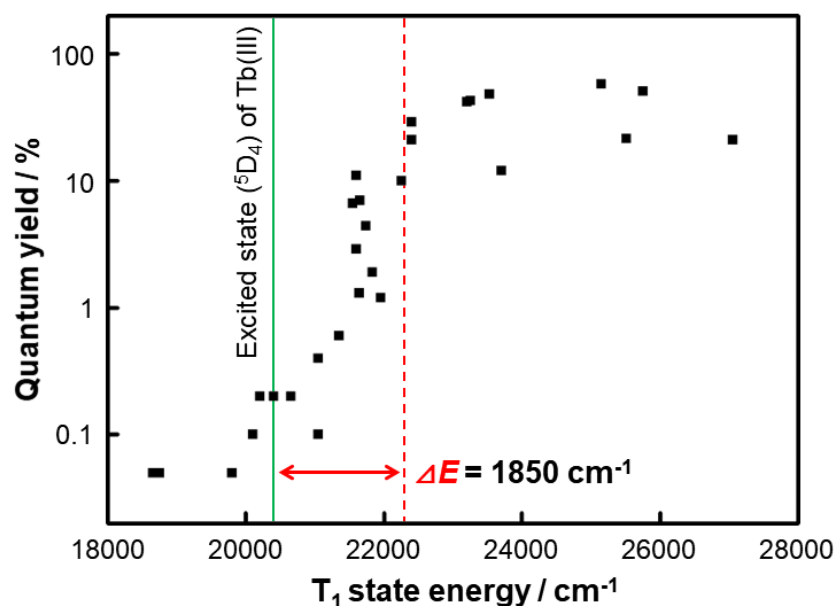


Figure 1.9 Relationship between the T_1 state energy and the quantum yield of Tb(III) complexes. Reproduced from ref [59].

reported. Studying the details of the BET mechanism may provide new insight into suppressing BET and achieving high sensitization efficiency.

Raising the $S_1 \rightarrow T_1$ ISC efficiency has been largely neglected since they are considered to proceed *efficiently* due to the heavy atom effect of lanthanides.^[60,61] In a more general sense, $S_1 \rightarrow T_1$ ISC is induced by spin-orbit coupling, which includes the heavy atom effect and the “paramagnetic effect” (caused by the intrinsic magnetic moment produced by the 4f-electrons).^[62,63] Reports are limited in numbers, but available reports showed that within the lanthanide series, the effect of heavy atom effect is not as pronounced as the paramagnetic effect. D. M. Guldi et al. demonstrated the effect of spin-orbit coupling on various processes within the ligands. In particular, Gd(III) complex showed the larger $S_1 \rightarrow T_1$ ISC rate constant of $3.8 \times 10^9 \text{ s}^{-1}$ compared to that of Lu(III) complex of $1.9 \times 10^9 \text{ s}^{-1}$, despite the latter being the heavier atom. Furthermore, the T_1 nonradiative process is also enhanced for the Gd(III) complex.^[63] This is expected because spin-orbit coupling mixes states of different multiplicity, i.e., S_1 and T_1 states as well as T_1 and S_0 states.^[64]

1.3.2. Polynuclear Lanthanide Complexes

Polynuclear Ln(III) complex is a general term for Ln(III) complexes with multiple Ln(III) ions within a single molecule. The advantage of polynuclear Ln(III) complexes is that different Ln(III) ions can be used in a single molecule, allowing multiple emission bands.^[65,66] Moreover, when there are two or more Ln(III) ions, ET between Ln(III) ions (LnLnET) occurs depending on the distance between them.^[65,67] Figure 1.10 shows several of the reported polynuclear Ln(III) complexes.^[68–70]

In general, ET is a distance-dependent process. Förster mechanism and Dexter mechanism are two widely known mechanisms of the ET process, each corresponding to the direct Coulomb interaction and exchange interaction, respectively, of the approximated electrostatic coupling matrix element.^[71,72] Both are distance dependent, but Förster mechanism^[72] has a distance dependence of R^{-6} while Dexter mechanism^[71] has an $\exp(2R/L)$ dependence (L is the

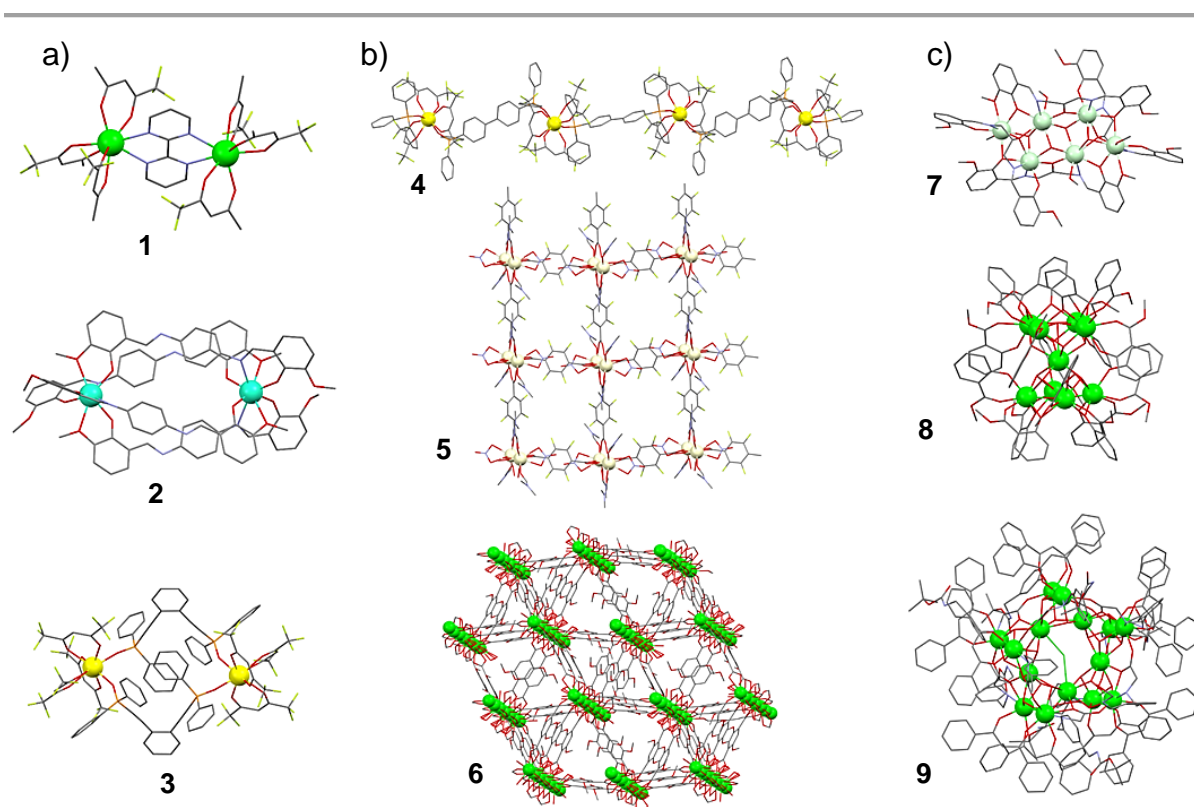


Figure 1.10 Examples of a) polynuclear Ln(III) complexes, b) Ln(III) coordination polymers, and c) Ln(III) clusters. **1:** ref [68], **2:** ref [69], **3:** ref [70], **4:** ref [73], **5:** ref [74], **6:** ref [75], **7:** ref [84], **8:** ref [85], and **9:** ref [86].

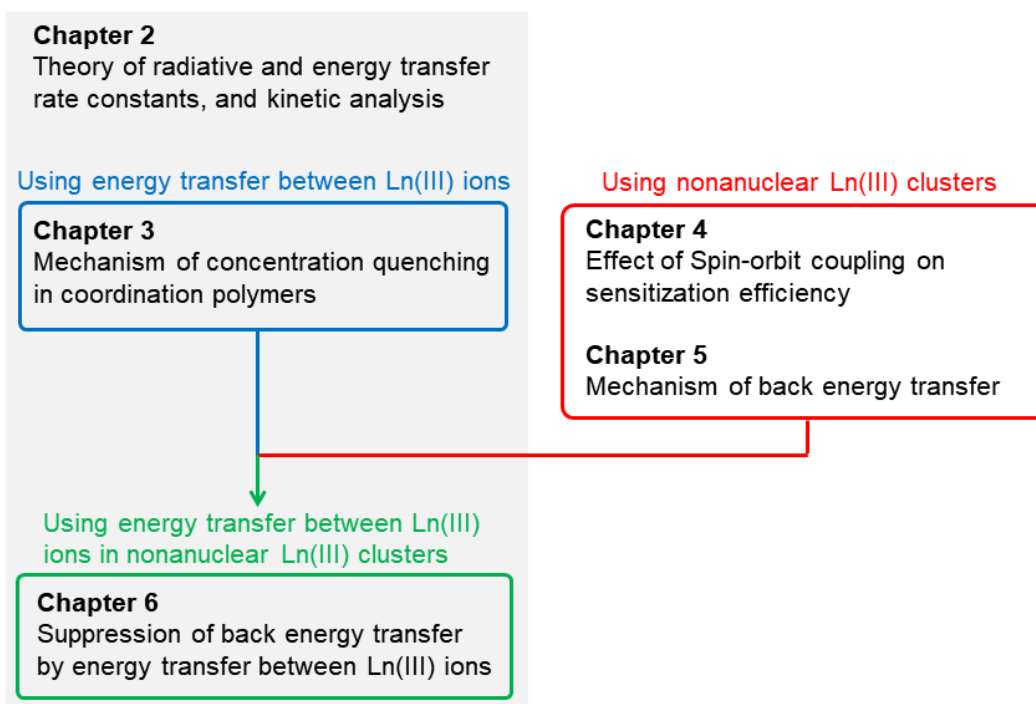
effective Bohr radius). Ln(III) coordination polymers are polynuclear Ln(III) complexes with polymer structure (Figure 1.10b).^[73–75] They are characterized by chain of Ln(III) ions and bridging ligands between them. Porous coordination polymers (PCP), also known as metal-organic frameworks (MOF, Figure 1.10b bottom), are coordination polymers with large spatial vacancy between the chains.^[75] Depending on the ligand design, some of these coordination polymers have high thermostability.^[74,76,77] MOF, in particular, can be used as an adsorbing agent for their porous structure.^[78,79] Regarding LnLnET, numerous reports are available that utilize temperature dependent LnLnET for thermosensing functions.^[80–83]

Ln(III) clusters are polynuclear complexes with Ln(III) rich core and multiple ligands coordinating around the core (Figure 1.10c).^[84–86] The Ln(III) ions in the core are often bridged by OH⁻ ions and therefore have very short Ln(III)-Ln(III) distance. It is not easy to “design” a synthetic procedure to produce Ln(III) clusters, and their formation remains serendipitous.^[87–89] The numbers of reports of Ln(III) clusters are limited compared to those of other class of polynuclear Ln(III) complexes likely because of the unpredictable nature of the synthesis of the clusters. Reports regarding luminescent properties of Ln(III) clusters are further limited.^[86,90–92] Structurally, Ln(III) clusters share the traits of both coordination polymers and mononuclear complexes; they involve LnLnET but with a discrete structure (such as size, shape, and molecular weight). Considering the close Ln(III)-Ln(III) distance, LnLnET is expected to be very fast compared to the other polynuclear complexes and could lead to new properties that cannot be achieved in mononuclear complexes or coordination polymers. The structural and luminescent properties of clusters potentially provide a new aspect in Ln(III) complexes.

1.4. Outline

The objective of the study is to elucidate various unexplored photophysical processes that could affect the photoluminescence efficiency with emphasis on energy transfer processes between the ligand and Ln(III) ion or between Ln(III) ions. Ln(III) coordination polymers and Ln(III) clusters are the central part of the study. This thesis provides new insight into strategies of molecular design for highly efficient Ln(III) complexes. The outline of this thesis is summarized in Scheme 1.1.

In order to analyze the photophysics of a complicated system of coordination polymers and clusters, quantum mechanical analysis and kinetic analysis are employed. In **Chapter 2**, the theories that are relevant to the discussion in the following chapters are discussed. The chapter



Scheme 1.1 The outline of this thesis.

covers the (quantum mechanical) theory of the transition and energy transfer of Ln(III) ions, as well as derivation of rate equations that model the excited state dynamics. The former describes the photophysical property of individual Ln(III) ion, whereas the latter describes how the interaction of these Ln(III) ions through energy transfer results in the actual observed photophysical properties. These two theories are useful in describing complicated photophysical processes where microscopic and macroscopic effects are needed to be accounted for.

Concentration quenching is considered to be an inevitable effect when Ln-to-Ln energy transfer (LnLnET) occurs in Ln(III) doped ceramics.^[93,94] In Ln(III) complexes, this is experimentally considered as a small effect, although their mechanism is not known.^[80,95,96] In **Chapter 3**, the concentration quenching mechanism in Yb(III) coordination polymer (in which this host is already reported to show LnLnET) is described both experimentally and theoretically. The theoretical results qualitatively match well with the experimental results when considered with the phonon-assisted energy transfer relaxation model,^[97] a type of concentration quenching observed only for high-purity solids.

Strong spin-orbit coupling promotes intersystem crossing from the singlet excited state (S_1) to the triplet excited state (T_1) but at the same time promotes relaxation from T_1 state to the ground state (S_0). The latter is an unfavorable effect (Equation [1.6]) but is experimentally difficult to confirm because spin-orbit coupling is intrinsic for each Ln(III) ion, and changing Ln(III) ions changes all the other processes unrelated to spin-orbit coupling as well. Ln(III) clusters make this investigation possible because Ln(III) ions can be mixed. **Chapter 4** describes the effect of spin-orbit coupling induced by the Gd(III), Yb(III), or Lu(III) ions on the photophysical processes within the organic ligands and their effect on the Yb sensitization efficiency (η_{sens}) using nonanuclear Yb/Gd or Yb/Lu mixed clusters.

Regarding ligand-Ln energy transfer, back energy transfer (BET) is the reverse process of forward energy transfer (FET) that reduces the overall sensitization efficiency η_{sens} . In **Chapter 5**, the effect of the excited state energy of the ligands on the FET and BET rate constants in nonanuclear Tb(III) clusters is described. The factors that affect BET rate constant is derived. This chapter also describes the rigidity of the core structure.

Tb-to-Tb energy transfer (TbTbET) is a competitive process with BET since they both occur from the excited state of a Tb(III) ion. In the case of Tb(III) clusters, the distance between Tb(III) ions is short, and fast TbTbET can be expected. **Chapter 6** describes the effect of Tb-to-Tb energy transfer (TbTbET) on the photophysical properties of nonanuclear Tb(III) clusters in the presence of BET.

Chapter 7 summarizes the study described from Chapters 1 to 6 along with a new insight into the strategy for molecular design to achieve Ln(III) complexes with high luminescence efficiency. The chapter is concluded with an outlook.

1.5. References

- [1] W. Bragg, *The Universe of Light*, The Hegeler Institute, **1935**.
- [2] “New York City Picture,” can be found under http://www.grayline.com/tours/new-york-city/night-tour-5870_25/, **2017**.
- [3] “LED Display,” can be found under <https://www.currys.co.uk/gbuk/tv-and-home-entertainment/televisions/televisions/jvc-lt-42c550-42-led-tv-10142379-pdt.html>, **2017**.
- [4] “Optical Fiber,” can be found under <http://www.m2optics.com/blog/what-is-optical-fiber>, **2017**.
- [5] “Laser Picture,” can be found under <http://www.directindustry.com/prod/continuum/product-27505-1290451.html>, **2017**.
- [6] H. Imada, K. Miwa, M. Imai-Imada, S. Kawahara, K. Kimura, Y. Kim, *Nature* **2016**, 538, 364–367.
- [7] B. Di Bartolo, V. Goldberg, *Radiationless Processes*, Plenum Press, **1980**.
- [8] M. Kasha, *Faraday Discuss.* **1950**, 9, 14–19.
- [9] C. Huang, *Rare Earth Coordination Chemistry: Fundamentals And Applications*, John Wiley & Sons (Asia) Pte. Ltd., **2010**.
- [10] J. G. Bünzli and S. V. Eliseeva, Basics of Lanthanide Photophysics, in *Springer Series on Fluorescence*, Springer, **2011**.
- [11] O. A. Blackburn, N. F. Chilton, K. Keller, C. E. Tait, W. K. Myers, E. J. L. McInnes, A. M. Kenwright, P. D. Beer, C. R. Timmel, S. Faulkner, *Angew. Chem. Int. Ed.* **2015**, 54, 10783–10786.
- [12] G. Liu, B. Jacquier, *Spectroscopic Properties of Rare Earths in Optical Materials*, Springer, **2005**.
- [13] W. T. Carnall, P. R. Fields, K. Rajnak, *J. Chem. Phys.* **1968**, 49, 4424–4442.
- [14] W. T. Carnall, P. R. Fields, K. Rajnak, *J. Chem. Phys.* **1968**, 49, 4443–4446.
- [15] W. T. Carnall, P. R. Fields, K. Rajnak, *J. Chem. Phys.* **1968**, 49, 4447–4449.
- [16] W. T. Carnall, P. R. Fields, K. Rajnak, *J. Chem. Phys.* **1968**, 49, 4450–4455.
- [17] G. H. Dieke and H. M. Crosswhite, *Appl. Opt.* **1963**, 2, 675–686.
- [18] W. T. Carnall, P. R. Fields, B. G. Wybourne, *J. Chem. Phys.* **1965**, 42, 3797–3806.
- [19] W. T. Carnall, P. R. Fields, K. Rajnak, *J. Chem. Phys.* **1968**, 49, 4412–4423.
- [20] M. D. Marcantonatos, *J. Chem. Soc. Faraday Trans. 2* **1986**, 82, 381–393.
- [21] K. K. Pukhov, T. T. Basiev, F. Auzel, F. Pellé, J. Heber, *J. Lumin.* **2001**, 94–95, 737–741.

- [22] T. Miyakawa, D. L. Dexter, *Phys. Rev. B* **1970**, 1, 2961–2969.
- [23] F. Auzel, *Chem. Rev.* **2004**, 104, 139–173.
- [24] K. Binnemans, *Coord. Chem. Rev.* **2015**, 295, 1–45.
- [25] N. B. D. Lima, S. M. C. Gonçalves, S. A. Júnior, A. M. Simas, *Sci. Rep.* **2013**, 3, 2395.
- [26] K. Yanagisawa, Y. Kitagawa, T. Nakanishi, T. Akama, M. Kobayashi, T. Seki, K. Fushimi, H. Ito, T. Taketsugu, Y. Hasegawa, *Eur. J. Inorg. Chem.* **2017**, 3843–3848.
- [27] B. R. Judd, *Phys. Rev.* **1962**, 127, 750–761.
- [28] G. S. Ofelt, *J. Chem. Phys.* **1962**, 37, 511–520.
- [29] M. P. Hehlen, M. G. Brik, K. W. Krämer, *J. Lumin.* **2013**, 136, 221–239.
- [30] J.-C. G. Bünzli, S. V. Eliseeva, *Chem. Sci.* **2013**, 4, 1939–1949.
- [31] Y. Hasegawa, Y. Wada, S. Yanagida, *J. Photochem. Photobiol. C* **2004**, 5, 183–202.
- [32] J.-C. G. Bünzli, *Chem. Rev.* **2010**, 110, 2729–2755.
- [33] J.-C. G. Bünzli, C. Piguet, *Chem. Soc. Rev.* **2005**, 34, 1048–1077.
- [34] S. V. Eliseeva, J.-C. G. Bünzli, *New J. Chem.* 2011, 35, 1165.
- [35] A. Rodríguez-Rodríguez, D. Esteban-Gómez, R. Tripier, G. Tircsó, Z. Garda, I. Tóth, A. de Blas, T. Rodríguez-Blas, C. Platas-Iglesias, *J. Am. Chem. Soc.* **2014**, 136, 17954–17957.
- [36] N. Souri, P. Tian, A. Lecointre, Z. Lemaire, S. Chafaa, J.-M. Strub, S. Cianférani, M. Elhabiri, C. Platas-Iglesias, L. J. Charbonnière, *Inorg. Chem.* **2016**, 55, 12962–12974.
- [37] A.-S. Chauvin, S. Comby, B. Song, C. D. B. Vandevyver, J.-C. G. Bünzli, *Chem. Eur. J.* **2008**, 14, 1726–1739.
- [38] S. V. Eliseeva, J.-C. G. Bünzli, *Chem. Soc. Rev.* **2010**, 39, 189–227.
- [39] R. Y. Tsien, L. Ernst, A. Waggoner, Fluorophores for Confocal Microscopy: Photophysics and Photochemistry, in *Handbook of Biological Confocal Microscopy*, Springer, **2006**.
- [40] V. Placide, A. T. Bui, A. Grichine, A. Duperray, D. Pitrat, C. Andraud, O. Maury, *Dalton Trans.* **2015**, 44, 4918–4924.
- [41] K. Nakamura, Y. Hasegawa, H. Kawai, N. Yasuda, N. Kanehisa, Y. Kai, T. Nagamura, S. Yanagida, Y. Wada, *J. Phys. Chem. A* **2007**, 111, 3029–3037.
- [42] S. Marchionna, F. Meinardi, M. Acciarri, S. Binetti, A. Papagni, S. Pizzini, V. Malatesta, R. Tubino, *J. Lumin.* **2006**, 118, 325–329.
- [43] T. Gunnlaugsson, J. P. Leonard, *Chem. Commun.* **2005**, 3114–3131.
- [44] S. J. Bradberry, A. J. Savyasachi, M. Martinez-Calvo, T. Gunnlaugsson, *Coord. Chem. Rev.* **2014**, 273–274, 226–241.

- [45] I. V. Taydakov, A. A. Akkuzina, R. I. Avetisov, A. V. Khomyakov, R. R. Saifutyarov, I. C. Avetissov, *J. Lumin.* **2016**, *177*, 31–39.
- [46] J. Kido, Y. Okamoto, *Chem. Rev.* **2002**, *102*, 2357–2368.
- [47] A. de Bettencourt-Dias, *Dalton Trans.* **2007**, 2229–2241.
- [48] P. K. Shahi, A. K. Singh, S. B. Rai, B. Ullrich, *Sens. Actuators, A* **2015**, *222*, 255–261.
- [49] E. S. Teixeira, B. B. Neto, P. M. C. de Oliveira, R. L. Longo, *J. Lumin.* **2016**, *170*, 602–613.
- [50] A. Beeby, I. M. Clarkson, R. S. Dickins, S. Faulkner, D. Parker, L. Royle, A. S. de Sousa, J. A. G. Williams, M. Woods, *J. Chem. Soc. Perkin Trans. 2* **1999**, 493–504.
- [51] Y. Hasegawa, Y. Kimura, K. Murakoshi, Y. Wada, J.-H. Kim, N. Nakashima, T. Yamanaka, S. Yanagida, *J. Phys. Chem.* **1996**, *100*, 10201–10205.
- [52] Y. Hasegawa, K. Murakoshi, Y. Wada, S. Yanagida, J.-H. Kim, N. Nakashima, T. Yamanaka, *Chem. Phys. Lett.* **1996**, *248*, 8–12.
- [53] C. Doffek, N. Alzakhem, C. Bischof, J. Wahsner, T. Guden-Silber, J. Lgger, C. Platas-Iglesias, M. Seitz, *J. Am. Chem. Soc.* **2012**, *134*, 16413–16423.
- [54] J. Andres, A.-S. Chauvin, *Phys. Chem. Chem. Phys.* **2013**, *15*, 15981–94.
- [55] R. Q. Albuquerque, N. B. Da Costa, R. O. Freire, *J. Lumin.* **2011**, *131*, 2487–2491.
- [56] F. Gutierrez, C. Tedeschi, L. Maron, J.-P. Daudey, R. Poteau, J. Azema, P. Tisns, C. Picard, *Dalton Trans.* **2004**, 1334–1347.
- [57] F. Gutierrez, C. Tedeschi, L. Maron, J.-P. Daudey, J. Azema, P. Tisns, C. Picard, R. Poteau, *J. Mol. Struct. (Theochem.)* **2005**, *756*, 151–162.
- [58] M. B. S. Botelho, M. D. Glvez-Lpez, L. De Cola, R. Q. Albuquerque, A. S. S. de Camargo, *Eur. J. Inorg. Chem.* **2013**, 5064–5070.
- [59] M. Latva, H. Takalo, V.-M. Mkkala, C. Matachescu, J. C. Rodrguez-Ubis, J. Kankare, *J. Lumin.* **1997**, *75*, 149–169.
- [60] M.-H. Ha-Thi, J. A. Delaire, V. Michelet, I. Leray, *J. Phys. Chem. A* **2010**, *114*, 3264–3269.
- [61] L.-M. Fu, X.-C. Ai, M. Y. Li, X. F. Wen, R. Hao, Y.-S. Wu, Y. Wang, J.-P. Zhang, *J. Phys. Chem. A* **2010**, *114*, 4494–4500.
- [62] S. Tobita, M. Arakawa, I. Tanaka, *J. Phys. Chem.* **1985**, *89*, 5649–5654.
- [63] D. M. Guldi, T. D. Mody, N. N. Gerasimchuk, D. Magda, J. L. Sessler, *J. Am. Chem. Soc.* **2000**, *122*, 8289–8298.
- [64] C. M. Marian, *WIREs Comput. Mol. Sci.* **2012**, *2*, 187–203.

- [65] D. J. Lewis, P. B. Glover, M. C. Solomons, Z. Pikramenou, *J. Am. Chem. Soc.* **2011**, *133*, 1033–1043.
- [66] A. D'Aléo, F. Pointillart, L. Ouahab, C. Andraud, O. Maury, *Coord. Chem. Rev.* **2012**, *256*, 1604–1620.
- [67] A. Zaïm, S. V. Eliseeva, L. Guénée, H. Nozary, S. Petoud, C. Piguet, *Chem. Eur. J.* **2014**, *20*, 12172–12182.
- [68] R. Ilmi, K. Iftikhar, *Polyhedron* **2015**, *102*, 16–26.
- [69] F. Habib, J. Long, P.-H. Lin, I. Korobkov, L. Ungur, W. Wernsdorfer, L. F. Chibotaru, M. Murugesu, *Chem. Sci.* **2012**, *3*, 2158.
- [70] Y. Hirai, T. Nakanishi, Y. Kitagawa, K. Fushimi, T. Seki, H. Ito, H. Fueno, K. Tanaka, T. Satoh, Y. Hasegawa, *Inorg. Chem.* **2015**, *54*, 4364–4370.
- [71] D. L. Dexter, *J. Chem. Phys.* **1953**, *21*, 836–850.
- [72] T. Förster, *Disc. Faraday Soc.* **1959**, 7–17.
- [73] C. Seidel, C. Lorbeer, J. Cybińska, A.-V. Mudring, U. Ruschewitz, *Inorg. Chem.* **2012**, *51*, 4679–4688.
- [74] K. Miyata, T. Ohba, A. Kobayashi, M. Kato, T. Nakanishi, K. Fushimi, Y. Hasegawa, *Chempluschem* **2012**, *77*, 277–280.
- [75] Y. Cui, H. Xu, Y. Yue, Z. Guo, J. Yu, Z. Chen, J. Gao, Y. Yang, G. Qian, B. Chen, *J. Am. Chem. Soc.* **2012**, *134*, 3979–3982.
- [76] A. Nakajima, T. Nakanishi, Y. Kitagawa, T. Seki, H. Ito, K. Fushimi, Y. Hasegawa, *Sci. Rep.* **2016**, *6*, 24458.
- [77] H. Zhang, L. Zhou, J. Wei, Z. Li, P. Lin, S. Du, *J. Mater. Chem.* **2012**, *22*, 21210–21217.
- [78] Y. Zhu, M. Zhu, L. Xia, Y. Wu, H. Hua, J. Xie, *Sci. Rep.* **2016**, *6*, 29728.
- [79] W.-G. Lu, D.-C. Zhong, L. Jiang, T.-B. Lu, *Cryst. Growth Des.* **2012**, *12*, 3675–3683.
- [80] Y. Cui, B. Chen, G. Qian, *Coord. Chem. Rev.* **2014**, *273–274*, 76–86.
- [81] Y. Cui, R. Song, J. Yu, M. Liu, Z. Wang, C. Wu, Y. Yang, Z. Wang, B. Chen, G. Qian, *Adv. Mater.* **2015**, *27*, 1420–1425.
- [82] Y. Hirai, T. Nakanishi, K. Miyata, K. Fushimi, Y. Hasegawa, *Mater. Lett.* **2014**, *130*, 91–93.
- [83] J. Rocha, C. D. S. Brites, L. D. Carlos, *Chem. Eur. J.* **2016**, *22*, 14782–14795.
- [84] S. Liao, X. Yang, R. A. Jones, *Cryst. Growth Des.* **2012**, *12*, 970–974.
- [85] T. Nakanishi, Y. Suzuki, Y. Doi, T. Seki, H. Koizumi, K. Fushimi, K. Fujita, Y. Hinatsu, H. Ito, K. Tanaka, Y. Hasegawa, *Inorg. Chem.* **2014**, *53*, 7635–7641.

- [86] D. T. Thielemann, A. T. Wagner, E. Rösch, D. K. Kölmel, J. G. Heck, B. Rudat, M. Neumaier, C. Feldmann, U. Schepers, S. Bräse, P. W. Roesky, *J. Am. Chem. Soc.* **2013**, *135*, 7454–7457.
- [87] S. Petit, F. Baril-Robert, G. Pilet, C. Reber, D. Luneau, *Dalton Trans.* **2009**, 6809–6815.
- [88] R. Wang, D. Song, S. Wang, *Chem. Commun.* **2002**, 368–369.
- [89] Z. Zheng, *Chem. Commun.* **2001**, 2521–2529.
- [90] A. Kornienko, T. J. Emge, G. A. Kumar, R. E. Riman, J. G. Brennan, *J. Am. Chem. Soc.* **2005**, *127*, 3501–3505.
- [91] D. I. Alexandropoulos, S. Mukherjee, C. Papatriantafyllopoulou, C. P. Raptopoulou, V. Psycharis, V. Bekiari, G. Christou, T. C. Stamatatos, *Inorg. Chem.* **2011**, *50*, 11276–11278.
- [92] E. C. Mazarakioti, K. M. Poole, L. Cunha-Silva, G. Christou, T. C. Stamatatos, *Dalton Trans.* **2014**, *43*, 11456–11460.
- [93] F. Auzel, G. Baldacchini, L. Laversenne, G. Boulon, *Opt. Mater.* **2003**, *24*, 103–109.
- [94] F. Auzel and F. Pellé, *J. Lumin.* **1996**, *69*, 249–255.
- [95] B. Yan, Y. Bai, Z. Chen, *J. Mol. Struct.* **2005**, *741*, 141–147.
- [96] J. Heine and K. Müller-Buschbaum, *Chem. Soc. Rev.* **2013**, *43*, 9232–9242.
- [97] F. Auzel, *J. Lumin.* **2002**, *100*, 125–130.

1.6. Abbreviations

This thesis contains many abbreviations to prevent ambiguities in combining technical terms and words. Below is the comprehensive list of abbreviations used in this thesis.

BET:	Back Energy Transfer ($\text{Ln} \rightarrow \text{T}_1$ ET)
ET:	Energy Transfer
FET:	Forward Energy Transfer ($\text{T}_1 \rightarrow \text{Ln}$ ET)
ISC:	Intersystem Crossing
KS:	Killer-Site
Ln:	Lanthanide
LnLnET:	Ln-to-Ln Energy Transfer
NIR:	Near-Infrared
PAETR:	Phonon-Assisted Energy Transfer Relaxation
S ₀ :	Singlet Ground State
S ₁ :	Singlet Excited State
SOC	Spin-Orbit Coupling
T ₁ :	Triplet Excited State
UV:	Ultraviolet

Chapter 2

THEORY

2.1. Introduction

Photophysical properties of a material can be characterized by emission and absorption spectroscopy, emission lifetime measurements, and emission quantum yield measurements. These spectroscopic methods measure photophysical properties of an ensemble of multiple emission centers within a material. The photophysical properties of a single emission center can be measured, provided that the measurement apparatus is observing an ideal system, i.e., the emission centers are homogeneous and non-interacting. In a system with inhomogeneous and interacting emission centers, the obtained data requires statistically rigorous treatment. Many of the photophysical properties of lanthanide complexes described in this thesis result from the emission from an ensemble of species that are interacting with each other. For instance, Chapter 3 describes Yb(III) ions that are distributed inhomogeneously throughout the coordination polymer host. Chapter 6 discusses the energy transfer between Tb(III) ions as well as the energy transfer of Tb(III) ions to and from the organic ligands. Although the details will be discussed in their respective chapters, these inhomogeneous and interacting system complicates the interpretation of the data.

The theory that models the dynamics of a system, in general, comprises of microscopic and macroscopic theories that are independent of each other. To a microscopic scale, each species is emitting a photon, nonradiatively relaxing to ground state, and/or transferring its energy to other species. Such properties can be calculated quantum mechanically. In section 2.2., the theories of radiative transitions and energy transfer in Ln(III) ions are reviewed. The theory of radiative transitions for Ln(III) ions is widely known as the Judd-Ofelt theory.^[1,2] The theory of energy transfer was provided by T. Kushida in 1973 under the framework of the Judd-Ofelt theory.^[3] In section 2.3., the theory for modeling and deriving the rate equation of photophysical properties of a system of interacting species is reviewed.^[4] A simple model of mononuclear Ln(III) complex is provided as an example.

2.2. Lanthanides

As mentioned in Chapter 1, the radiative transition and nonradiative energy transfer of Ln(III) ions have been extensively investigated in the early 1900s. The breakthrough in understanding the photophysical properties of Ln(III) ions came after B. R. Judd and G. S. Ofelt who separately reported a semi-empirical, quantum mechanical theory in 1962.^[1,2] The theory is commonly referred to as the “Judd-Ofelt theory,”^[5] and it is the framework for the

theory of energy transfer between Ln(III) ions by T. Kushida^[3] and the theory that was later revisited by O. L. Malta.^[6] The following subsections describe the essential part of the theory with emphasis on the applicative aspect as they will become important in the following chapters. The rigorous derivation of the equations is beyond the scope of this work and will be kept to a minimum.

The calculation of radiative transition rate constant in Judd-Ofelt theory is a multistep calculation. The basic procedure is as follows:^[5]

- 1) Calculation of reduced matrix elements for various tensor operators arising from transition dipole moment operator.
- 2) Fit the Slater radial integrals and spin-orbit coupling parameters to the experimental 4f-state energy levels to obtain the “mixed” 4f-state wavefunctions.
- 3) Calculation of theoretical oscillator strengths for electric dipole and magnetic dipole transitions between 4f-states using the “mixed” 4f-state wavefunctions.
- 4) Fit the “Judd-Ofelt” parameters (which includes 4f5d-state mixed by crystal field perturbation) to the experimental 4f-state transition oscillator strengths to obtain the transition rate constants.

The calculation of energy transfer rate constant in the study reported by T. Kushida and O. L. Malta is based on the Judd-Ofelt theory. As such, most of the parameters needed for the calculation can be directly taken from the parameters obtained in the above procedure. The focus here is the resonance mechanism, and the exchange mechanism is neglected. The details of the entire procedure are explained below.

2.1.1. Energy Levels and Wavefunctions

The 4f-electronic states in Judd-Ofelt theory are treated as a hydrogen-like atom under a central-field approximation. The intermediate coupling (electrostatic and spin-orbit interactions in a fairly equal contribution) can then be considered to provide a first-order description to the wavefunction and the energy levels of 4f-states.^[7] Finally, the effect of crystal-field is treated once again as a first-order perturbation in which experimental parameters are used.^[5]

First, the quantum numbers relevant to the initial wavefunctions (the “pure” 4f-states) are reviewed. Since the electrons only in the 4f-orbitals are being considered, the principal quantum number is $n = 4$ and the orbital angular momentum (a.k.a. azimuthal) quantum number is $l = 3$. Electrons also have intrinsic angular momentum called spin with electron spin

(projection) quantum number m_s . For a given $4f^N$ electron configuration (N being the number of electrons), there are N electron spins each with angular momentum s_i (quantum number $m_s = \pm \frac{1}{2}$) and N 4f-orbitals each with angular momentum l_i (quantum number $m_l = -3, \dots, 3$), where $i = 1, 2, \dots, N$. These two angular momenta are combined to give a total spin angular momentum $S = \sum_i s_i$ and total orbital angular momentum $L = \sum_i l_i$. Each of these momentum has quantum numbers of $M_s = -S, \dots, S$ and $M_l = -L, \dots, L$, respectively. The combination must be within the Pauli's exclusion principle, so for N 4f-electrons, there are $\frac{14!}{N!(14-N)!}$ possible combinations. At this point, the initial quantum numbers m_s and m_l can no longer represent each state and instead S and L become good quantum numbers. It should be noted that some lanthanide $4f^N$ -states have two or more states of the same S and L . These two states are distinguished by seniority quantum number α . The splitting of the zeroth-order degenerate $4f^N$ -states into these new states is caused by electrostatic coupling between electrons. Furthermore, spin-orbit coupling causes magnetic moment arising from the electron spin to be coupled with the magnetic moment arising from the electron's orbit. The resulting total angular momentum quantum number J becomes a good quantum number in this coupling. In the LS-coupling scheme (in contrast to jj-coupling), the states produced by the electrostatic coupling are further split into $J = |L - S|, |L - S + 1|, \dots, |L + S|$. These states are described using the Russel-Saunders term symbol $^{2S+1}L_J$. Finding all of the combination of angular momenta for all lanthanides shows that a lanthanide with N electrons will have same $^{2S+1}L_J$ term symbols as that with $14-N$ electrons. The term "intermediate coupling" refers to a case where the electrostatic coupling and spin-orbit coupling are approximately in the same order of energy.^[5]

Using the wavefunctions of "pure" Russel-Saunders 4f-states as a basis, the "mixed" 4f-states under the intermediate coupling scheme are calculated. The Hamiltonian for the intermediate coupling scheme is

$$H = H_{ee} + H_{SO} , \quad [2.1]$$

where H_{ee} is the electrostatic coupling Hamiltonian and H_{SO} is the spin-orbit coupling Hamiltonian. Since a hydrogen-like atom is being considered, the wavefunction $\Psi(r, \theta, \phi)$ is a product of radial wavefunction $R_{n,l}(r)$ and spherical harmonics $Y_{l,m}(\theta, \phi)$, i.e., $\Psi(r, \theta, \phi) = R_{n,l}(r)Y_{l,m}(\theta, \phi)$. For spherical harmonics, tensor operator technique can be utilized. Electrostatic coupling Hamiltonian for 4f-electrons is given by:

$$H_{ee} = \sum_{i \neq j} \frac{e^2}{4\pi\epsilon_0} \frac{1}{r_{ij}} = \frac{1}{4\pi\epsilon_0} \sum_{i \neq j} \sum_{k=0,2,4,6} C_i^{(k)} C_j^{(k)} , \quad [2.2]$$

where e , ε_0 , and r_{ij} are elementary charge, vacuum permittivity, and the distance between electron i and j . $C_q^{(k)} = \left(\frac{4\pi}{2k+1}\right)^{\frac{1}{2}} Y_{k,q}$ is the tensor operator with spherical harmonics $Y_{k,q}$. The matrix element of H_{ee} is expressed for 4f-electrons as:

$$\begin{aligned} \langle l^N SL | C_i^{(k)} C_j^{(k)} | l^N S' L' \rangle &= \delta_{SS'} \delta_{LL'} (-1)^{4 \times 3} (-1)^L (2L + 1)^2 \\ &\times \sum_{k=0,2,4,6} \begin{pmatrix} 3 & k & 3 \\ 0 & 0 & 0 \end{pmatrix}^2 \begin{Bmatrix} 3 & 3 & k \\ 3 & 3 & L \end{Bmatrix} F_{(k)} , \end{aligned} \quad [2.3]$$

where $\begin{pmatrix} a & b & c \\ d & e & f \end{pmatrix}$ and $\begin{Bmatrix} a & b & c \\ d & e & f \end{Bmatrix}$ are the Wigner 3-j symbol and Wigner 6-j symbol, respectively. These coefficients arise from the coupling of angular momentum, and allow great simplification of the calculation of the matrix elements. $F_{(k)}$ is the Slater integrals. The Dirac's delta arises from the fact that H_{ee} does not act on a spin. In order to prevent off-diagonal elements due to some lanthanides having multiple $4f^N$ -states of the same S and L , C. W. Nielson and G. F. Koster have provided matrix element in the form:

$$\langle l^N SL | H_{ee} | l^N S' L' \rangle = \sum_{p=0.1.2.3} e_p E^{(p)} \quad [2.4]$$

where e_p are coefficients listed in the book by the two authors, and $E^{(p)}$ are expressed with Slater integrals as:

$$E^{(0)} = F_{(0)} - 10F_{(2)} - 33F_{(4)} - 286F_{(6)} , \quad [2.5a]$$

$$E^{(1)} = \frac{1}{9}(70F_{(2)} + 231F_{(4)} + 2002F_{(6)}) , \quad [2.5b]$$

$$E^{(2)} = \frac{1}{9}(F_{(2)} - 3F_{(4)} + 7F_{(6)}) , \quad [2.5c]$$

$$E^{(3)} = \frac{1}{3}(5F_{(2)} + 6F_{(4)} - 91F_{(6)}) . \quad [2.5d]$$

$F_{(0)}$ is usually considered to be zero since it will only shift all of the energies in uniform and does not provide any meaningful information since the ground state energy is considered to be zero.^[5]

As for the spin-orbit coupling H_{SO} :

$$H_{SO} = \sum_i \xi(r_i) s_i \cdot l_i = \sum_i \frac{\hbar^2}{m_e^2 c^2 r_i} \frac{dU(r_i)}{dr_i} s_i \cdot l_i , \quad [2.6]$$

where \hbar , m_e , and c are Planck constant, electron mass, and the speed of light in vacuum, respectively. $\xi(r_i)$ is the spin-orbit coupling parameter that includes $U(r_i)$, the central-field potential arising from the central-field approximation.^[7] The spin-orbit coupling parameter is independent of spin and angular momenta so it is the same for all $4f^N$ -states for a given N . The matrix element of H_{SO} is expressed in a simplified form under Wigner-Eckart theorem^[8] as:

$$\begin{aligned} \langle l^N SLJ | H_{SO} | l^N S' L' J' \rangle &= \xi (-1)^{J+L+S'} \sqrt{3(3+1)(23+1)} \\ &\times \left\{ \begin{matrix} S & S' & k \\ L' & L & J \end{matrix} \right\} \langle l^N SL || V^{(11)} || l^N S' L' \rangle , \end{aligned} \quad [2.7]$$

where $\langle l^N SL || V^{(11)} || l^N S' L' \rangle$ is the reduced matrix element with tensor operator $V^{(11)}$. Equation [2.5] shows that the matrix element of H_{SO} can be split into two factors: Clebsch-Gordan coefficient (which is directly related to the Wigner 6-j symbol hence their existence in Equation [2.5]) and the reduced matrix element.^[5,7,8] The former is a geometrical factor that does not depend on the nature of the tensor operator while the latter depends on the nature of the tensor operator but does not depend on the geometrical factor. This greatly simplifies the calculation. The $V^{(11)}$ is given by:

$$\begin{aligned} \langle l^N SL || V^{(11)} || l^N S' L' \rangle &= N \sqrt{\frac{1}{2} \left(\frac{1}{2} + 1 \right) (2S+1)(2L+1)(2S'+1)(2L'+1)} \\ &\times \sum_{\psi(l^{N-1})} \langle l^{N-1} \bar{S} \bar{L} | l^N SL \rangle \left\{ \begin{matrix} S & S' & 1 \\ \frac{1}{2} & \frac{1}{2} & \bar{S} \end{matrix} \right\} \left\{ \begin{matrix} L & L' & 1 \\ 3 & 3 & \bar{L} \end{matrix} \right\} (-1)^{\bar{S}+\bar{L}+S+L+\frac{1}{2}+3+1+1} , \end{aligned} \quad [2.8]$$

where $\langle l^{N-1} \bar{S} \bar{L} | l^N SL \rangle$ is coefficient of fractional parentage and they are summed over all the $4f^{N-1}$ -states ($4f$ states of the previous atomic number). The values are available from the works of C. W. Nielson and G. F. Koster.^[9] It should be noted that the relationship between $4f^N$ and $4f^{14-N}$ lanthanides for the reduced matrix element of tensor operator of $V^{(11)}$ is:

$$\langle l^{14-N} SL || V^{(11)} || l^{14-N} S' L' \rangle = -\langle l^N SL || V^{(11)} || l^N S' L' \rangle . \quad [2.9]$$

H_{SO} contains off-diagonal matrix elements and mixes all states of the same J .

Using Equations [2.4] and [2.8], the matrix element of Equation [2.1] can be calculated. Diagonalization of Equation [2.1] along with experimental energies of $4f^N$ -states derived from absorption spectrum provides an overdetermined system of equations. Nonlinear optimization of the system of equations provides $F_{(2)}$, $F_{(4)}$, $F_{(6)}$, and ξ . Using these parameters, the ‘‘mixed’’ wavefunctions of the $4f^N$ -states $|l^N SLJ_{\text{mixed}}\rangle$ can be derived from linear combinations of ‘‘pure’’ wavefunctions $|l^N S' L' J_{\text{pure}}\rangle$:

$$|l^N SLJ_{\text{mixed}}\rangle = \sum_i c_i |l^N S' L' J_{\text{pure}}\rangle . \quad [2.10]$$

The importance of considering electrostatic and spin-orbit coupling is that these coupling sometimes leads to a significant mixture of pure wavefunctions, leading to mixed wavefunctions that do not retain almost 50% of its pure state.^[5] It is also worth mentioning that the Slater integrals $F_{(2)}$, $F_{(4)}$, $F_{(6)}$, and spin-orbit coupling parameter ξ are host-dependent values although they are similar among hosts for a same lanthanide. This means that the

optimization of the wavefunctions must be performed for every host material that is being considered.

Several things can be said about the energy levels of lanthanides presented here from the details of the theory. First, looking at the Dieke diagram^[10] (Figure 1.7a in Chapter 1) in the large energy scale, the energy levels seem symmetric in respect to Gd(III) ion. The number of configurations of 4f-electrons is equal (and so is the term symbols) for lanthanide with N and $14-N$ electrons, and the number of configurations increases from $N = 1$ to 7 and then decreases from $N = 7$ to 13 (hence Equation [2.9]).

Second, looking at the small energy scale, the energy gap between $4f^N$ -states of the same S and L is larger with an increase in the number of 4f-electrons. For example, Ce(III) and Yb(III) ions both have the same ${}^2F_{7/2}$ and ${}^2F_{5/2}$ terms but Yb(III) ion shows more than twice as large energy gap between these two terms. This is due to the stronger spin-orbit coupling parameter ξ of lanthanide with larger N (heavier atom).

2.1.2. Radiative Rate Constants

The 4f-4f transition of lanthanide is a parity forbidden transition (also known as Laporte forbidden transition). A transition moment $\vec{\mu}_{if}$ between an initial Ψ_i and a final state Ψ_f is expressed with an electric dipole moment operator $\vec{\mu}$ as $\vec{\mu}_{if} = \int \Psi_i \vec{\mu} \Psi_f d\tau$. The electric dipole moment operator and 4f-orbitals have odd parity. Therefore, the product in the integral also have odd parity if the $4f^N$ -wavefunctions of a lanthanide are odd (odd number of 4f-electrons) or even (even number of 4f-electrons). The integration over the product leads to a value of zero. This is the origin of the Laporte forbidden transition of 4f-4f transition. In reality, however, the 4f-4f transitions of lanthanides are observed both in the absorption and emission spectra. The premise of the Judd-Ofelt theory is that the energetically close state, i.e., the $4f^{N-1}5d$ -state, is mixed into the $4f^N$ -state wavefunctions by crystal field perturbation:^[1,2,5]

$$|l^N SLJ_{\text{actual}}\rangle = |l^N SLJ_{\text{mixed}}\rangle + \sum_{\varphi_{n,l}} \left\{ \frac{\langle l^N SLJ_{\text{mixed}} | V | \varphi_{n,l} \rangle}{E(l^N SLJ_{\text{mixed}}) - E(\varphi_{n,l})} | \varphi_{n,l} \rangle \right\}, \quad [2.11]$$

where $|l^N SLJ_{\text{actual}}\rangle$ and $|\varphi_{n,l}\rangle$ are wavefunction of $4f^N$ -state after mixture of even parity states and wavefunction of the even parity state, respectively. V represents the crystal field interaction operator. With an electric dipole moment operator in tensor operator form, the matrix element of the electric dipole moment is:

$$\begin{aligned} \langle l^N SLJ_{\text{actual}} | D_q^{(1)} | l^N S'L'J'_{\text{actual}} \rangle &= \sum_{\varphi_{n,l}} \left\{ \frac{\langle l^N SLJ_{\text{mixed}} | V | \varphi_{n,l} \rangle \langle l^N S'L'J'_{\text{mixed}} | D_q^{(1)} | \varphi_{n,l} \rangle}{E(l^N SLJ) - E(\varphi_{n,l})} \right. \\ &\quad \left. + \frac{\langle l^N S'L'J'_{\text{mixed}} | V | \varphi_{n,l} \rangle \langle l^N SLJ_{\text{mixed}} | D_q^{(1)} | \varphi_{n,l} \rangle}{E(l^N S'L'J') - E(\varphi_{n,l})} \right\}. \end{aligned} \quad [2.12]$$

In order to simplify Equation [2.12], two rough assumptions are made: 1) even parity states are all degenerate, and 2) $E(l^N SLJ) - E(\varphi_{n,l}) = E(l^N S'L'J') - E(\varphi_{n,l})$. With these assumptions, the oscillator strength of electric dipole transition f_{ED} :

$$f_{\text{ED}} = \frac{8\pi^2 m_e v_{\text{abs}}}{3h} \chi_{\text{abs}} \sum_{\lambda=2,4,6} \Omega_{\lambda} |\langle l^N SLJ_{\text{mixed}} \| U^{(\lambda)} \| l^N S'L'J'_{\text{mixed}} \rangle|^2, \quad [2.13]$$

where v_{abs} , h , and χ_{abs} are the absorption frequency, Planck constant, and local-field correction ($\chi_{\text{abs}} = \{(n^2+2)/3\}^2$ in the Lorentz model, where n is refractive index). Ω_{λ} are the Judd-Ofelt parameters. The reduced matrix element $\langle l^N SLJ_{\text{mixed}} \| U^{(\lambda)} \| l^N S'L'J'_{\text{mixed}} \rangle$ can be expanded using Equation [2.10] as:

$$\langle l^N SLJ_{\text{mixed}} \| U^{(\lambda)} \| l^N S'L'J'_{\text{mixed}} \rangle = \sum_{i,j} c_i c_j \langle l^N SLJ_{\text{pure}} \| U^{(\lambda)} \| l^N S'L'J'_{\text{pure}} \rangle. \quad [2.14]$$

$\langle l^N SLJ_{\text{pure}} \| U^{(\lambda)} \| l^N S'L'J'_{\text{pure}} \rangle$ is expressed by tensor operator technique as:

$$\begin{aligned} \langle l^N SLJ \| U^{(\lambda)} \| l^N S'L'J' \rangle \\ = (-1)^{S+L'+J+\lambda} \sqrt{(2J+1)(2J'+1)} \begin{Bmatrix} J & J' & \lambda \\ L' & L & S \end{Bmatrix} \langle l^N SL \| U^{(\lambda)} \| l^N SL' \rangle, \end{aligned} \quad [2.15]$$

in which $\langle l^N SL \| U^{(\lambda)} \| l^N SL' \rangle$ can be further reduced to:

$$\begin{aligned} \langle l^N SL \| U^{(\lambda)} \| l^N SL' \rangle \\ = N \sqrt{(2L+1)(2L'+1)} \sum_{\psi(l^{N-1})} \langle l^{N-1} \bar{S} L | l^N SL \rangle \begin{Bmatrix} L & l & \bar{L} \\ l & L' & \lambda \end{Bmatrix} (-1)^{\bar{L}+L+l+\lambda}. \end{aligned} \quad [2.16]$$

Here, like Equation [2.9]:

$$\langle l^{14-N} SL \| U^{(\lambda)} \| l^{14-N} SL' \rangle = -(-1)^{\lambda} \langle l^N SL \| U^{(\lambda)} \| l^N SL' \rangle. \quad [2.17]$$

Meanwhile, the oscillator strength of magnetic dipole transition f_{MD} is:

$$f_{\text{MD}} = \frac{hv_{\text{abs}}}{6m_e c^2} \frac{n}{2J+1} |\langle l^N SLJ_{\text{mixed}} \| L + gS \| l^N S'L'J'_{\text{mixed}} \rangle|^2. \quad [2.18]$$

Similarly to Equation [2.13], the reduced matrix element can be expanded with pure wavefunctions. Magnetic-dipole transitions are allowed when $\Delta J = 0, \pm 1$. The reduced matrix element can be calculated by:

$$\langle l^N SLJ \| L + gS \| l^N SLJ' \rangle = (g-1) \sqrt{\frac{(S+L+J+1)(J+L-S)(J+S-L)(S+L-J+1)}{4J}}, \quad [2.19]$$

for $J' = J - 1$ and

$$\langle l^N SLJ \| L + gS \| l^N SLJ' \rangle = g \sqrt{J(J+1)(2J+1)}, \quad [2.20]$$

for $J' = J$, where $g = 2.002319304362 \dots$ is the g-factor of the electron. Unlike the oscillator strength of electric dipole transition f_{ED} , there is no Judd-Ofelt parameter Ω_λ . Therefore, the value of f_{MD} can be calculated unlike f_{ED} , which requires optimization of Judd-Ofelt parameters Ω_λ from experimental oscillator strengths.

From the oscillator strength obtained from the absorption spectra of a lanthanide in a material under investigation, the value of total oscillator strength f_{tot} is derived:

$$f_{tot} = f_{ED} + f_{MD} . \quad [2.21]$$

After obtaining oscillator strength for multiple transitions, they are fitted to Equation [2.13] to yield an overdetermined system of equations. Through optimization, the values of the Judd-Ofelt parameters Ω_λ can be obtained.

The radiative rate constant A_{rad} is composed of electric dipole transition $A_{rad(ED)}$ and magnetic dipole transition $A_{rad(MD)}$ and they are given by the following equations:

$$A_{rad} = A_{rad(ED)} + A_{rad(MD)} , \quad [2.22]$$

$$A_{rad(ED)} = \frac{2\pi\nu_{em}^2 e^2}{\epsilon_0 c^3 m} n^2 f_{ED} , \quad [2.23]$$

$$A_{rad(MD)} = \frac{2\pi\nu_{em}^2 e^2}{\epsilon_0 c^3 m} n^2 f_{MD} . \quad [2.24]$$

2.1.3. Energy Transfer Rate Constants

The derivation of energy transfer matrix element between two Ln(III) ions can be expressed by using the operator for Coulomb interaction between two Ln(III) ions. As stated in the beginning of this section, exchange interaction will be neglected. With tensor operator technique for diatomic molecules, the operator for resonance interaction is:

$$H_{AB} = e^2 \sum_{q_1, q_2}^{k_1, k_2} (-1)^{k_1} \left\{ \frac{(2k_1 + 2k_2 + 1)}{(2k_1)!(2k_2)!} \right\}^{\frac{1}{2}} \begin{pmatrix} k_1 & k_2 & k_1 + k_2 \\ q_1 & q_2 & -(q_1 + q_2) \end{pmatrix} \frac{C_{q_1 + q_2}^{k_1 + k_2}}{R^{k_1 + k_2 + 1}} D_{A q_1}^{(k_1)} D_{B q_2}^{(k_2)} , \quad [2.25]$$

where R is the distance between atom A and B, and $D_{A q_1}^{(k_1)}$ and $D_{B q_2}^{(k_2)}$ are the electric multipole operator ($D_q^{(k)} = \sum_i r_i^k C_q^{(k)}$) for A and B centers, respectively. Calculating the squared matrix elements using this operator leads to infinite series of interaction types, e.g., dipole-dipole, dipole-quadrupole (and vise-versa), quadrupole-quadrupole, quadrupole-hexadecapole, and so on.^[11] However, the theoretical energy transfer rate constant reported by T. Kushida^[12] under the formulation of Judd-Ofelt theory concluded that higher-order interactions above quadrupole-quadrupole could be neglected in most cases. Since the interaction between Ln(III)

ions are very small, H_{AB} can be considered as a perturbation to the system. Inserting the matrix element of the energy transfer into the Fermi's Golden rule, the rate constant of the energy transfer is given by:

$$W_{ET} = \frac{2\pi}{\hbar} |\langle AB|H_{AB}|A'B'\rangle|^2 F, \quad [2.26]$$

where $F (= \int S_{A \rightarrow A'}(E) S_{B \rightarrow B'}(E) dE)$ is the spectral overlap between the transitions of A and B to A' and B' , respectively. For dipole-dipole, dipole-quadrupole (and vice-versa), and quadrupole-quadrupole interaction of energy transfer between two Ln(III) ions A and B , the rate constants are:

$$W_{ET(dd)} = \frac{1}{(2J_a+1)(2J_b+1)} \frac{2}{3} \frac{4\pi^2}{h} \frac{e^4}{R^6} \left[\sum_{\lambda=2,4,6} \Omega_{\lambda}^A |\langle l^N SLJ \| U^{(\lambda)} \| l^N S' L' J' \rangle|^2 \right] \\ \times \left[\sum_{\lambda=2,4,6} \Omega_{\lambda}^B |\langle l^N SLJ \| U^{(\lambda)} \| l^N S' L' J' \rangle|^2 \right] F, \quad [2.27]$$

$$W_{ET(dq)} = \frac{1}{(2J_a+1)(2J_b+1)} \frac{4\pi^2}{h} \frac{e^4}{R^8} \left[\sum_{\lambda=2,4,6} \Omega_{\lambda}^A |\langle l^N SLJ \| U^{(\lambda)} \| l^N S' L' J' \rangle|^2 \right] \\ \times \left[|\langle 4f \| r_B^2 \| 4f \rangle|^2 |\langle l \| C^{(2)} \| l \rangle|^2 |\langle l^N SLJ \| U^{(2)} \| l^N S' L' J' \rangle|^2 \right] F, \quad [2.28]$$

$$W_{ET(qq)} = \frac{1}{(2J_a+1)(2J_b+1)} \frac{14}{5} \frac{4\pi^2}{h} \frac{e^4}{R^{10}} |\langle l \| C^{(2)} \| l \rangle|^4 \left[|\langle 4f \| r_A^2 \| 4f \rangle|^2 |\langle l^N SLJ \| U^{(2)} \| l^N S' L' J' \rangle|^2 \right] \\ \times \left[|\langle 4f \| r_B^2 \| 4f \rangle|^2 |\langle l^N SLJ \| U^{(2)} \| l^N S' L' J' \rangle|^2 \right] F, \quad [2.29]$$

where R , $\langle l \| C^{(2)} \| l \rangle$, $\langle 4f \| r_A^2 \| 4f \rangle$, and $\langle l^N SLJ \| U^{(2)} \| l^N S' L' J' \rangle$ are the distance between Ln(III) ions, one-electron reduced matrix element, and reduced matrix elements of the tensor operator $U^{(2)}$ that is calculated from Equation [2.15] and [2.16]. The mixed wavefunctions due to intermediate coupling must also be accounted for in the reduced matrix elements. $\langle l \| C^{(2)} \| l \rangle$ is calculated by the following equation:

$$\langle l \| C^{(2)} \| l \rangle = (-1)^l (2l+1) \begin{pmatrix} l & 2 & l \\ 0 & 0 & 0 \end{pmatrix}. \quad [2.30]$$

The values of $\langle 4f \| r_A^2 \| 4f \rangle$ for Ln(III) ions are provided in the literature.^[3] F is conveniently expressed as the overlap integral of emission and absorption given by the following equation:^[6]

$$F = \frac{\ln 2}{\sqrt{\pi}} \frac{1}{\hbar\gamma_D \hbar\gamma_A} \sqrt{\left\{ \left(\frac{1}{\hbar\gamma_D} \right)^2 + \left(\frac{1}{\hbar\gamma_A} \right)^2 \right\} \ln 2} \times \exp \left[\frac{1}{4} \frac{\left(\frac{2\Delta}{\hbar\gamma_D^2 \ln 2} \right)^2}{\left\{ \left(\frac{1}{\hbar\gamma_D} \right)^2 + \left(\frac{1}{\hbar\gamma_A} \right)^2 \right\} \ln 2} - \left(\frac{\Delta}{\hbar\gamma_D} \right)^2 \ln 2 \right], \quad [2.31]$$

where $\hbar\gamma_D$, $\hbar\gamma_A$, and Δ are FWHM of emission, FWHM of absorption, and the centroid-to-centroid gap between emission and absorption, respectively.

$W_{ET(dd)}$ and $W_{ET(dq)}$ (Equations [2.27] and [2.28]) contain the Judd-Ofelt parameter Ω_{λ} . Under the assumption that the 4f-state wavefunctions are already optimized ($\langle l^N SLJ_{\text{mixed}} \rangle$), the

energy transfer rate constants can still be calculated without Ω_λ because the equation only requires the value for the entire sum of the reduced matrix element. Looking at the total oscillator strength f_{tot} in Equation [2.21], which can be derived experimentally through absorption spectroscopy, the oscillator strength of electric dipole transition f_{ED} can be determined once f_{MD} is calculated from Equation [2.18]. From Equation [2.13], the sum of the matrix elements can be calculated, and thus the values for $W_{\text{ET}(\text{dd})}$ and $W_{\text{ET}(\text{dq})}$ as well.

2.3. Kinetic Analysis of Excited State

Kinetics dominate any photophysical processes in a material. In the simplest case (such as two-level system), it is sometimes easy to visualize the excited state dynamics. However, a process such as energy transfer that could cause interaction between emitting species to span over a large spatial area could lead to a complicated excited state dynamics. The photophysical properties of a system with interactions are sometimes hard to intuitively understand and analyze. This is especially common for an inhomogeneous system where local dynamics are significantly different from the other parts of the system. Kinetic analysis is a powerful tool to model and analyze a system mathematically.^[4]

Consider N species where each species i ($i = 1, 2, \dots, N$) is transitioning from ground to excited state and vice-versa, with or without interaction with another species. Let all of the processes to be a linear processes, meaning that the order of process of all processes are one, in contrast to a nonlinear process where the order of process is not one. Quantum cutting is one example of a nonlinear process because it produces two excited states from one excited state in a single process. The population density of the entire system is constant and normalized in a closed system, that is:

$$\sum_i x_i(t) + \sum_i x_i'(t) = 1 \quad [2.32]$$

where $x_i(t)$ and $x_i'(t)$ are the i th species at excited and ground state, respectively. Let the population density of ground states be significantly larger than excited states (excitation source with reasonable power is being used), i.e. $\sum_i x_i(t) \ll \sum_i x_i'(t) = 1$ (steady state approximation). With these premises, a system of N linear differential equations are expressed as:

$$\begin{aligned} \frac{d}{dt} x_1(t) &= A_{1,1}x_1(t) + A_{2,1}x_2(t) + \dots + A_{N,1}x_N(t), \\ \frac{d}{dt} x_2(t) &= A_{1,2}x_1(t) + A_{2,2}x_2(t) + \dots + A_{N,2}x_N(t), \end{aligned}$$

$$\frac{d}{dt}x_N(t) = A_{1,N}x_1(t) + A_{2,N}x_2(t) + \cdots + A_{N,N}x_N(t), \quad [2.33]$$

where $A_{i,j}$ ($i \neq j$) is the interaction rate constant involving $x_i(t)$ and $x_j(t)$. $A_{i,i}$ is the relaxation rate constant of $x_i(t)$. At this point, the system is closed and there is no excitation source to produce any excited state. So we add input functions $J_i(t)$ to Equations [2.33]:

$$\begin{aligned} \frac{d}{dt}x_1(t) &= A_{1,1}x_1(t) + A_{2,1}x_2(t) + \cdots + A_{N,1}x_N(t) + J_1(t), \\ \frac{d}{dt}x_2(t) &= A_{1,2}x_1(t) + A_{2,2}x_2(t) + \cdots + A_{N,2}x_N(t) + J_2(t), \\ &\vdots \\ \frac{d}{dt}x_N(t) &= A_{1,N}x_1(t) + A_{2,N}x_2(t) + \cdots + A_{N,N}x_N(t) + J_N(t). \end{aligned} \quad [2.34]$$

This is now a system of inhomogeneous N linear differential equations. It is possible to write Equation [2.32] in the matrix form:

$$\frac{d}{dt}\mathbf{X}(t) = \mathbf{A}\mathbf{X}(t) + \mathbf{J}(t), \quad [2.35]$$

$$\text{where } \mathbf{X}(t) = \begin{pmatrix} x_1(t) \\ x_2(t) \\ \vdots \\ x_N(t) \end{pmatrix}, \quad [2.36]$$

$$\mathbf{A} = \begin{pmatrix} A_{1,1} & A_{2,1} & \cdots & A_{N,1} \\ A_{1,2} & A_{2,2} & & \vdots \\ \vdots & & \ddots & \vdots \\ A_{1,N} & \cdots & \cdots & A_{N,N} \end{pmatrix}, \quad [2.37]$$

$$\mathbf{J}(t) = \begin{pmatrix} J_1(t) \\ J_2(t) \\ \vdots \\ J_N(t) \end{pmatrix}. \quad [2.38]$$

There is no mathematical difficulty in deriving Equation [2.35]. The matrix multiplication in Equation [2.35] will easily yield Equation [2.34]. Let the excitation begin at $t = 0$, and the analytical solution of [2.35] is:

$$\mathbf{X}(t) = \int_0^t \exp\{(t-t')\mathbf{A}\}\mathbf{J}(t')dt'. \quad [2.39]$$

Using this equation, it is possible to solve for $\mathbf{X}(t)$ with $\mathbf{J}(t)$ of impulse function, corresponding to a pulse excitation, or a constant, corresponding to a steady state excitation.

2.2.1. Rate Equation for Impulse Excitation

Solving the rate equation $\mathbf{X}(t)$ with $\mathbf{J}(t)$ of impulse function leads to population density directly related to emission lifetimes. Emission lifetimes are linearly proportional to the population density. Let only the species $i = 1$ is excited, and then the input function $\mathbf{J}(t)$ can be expressed as:

$$\mathbf{J}(t) = \begin{pmatrix} J_1(t) \\ J_2(t) \\ \vdots \\ J_N(t) \end{pmatrix} = j_1 \begin{pmatrix} \delta(t) \\ 0 \\ \vdots \\ 0 \end{pmatrix}, \quad [2.40]$$

where j_1 is the amplitude of the input, which for convenience will be set to 1. The impulse function, or the Dirac delta function $\delta(x)$ is defined (actually one of the definitions) as:

$$\int_{a-\epsilon}^{a+\epsilon} f(x)\delta(x-a)dx = f(a) \quad (\epsilon > 0). \quad [2.41]$$

Using Equation [2.41], Equation [2.39] with input function defined in Equation [2.40] is further solved to give:

$$\mathbf{X}(t) = \exp(\mathbf{A}t)\mathbf{B}, \quad [2.42]$$

$$\text{where } \mathbf{B} = \begin{pmatrix} j_1 \\ 0 \\ \vdots \\ 0 \end{pmatrix} = \begin{pmatrix} 1 \\ 0 \\ \vdots \\ 0 \end{pmatrix}. \quad [2.43]$$

$\exp(\mathbf{A}t)$ is called matrix exponential. Equation [2.42] is now an eigenvalue problem and diagonalization of the matrix exponential leads to the rate equations for each $x_i(t)$. Equation [2.42] may not be solved analytically for $N > 4$ with some exception. However, unlike the numerical methods to solve for differential equation in the form of Equation [2.34] (such as 4th order Runge-Kutta method), many numerical (iterative) methods for the diagonalization of matrices are comparatively accurate and faster in the practical level.

2.2.2. Rate Equation for Constant Excitation

Solving the rate equation $\mathbf{X}(t)$ with $\mathbf{J}(t)$ of constant leads to population density related to quantum yields. Let only the species $i = 1$ is excited, and then the input function $\mathbf{J}(t)$ can be expressed as:

$$\mathbf{J}(t) = \begin{pmatrix} J_1(t) \\ J_2(t) \\ \vdots \\ J_N(t) \end{pmatrix} = j_1 \begin{pmatrix} 1 \\ 0 \\ \vdots \\ 0 \end{pmatrix}, \quad [2.44]$$

where j_1 is the amplitude of the input, which for convenience will be set to 1 once again. Equation [2.39] with input function defined in Equation [2.44] is further solved to give:

$$\mathbf{X}(t) = \mathbf{A}^{-1}\{\exp(\mathbf{A}t) - \mathbf{I}\}\mathbf{B}, \quad [2.45]$$

$$\text{where } \mathbf{B} = \begin{pmatrix} j_1 \\ 0 \\ \vdots \\ 0 \end{pmatrix} = \begin{pmatrix} 1 \\ 0 \\ \vdots \\ 0 \end{pmatrix}. \quad [2.46]$$

2.2.3. Simple Mononuclear Case

The simplest form of mononuclear Ln(III) complex is shown in Figure 1.8a and the simplest mechanism is shown in Figure 1.8b of Chapter 1. The rate equations are derived for this simple case with BET as an example of kinetic analysis. Absorption of a photon leads to a transition from singlet ground state S_0 of the ligand to singlet excited state S_1 and is immediately followed by intersystem crossing to the triplet excited state T_1 . Energy transfer from the T_1 state to two-level Ln(III) ion leads to excited state of Ln(III) ion (Ln^*). The rate equation for this system is:

$$\frac{d}{dt}\mathbf{X}(t) = \mathbf{A}\mathbf{X}(t) + \mathbf{J}(t), \quad [2.35]$$

$$\mathbf{X}(t) = \begin{pmatrix} S_1(t) \\ T_1(t) \\ \text{Ln}^*(t) \end{pmatrix}, \quad [2.47]$$

$$\mathbf{A} = \begin{pmatrix} -a_{11} & 0 & 0 \\ a_{21} & -a_{22} & a_{23} \\ 0 & a_{32} & -a_{33} \end{pmatrix}, \quad [2.48]$$

where

$$a_{11} = kr_{S_1} + knr_{S_1} + k_{\text{ISC}}, \quad [2.49]$$

$$a_{21} = k_{\text{ISC}}, \quad [2.50]$$

$$a_{22} = kr_{T_1} + knr_{T_1} + k_{\text{FET}}, \quad [2.51]$$

$$a_{23} = k_{\text{BET}}, \quad [2.52]$$

$$a_{33} = kr_{\text{Ln}^*} + knr_{\text{Ln}^*} + k_{\text{BET}}, \quad [2.53]$$

$$a_{32} = k_{\text{FET}}, \quad [2.54]$$

and k_{ISC} , kr , knr , k_{FET} , and k_{BET} are defined as intersystem-crossing, radiative, nonradiative, FET, and BET, respectively. The subscript indicates a species.

For both the impulse and constant excitations, analytical solution is available because solving for $\mathbf{X}(t)$ is an eigenvalue problem of 3×3 square matrix. Eigenvalue problem of 3×3

square matrix is essentially about solving the cubic equation in which an algebraic solution is available. For impulse excitation, the rate equations are:

$$S_1(t) = \exp(-a_{11}t), \quad [2.55]$$

$$T_1(t) = \frac{a_{21}}{4(a_{11}a_{22} + a_{11}a_{33} - a_{22}a_{33} + a_{23}a_{32} - a_{11}^2)} \left\{ 4(a_{11} - a_{33})\exp(-a_{11}t) + \frac{(-a_{22} + a_{33} - \sqrt{a_{22}^2 - 2a_{22}a_{33} + a_{33}^2 + 4a_{23}a_{32}})(2a_{11} - a_{22} - a_{33} + \sqrt{a_{22}^2 - 2a_{22}a_{33} + a_{33}^2 + 4a_{23}a_{32}})}{\sqrt{a_{22}^2 - 2a_{22}a_{33} + a_{33}^2 + 4a_{23}a_{32}}} \exp\left(-\frac{a_{22} + a_{33} + \sqrt{a_{22}^2 - 2a_{22}a_{33} + a_{33}^2 + 4a_{23}a_{32}}}{2}t\right) - \frac{(a_{22} + a_{33} + \sqrt{a_{22}^2 - 2a_{22}a_{33} + a_{33}^2 + 4a_{23}a_{32}})(-2a_{11} + a_{22} + a_{33} + \sqrt{a_{22}^2 - 2a_{22}a_{33} + a_{33}^2 + 4a_{23}a_{32}})}{\sqrt{a_{22}^2 - 2a_{22}a_{33} + a_{33}^2 + 4a_{23}a_{32}}} \exp\left(-\frac{a_{22} + a_{33} - \sqrt{a_{22}^2 - 2a_{22}a_{33} + a_{33}^2 + 4a_{23}a_{32}}}{2}t\right) \right\}, \quad [2.56]$$

$$Ln^*(t) = \frac{a_{21}a_{32}}{2(a_{11}a_{22} + a_{11}a_{33} - a_{22}a_{33} + a_{23}a_{32} - a_{11}^2)} \left\{ -2\exp(-a_{11}t) + \frac{2a_{11} - a_{22} - a_{33} + \sqrt{a_{22}^2 - 2a_{22}a_{33} + a_{33}^2 + 4a_{23}a_{32}}}{\sqrt{a_{22}^2 - 2a_{22}a_{33} + a_{33}^2 + 4a_{23}a_{32}}} \exp\left(-\frac{a_{22} + a_{33} + \sqrt{a_{22}^2 - 2a_{22}a_{33} + a_{33}^2 + 4a_{23}a_{32}}}{2}t\right) + \frac{-2a_{11} + a_{22} + a_{33} + \sqrt{a_{22}^2 - 2a_{22}a_{33} + a_{33}^2 + 4a_{23}a_{32}}}{\sqrt{a_{22}^2 - 2a_{22}a_{33} + a_{33}^2 + 4a_{23}a_{32}}} \exp\left(-\frac{a_{22} + a_{33} - \sqrt{a_{22}^2 - 2a_{22}a_{33} + a_{33}^2 + 4a_{23}a_{32}}}{2}t\right) \right\}. \quad [2.57]$$

These population density equations are exponential equations. The emission decay profile and population density are equivalent regarding lifetimes since emission intensity is proportional to the population density. Thus the emission lifetime is defined as the amount of time it takes for the intensity to drop to $1/e$ of the initial intensity. The equations are quite complicated but by breaking down the equations into terms and interpreting them each, the equations provide meaningful information. Equation [2.55] is a straight forward equation that represents the time evolution of the S_1 state. Equation [2.56] has three terms. The first term represents the contribution of S_1 state decay and corresponds to the rise of the time evolution of the T_1 state. The second term represents the decay of the T_1 state. The last term represents the contribution of the BET from the Ln^* state. For Equation [2.57], it can be seen that the BET contributes directly into the Ln^* state, similar to the second term of Equation [2.56]. BET mixes pure T_1 and Ln^* state dynamics into mixed dynamics. In the absence of BET, the equations become much simpler:

$$S_1(t) = \exp(-a_{11}t), \quad [2.55']$$

$$T_1(t) = \frac{a_{21}}{2(a_{22} - a_{33})(a_{11}a_{22} + a_{11}a_{33} - a_{22}a_{33} - a_{11}^2)} \{ 2(a_{22} - a_{33})(a_{11} - a_{33})\exp(-a_{11}t) - 2(a_{11} - a_{33})\exp(-a_{22}t) + a_{22}(a_{11} - a_{22})\exp(-a_{33}t) \}, \quad [2.56']$$

$$Ln^*(t) = \frac{a_{21}a_{32}}{(a_{22} - a_{33})(a_{11}a_{22} + a_{11}a_{33} - a_{22}a_{33} - a_{11}^2)} \{ -(a_{22} - a_{33})\exp(-a_{11}t) + (a_{11} - a_{33})\exp(-a_{22}t) - (a_{11} - a_{22})\exp(-a_{33}t) \}. \quad [2.57']$$

Now the exponential terms of these three equations are pure. In most cases, S_1 and T_1 states have very short lifetimes ($a_{11} \gg a_{22} \gg a_{33}$), and Equation [2.57'] can be further simplified to:

$$\text{Ln}^*(t) = \frac{a_{21}a_{32}}{(a_{22}-a_{33})(a_{11}-a_{33})} \exp(-a_{33}t) = \text{Ln}^*(0)\exp(-a_{33}t) . \quad [2.57'']$$

This equation is now the commonly seen emission decay with lifetime of $\frac{1}{a_{33}} = \frac{1}{kr_{\text{Ln}^*} + knr_{\text{Ln}^*}} = \tau_{\text{obs}}$ in literature. Equation [2.57''] is merely an equation derived with the assumption that the S_1 and T_1 states have short lifetimes compared to the excited state of Ln(III) ion. Sometimes, however, T_1 states may have a long lifetime (still shorter than Ln(III)) with those of Ln(III) ion. In that case, the emission decay profile of Ln(III) will have an initial rise in the intensity corresponding to the donor lifetime (= T_1 state).

For constant excitation, the rate equations are:

$$S_1(t) = -\frac{1}{a_{11}} \{ \exp(-a_{11}t) - 1 \} , \quad [2.58]$$

$$\begin{aligned} T_1(t) = & -\frac{a_{21}}{a_{22}a_{33}-a_{23}a_{32}} \left[\frac{a_{33}}{4(a_{11}a_{22}-a_{11}^2+a_{11}a_{33}-a_{22}a_{33}+a_{23}a_{32})} \{ 4(a_{11}-a_{33})\exp(-a_{11}t) \right. \\ & - \frac{(a_{22}-a_{33}+\sqrt{a_{22}^2-2a_{22}a_{33}+a_{33}^2+4a_{23}a_{32}})(2a_{11}-a_{22}-a_{33}+\sqrt{a_{22}^2-2a_{22}a_{33}+a_{33}^2+4a_{23}a_{32}})}{\sqrt{a_{22}^2-2a_{22}a_{33}+a_{33}^2+4a_{23}a_{32}}} \exp\left(-\frac{a_{22}+a_{33}-\sqrt{a_{22}^2-2a_{22}a_{33}+a_{33}^2+4a_{23}a_{32}}}{2}t\right) \\ & \left. - \frac{(a_{22}-a_{33}-\sqrt{a_{22}^2-2a_{22}a_{33}+a_{33}^2+4a_{23}a_{32}})(a_{22}-2a_{11}+a_{33}+\sqrt{a_{22}^2-2a_{22}a_{33}+a_{33}^2+4a_{23}a_{32}})}{\sqrt{a_{22}^2-2a_{22}a_{33}+a_{33}^2+4a_{23}a_{32}}} \exp\left(-\frac{a_{22}+a_{33}+\sqrt{a_{22}^2-2a_{22}a_{33}+a_{33}^2+4a_{23}a_{32}}}{2}t\right) \right\} \\ & + \frac{a_{23}a_{32}}{2(a_{11}a_{22}-a_{11}^2+a_{11}a_{33}-a_{22}a_{33}+a_{23}a_{32})} \{ -2\exp(-a_{11}t) \\ & + \frac{2a_{11}-a_{22}-a_{33}+\sqrt{a_{22}^2-2a_{22}a_{33}+a_{33}^2+4a_{23}a_{32}}}{\sqrt{a_{22}^2-2a_{22}a_{33}+a_{33}^2+4a_{23}a_{32}}} \exp\left(-\frac{a_{22}+a_{33}+\sqrt{a_{22}^2-2a_{22}a_{33}+a_{33}^2+4a_{23}a_{32}}}{2}t\right) \\ & + \frac{a_{22}-2a_{11}+a_{33}+\sqrt{a_{22}^2-2a_{22}a_{33}+a_{33}^2+4a_{23}a_{32}}}{\sqrt{a_{22}^2-2a_{22}a_{33}+a_{33}^2+4a_{23}a_{32}}} \exp\left(-\frac{a_{22}+a_{33}-\sqrt{a_{22}^2-2a_{22}a_{33}+a_{33}^2+4a_{23}a_{32}}}{2}t\right) \} \\ & + \frac{a_{33}}{a_{11}} \{ \exp(-a_{11}t) - 1 \} , \end{aligned} \quad [2.59]$$

$$\begin{aligned} \text{Ln}^*(t) = & -\frac{a_{21}a_{32}}{a_{22}a_{33}-a_{23}a_{32}} \left[\frac{1}{4(a_{11}a_{22}-a_{11}^2+a_{11}a_{33}-a_{22}a_{33}+a_{23}a_{32}-a_{11}^2)} \{ 4(a_{11}-a_{33})\exp(-a_{11}t) \right. \\ & - \frac{(a_{22}-a_{33}+\sqrt{a_{22}^2-2a_{22}a_{33}+a_{33}^2+4a_{23}a_{32}})(2a_{11}-a_{22}-a_{33}+\sqrt{a_{22}^2-2a_{22}a_{33}+a_{33}^2+4a_{23}a_{32}})}{\sqrt{a_{22}^2-2a_{22}a_{33}+a_{33}^2+4a_{23}a_{32}}} \exp\left(-\frac{a_{22}+a_{33}+\sqrt{a_{22}^2-2a_{22}a_{33}+a_{33}^2+4a_{23}a_{32}}}{2}t\right) \\ & \left. - \frac{(a_{22}-a_{33}-\sqrt{a_{22}^2-2a_{22}a_{33}+a_{33}^2+4a_{23}a_{32}})(a_{22}-2a_{11}+a_{33}+\sqrt{a_{22}^2-2a_{22}a_{33}+a_{33}^2+4a_{23}a_{32}})}{\sqrt{a_{22}^2-2a_{22}a_{33}+a_{33}^2+4a_{23}a_{32}}} \exp\left(-\frac{a_{22}+a_{33}-\sqrt{a_{22}^2-2a_{22}a_{33}+a_{33}^2+4a_{23}a_{32}}}{2}t\right) \right\} \\ & + \frac{a_{22}}{2(a_{11}a_{22}-a_{11}^2+a_{11}a_{33}-a_{22}a_{33}+a_{23}a_{32})} \{ -2\exp(-a_{11}t) \\ & + \frac{1}{(2a_{11}-a_{22}-a_{33}+\sqrt{a_{22}^2-2a_{22}a_{33}+a_{33}^2+4a_{23}a_{32}})\sqrt{a_{22}^2-2a_{22}a_{33}+a_{33}^2+4a_{23}a_{32}}} \exp\left(-\frac{a_{22}+a_{33}+\sqrt{a_{22}^2-2a_{22}a_{33}+a_{33}^2+4a_{23}a_{32}}}{2}t\right) \\ & + \frac{1}{(a_{22}-2a_{11}+a_{33}+\sqrt{a_{22}^2-2a_{22}a_{33}+a_{33}^2+4a_{23}a_{32}})\sqrt{a_{22}^2-2a_{22}a_{33}+a_{33}^2+4a_{23}a_{32}}} \exp\left(-\frac{a_{22}+a_{33}-\sqrt{a_{22}^2-2a_{22}a_{33}+a_{33}^2+4a_{23}a_{32}}}{2}t\right) \} \\ & + \frac{1}{a_{11}} \{ \exp(-a_{11}t) - 1 \} . \end{aligned} \quad [2.60]$$

The rate equation seems complicated at first, but considering that the emission lifetime of Ln(III) ions is in the order of milliseconds, at sufficient elapsed time (order of seconds), above equations reduce to:

$$S_1 = \frac{1}{a_{11}} = \frac{1}{kr_{S_1} + knr_{S_1} + k_{\text{ISC}}} , \quad [2.58']$$

$$T_1 = \frac{a_{21}a_{33}}{a_{11}(a_{22}a_{33}-a_{23}a_{32})} = \frac{k_{ISC}}{kr_{S_1}+knr_{S_1}+k_{ISC}} \times \frac{kr_{Ln^*}+knr_{Ln^*}+k_{BET}}{(kr_{T_1}+knr_{T_1}+k_{FET})(kr_{Ln^*}+knr_{Ln^*}+k_{BET})-k_{BET}k_{FET}}$$

$$= \eta_{ISC} \times \frac{kr_{Ln^*}+knr_{Ln^*}+k_{BET}}{(kr_{T_1}+knr_{T_1}+k_{FET})(kr_{Ln^*}+knr_{Ln^*}+k_{BET})-k_{BET}k_{FET}}, \quad [2.59']$$

$$Ln^* = \frac{a_{21}a_{32}}{a_{11}(a_{22}a_{33}-a_{23}a_{32})} = \frac{k_{ISC}}{kr_{S_1}+knr_{S_1}+k_{ISC}} \times \frac{k_{FET}}{(kr_{T_1}+knr_{T_1}+k_{FET})(kr_{Ln^*}+knr_{Ln^*}+k_{BET})-k_{BET}k_{FET}}$$

$$= \eta_{ISC} \times \frac{k_{FET}}{(kr_{T_1}+knr_{T_1}+k_{FET})(kr_{Ln^*}+knr_{Ln^*}+k_{BET})-k_{BET}k_{FET}}. \quad [2.60']$$

The obtained rate equations (now constant at all time) each represents the (average) amount of time the species requires until any photophysical process proceeds. Therefore, by multiplying the rate constant of the particular process in question to the rate equation, the efficiency of the process can be derived. In the absence of BET, the equations above are simplified to:

$$S_1 = \frac{1}{kr_{S_1}+knr_{S_1}+k_{ISC}}, \quad [2.58'']$$

$$T_1 = \eta_{ISC} \times \frac{1}{(kr_{T_1}+knr_{T_1}+k_{FET})}, \quad [2.59'']$$

$$Ln^* = \eta_{sens} \times \frac{k_{FET}}{(kr_{T_1}+knr_{T_1}+k_{FET})(kr_{Ln^*}+knr_{Ln^*})}$$

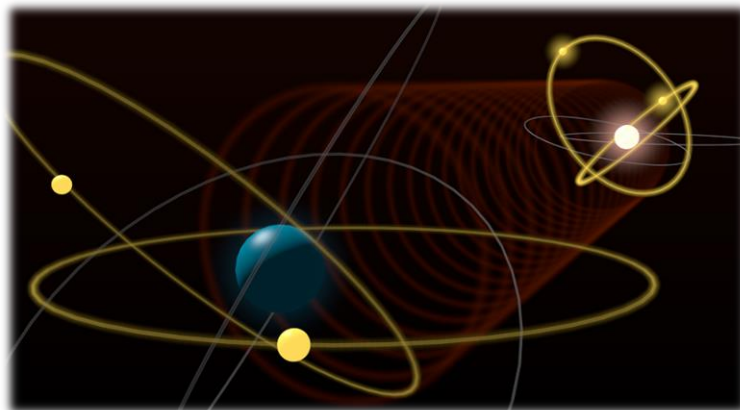
$$= \eta_{ISC} \times \eta_{FET} \times \frac{1}{kr_{Ln^*}+knr_{Ln^*}} = \eta_{sens} \times \frac{1}{kr_{Ln^*}+knr_{Ln^*}}. \quad [2.60'']$$

By multiplying the radiative rate constant of Ln(III) ion kr_{Ln^*} , Equation [2.60''] becomes:

$$Ln^*kr_{Ln^*} = \eta_{sens} \times \frac{kr_{Ln^*}}{kr_{Ln^*}+knr_{Ln^*}} = \eta_{sens} \times \Phi_{Ln} = \Phi_{ligand}. \quad [2.61]$$

Now the equation is equivalent to Equation [1.3] in Chapter 1 and defines the quantum yield of the Ln(III) complexes.

For more complicated models such as those described in this thesis, these kinetic analyses become necessary since the rate equations become sophisticated and the oversimplified model shown in this section may or may not apply.



2.4. References

- [1] B. R. Judd, *Phys. Rev.* **1962**, *127*, 750–761.
- [2] G. S. Ofelt, *J. Chem. Phys.* **1962**, *37*, 511–520.
- [3] T. Kushida, *J. Phys. Soc. Japan* **1973**, *34*, 1334–1337.
- [4] M. E. Starzak, *Mathematical Methods in Chemistry and Physics*, Springer, **1989**.
- [5] M. P. Hehlen, M. G. Brik, K. W. Krämer, *J. Lumin.* **2013**, *136*, 221–239.
- [6] O. L. Malta, *J. Non. Cryst. Solids* **2008**, *354*, 4770–4776.
- [7] B. R. Judd, *Operator Techniques in Atomic Spectroscopy*, Princeton University Press, **2014**.
- [8] J. J. Sakurai, J. Napolitano, *Modern Quantum Mechanics*, Addison-Wesley, **2011**.
- [9] C. W. Nielson and G. F. Koster, *Spectroscopic Coefficients for the p^n , d^n , and f^n Configurations*, M.I.T. Press, **1963**.
- [10] G. H. Dieke, H. M. Crosswhite, B. Dunn, *J. Opt. Soc. Am.* **1961**, *51*, 820.
- [11] B. Dibartolo, *Energy Transfer Processes in Condensed Matter*, Springer, **2012**.
- [12] T. Kushida, *J. Phys. Soc. Japan* **1973**, *34*, 1327–1333.

Chapter 3

***CONCENTRATION QUENCHING IN
YTTERBIUM COORDINATION POLYMERS***

3.1. Introduction

In 1.1., the energy transfer (ET) between Ln(III) ions and the unique properties arising from it was briefly mentioned. However, one of the major consequences of ET between Ln(III) ions is the concentration quenching.^[1,2] Concentration quenching has been extensively studied in Ln(III)-doped ceramics, and are known to reduce the emission quantum yield significantly.^[3-7] For example, L. G. Jacobsohn showed that bulk Tb:Y₂O₃ with 1% Tb(III) concentration exhibit only half of the emission intensity of that of 0.5% Tb(III) concentration.^[8] At 5% Tb(III) concentration, the intensity falls further down to 5%. Most commercially available Ln(III) doped materials thus contain only a few percent of Ln(III) ions to prevent the ET between them. Meanwhile, Ln(III) complexes, specifically Ln(III) coordination polymers, are known to show the less pronounced effect of concentration quenching.^[9-11] Elucidation of the concentration quenching mechanism in Ln(III) coordination polymers could become important not only in achieving insights into the fundamental differences between Ln(III) coordination polymers and Ln(III)-doped ceramics, but also in obtaining strategies to suppress concentration quenching.

There are mainly four models for concentration quenching: self-trapping model, killer-site model, cross-relaxation model, and phonon-assisted ET relaxation (PAETR) as depicted in Figure 3.1.^[3,12] In the self-trapping model (Figure 3.1a), the emitted light of a Ln(III) ion is

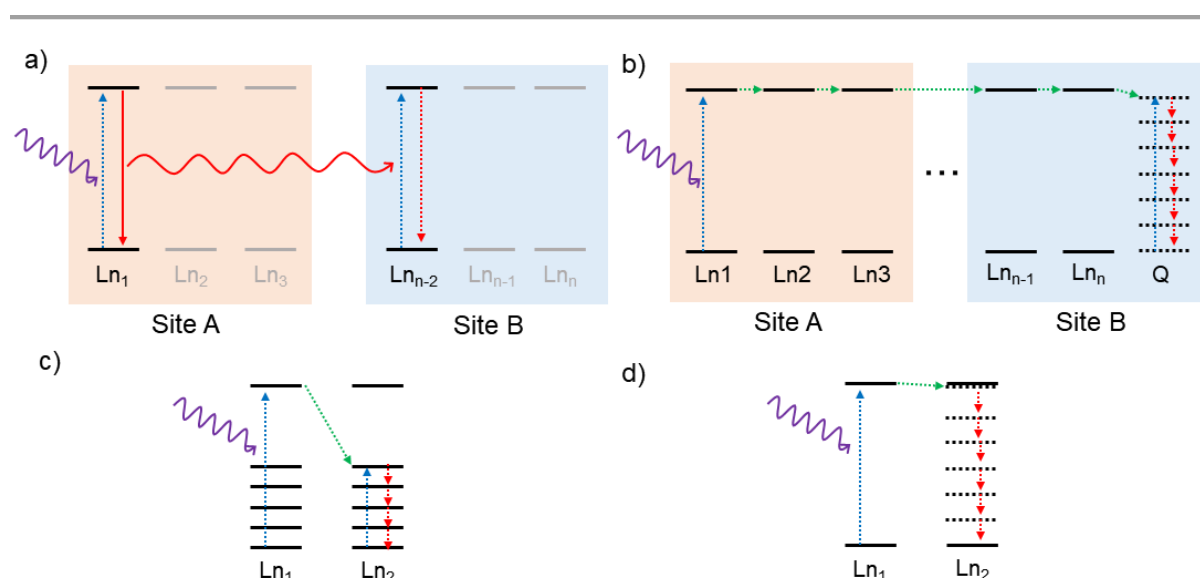


Figure 3.1 Concentration quenching models reported for Ln(III)-doped ceramics. a) Self-trapping, b) killer-site (KS), c) cross-relaxation, and d) phonon-assisted ET relaxation (PAETR).

reabsorbed by the same species.^[3] The killer-site model is characterized by nonradiative ET between multiple Ln(III) ions (energy migration) to “killer-sites” (impurities and defect sites, Figure 3.1b).^[12,13] The self-quenching model can be further divided into limited-diffusion and fast-diffusion cases. The former refers to the case in which energy migration rate is comparable to the decay rate of the Ln(III) ions and is locally quenched. The latter refers to the case in which energy migration rate is much faster than the decay rate of the Ln(III) ions and the excited state spans over a large spatial area, probabilistically. Cross-relaxation occurs when ET from a Ln(III) ion with multiple energy levels populates different levels of identical Ln(III) ion and non-radiatively decays to the ground state (Figure 3.1c).^[14] Finally, PAETR is a process where the energy from a donor is directly transferred to the phonon modes of the acceptor (Figure 3.1d).^[15] This was proposed by F. Auzel in 2002 under the framework of phonon-assisted ET by Miyakawa and Dexter.^[16] Concentration quenching in a material is usually comprised of more than one of these mechanisms and must be separately considered.

Experimental determination of the mechanism of concentration quenching in a material usually relies on Ln(III) concentration dependence of emission lifetimes instead of emission quantum yield.^[3-7] Quantum yield only shows the number of emitted photons per absorbed photons, and thus it will simply decrease in value with increasing concentration of Ln(III) ions regardless of the mechanism. There is also an intrinsic problem in this method when used for Ln(III) coordination polymers because the ligands are excited instead of Ln(III) ions. This means that a change in Ln(III) concentration inevitably changes ligand-to-Ln(III) sensitization efficiency and thus the quantum yield. On the other hand, emission lifetimes (or more precisely, emission decay profiles) provide information on the excited state dynamics as long as the dynamics involve the Ln(III) ions that is being monitored. For example, self-trapping is known to increase the emission lifetimes because there is a time lag between emitting and absorbing Ln(III) ions without any lifetime changes in the individual Ln(III) ions. In the limited-diffusion scheme of the killer-site model, the lifetimes of Ln(III) ions surrounding the killer-site is decreased while other Ln(III) far from the killer-site remains the same, leading to a multi-exponential decay profile.^[17] In this study, relying mainly on emission lifetimes, the mechanism of concentration quenching in Ln(III) coordination polymers is elucidated.

Some reports consider concentration quenching in Ln(III) coordination polymers to arise from cross-quenching.^[10] This is indeed a plausible explanation when considering Ln(III) ions with multiple excited states such as Er(III) ions. However, a report by Utochnikova and her coworkers indicate that concentration quenching occurs for coordination polymers with Yb(III) ions, which only have two 4f-states, namely the ground state $^2F_{7/2}$ and the excited state $^2F_{5/2}$.^[18]

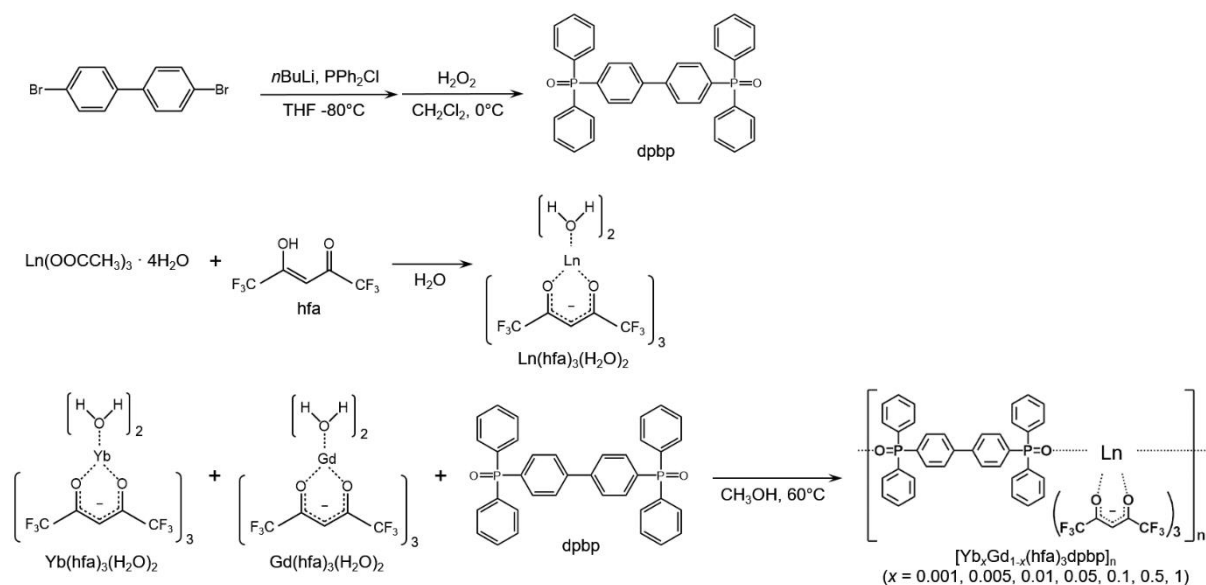
This two-level system simplifies ET from the ligands, ET between Yb(III) ions (YbYbET), and emission from the Yb(III) ions, and thus cross-quenching can be omitted from consideration. Thus, cross-quenching is not necessarily the only reason for concentration quenching. Furthermore, the nonradiative rate constant is generally large in Ln(III) coordination polymers, and this results in the lowered contribution of concentration quenching as well. Thus a small decrease in the emission lifetimes with increasing concentration of Ln(III) ions could be an indirect effect caused by the large nonradiative rate constant and not the fundamental property of Ln(III) coordination polymers. Judging concentration quenching as a small effect in Ln(III) coordination polymers based on a small decrease in the emission lifetimes could be a poor practice. This chapter focuses on $[\text{Ln}(\text{hfa})_3\text{dpbp}]_n$ (hfa: hexafluoroacetylacetonate, dpbp: 4,4'-bis(diphenylphosphoryl)-biphenyl) to investigate Yb(III) concentration quenching.^[19,20] First, the energy transfer between Ln(III) ions (LnLnET) has been confirmed to occur for this system, which means that the concentration quenching is also likely to be observed. Second, the minimum distance between Ln(III) ions is 10.4 Å, allowing complete omission of any contribution from exchange interactions.

We synthesized $[\text{Yb}_x\text{Gd}_{1-x}(\text{hfa})_3\text{dpbp}]_n$ ($x = 0.001, 0.005, 0.01, 0.05, 0.1, 0.5, 1$, product of Scheme 3.1) and investigated the effect of concentration quenching of Yb(III) emission. The periodic structure and the local coordination geometry around Yb(III) ions of the prepared coordination polymers were characterized by powder XRD and diffuse reflectance spectra of the 4f-4f transition of Yb(III) ions, respectively. Emission spectra and lifetimes were measured to elucidate the concentration quenching mechanisms. It is suggested that the concentration mechanism in $[\text{Yb}_x\text{Gd}_{1-x}(\text{hfa})_3\text{dpbp}]_n$ is the self-generated quenching center by the PAETR, which was suggested in the report of Auzel in 2002. This is further qualitatively supported from theoretical calculations of the emission lifetimes. This investigation shows the fundamental difference between concentration quenching in Ln(III)-doped inorganic hosts and Ln(III) coordination polymers, and also provides a strategy to reduce the concentration quenching in Ln(III) coordination polymers.

3.2. Experimental Section

3.2.1. Material

$\text{Yb}(\text{OOCCH}_3)_3 \cdot 4\text{H}_2\text{O}$ (99.9%) were purchased from Sigma-Aldrich Co. $\text{Gd}(\text{OOCCH}_3)_3 \cdot 4\text{H}_2\text{O}$ (>99.9) were purchased from Wako Pure Chemical Industries, Ltd. 4,4-



Scheme 3.1 General synthetic method of $[\text{Yb}_x\text{Gd}_{1-x}(\text{hfa})_3\text{dpbp}]_n$ coordination polymers (three step process). $\text{Ln} = \text{Yb}$ or Gd .

dibromobiphenyl (>98.0%), chlorodiphenylphosphine (>97.0%), and hexafluoroacetylacetonate (>95.0%) were purchased from Tokyo Chemicals Industries Co. Ltd.

3.2.2. Apparatus

ESI-MS was measured on a JEOL JMS-T100LP. Elemental analyses were performed by an Exter Analytical CE440. Infrared spectra were recorded on a JASCO FT/IR-4600 spectrometer. XRD patterns were characterized by a RIGAKU X-ray diffractometer RINT 2200. ICP-AES were obtained by using a Shimadzu ICPE-9000.

3.2.3. Synthesis

The general synthetic method of the precursors and the coordination polymers are shown in Scheme 3.1.^[21] The synthetic procedures of the linker ligand, the precursor complexes, and the coordination polymers are based on the previous reports. Dpbp , $\text{Yb}(\text{hfa})_3(\text{H}_2\text{O})_2$, $\text{Gd}(\text{hfa})_3(\text{H}_2\text{O})_2$, and the coordination polymers were synthesized also following the procedures previously reported. The procedure for the synthesis of $[\text{Yb}_x\text{Gd}_{1-x}(\text{hfa})_3\text{dpbp}]_n$ ($x = 1, 0.5, 0.1, 0.05, 0.01, 0.005, 0.001$) coordination polymers is as follows: required amount of $\text{Yb}(\text{hfa})_3(\text{H}_2\text{O})_2$ and $\text{Gd}(\text{hfa})_3(\text{H}_2\text{O})_2$ (total 1 mmol) were dissolved in 10 mL of methanol and

stirred for 5 minutes. Dpbp ligand (1 mmol, 0.56 g) dispersed in 20 mL of methanol was added subsequently and stirred for 5 hours. The resulting white precipitate was vacuum filtered, washed with methanol, and dried in vacuum.

[Yb_xGd_{1-x}(hfa)₃dpbp]_n coordination polymers were identified by infrared spectroscopy (IR), electron spray ionization mass spectroscopy (ESI-MS), and elemental analysis. Yb(III) ion concentration in each of the coordination polymers was determined by inductively coupled plasma atomic emission spectroscopy (ICP-AES). Diluted 1000 ppm standards of Yb and Gd nitrate aqueous solution were used as calibration standards. Calibration curves were made from three emission wavelengths of Yb (289.138, 328.937, 369.419 nm) and Gd (335.047, 336.223, 342.47 nm). The concentration of each coordination polymers were determined from the emission intensity of the three Yb and the three Gd wavelengths.

[Yb_{0.001}Gd_{0.999}(hfa)₃dpbp]_n: Yield: 1.21 g (91%, monomer). Selected IR (KBr, cm⁻¹): 3141 (w, arC-H), 3067 (w, arC-H), 1654 (st, C=O), 1599 (m, arC=C), 1551 (m, arC=C), 1527 (st, arC=C), 1498 (st, arC=C), 1439 (m, arP-C), 1254 (st, P=O), 1100 – 1200 (st, C-F). ESI-MS: m/z = 1126.06 [Gd(hfa)₂dpbp]⁺, 1142.07 [Yb(hfa)₂dpbp]⁺, 2459.10 [Gd(hfa)₃dpbp][Gd(hfa)₂dpbp]⁺, 3792.13 [Gd(hfa)₃dpbp]₂[Gd(hfa)₂dpbp]⁺. Elemental analysis calculated for [C₅₁H₃₁F₁₈O₈P₂Yb_{0.001}Gd_{0.999}]_n: C, 45.95%, H, 2.34%. Found: C, 46.18%, H, 2.23%. Yb and Gd ratio from ICP-AES: Yb:Gd = 0.001517:0.9915 (calcd. 0.002:0.998).

[Yb_{0.005}Gd_{0.995}(hfa)₃dpbp]_n: Yield: 1.23 g (92%, monomer). Selected IR (KBr, cm⁻¹): 3141 (w, arC-H), 3067 (w, arC-H), 1654 (st, C=O), 1599 (m, arC=C), 1551 (m, arC=C), 1527 (st, arC=C), 1498 (st, arC=C), 1439 (m, arP-C), 1254 (st, P=O), 1100 – 1200 (st, C-F). ESI-MS: m/z = 1126.07 [Gd(hfa)₂dpbp]⁺, 1142.08 [Yb(hfa)₂dpbp]⁺, 2459.09 [Gd(hfa)₃dpbp][Gd(hfa)₂dpbp]⁺, 3791.10 [Gd(hfa)₃dpbp]₂[Gd(hfa)₂dpbp]⁺. Elemental analysis calculated for [C₅₁H₃₁F₁₈O₈P₂Yb_{0.005}Gd_{0.995}]_n: C, 45.95%, H, 2.34%. Found: C, 46.15%, H, 2.23%. Yb and Gd ratio from ICP-AES: Yb:Gd = 0.00278:0.9944 (calcd. 0.003:0.997).

[Yb_{0.01}Gd_{0.99}(hfa)₃dpbp]_n: Yield: 1.25 g (93%, monomer). Selected IR (KBr, cm⁻¹): 3141 (w, arC-H), 3067 (w, arC-H), 1654 (st, C=O), 1599 (m, arC=C), 1551 (m, arC=C), 1527 (st, arC=C), 1498 (st, arC=C), 1439 (m, arP-C), 1254 (st, P=O), 1100 – 1200 (st, C-F). ESI-MS: m/z = 1126.04 [Gd(hfa)₂dpbp]⁺, 1142.05 [Yb(hfa)₂dpbp]⁺, 2459.06 [Gd(hfa)₃dpbp][Gd(hfa)₂dpbp]⁺, 3791.7 [Gd(hfa)₃dpbp]₂[Gd(hfa)₂dpbp]⁺. Elemental analysis calculated for [C₅₁H₃₁F₁₈O₈P₂Yb_{0.01}Gd_{0.99}]_n: C, 45.95%, H, 2.34%. Found: C, 46.07%, H, 2.22%. Yb and Gd ratio from ICP-AES: Yb:Gd = 0.005969:1.0175 (calcd. 0.006:0.994).

[Yb_{0.05}Gd_{0.95}(hfa)₃dpbp]_n: Yield: 1.22 g (92%, monomer). Selected IR (KBr, cm⁻¹): 3141 (w, arC-H), 3067 (w, arC-H), 1654 (st, C=O), 1599 (m, arC=C), 1551 (m, arC=C), 1527 (st, arC=C),

1498 (st, arC=C), 1439 (m, arP-C), 1254 (st, P=O), 1100 – 1200 (st, C-F).. ESI-MS: $m/z = 1126.04$ $[\text{Gd}(\text{hfa})_2\text{dpbp}]^+$, 1142.05 $[\text{Yb}(\text{hfa})_2\text{dpbp}]^+$, 2459.06 $[\text{Gd}(\text{hfa})_3\text{dpbp}][\text{Gd}(\text{hfa})_2\text{dpbp}]^+$, 3791.07 $[\text{Gd}(\text{hfa})_3\text{dpbp}]_2[\text{Gd}(\text{hfa})_2\text{dpbp}]^+$. Elemental analysis calculated for $[\text{C}_{51}\text{H}_{31}\text{F}_{18}\text{O}_8\text{P}_2\text{Yb}_{0.05}\text{Gd}_{0.95}]_n$: C, 45.93%, H, 2.34%. Found: C, 46.19%, H, 2.24%. Yb and Gd ratio from ICP-AES: Yb:Gd = 0.03498:0.9605 (calcd. 0.04:0.96).

$[\text{Yb}_{0.1}\text{Gd}_{0.9}(\text{hfa})_3\text{dpbp}]_n$: Yield: 1.18 g (89%, monomer). Selected IR (KBr, cm^{-1}): 3141 (w, arC-H), 3067 (w, arC-H), 1654 (st, C=O), 1599 (m, arC=C), 1551 (m, arC=C), 1527 (st, arC=C), 1498 (st, arC=C), 1439 (m, arP-C), 1254 (st, P=O), 1100 – 1200 (st, C-F). ESI-MS: $m/z = 1126.04$ $[\text{Gd}(\text{hfa})_2\text{dpbp}]^+$, 1142.05 $[\text{Yb}(\text{hfa})_2\text{dpbp}]^+$, 2459.06 $[\text{Gd}(\text{hfa})_3\text{dpbp}][\text{Gd}(\text{hfa})_2\text{dpbp}]^+$, 2475.09 $[\text{Gd}(\text{hfa})_3\text{dpbp}][\text{Yb}(\text{hfa})_2\text{dpbp}]^+$ and $[\text{Yb}(\text{hfa})_3\text{dpbp}][\text{Gd}(\text{hfa})_2\text{dpbp}]^+$, 3791.08 $[\text{Gd}(\text{hfa})_3\text{dpbp}]_2[\text{Gd}(\text{hfa})_2\text{dpbp}]^+$. Elemental analysis calculated for $[\text{C}_{51}\text{H}_{31}\text{F}_{18}\text{O}_8\text{P}_2\text{Yb}_{0.1}\text{Gd}_{0.9}]_n$: C, 45.90%, H, 2.34%. Found: C, 46.11%, H, 2.22%. Yb and Gd ratio from ICP-AES: Yb:Gd = 0.07413:0.9383 (calcd. 0.07:0.93).

$[\text{Yb}_{0.5}\text{Gd}_{0.5}(\text{hfa})_3\text{dpbp}]_n$: Yield: 1.21 g (91%, monomer). Selected IR (KBr, cm^{-1}): 3141 (w, arC-H), 3067 (w, arC-H), 1654 (st, C=O), 1599 (m, arC=C), 1551 (m, arC=C), 1527 (st, arC=C), 1498 (st, arC=C), 1439 (m, arP-C), 1254 (st, P=O), 1100 – 1200 (st, C-F). ESI-MS: $m/z = 1126.05$ $[\text{Gd}(\text{hfa})_2\text{dpbp}]^+$, 1142.06 $[\text{Yb}(\text{hfa})_2\text{dpbp}]^+$, 2459.08 $[\text{Gd}(\text{hfa})_3\text{dpbp}][\text{Gd}(\text{hfa})_2\text{dpbp}]^+$, 2475.09 $[\text{Gd}(\text{hfa})_3\text{dpbp}][\text{Yb}(\text{hfa})_2\text{dpbp}]^+$ and $[\text{Yb}(\text{hfa})_3\text{dpbp}][\text{Gd}(\text{hfa})_2\text{dpbp}]^+$, 3791.09 $[\text{Gd}(\text{hfa})_3\text{dpbp}]_2[\text{Gd}(\text{hfa})_2\text{dpbp}]^+$, 3808.12 $[\text{Yb}(\text{hfa})_3\text{dpbp}][\text{Gd}(\text{hfa})_3\text{dpbp}][\text{Gd}(\text{hfa})_2\text{dpbp}]^+$, 3822.13 $[\text{Gd}(\text{hfa})_3\text{dpbp}][\text{Yb}(\text{hfa})_3\text{dpbp}][\text{Yb}(\text{hfa})_2\text{dpbp}]^+$, 3839.15 $[\text{Yb}(\text{hfa})_3\text{dpbp}]_2[\text{Yb}(\text{hfa})_2\text{dpbp}]^+$. Elemental analysis calculated for $[\text{C}_{51}\text{H}_{31}\text{F}_{18}\text{O}_8\text{P}_2\text{Yb}_{0.5}\text{Gd}_{0.5}]_n$: C, 45.68%, H, 2.33%. Found: C, 45.87%, H, 2.22%. Yb and Gd ratio from ICP-AES: Yb:Gd = 0.4001:0.5965 (calcd. 0.4:0.6).

$[\text{Yb}_1(\text{hfa})_3\text{dpbp}]_n$: Yield: 1.25 g (93%, monomer). Selected IR (KBr, cm^{-1}): 3141 (w, arC-H), 3067 (w, arC-H), 1654 (st, C=O), 1599 (m, arC=C), 1551 (m, arC=C), 1527 (st, arC=C), 1498 (st, arC=C), 1439 (m, arP-C), 1254 (st, P=O), 1100 – 1200 (st, C-F). ESI-MS: $m/z = 1142.06$ $[\text{Yb}(\text{hfa})_2\text{dpbp}]^+$, 2491.10 $[\text{Yb}(\text{hfa})_3\text{dpbp}][\text{Yb}(\text{hfa})_2\text{dpbp}]^+$, 3839.13 $[\text{Yb}(\text{hfa})_3\text{dpbp}]_2[\text{Yb}(\text{hfa})_2\text{dpbp}]^+$. Elemental analysis calculated for $[\text{C}_{51}\text{H}_{31}\text{F}_{18}\text{O}_8\text{P}_2\text{Yb}]_n$: C, 45.42%, H, 2.32%. Found: C, 45.48%, H, 2.20%. Yb and Gd ratio from ICP-AES: Yb:Gd = 0.9917:0 (calcd. 1:0).

3.2.4. Spectroscopy

Absorption spectra were obtained by using a JASCO V-670 spectrometer. Emission spectra and lifetimes were measured using a Horiba/Jobin-Yvon FluoroLog-3ps spectrofluorometer. The spectrofluorometer was equipped with a Hamamatsu R5509-43 photomultiplier for detecting NIR emission, and SpectraLED 356 nm light source was used as the excitation light source for the lifetime measurements.

3.2.5. Crystallography

Single crystals of $[\text{Yb}_1(\text{hfa})_3\text{dpbp}]_n$ coordination polymer were obtained by liquid-liquid diffusion of dpbp dichloromethane solution and $\text{Yb}(\text{hfa})_3(\text{H}_2\text{O})_2$ methanol solution. One of the obtained colorless block crystals was mounted on a glass fiber by epoxy resin glue and cooled to -150°C . All measurements were made using a Rigaku RAXIS RAPID imaging plate area detector with graphite-monochromated $\text{MoK}\alpha$ radiation. Corrections for decay and Lorentz-polarization effects were made using a spherical absorption correction, solved by direct methods, and expanded using Fourier techniques. Non-hydrogen atoms were refined anisotropically. Hydrogen atoms were refined using the riding model. The final cycle of full-matrix least-squares refinement was based on observed reflections and variable parameters. All calculations were performed using a CrystalStructure crystallographic software package. The CIF was checked using the checkCIF/PLATON service. The CIF was deposited to The Cambridge Crystallographic Data Center (CCDC) with the deposition number CCDC-1046310 ($[\text{Yb}_1(\text{hfa})_3\text{dpbp}]_n$). The data can be obtained free of charge from CCDC via www.ccdc.cam.ac.uk/data_request/cif.

3.3. Theoretical Methods

3.3.1. Rate Constants

The rate constants for the radiative process (electric dipole and magnetic dipole transitions), as well as energy transfer of various interactions, are provided in 2.2. Here, the relevant equations are listed. The radiative rate constants are:^[22–24]

$$A_{\text{rad(ED)}} = \frac{2\pi\nu_{\text{em}}^2 e^2}{\epsilon_0 c^3 m} n^2 f_{\text{ED}} , \quad [2.23]$$

$$A_{\text{rad(MD)}} = \frac{2\pi\nu_{\text{em}}^2 e^2}{\epsilon_0 c^3 m} n^2 f_{\text{MD}} , \quad [2.24]$$

where

$$f_{\text{ED}} = \frac{8\pi^2 m_e v_{\text{abs}}}{3h} \chi_{\text{abs}} \sum_{k=2,4,6} \Omega_k \left| \langle l^N SLJ_{\text{mixed}} \| U^{(k)} \| l^N S'L'J'_{\text{mixed}} \rangle \right|^2, \quad [2.13]$$

$$f_{\text{MD}} = \frac{hv_{\text{abs}}}{6m_e c^2} \frac{n}{2J+1} \left| \langle l^N SLJ_{\text{mixed}} \| L + gS \| l^N S'L'J'_{\text{mixed}} \rangle \right|^2. \quad [2.18]$$

The energy transfer rate constants are:^[25,26]

$$W_{\text{ET(dd)}} = \frac{1}{(2J_a+1)(2J_b+1)} \frac{2}{3} \frac{4\pi^2}{h} \frac{e^4}{R^6} \left[\sum_{k=2,4,6} \Omega_k^A \left| \langle l^N SLJ \| U^{(k)} \| l^N S'L'J' \rangle \right|^2 \right] \\ \times \left[\sum_{k=2,4,6} \Omega_k^B \left| \langle l^N SLJ \| U^{(k)} \| l^N S'L'J' \rangle \right|^2 \right] F, \quad [2.27]$$

$$W_{\text{ET(dq)}} = \frac{1}{(2J_a+1)(2J_b+1)} \frac{4\pi^2}{h} \frac{e^4}{R^8} \left[\sum_{k=2,4,6} \Omega_k^A \left| \langle l^N SLJ \| U^{(k)} \| l^N S'L'J' \rangle \right|^2 \right] \\ \times \left[\left| \langle 4f \| r_B^2 \| 4f \rangle \right|^2 \left| \langle l \| C^{(2)} \| l \rangle \right|^2 \left| \langle l^N SLJ \| U^{(2)} \| l^N S'L'J' \rangle \right|^2 \right] F, \quad [2.28]$$

$$W_{\text{ET(qq)}} = \frac{1}{(2J_a+1)(2J_b+1)} \frac{14}{5} \frac{4\pi^2}{h} \frac{e^4}{R^{10}} \left| \langle l \| C^{(2)} \| l \rangle \right|^4 \left[\left| \langle 4f \| r_A^2 \| 4f \rangle \right|^2 \left| \langle l^N SLJ \| U^{(2)} \| l^N S'L'J' \rangle \right|^2 \right] \\ \times \left[\left| \langle 4f \| r_B^2 \| 4f \rangle \right|^2 \left| \langle l^N SLJ \| U^{(2)} \| l^N S'L'J' \rangle \right|^2 \right] F. \quad [2.29]$$

In general, these rate constants require several fitting procedures with experimental data to calculate the values. However, below is an explanation how this is not necessary for this investigation.

Ce(III) ion can be considered as a one-electron system (only 2F_J term) as far as the 4f-electrons are concerned. Since the terms for lanthanides with N and $14-N$ electrons are the same (see Chapter 2), Yb(III) ions can also be considered as a one-electron system. In such case, electrostatic coupling does not exist, and only spin-orbit coupling contribute to the splitting of $4f^N$ -states. Furthermore, spin-orbit coupling mixes states of the same J , which does not exist for Ce(III) and Yb(III) ions. Therefore, the wavefunctions of these ions are not mixed in the intermediate coupling scheme. The reduced matrix element in Equations [2.13], [2.18], [2.27], and [2.28] can now be directly calculated without accounting for mixed wavefunctions, and therefore Equation [2.23] and [2.24] as well.

Yb(III) ions only have one excited state (i.e., ${}^2F_{5/2}$). Since $f_{\text{tot}} = f_{\text{ED}} + f_{\text{MD}}$ (Equation [2.21]), the value of the only f_{ED} can be calculated simply from oscillator strength measured from absorption spectra. The entire sum $\sum_{k=2,4,6} \Omega_k \left| \langle l^N SLJ_{\text{mixed}} \| U^{(k)} \| l^N S'L'J'_{\text{mixed}} \rangle \right|^2$ can be calculated from Equation [2.13]. The low solubility of $[\text{Yb}(\text{hfa})_3\text{dpbp}]_n$ coordination polymers rendered the oscillator strength of Yb(III) ions undetermined, so instead a typical oscillator strength $f_{\text{tot}} = 3 \times 10^{-6}$ was used.^[25,26] Therefore, the discussion is restricted to the qualitative side of the theoretical results and not the quantitative side.

Phonon-assisted ET relaxation (PAETR) is an additional relaxation process that occurs when two luminescent centers are close in the distance. The principle of this type of ET is the

same as the phonon-assisted ET, where one luminescent center in its excited state transfers its energy to a ground state luminescent center with different excited state energy, assisted with a phonon(s) to compensate for the difference in energy. Auzel proposed in 2002 that phonon-assisted ET can also occur as a relaxation process when one luminescent center transfers directly to the phonon state of the neighboring luminescent center (hence can be considered as being “fully phonon-assisted”).^[15] The rate constant of phonon-assisted ET W_{PAET} is given by the following equation provided by Miyakawa and Dexter:^[16]

$$W_{\text{PAET}} = W_{\text{tot}} e^{-\frac{\Delta E}{\hbar\omega} \ln \frac{N}{se(n+1)(1+s_1/s_2)}} \quad [3.1]$$

where W_{tot} is phonon-unassisted ET rate constant ($= W_{\text{ET(dd)}} + W_{\text{ET(qd)}} + W_{\text{ET(dq)}} + W_{\text{ET(qq)}}$), ΔE is energy gap between the excited state of two Ln(III) ions, $\hbar\omega$ is the phonon energy relevant to the assist, s is the Huang-Rhys parameter (s_1 and s_2 refers to donor and acceptor), n is number of phonon at a given temperature, N is the multi-phonon order given by the integer part of $N = \frac{\Delta E}{\hbar\omega}$. In the case of PAETR, Auzel described that ΔE is the energy gap between ground and excited state of the donor ($= \nu_{\text{em}}$). When the donor and the acceptor are the same species, s_1 and s_2 are identical and Equation [3.1] can be modified for PAETR and becomes:

$$W_{\text{PAETR}} = W_{\text{tot}} e^{-\frac{\Delta E}{\hbar\omega} \ln \frac{N}{2se(n+1)}} \quad [3.2]$$

s is provided by the Stokes shift between absorption and emission spectra Δ , which for lanthanides are typically in the order of 1×10^{-2} :

$$s = \frac{\Delta}{2 \times \hbar\omega} \quad [3.3]$$

n can be derived from Boltzmann distribution:

$$n = \frac{1}{\frac{\hbar\omega}{e^{k_{\text{B}}T} - 1}} \quad [3.4]$$

The C-H stretching mode of the alpha position of hfa ligands (3141 cm^{-1} , see 3.2.3.) was considered as the relevant phonon for this process since it has been shown in previous reports that this vibration is important in suppressing vibrational relaxation of lanthanide complexes. The various constants (experimental and calculated) are summarized in Table 3.1.

Table 3.1 Values for various constants needed for rate equation calculation.

Constant	Value	Constant	Value
ν_{abs}	$1.039 \times 10^4 \text{ cm}^{-1}$	f_{ED}	2.729×10^{-6}
ν_{em}	$1.007 \times 10^4 \text{ cm}^{-1}$	$\sum_{k=2,4,6} \Omega_k \langle l^N SLJ \ U^{(k)} \ l^N S'L'J' \rangle ^2$	$9.652 \times 10^{-21} \text{ cm}^2$
$\hbar\gamma_{\text{D}}$	$5.845 \times 10^2 \text{ cm}^{-1}$	$A_{\text{rad(MD)}}$	$4.395 \times 10^1 \text{ s}^{-1}$
$\hbar\gamma_{\text{A}}$	$6.794 \times 10^2 \text{ cm}^{-1}$	$A_{\text{rad(ED)}}$	$4.420 \times 10^2 \text{ s}^{-1}$
A_{tot}	$4.611 \times 10^4 \text{ s}^{-1}$	A_{nrad}	$4.562 \times 10^4 \text{ s}^{-1}$
χ_{abs}	2.007	$W_{\text{ET(dd)}}$	$9.688 \times 10^8 \times R^{-6} [\text{s}^{-1}]$
\mathcal{A}	$3.178 \times 10^2 \text{ cm}^{-1}$	$W_{\text{ET(dq)}}$	$1.289 \times 10^{11} \times R^{-8} [\text{s}^{-1}]$
F	$4.804 \times 10^{-4} \text{ cm}$	$W_{\text{ET(qq)}}$	$3.201 \times 10^{13} \times R^{-10} [\text{s}^{-1}]$
f_{total}	3×10^{-6}	$\hbar\omega$	3141 cm^{-1}
$\langle l^N SLJ \ L + gS \ l^N SL(J-1) \rangle$	1.856	s	0.096
$\langle l^N SL \ U^{(k)} \ l^N SL' \rangle$	$-1.000 (k=2, 4, 6)$	n	2.869×10^{-7}
$\langle l^N SLJ \ U^{(k)} \ l^N SL'J' \rangle$	$0.3499 (k=2)$ $0.6389 (k=4)$ $0.9258 (k=6)$	N	3
$\langle l \ C^{(2)} \ l \rangle$	-1.366	W_{PAETR}	$W_{\text{tot}} \times 3.670 \times 10^{-3} [\text{s}^{-1}]$
f_{MD}	2.713×10^{-7}		

3.3.2. Rate Equations

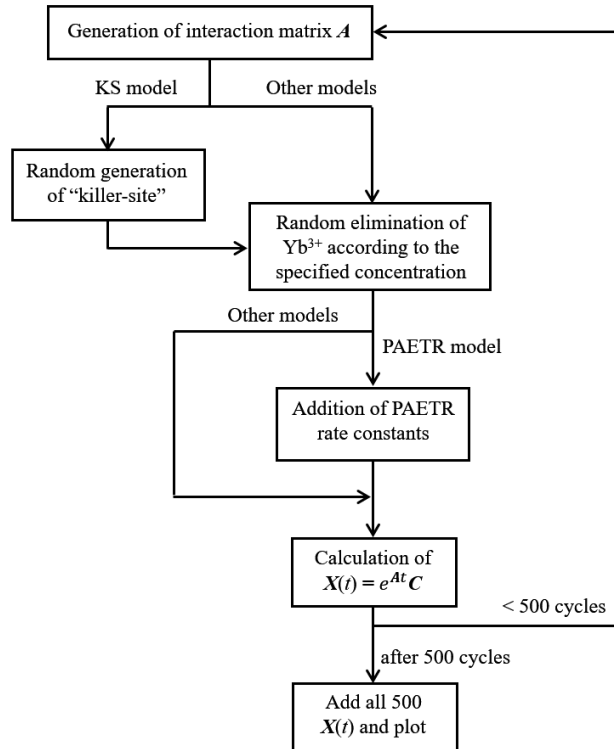
The concept of the theory and the program to automatically generate rate equations are briefly explained in this section. The flow chart of the calculation method is summarized in Scheme 3.2. As mentioned in the main text, “active sphere” considered for calculation consists of 135 Ln(III) ions, which is approximately 40 Å in diameter (Figure 3.2). In this active sphere, the minimum concentration is 0.01 where only the center Ln(III) ion is Yb(III) ion (red dot), and the rest is considered to be Gd(III) ions, and the maximum concentration is unity where all of the sites are Yb(III) ions. With reasonable excitation power (under 0.02 W mm^{-2}), multiple excitations in the same sphere are neglected,^[27] thus for this calculation, initial excitation can be considered to begin at the center Yb(III) ion. With these considerations, this active sphere can be modeled as a system of inhomogeneous linear differential equations, and its matrix form (See 2.3.) is given by the following equation:^[28]

$$\frac{d\mathbf{X}(t)}{dt} = \mathbf{A}\mathbf{X}(t) + \mathbf{J}(t) , \quad [2.33]$$

where $\mathbf{X}(t)$ is the vector of population density, and each of the elements represents each excited Yb(III) ion, and $\mathbf{J}(t)$ is the input function of the system. \mathbf{A} is the “interaction matrix,” a 135×135 square matrix consisting of rate constants that models the interaction between Yb(III) ions as well as the fundamental decay rate constant of each Yb(III) ion:

$$\mathbf{A} = \begin{bmatrix} -(A_{\text{tot}} + W_{\text{tot}-67}) & W_{\text{ET}-66,-67} & \cdots & W_{\text{ET}0,-67} & \cdots & \cdots & W_{\text{ET}67,-67} \\ W_{\text{ET}-67,-66} & \ddots & \ddots & \vdots & \cdots & \cdots & \vdots \\ \vdots & \ddots & -(A_{\text{tot}} + W_{\text{tot}-1}) & W_{\text{ET}0,-1} & \cdots & \ddots & \vdots \\ W_{\text{ET}-67,0} & \cdots & W_{\text{ET}-1,0} & -(A_{\text{tot}} + W_{\text{tot}0}) & W_{\text{ET}1,0} & \cdots & W_{\text{ET}67,0} \\ \vdots & \cdots & \cdots & W_{\text{ET}0,1} & -(A_{\text{tot}} + W_{\text{tot}1}) & \ddots & \vdots \\ \vdots & \cdots & \cdots & \vdots & \ddots & \ddots & W_{\text{ET}67,66} \\ W_{\text{ET}-67,67} & \cdots & \cdots & W_{\text{ET}0,67} & \cdots & W_{\text{ET}66,67} & -(A_{\text{tot}} + W_{\text{tot}67}) \end{bmatrix}, \quad [3.5]$$

where $A_{\text{tot}} = A_{\text{rad}} + A_{\text{nrad}}$, $W_{\text{ET}i,j}$ is the ET rate constant between i th and j th Yb(III) ions, and $W_{\text{tot}i}$ is the total rate constant ($= W_{\text{ET}i,1} + W_{\text{ET}i,2} + \cdots + W_{\text{ET}i,135}$) of the ET from the i th Yb(III) ion. The diagonal elements represent decay rate of each Yb(III) ion, and the off-diagonal elements represent the ET rate constant between Yb(III) ions. Delta function is used



Scheme 3.2 The flow chart of the rate equation calculation.

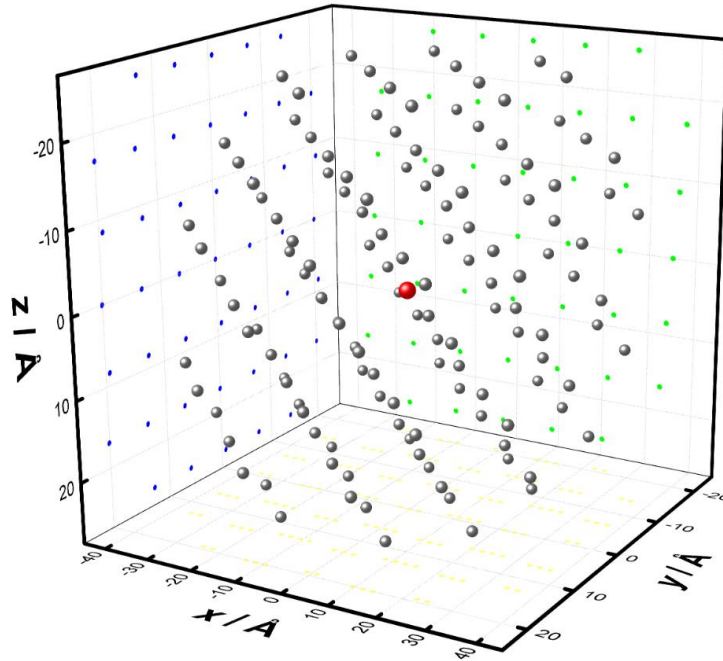


Figure 3.2 “Active sphere” of the calculation consisting of 135 Ln(III) ions. The grey spheres represent Yb(III) ions. The red sphere represents the center Yb(III) ion. The coordinates were taken from single crystal x-ray analysis. The diameter is approximately 40 Å.

for the center Yb(III) ion as the input function $J(t)$ for the calculation of emission decay profile, and thus Equation [2.33] can be solved to give:

$$\mathbf{X}(t) = \exp(\mathbf{A}t)\mathbf{B} , \quad [2.40]$$

where \mathbf{B} is the vector of the initial population density for all Yb(III) ions, which is zero for all elements except for the element corresponding to the center Yb(III) ion (68th element). $\exp(\mathbf{A})$ is the matrix exponential of the interaction matrix. Diagonalization of $\exp(\mathbf{A})$ in Equation [2.40] solves for $\mathbf{X}(t)$. The calculated $\mathbf{X}(t)$ provides the population density decay profiles of the active sphere. This procedure applies for all of the calculations in this section.

The following part of this section explains the modification of the interaction matrix \mathbf{A} (Equation [3.5]) corresponding to the specified concentration and the concentration quenching model. In order to account for the inhomogeneity of the distribution of Yb(III) ions, the row and column were changed to zero for those corresponding to the Yb(III) ions randomly specified by uniformly distributed random integer generator. Then all the elements of each

column except the diagonal element were added, and the diagonal element was replaced with the sum along with A_{rad} and A_{nrad} . This efficiently erases all the rate constants existent in the system that involves the specified Yb(III) ion.

In the killer-site (KS) model, an abstract form of “killer-site” was introduced. Identifying the specific type of killer-site is difficult and is beyond the scope of this work. For the sake of discussion, non-radiative impurity-like killer-site was considered, which is acting as strong quenching center (rate constant of the ET to this site is 1000 times larger than the YbYbET). The concentration of the killer-site is decided randomly from 0 to 1 (corresponds to approx. 0.007 of all Ln(III) ion sites), and the distribution is also decided randomly, both using uniformly distributed random integer generator. The column corresponding to the killer-site chosen by the uniformly random integer generator is set to zero, and the diagonal element is changed to A_{nrad} only, which removes all of the ET back to the Yb(III) ions and decays without emission. The row corresponding to the killer-site is multiplied by 1000 to model the killer-site as strong quenching center.

In the PAETR model, an additional relaxation rate is described by Equation [3.2]. W_{tot} is the total ET rate constant for individual Yb(III) ion, and this is the origin of concentration dependence. The interaction matrix A is modified for PAETR model by adding the exponential part of Equation S15 multiplied with W_{tot} of individual Yb(III) ion to the diagonal elements.

Above method describes single calculation for a single active sphere. Experimentally, the emission lifetime of the combination of multiple active spaces is observed, each with a different distribution of Yb(III) ions. To account for this inhomogeneity, 500 cycles of the calculation were performed and combined by adding each of the derived equations. The calculation was done in MATLAB R2015b, and the scripts are provided in 3.6.2.

3.4. Results and Discussion

3.4.1. Structure

The crystal structure of $[\text{Yb}_1(\text{hfa})_3\text{dpbp}]_n$ coordination polymer was determined by single-crystal X-ray analysis (Figure 3.3a). $[\text{Yb}_1(\text{hfa})_3\text{dpbp}]_n$ forms a polymer structure with each of the Yb(III) ions coordinated by two dpbp and three hfa ligands. As shown in Figure 3.3b, the shortest pair of Yb(III) is between the neighboring polymer chains, separated by 10.4 Å. The structure is similar to that of the previously reported $[\text{Eu}(\text{hfa})_3\text{dpbp}]_n$.^[21] Powder XRD analyses of $[\text{Yb}_x\text{Gd}_{1-x}(\text{hfa})_3\text{dpbp}]_n$ ($x = 1, 0.5, 0.1, 0.05, 0.01, 0.005, 0.001$) coordination polymers

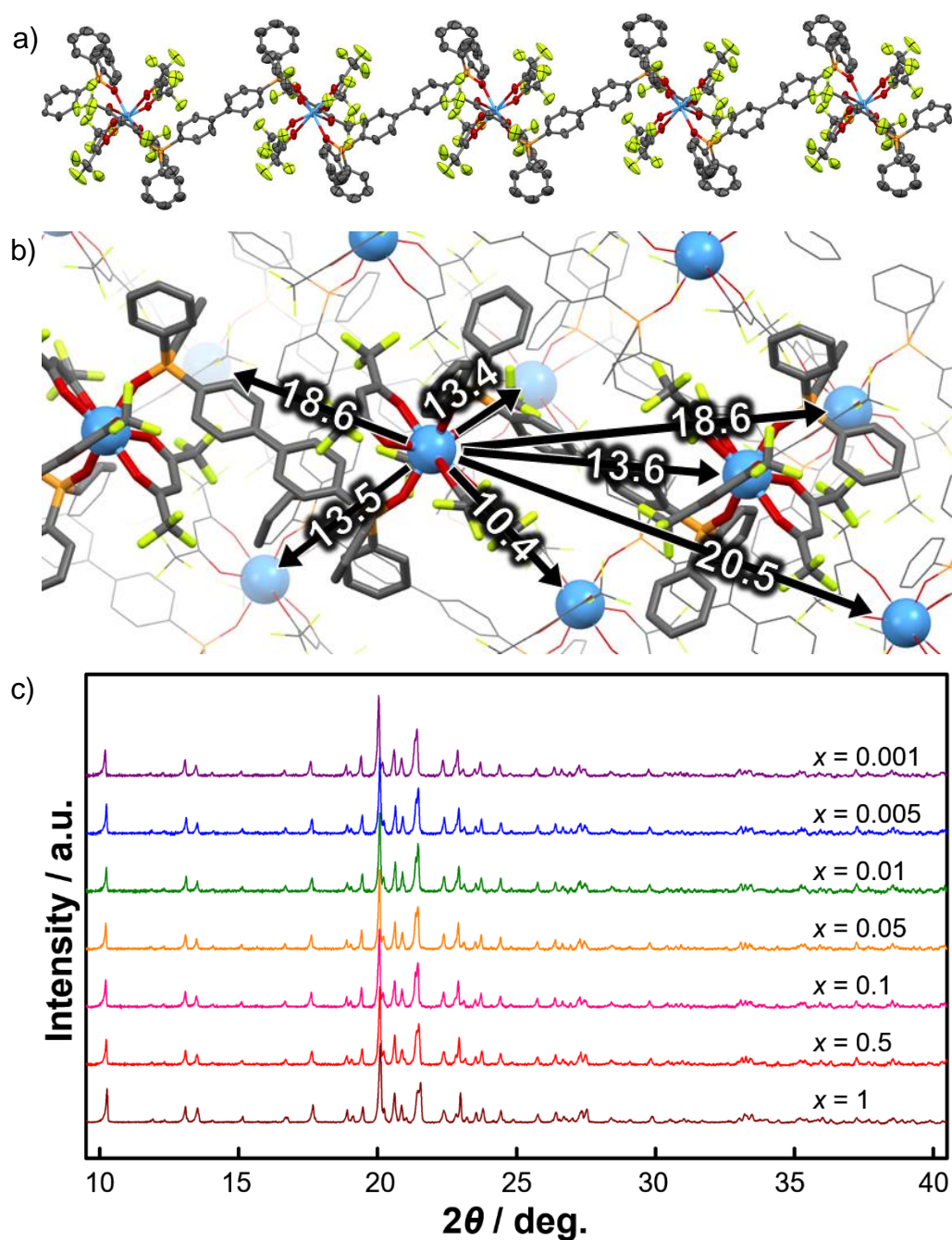


Figure 3.3 a) Molecular structure of the $[\text{Yb}_1(\text{hfa})_3\text{dppb}]_n$ coordination polymer, showing 50% probability displacement ellipsoids. Hydrogen atoms are omitted for clarity. Blue: Yb, red: O, gray: C, yellow: F, and orange: P. b) Packing structure of $[\text{Yb}_1(\text{hfa})_3\text{dppb}]_n$ polymer chains and the distance between Yb(III) ions in angstroms (\AA). c) Powder XRD patterns of $[\text{Yb}_x\text{Gd}_{1-x}(\text{hfa})_3\text{dppb}]_n$.

allows comparison of the periodic structures. As shown in Figure 3.3c, the main peaks at around 10.2, 20.1, and 21.5 degrees of the polymers are within negligibly small shifts of 0.1 degrees, with similar FWHMs. The diffuse reflectance spectra, which is directly related to the absorption spectra, in the NIR region of $[\text{Yb}_1(\text{hfa})_3\text{dpbp}]_n$ and $[\text{Yb}_{0.01}\text{Gd}_{0.99}(\text{hfa})_3\text{dpbp}]_n$ were recorded to determine the dependence of concentration on the local coordination geometry around Yb(III) ions (Figure A3.1, see 3.6.1.). The emission and absorption spectral shapes of Ln(III) ions are known to be sensitive to the local coordination geometry around Ln(III) ion.^[29] The resulting spectrum was not of high quality for $[\text{Yb}_{0.01}\text{Gd}_{0.99}(\text{hfa})_3\text{dpbp}]_n$, and thus it was not possible to compare the spectral shape. The diffuse reflectance spectrum of $[\text{Yb}_{0.01}\text{Gd}_{0.99}(\text{hfa})_3\text{dpbp}]_n$ took about 11 days to complete due to the small absorption coefficient of Yb(III) ions while that of $[\text{Yb}_1(\text{hfa})_3\text{dpbp}]_n$ took only about 10 hours. The resolution, sensitivity, correction, and the baseline might have changed during such extreme time duration differences. Nonetheless, the lack of notable change in the powder XRD patterns shows that the structures of $[\text{Yb}_x\text{Gd}_{1-x}(\text{hfa})_3\text{dpbp}]_n$ coordination polymers are identical.

3.4.2. Photophysical Properties

In order to consider the effect of self-trapping, emission spectra of $[\text{Yb}_x\text{Gd}_{1-x}(\text{hfa})_3\text{dpbp}]_n$ coordination polymers in the NIR region were measured in powder state (excitation at 356

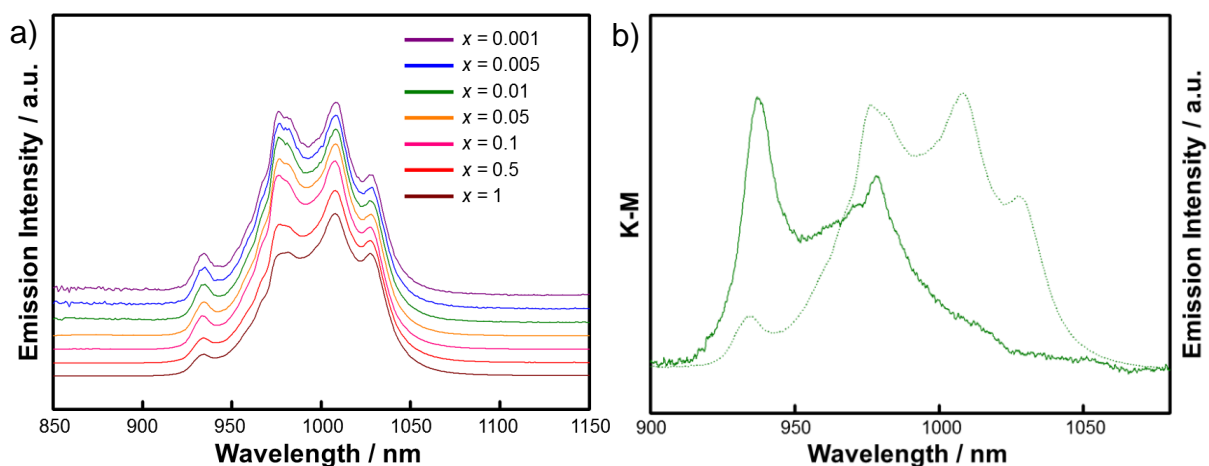


Figure 3.4 a) Emission spectra of $[\text{Yb}_x\text{Gd}_{1-x}(\text{hfa})_3\text{dpbp}]_n$ coordination polymers ($\lambda_{\text{EX}} = 356$ nm). The spectra were normalized at the 1025 nm peak, and offsets were made for clarity. b) Diffuse reflectance spectrum (solid line) and emission spectrum (dotted line) of $[\text{Yb}_{0.01}\text{Gd}_{0.99}(\text{hfa})_3\text{dpbp}]_n$.

nm). The emission spectra of the polymers are shown in Figure 3.4a. Multiple emission peaks from 900 to 1100 nm attributed to the ${}^2F_{5/2} \rightarrow {}^2F_{7/2}$ transition of Yb(III) ions with Stark splitting were observed. The height of the peaks at a shorter wavelength decreased with increasing concentration of Yb(III) ions. Figure 3.4b shows the comparison of diffuse reflectance and emission spectra of $[\text{Yb}_{0.01}\text{Gd}_{0.99}(\text{hfa})_3\text{dpbp}]_n$. The longer wavelength region of the diffuse reflectance spectrum overlaps with the shorter wavelength region of the emission spectrum. The overlap leads to the reabsorption of emission in the shorter wavelength region when the

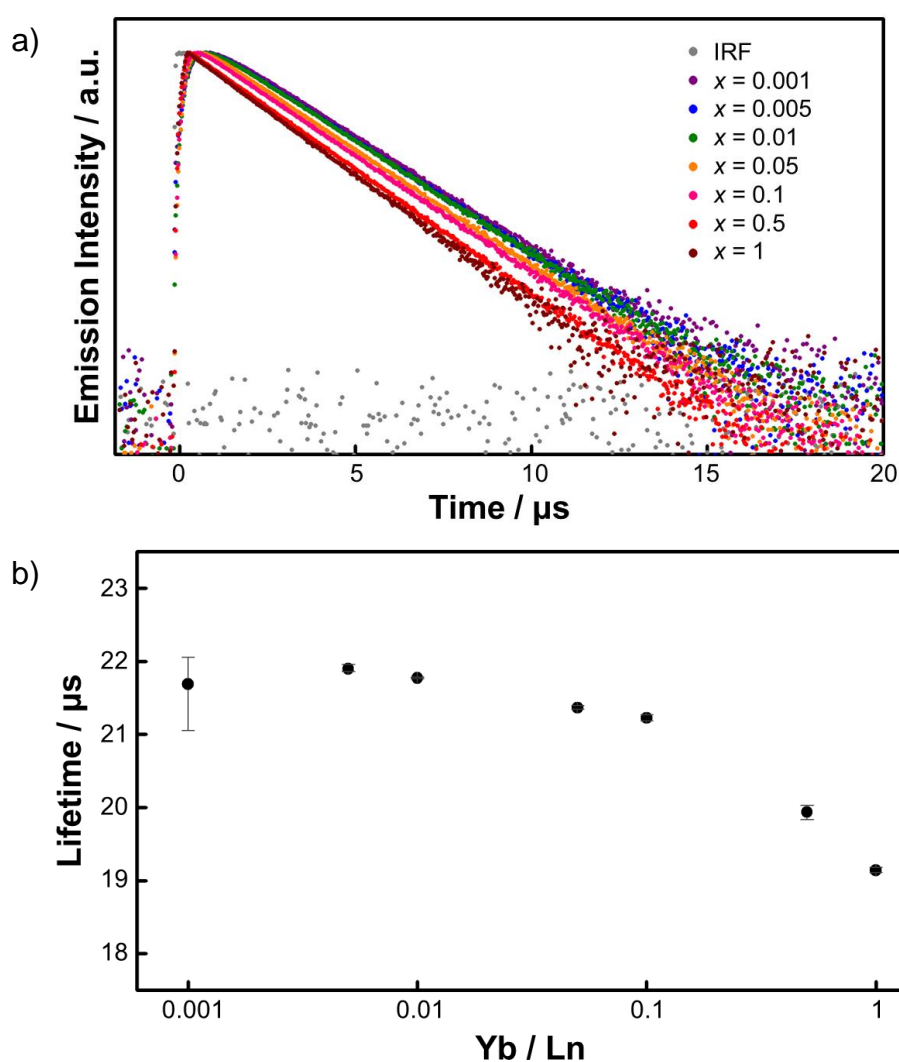


Figure 3.5 a) Emission lifetime decay profile of $[\text{Yb}_x\text{Gd}_{1-x}(\text{hfa})_3\text{dpbp}]_n$ coordination polymers ($\lambda_{\text{EX}} = 356 \text{ nm}$, $\lambda_{\text{EM}} = 1007 \text{ nm}$). IRF: instrument response function. b) Plot of emission lifetimes for all Yb(III) concentration in $[\text{Yb}_x\text{Gd}_{1-x}(\text{hfa})_3\text{dpbp}]_n$ coordination polymers.

Yb(III) ion concentration is high. This result confirms the existence of self-trapping in $[\text{Yb}_x\text{Gd}_{1-x}(\text{hfa})_3\text{dpbp}]_n$ coordination polymers.

Emission lifetimes provide information on the mechanism of concentration quenching. Emission decay profiles of $[\text{Yb}_x\text{Gd}_{1-x}(\text{hfa})_3\text{dpbp}]_n$ coordination polymers excited at 356 nm and monitored at 1007 nm (Yb(III) ion emission) are shown in Figure 3.5a. The emission decay profiles were single-exponential at all concentrations of Yb(III) ions in the polymers. The emission lifetimes remained constant at approximately 21.8 μs for $x = 0.001$ to $x = 0.01$, and gradually decreased for higher concentrations (Figure 3.5b). The emission lifetimes ultimately decreased to 19.2 μs for $x = 1$. According to the previous reports, self-trapping leads to an increase in emission lifetimes, while self-quenching leads to a decrease in emission lifetimes.^[12,30] An increase in the emission lifetimes was not observed, indicating the dominant effect of self-quenching over the effect of self-trapping. The weak effect of self-trapping is because the optical measurements were performed on the fine powder sample. The long minimum Yb(III) – Yb(III) distance of 10.4 Å typically means a limited-diffusion type of concentration quenching due to the slow energy migration. Since this type of concentration quenching leads to multi-exponential decay at high concentration in the presence of killer-sites, there is an inconsistency with the experimental result that showed single exponential decay. Therefore, interpreting the concentration quenching mechanism from the shape of the decay profiles is not simple. In the following section, the concentration quenching mechanisms is elucidated by qualitatively comparing the experimental lifetimes to those of theoretically calculated lifetimes.

3.4.3. Theoretical Lifetimes

The theoretical lifetimes were calculated for “no concentration quenching (NCQ),” “killer-site (KS),” and “phonon-assisted ET relaxation” (PAETR) models by the method provided in 3.3. Theoretical Methods. The theoretical emission decay profiles of $[\text{Yb}_x\text{Gd}_{1-x}(\text{hfa})_3\text{dpbp}]_n$ coordination polymers in the NCQ model for $x = 0.01, 0.05, 0.1, 0.5,$ and 1 are given in Figure 3.6a. All emission lifetimes were identical both in the shape of the decay profile (being single-component) and the slope. The result indicates that the emission lifetimes do not depend on the concentration of Yb(III) ions (and thus the energy migration rate), in the absence of concentration quenching even when the distribution of Yb(III) ions is inhomogeneous.

In the presence of concentration quenching, the coordination polymers exhibit different photophysical behavior between the KS model and the PAETR model. In the presence of a

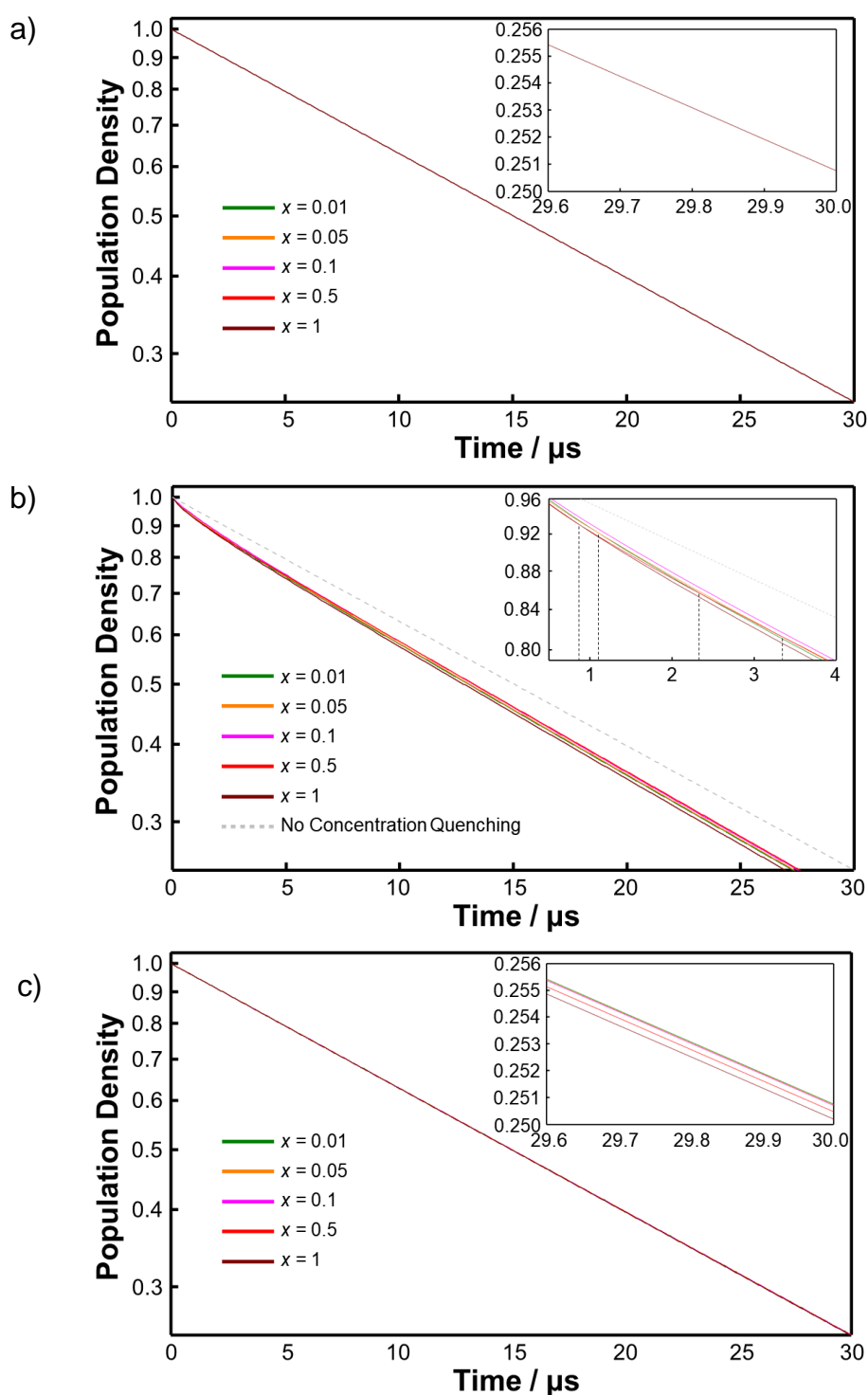


Figure 3.6 Theoretical time-evolution of the population density of the excited state Yb(III) ions of $[\text{Yb}_x\text{Gd}_{1-x}(\text{hfa})_3\text{dpbp}]_n$ coordination polymers for $x = 0.01 - 1$: a) "No concentration quenching" (NCQ) model, b) "killer-site" (KS) model, and c) "phonon-assisted ET relaxation" (PAETR) model. The inset shows the close-up of the decay profiles. Time-evolution of the population density of the excited state Yb(III) ions is directly related to emission lifetimes.

killer-site, the shape of the decay profile was multi-component for all concentration, even at $x = 0.01$ (Figure 3.6b). The average lifetimes did not change significantly with concentration, contrary to what would generally be expected for this model. There are several points of the decay profiles of each concentration that crosses (Figure 3.6b inset), indicating that the concentrations considered in this calculation are within the range of transition phase from a limited-diffusion to a fast-diffusion scheme. These features are not observed in the case of PAETR model as the decay profile remains single-component throughout all concentrations and gradually decreases with increasing concentration (Figure 3.6c). The difference in the photophysical behavior between the two concentration quenching mechanisms arises from the degree of localization of the quenching. Concentration quenching in the KS model is a localized mechanism where the excited state energy is delivered to the killer-site via energy migration. In the case of $[\text{Yb}_x\text{Gd}_{1-x}(\text{hfa})_3\text{dpbp}]_n$ coordination polymers, the maximum ET rate for the central Yb(III) ion (red dot in Figure 3.2) is 20378 s^{-1} , which is approximately only the half of the fundamental decay rate constant ($A_{\text{rad}}+A_{\text{nrad}}$) of 46109 s^{-1} . This implies that energy migration does not diffuse to large spatial area and average out the lifetimes of individual Yb(III) ion. Depending on the position of the killer-site relative to the excited Yb(III) ion, the effect of the quenching can change drastically. In total, the emission from multiple spherical ensembles with the various position of killer-sites lead to the multi-component decay. On the other hand, concentration quenching in the PAETR model is a well-distributed effect since

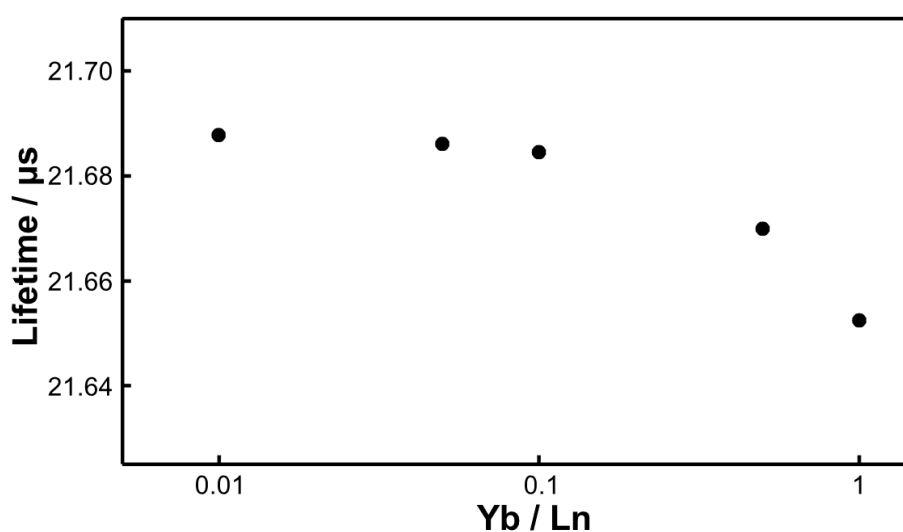


Figure 3.7 Plot of theoretical lifetimes for the PAETR model.

phonon-assisted ET relaxation occurs between all Yb(III) ions that are close. This results in the decay profile that is apparently single-component for all concentrations.

Of the three different models, the experimental emission decay profiles (Figure 3.5a) are more consistent with the theoretical emission decay profiles for the PAETR model (Figure 3.6c). Both show similar shape for the decrease in the emission lifetimes with concentration beyond $x = 0.01$ (Figure 3.5b and 3.7), and the profiles are single-component at all concentrations. Meanwhile, the rate of decrease in the lifetimes is significantly smaller for the theoretical lifetime. This is likely because of two reasons: the increased electron-phonon coupling between Yb(III) ion pairs and the larger actual ET rate than the calculated values (see 3.6.3.). Auzel^[31,32] and Vink^[33] both reported that electron-phonon coupling strength itself increases with increased concentration of luminescent center. This could slightly increase in both A_{nrad} and W_{PAETR} . Also, the theoretical lifetimes are calculated based on typical Yb(III) oscillator strength of 3×10^{-6} but can range between $1 \times 10^{-6} - 8 \times 10^{-6}$ according to the previous studies.^[34-38] Since the ET rate constant was calculated from the oscillator strength (by deriving values for $\sum_{k=2,4,6} \Omega_k |\langle l^N SLJ || U^{(k)} || l^N S' L' J' \rangle|^2$ in Equations [2.23] and [2.24]), deviation in the oscillator strength (and refractive index) can lead to deviations in the ET rate constant roughly from 0.04 to 36 times the calculated value (which also increases W_{PAETR} around this order). In total, the deviations in the quantitative values in this case are within expected order. The single component lifetime and the similar shape of the plot of the emission lifetimes qualitatively suggest that the concentration quenching mechanism in $[\text{Yb}_x\text{Gd}_{1-x}(\text{hfa})_3\text{dpbp}]_n$ coordination polymers is the phonon-assisted ET relaxation.

The nonradiative rate constant, ET rate constant, and the model of concentration quenching are important factors that affect lifetimes, and they must be considered. As stated above, the ET rate constant is comparatively smaller than the fundamental decay rate constant in $[\text{Yb}_x\text{Gd}_{1-x}(\text{hfa})_3\text{dpbp}]_n$ coordination polymers. The maximum ET efficiency is 30.6%, and thus the excited Yb(III) ions are rather localized. The large nonradiative rate constant A_{nrad} of 45623 s^{-1} is due to the use of organic ligands with high-frequency vibration modes. In this sense, the small effect of concentration quenching in Ln(III) coordination polymers is not only because of the PAETR mechanism. The effect of concentration quenching is also lowered by the reduction in the energy migration due to the large fundamental decay rate constant of Ln(III) ions. This especially applies for NIR emitting Ln(III) ions because they are significantly more vulnerable to multi-phonon relaxation, as in the case of $[\text{Yb}(\text{hfa})_3\text{dpbp}]_n$ coordination polymer. Therefore, an extra care needs to be taken before judging that concentration quenching is a

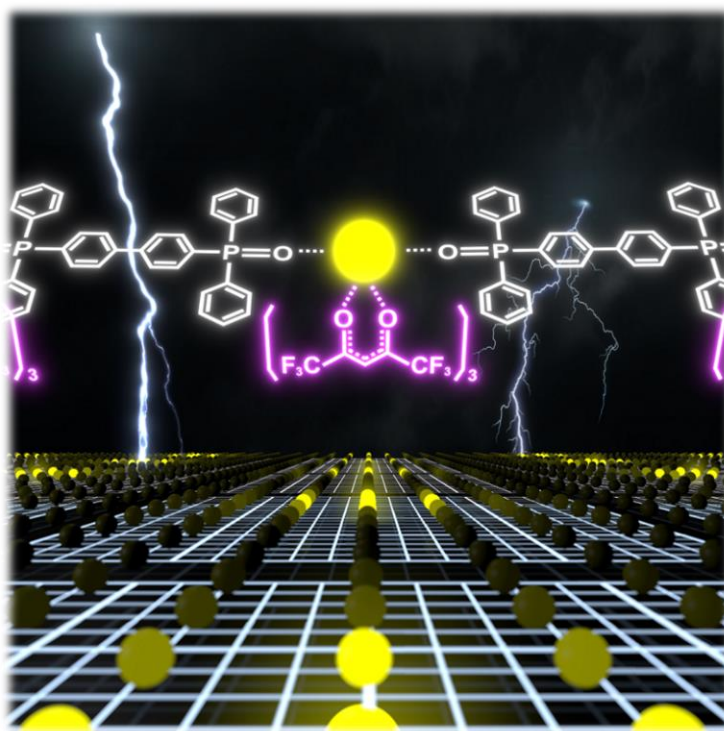
small effect in lanthanide coordination polymers, because it may simply be due to the large nonradiative rate constant and not the fundamental property of lanthanide coordination polymers.

The fundamental difference between Ln(III) doped inorganic host and Ln(III) coordination polymers is likely the concentration quenching mechanism. Inorganic hosts usually show multi-component decay, suggesting the existence of killer-sites. On the other hand, various reported Ln(III) coordination polymers, including $[\text{Yb}(\text{hfa})_3\text{dpbp}]_n$, at maximum concentration still show single-component emission lifetimes,^[39–43] implying that coordination polymers in general lack or have an extremely low concentration of killer-sites. Therefore, the concentration quenching for coordination polymers is suggested to be dominated by the PAETR, a small effect compared to strongly quenching killer-sites. Other than to lower the concentration of Ln(III) ions, the strategy to reduce the effect of concentration quenching in both types of the host is different. For inorganic hosts, this is reducing the concentration of killer-sites (high purity host). For Ln(III) coordination polymers, the general strategy to achieve high emission quantum yield in lanthanide complexes of eliminating phonon modes responsible for multi-phonon relaxation is also effective in reducing concentration quenching. Equation [3.2] indicates that smaller phonon energy $\hbar\omega$ leads to smaller PAETR rate constant W_{PAETR} . The results provides a new meaning in using Ln(III) coordination polymers as functional luminescent materials based on energy transfer.

3.5. Conclusion

The concentration quenching mechanism and the extent of its effect in $[\text{Yb}_x\text{Gd}_{1-x}(\text{hfa})_3\text{dpbp}]_n$ ($x = 0.001, 0.005, 0.01, 0.05, 0.1, 0.5, 1$) coordination polymers were investigated. Emission spectra revealed that the shorter wavelength region of the Yb(III) emission is deformed with increasing concentration of Yb(III) ions, indicating self-trapping. Emission lifetimes were single-component at all concentrations and decreased with increasing concentration of Yb(III) ions. The minimum Yb–Yb distance of the polymer of 10.4 Å suppresses long-range energy migration. For this reason, the concentration mechanism is in the limited-diffusion regime. Theoretical calculation of emission lifetimes was performed for the killer-site model and phonon-assisted energy transfer relaxation model. The calculated and experimental results were qualitatively more consistent in the latter model, suggesting that $[\text{Yb}_x\text{Gd}_{1-x}(\text{hfa})_3\text{dpbp}]_n$ acts as a high-purity host in terms of luminescence. This report is

another step forward in understanding the fundamentals of lanthanide chemistry, especially lanthanide coordination polymers and lanthanide-doped inorganic hosts.



3.6. Appendix

3.6.1. Absorption Spectra of Yb(III) Ions

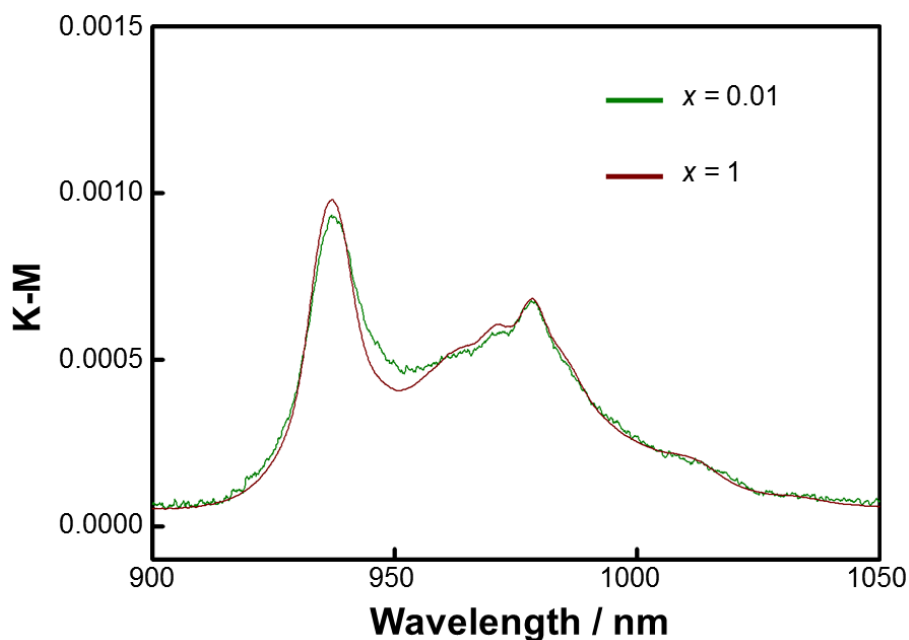


Figure A3.1 Diffuse reflectance spectra of $[\text{Yb}_1(\text{hfa})_3\text{dpbp}]_n$ and $[\text{Yb}_{0.01}\text{Gd}_{0.99}(\text{hfa})_3\text{dpbp}]_n$ in the NIR region.

3.6.2. MATLAB Script for Calculation of Theoretical Lifetimes

Calculations of theoretical lifetimes were performed using MATLAB software. The procedures are explained in 3.3.2. Rate Equations. Below is an example of the script for the calculation of $[\text{Yb}_{0.5}\text{Gd}_{0.5}(\text{hfa})_3\text{dpbp}]_n$ in the PAETR model. The section of the script defining the rate constants as well as the interaction matrix \mathbf{A} is omitted since it is a tedious work that was done on a spreadsheet software.

```
clear

how_long = tic
clear CLEAN

=> Defining various rate constants here
```

=> Defining Interaction Matrix A here

```

m = 500                                % Cycle of calculation

%Yb0.5
S1 = sym(zeros(1, m))
clear S2 t
syms t S2(t)
S2(t) = 0

wb = waitbar(0, 'Calculating for x = 0.5')
CLEAN = onCleanup(@() close(wb))

for n = 1:m
    waitbar(n/m, wb, 'Calculating for x = 0.5');
    A2 = A1

% Random generation of a quenching center (s)
    h = 0                                % max# of QCs
    r = h + 1
    B1 = setdiff(1:135, 68) .'
    q = randi(r, 1) - 1                   % Random number of QCs
    if q == 0
        B2 = []                           % Do nothing to B1
    else
        B2 = zeros(q, 1)
        for i = 1:q
            k = randi(length(B1), 1)
            B2(i) = B1(k)
            B1(k) = []
            A2(:, B2(i)) = 0
            A2(B2(i), :) = A2(B2(i), :)*1000    % Strong Quenching Center
            A2(B2(i), B2(i)) = -Anrad
        end
    end
end

```


done to the interaction matrix A to account for the inhomogeneity, and the complexity of the equation for each cycle. For example, the calculation for the KS model took approximately 4.6 days to complete while the calculation for the PAETR model took approximately 6.1 days to complete.

3.6.3. Quantitative Considerations of Theoretical Lifetimes

The plot of the experimental (Figure 3.5b) and theoretical lifetimes (Figure 3.7) differ in the order of decrease; the former decreased from 21.7 μs to 19.2 μs while the latter decreased from 21.69 μs to only 21.65 μs . As explained in 3.4.3., this is likely due to assumed oscillator strength and Huang-Rhys parameter. In order to account for this, the absorption spectrum of $\text{Yb}(\text{hfa})_3(\text{TPPO})_2$ ^[44] was measured to estimate the oscillator strength. This Yb(III) complex have similar ligands (hfa and phosphine oxide ligands) that are coordinated in a similar geometrical form as that of $[\text{Yb}(\text{hfa})_3\text{dpbp}]_n$. Thus, the oscillator strength between these two complexes are likely similar as well.

The absorption spectra of $\text{Yb}(\text{hfa})_3(\text{TPPO})_2$ in 1.0×10^{-2} M chloroform solution ($n = 1.43$ at 1000 nm^[45-47]) is shown in Figure A3.2. The oscillator strength calculated from the area of the

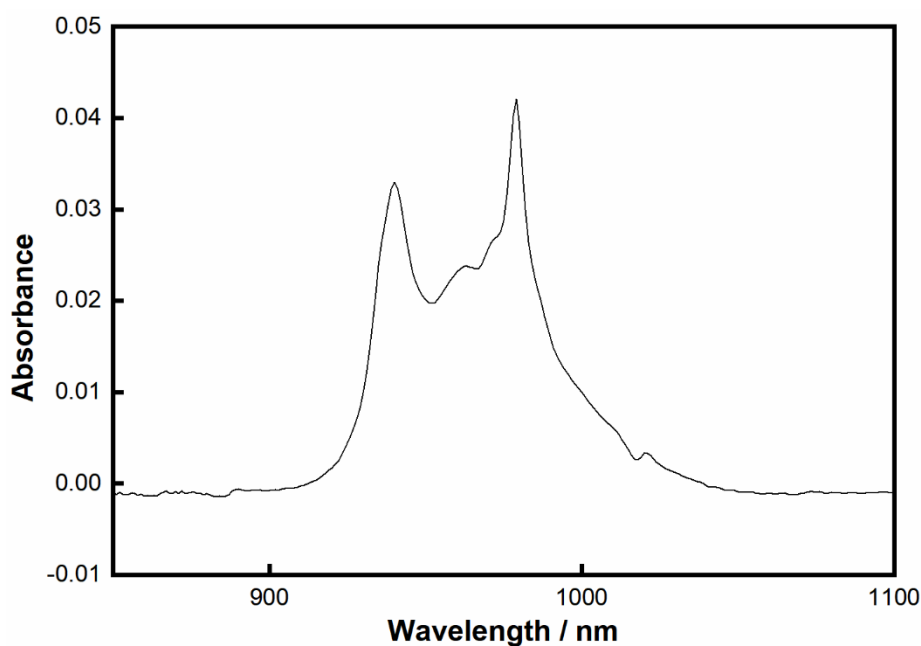


Figure A3.2 Absorption spectrum of $\text{Yb}(\text{hfa})_3(\text{TPPO})_2$ in 1.0×10^{-2} M chloroform solution.

absorption spectra was 7.24×10^{-6} . This is more than twice as stronger than the assumed oscillator strength (3×10^{-6}), which means the energy transfer rate constant is significantly increased and thus the PAETR rate constant as well.

The Huang-Rhys parameter was determined from absorption and emission spectra, but it is known from previous reports that this will not provide a very accurate value, and instead should be calculated from the ratio of intensity of phonon sideband and zero-phonon band.^[48-50] Because of the complex absorption spectra (Figure A3.1), it is difficult to consider the phonon sideband. As such, we instead assume a value. Huang-Rhys parameter s can range from 10^{-2} to 10^{-1} order in lanthanides.^[48-50] Here, the $s = 2 \times 10^{-1}$ were used based on ref 49. Also, in order to keep the discussion general, the refractive index was set to 1. The reconsidered parameters are given in Table A3.1.

The recalculated theoretical lifetimes for PAETR model is shown in Figure A3.3. The decay profile is still shown to be single exponential for all concentration and gradually decreases with increasing concentration. The lifetimes decreased from 21.69 μs to 18.31 μs . The decrease is now well within the order of decrease seen in the experiment.

Table A3.1 Values reconsidered for the theoretical calculation.

Constant	Value	Constant	Value
χ_{abs}	1	$\hbar\omega^{\text{a}}$	3141 cm^{-1} (ArC-H)
f_{total}	7.24×10^{-6} ($n = 1.43$)		3068 cm^{-1} (ArC-H)
f_{MD}	3.808×10^{-7}		1654 cm^{-1} (C=O)
f_{ED}	6.981×10^{-6}		1599 cm^{-1} (ArC=C)
A_{tot}	$4.611 \times 10^4 \text{ s}^{-1}$		1551 cm^{-1} (ArC=C)
$\sum_{k=2,4,6} \Omega_k \langle l^N S L J \ U^{(k)} \ l^N S' L' J' \rangle ^2$	$2.732 \times 10^{-20} \text{ cm}^2$		1527 cm^{-1} (ArC=C)
$A_{\text{rad(MD)}}$	$3.808 \times 10^1 \text{ s}^{-1}$		1439 cm^{-1} (P-C)
$A_{\text{rad(ED)}}$	$1.028 \times 10^2 \text{ s}^{-1}$		1254 cm^{-1} (P=O)
A_{nrad}	$4.504 \times 10^4 \text{ s}^{-1}$		1200 cm^{-1} (C-F)
$W_{\text{ET(dd)}}$	$7.729 \times 10^9 \times R^{-6} [\text{s}^{-1}]$	N^{a}	3 (ArC-H)
$W_{\text{ET(dq)}}$	$3.640 \times 10^{11} \times R^{-8} [\text{s}^{-1}]$		3 (ArC-H)
$W_{\text{ET(qq)}}$	$3.201 \times 10^{13} \times R^{-10} [\text{s}^{-1}]$		6 (C=O)
s	0.2		6 (ArC=C)
W_{PAETR}	$W_{\text{tot}} \times 7.443 \times 10^{-2} [\text{s}^{-1}]$		6 (ArC=C)
			6 (ArC=C)
			6 (P-C)
			8 (P=O)
			8 (C-F)

[a] Vibration below ArC-H have minor influence on the value of W_{PAETR}

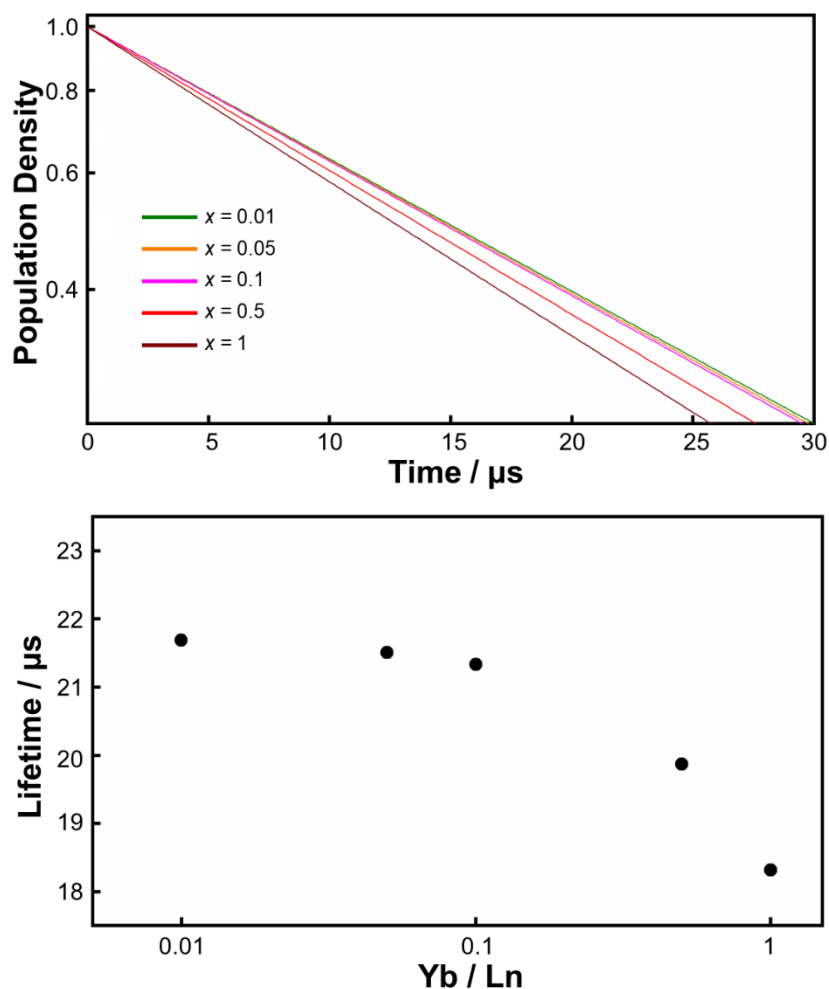


Figure A3.3 a) Recalculated theoretical time-evolution of the population density of the excited state Yb(III) ions of $[\text{Yb}_x\text{Gd}_{1-x}(\text{hfa})_3\text{dppb}]_n$ coordination polymers for $x = 0.01 - 1$ for PAETR model. b) Plot of the theoretical lifetimes for the PAETR model.

3.7. References

- [1] D. L. Dexter and J. H. Schulman, *J. Chem. Phys.* **1954**, *22*, 1063–1070.
- [2] B. Di Bartolo and V. Goldberg, *Radiationless Processes*, Plenum Press, **1980**.
- [3] F. Auzel, G. Baldacchini, L. Laversenne, G. Boulon, *Opt. Mater.* **2003**, *24*, 103–109.
- [4] F. Benz and H. P. Strunk, *AIP Adv.* **2012**, *2*, 2–7.
- [5] W. Wei, G. Chen, A. Baev, G. S. He, W. Shao, J. Damasco, P. N. Prasad, *J. Am. Chem. Soc.* **2016**, *138*, 15130–15133.

- [6] P. Yang, P. Deng, Z. Yin, *J. Lumin.* **2002**, *97*, 51–54.
- [7] M. Ito, G. Boulon, A. Bensalah, Y. Guyot, C. Goutaudier, H. Sato, *J. Opt. Soc. Am. B* **2007**, *24*, 3023–3032.
- [8] L. G. Jacobsohn, B. L. Bennett, R. E. Muenchausen, J. F. Smith, D. Wayne Cooke, *Radiat. Meas.* **2007**, *42*, 675–678.
- [9] Y. Cui, B. Chen, G. Qian, *Coord. Chem. Rev.* **2014**, *273–274*, 76–86.
- [10] J. Heine and K. Müller-Buschbaum, *Chem. Soc. Rev.* **2013**, *43*, 9232–9242.
- [11] B. Yan, Y. Bai, Z. Chen, *J. Mol. Struct.* **2005**, *741*, 141–147.
- [12] F. Auzel, F. Bonfigli, S. Gagliari, G. Baldacchini, *J. Lumin.* **2001**, *94–95*, 293–297.
- [13] J. Knoester, J. E. Van Himbergen, *J. Chem. Phys.* **1987**, *86*, 3571.
- [14] F. Auzel, *Chem. Rev.* **2004**, *104*, 139–173.
- [15] F. Auzel, *J. Lumin.* **2002**, *100*, 125–130.
- [16] T. Miyakawa and D. L. Dexter, *Phys. Rev. B* **1970**, *1*, 2961–2969.
- [17] R. Balda, J. Fernández, I. Saéz de Ocáriz, J. L. Adam, A. Mendioroz, E. Montoya, *Opt. Mater.* **1999**, *13*, 159–165.
- [18] V. V. Utochnikova, A. S. Kalyakina, I. S. Bushmarinov, A. A. Vashchenko, L. Marciniak, A. M. Kaczmarek, R. Van Deun, S. Bräse, N. P. Kuzmina, *J. Mater. Chem. C* **2016**, *4*, 9848–9855.
- [19] K. Miyata, Y. Konno, T. Nakanishi, A. Kobayashi, M. Kato, K. Fushimi, Y. Hasegawa, *Angew. Chem. Int. Ed.* **2013**, *52*, 6413–6416.
- [20] Y. Hirai, T. Nakanishi, K. Miyata, K. Fushimi, Y. Hasegawa, *Mater. Lett.* **2014**, *130*, 91–93.
- [21] K. Miyata, T. Ohba, A. Kobayashi, M. Kato, T. Nakanishi, K. Fushimi, Y. Hasegawa, *ChemPlusChem* **2012**, *77*, 277–280.
- [22] B. R. Judd, *Phys. Rev.* **1962**, *127*, 750–761.
- [23] G. S. Ofelt, *J. Chem. Phys.* **1962**, *37*, 511–520.
- [24] M. P. Hehlen, M. G. Brik, K. W. Krämer, *J. Lumin.* **2013**, *136*, 221–239.
- [25] T. Kushida, *J. Phys. Soc. Jpn.* **1973**, *34*, 1318–1326.
- [26] O. L. Malta, *J. Non. Cryst. Solids* **2008**, *354*, 4770–4776.
- [27] L. Aboshyan-Sorgho, H. Nozary, A. Aebischer, J. C. G. Bünzli, P. Y. Morgantini, K. R. Kittilstved, A. Hauser, S. V. Eliseeva, S. Petoud, C. Piguet, *J. Am. Chem. Soc.* **2012**, *134*, 12675–12684.
- [28] M. E. Starzak, *Mathematical Methods in Chemistry and Physics*, Springer, **1989**.
- [29] J.-C. G. Bünzli and S. V. Eliseeva, Basics of Lanthanide Photophysics, in *Springer Series*

- on Fluorescence*, Springer, **2011**.
- [30] M. Ito, C. Goutaudier, Y. Guyot, K. Lebbou, T. Fukuda, G. Boulon, *J. Phys. Condens. Matter* **2004**, *16*, 1501–1521.
- [31] F. Auzel, G. F. de Sá, W. M. de Azevedo, *J. Lumin.* **1980**, *21*, 187–192.
- [32] F. Auzel and F. Pellé, *J. Lumin.* **1996**, *69*, 249–255.
- [33] A. P. Vink, A. Meijerink, *Spectrochim. Acta Part A* **1998**, *54*, 1755–1761.
- [34] W. T. Carnall, P. R. Fields, K. Rajnak, *J. Chem. Phys.* **1968**, *49*, 4412.
- [35] F. Auzel, A. M. Jean-Louis, Y. Toudic, *J. Appl. Phys.* **1989**, *66*, 3952–3955.
- [36] K. Venkata Krishnaiah, R. Rajeswari, K. Upendra Kumar, S. Surendra Babu, I. R. Martin, C. K. Jayasankar, *J. Quant. Spectrosc. Radiat. Transf.* **2014**, *140*, 37–47.
- [37] E. A. Seregina, A. A. Seregin, G. V Tikhonov, *Opt. Spectrosc.* **2014**, *116*, 438–453.
- [38] S. Balaji, A. K. Mandal, K. Annapurna, *Opt. Mater.* **2012**, *34*, 1930–1934.
- [39] W.-G. Lu, D.-C. Zhong, L. Jiang, T.-B. Lu, *Cryst. Growth Des.* **2012**, *12*, 3675–3683.
- [40] R. Decadt, K. van Hecke, D. Depla, K. Leus, D. Weinberger, I. van Driessche, P. Van Der Voort, R. van Deun, *Inorg. Chem.* **2012**, *51*, 11623–11634.
- [41] S. Chen, R. Fan, C. Sun, P. Wang, Y. Yang, Q. Su, Y. Mu, *Cryst. Growth Des.* **2012**, *12*, 1337–1346.
- [42] Z. Y. Li, J. W. Dai, N. Wang, H. H. Qiu, S. T. Yue, Y. L. Liu, *Cryst. Growth Des.* **2010**, *10*, 2746–2751.
- [43] A. R. Ramya, D. Sharma, S. Natarajan, M. L. P. Reddy, *Inorg. Chem.* **2012**, *51*, 8818–26.
- [44] S. Kishimoto, T. Nakagawa, T. Kawai, Y. Hasegawa, *Bull. Chem. Soc. Jpn.* **2011**, *84*, 1–5.
- [45] A. Samoc, *J. Appl. Phys.* **2003**, *94*, 6167–6174.
- [46] H. El-Kashef, *Opt. Mater.* **2002**, *20*, 81–86.
- [47] S. Kedenburg, M. Vieweg, T. Gissibl, H. Giessen, *Opt. Mater. Express* **2012**, *2*, 1588.
- [48] C. de Mello Donegá, A. Meijerink, G. Blasse, *J. Phys. Condens. Matter* **1992**, *4*, 8889–8902.
- [49] C. de Mello Donegá, S. Schenker, H. F. Folkerts, A. Meijerink, G. Blasse, *J. Phys. Condens. Matter* **1994**, *6*, 6043–6056.
- [50] M. P. Hehlen, A. Kuditcher, S. C. Rand, M. A. Tischler, *J. Chem. Phys.* **1997**, *107*, 4886–4892.

Chapter 4

***SPIN-ORBIT COUPLING AND ENERGY TRANSFER
IN NONANUCLEAR LANTHANIDE CLUSTERS***

4.1. Introduction

Spin-orbit coupling (SOC) plays an important role in Ln(III) complexes to efficiently produce the T_1 state of organic ligands, which is the state that FET proceeds from.^[1–3] SOC mixes states of different multiplicity, and thus S_1 and T_1 , as well as T_1 and S_0 states are mixed (see 4.5.1.).^[4,5] This makes ISC and phosphorescence partially allowed processes. There are two ISC processes $S_1 \rightarrow T_1$ and $T_1 \rightarrow S_0$. So the relaxation of the T_1 state includes partially allowed phosphorescence and ISC to the ground state.

The SOC in Ln(III) complexes is strong due to 1) the large effective nuclear charge of Ln(III) ions (the “heavy atom effect”), and 2) the spin and orbital angular momentum of 4f-electrons (the “paramagnetic effect”). As a result, $S_1 \rightarrow T_1$ ISC rate in Ln(III) complexes are assumed to be fast and ranges anywhere between 10^7 to 10^{10} s^{-1} .^[6–8] Reports by S. Tobita and D. M. Guldi both showed that the difference in SOC arises predominantly from the paramagnetic effect rather than the heavy atom effect in the lanthanide series. For example, Gd(III) complex with methyl salicylate ligands showed an order of magnitude larger $S_1 \rightarrow T_1$ ISC and $T_1 \rightarrow S_0$ relaxation rates compared to Lu(III) complex despite Lu(III) being the heavier atom. D. M. Guldi and his coworkers further demonstrated that both $S_1 \rightarrow T_1$ ISC and $T_1 \rightarrow S_0$ relaxation rates are roughly proportional to the magnetic moment of the lanthanides.^[8]

Here, the effect of SOC on the sensitization efficiency of Ln(III) complexes is considered. As mentioned in the 1.3.1., the sensitization efficiency η_{sens} is given by the following equation:

$$\begin{aligned} \eta_{\text{sens}} &= \eta_{\text{ISC}} \times \eta_{\text{FET}} \\ &= \frac{k_{\text{ISC}}}{kr_{S_1} + knr_{S_1} + k_{\text{ISC}}} \times \frac{k_{\text{FET}}}{kr_{T_1} + knr_{T_1} + k_{\text{FET}}}, \end{aligned} \quad [4.1]$$

where k_{ISC} , k_{FET} , are $S_1 \rightarrow T_1$ ISC, FET rate constants, respectively. kr and knr are radiative and nonradiative rate constants, respectively, and the subscript denotes the states in which they apply to. Since SOC increases k_{ISC} , kr_{T_1} , and knr_{T_1} , it can be inferred from Equation [4.1] that strong SOC enhances η_{ISC} while reducing η_{FET} . The opposing effect that SOC has on η_{ISC} and η_{FET} indicate that the sensitization efficiency η_{sens} , which is the product of η_{ISC} and η_{FET} , should have an optimal point in terms of SOC strength.

Experimentally investigating the existence of the optimal point, however, is difficult. SOC is determined by the specific Ln(III) ion that is being used. Changing the Ln(III) ion also changes the FET rate constant k_{FET} as well (all Ln(III) ions have different 4f-state energy

levels) and thus, direct comparison of the effect of SOC induced by Ln(III) cannot be determined spectroscopically. Herein, nonanuclear Ln(III) clusters was selected as the suitable material.^[9] The clusters allow control of SOC by mixing different Ln(III) ions without significantly distorting the structure. Yb(III), Gd(III), and Lu(III) ions were chosen for this study. The Yb(III) ion with its two-level 4f-states ($^2F_{7/2}$ and $^2F_{5/2}$ states) is suitable as the emissive center for the simplicity in discussing $T_1 \rightarrow Yb(^2F_{5/2})$ ET process (the FET). Gd(III) and Lu(III) ions were chosen as the non-emissive paramagnetic and diamagnetic centers, respectively.

In this chapter, the effect of SOC strength induced by paramagnetic and diamagnetic Ln(III) ions on the sensitization efficiency is described. Nonanuclear Yb_nGd_{9-n} and Yb_nLu_{9-n} clusters with butyl salicylate ligands ($[Ln_9(\mu-OH)_{10}(\text{butyl salicylate})_{16}]NO_3$, $Ln = Yb_nGd_{9-n} / Yb_nLu_{9-n}$, $n = 0, 1, 3, 7, 9$) were synthesized. The clusters in the chapter are abbreviated as $Yb_nGd_{9-n}\text{-Bu}$ and $Yb_nLu_{9-n}\text{-Bu}$ (Bu = butyl salicylate ligands). The clusters were identified by IR, mass spectroscopy, and elemental analysis. The structural analysis was performed by the combination of powder and single-crystal XRD measurements. The effect of SOC was elucidated by emission spectra and lifetimes. This study explore whether the sensitization efficiency is improved or reduced in the presence of a strong SOC. Either result provides important insight into fundamental photophysics of Ln(III) complexes as well as factors to consider when designing them to optimize the energy transfer efficiency.

4.2. Experimental Section

4.2.1. Material

$Gd(NO_3)_3 \cdot 6H_2O$ (>99.95%) and $Lu(NO_3)_3 \cdot 4H_2O$ (>99.95%) were purchased from Kanto Chemical Co., and $Yb(NO_3)_3 \cdot 5H_2O$ (99.9%) was purchased from Sigma-Aldrich Japan. Butylsalicylate was purchased from Tokyo Chemical Industries. Methanol for spectroscopy was purchased from Wako Pure Chemical Industries, Ltd. All reagents were used without further purification.

4.2.2. Apparatus

FAB-MS and ESI-MS spectra were measured on a JEOL JMS-700TZ and a JEOL JMS-T100LP, respectively. Elemental analyses were performed by an Exter Analytical CE440. Infrared spectra were recorded on a JASCO FT/IR-4600 spectrometer. XRD spectra were

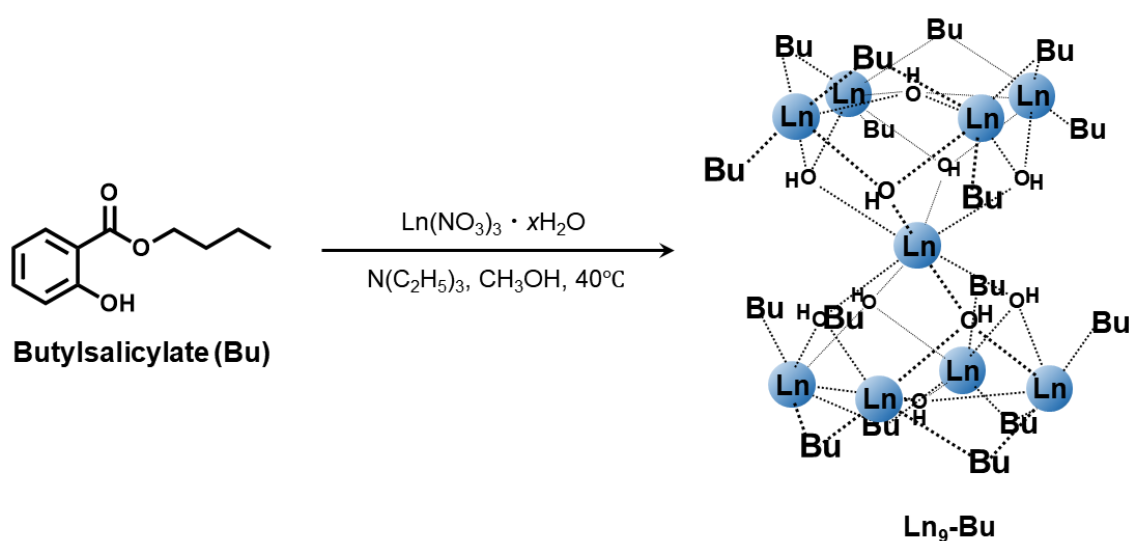
characterized by a RIGAKU SmartLab X-ray diffractometer. Single crystal X-ray diffractions were made on a RIGAKU RAXIS RAPID imaging plate area detector.

4.2.3. Synthesis

General synthetic procedures of $\text{Yb}_n\text{Gd}_{9-n}\text{-Bu}$ and $\text{Yb}_n\text{Lu}_{9-n}\text{-Bu}$: The general synthetic procedures are shown in Scheme 4.1. 2.7 mmol of butyl salicylate ligand (Bu) was dissolved in methanol, and triethylamine (0.44 mL, 4.40 mmol) was added to this solution while stirred at 40 °C. 1.52 mmol of the appropriate ratio of $\text{Gd}(\text{NO}_3)_3 \cdot 6\text{H}_2\text{O}$ and $\text{Yb}(\text{NO}_3)_3 \cdot 5\text{H}_2\text{O}$ or $\text{Lu}(\text{NO}_3)_3 \cdot 4\text{H}_2\text{O}$ dissolved in methanol was added dropwise to this solution and further stirred for 60 minutes. The resulting white precipitate (the target cluster) was vacuum filtered and dried in vacuum. The clusters were recrystallized by evaporation method from a concentrated methanol solution.

$\text{Gd}_9\text{-Bu}$: Yield: 68%. Selected IR (ATR, cm^{-1}): 3573 (w, O–H), 3235 (w, O–H), 2956 (m, C–H), 1319 (s, C–O). FAB-MS: $m/z = 4676.8$ [$\text{Gd}_9(\mu\text{-OH})_{10}(\text{Bu})_{16}$] $^+$. Elemental analysis calculated for $\text{C}_{176}\text{H}_{218}\text{NO}_{61}\text{Gd}_9$: C, 44.61%, H, 4.64%, N, 0.30%. Found: C, 44.30%, H, 4.53%, N, < 0.30%.

$\text{Yb}_1\text{Gd}_8\text{-Bu}$: Yield: 67%. Selected IR (ATR, cm^{-1}): 3572 (w, O–H), 3235 (w, O–H), 2957 (m, C–H), 1319 (s, C–O). FAB-MS: $m/z = 4692.2$ [$\text{Yb}_1\text{Gd}_8(\mu\text{-OH})_{10}(\text{Bu})_{16}$] $^+$. Elemental analysis calculated for $\text{C}_{176}\text{H}_{218}\text{NO}_{61}\text{Yb}_1\text{Gd}_8$: C, 44.46%, H, 4.62%, N, 0.29%. Found: C, 43.98%, H,



Scheme 4.1 Synthetic procedure of $\text{Ln}_9\text{-Bu}$. $\text{Ln}_9 = \text{Yb}_n\text{Gd}_{9-n}$ or $\text{Yb}_n\text{Lu}_{9-n}$.

4.45%, N, < 0.30%.

Yb₃Gd₆-Bu: Yield: 78%. Selected IR (ATR, cm⁻¹): 3572 (w, O–H), 3223 (w, O–H), 2957 (m, C–H), 1319 (s, C–O). FAB-MS: m/z = 4724.3 [Yb₃Gd₆(μ-OH)₁₀(Bu)₁₆]⁺. Elemental analysis calculated for C₁₇₆H₂₁₈NO₆₁Yb₃Gd₆: C, 44.17%, H, 4.59%, N, 0.29%. Found: C, 43.77%, H, 4.41%, N, < 0.30%.

Yb₇Gd₂-Bu: Yield: 85%. Selected IR (ATR, cm⁻¹): 3582 (w, O–H), 3210 (w, O–H), 2957 (m, C–H), 1321 (s, C–O). FAB-MS: m/z = 4785.8 [Yb₇Gd₂(μ-OH)₁₀(Bu)₁₆]⁺. Elemental analysis calculated for C₁₇₆H₂₁₈NO₆₁Yb₇Gd₂: C, 43.59%, H, 4.53%, N, 0.29%. Found: C, 43.27%, H, 4.36%, N, < 0.30%.

Yb₉-Bu: Yield: 78%. Selected IR (ATR, cm⁻¹): 3585 (w, O–H), 3206 (w, O–H), 2956 (m, C–H), 1320 (s, C–O). FAB-MS: m/z = 4819.0 [Yb₉(μ-OH)₁₀(Bu)₁₆]⁺. Elemental analysis calculated for C₁₇₆H₂₁₈NO₆₁Yb₉: C, 43.31%, H, 4.50%, N, 0.29%. Found: C, 42.99%, H, 4.37%, N, < 0.30%.

Yb₇Lu₂-Bu: Yield: 80%. Selected IR (ATR, cm⁻¹): 3585 (w, O–H), 3226 (w, O–H), 2956 (m, C–H), 1321 (s, C–O). ESI-MS: m/z = 4822.74 [Yb₇Lu₂(μ-OH)₁₀(Bu)₁₆]⁺. Elemental analysis calculated for C₁₇₆H₂₁₈NO₆₁Yb₇Lu₂: C, 43.27%, H, 4.50%, N, 0.29%. Found: C, 42.94%, H, 4.37%, N, < 0.30%.

Yb₃Lu₆-Bu: Yield: 28%. Selected IR (ATR, cm⁻¹): 3584 (w, O–H), 3206 (w, O–H), 2957 (m, C–H), 1321 (s, C–O). ESI-MS: m/z = 4830.73 [Yb₃Lu₆(μ-OH)₁₀(Bu)₁₆]⁺. Elemental analysis calculated for C₁₇₆H₂₁₈NO₆₁Yb₃Lu₆: C, 43.21%, H, 4.49%, N, 0.29%. Found: C, 42.73%, H, 4.31%, N, 0.25%.

Yb₁Lu₈-Bu: Yield: 81%. Selected IR (ATR, cm⁻¹): 3586 (w, O–H), 3208 (w, O–H), 2956 (m, C–H), 1321 (s, C–O). ESI-MS: m/z = 4834.75 [Yb₁Lu₈(μ-OH)₁₀(Bu)₁₆]⁺. Elemental analysis calculated for C₁₇₆H₂₁₈NO₆₁Yb₁Lu₈: C, 43.17%, H, 4.49%, N, 0.29%. Found: C, 43.04%, H, 4.36%, N, < 0.30%.

Lu₉-Bu: Yield: 80%. Selected IR (ATR, cm⁻¹): 3586 (w, O–H), 3207 (w, O–H), 2957 (m, C–H), 1321 (s, C–O). FAB-MS: m/z = 4836.1 [Lu₉(μ-OH)₁₀(Bu)₁₆]⁺. Elemental analysis calculated for C₁₇₆H₂₁₈NO₆₁Lu₉: C, 43.16%, H, 4.49%, N, 0.29%. Found: C, 42.82%, H, 4.33%, N, < 0.30%.

4.2.4. Spectroscopy

Absorption spectra of the clusters were obtained by using a JASCO V-670 spectrometer. Emission spectra and lifetimes were measured using a Horiba/Jobin-Yvon FluoroLog-3ps

spectrofluorometer. The emission spectra of UV-vis and NIR region were connected using $\text{Eu}(\text{hfa})_3(\text{TPPO})_2$ complex as a reference to match the detection level of both detectors. A combination of JASCO FP-6600 spectrometer and Oxford Instruments OptistatDN2 cryostat was used to measure emission spectra at low temperature. The absolute quantum yield was measured by a combination of JASCO FP-6600 and an integration sphere.

4.2.5. Crystallography

Colorless single crystal of $\text{Gd}_9\text{-Bu}$, $\text{Yb}_9\text{-Bu}$, and $\text{Lu}_9\text{-Bu}$ obtained from solutions in methanol were mounted on a glass fiber by using epoxy resin glue. All measurements were made using a Rigaku RAXIS RAPID imaging plate area detector with graphite-monochromated $\text{MoK}\alpha$ radiation. Corrections for decay and Lorentz-polarization effects were made using a spherical absorption correction, solved by direct methods, and expanded using Fourier techniques. Non-hydrogen atoms were refined anisotropically except for disordered atoms. Hydrogen atoms were refined using the riding model. The final cycle of full-matrix least-squares refinement was based on observed reflections and variable parameters. All calculations were performed using a CrystalStructure crystallographic software package. The CIF data were confirmed by using the checkCIF/PLATON service. CCDC-1479981 (“ Gd_9 cluster”), CCDC-1578015 (“ Yb_9 cluster”), and CCDC-1578016 (“ Lu_9 cluster”) contain the crystallographic data for this paper. These data can be obtained free of charge from The Cambridge Crystallographic Data Center via www.ccdc.cam.ac.uk/data_request/cif.

4.3. Results and Discussion

4.3.1. Structure and Identification

The crystal structures of $\text{Gd}_9\text{-Bu}$, $\text{Yb}_9\text{-Bu}$, and $\text{Lu}_9\text{-Bu}$ are shown in Figure 4.2 and the crystallographic data in Table 4.1. The crystallographic analysis showed that the Ln(III) ions in the cluster form an “hour-glass” structure in which the upper four and lower four Ln(III) ions are connected to the center Ln(III) ion via oxygen. All Ln(III) ions have an 8-coordination structure. The center Ln(III) ion is coordinated only by oxygen atoms and not by Bu ligands while each of the Ln(III) ions in the outer unit is coordinated by both Bu ligands and oxygen atoms. In the outer unit, the upper and the lower parts are twisted approximately 45 degrees with respect to the vertical axis that goes through the two $\mu_4\text{-O}$ and the center Ln(III) ion.

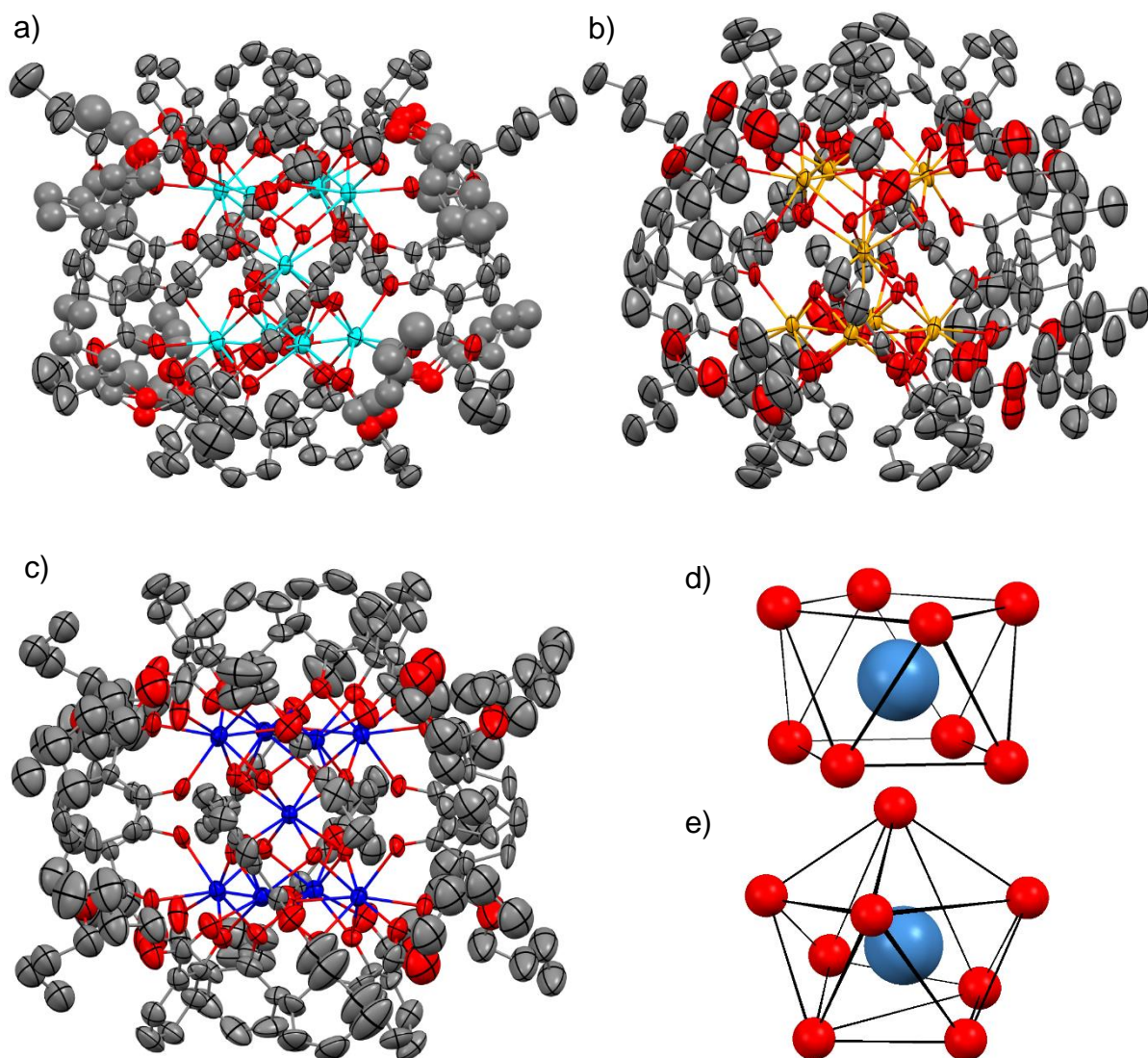


Figure 4.2 ORTEP drawing (50% probability displacement ellipsoids) of a) Gd₉-Bu, b) Yb₉-Bu, and c) Lu₉-Bu. d) center Ln(III) ion and e) other Ln(III) ions (taken from Gd₉-Bu as an example).

Continuous shape measure analysis (CShM) was employed for the Ln(III) ions in the clusters to investigate the coordination geometry.^[10,11] Continuous Shape Measures (CShM) was calculated using SHAPE program.^[12] The CShM criterion S is given by the following equation:

$$S_{\text{CShM}} = \min \frac{\sum_k^N |Q_k - P_k|^2}{\sum_k^N |Q_k - Q_0|^2} \times 100, \quad [4.2]$$

Table 4.1 Crystallographic information of Gd₉-Bu, Yb₉-Bu, and Lu₉-Bu

	Gd ₉ -Bu	Yb ₉ -Bu	Lu ₉ -Bu
Chemical formula	C ₁₇₆ H ₂₁₈ Gd ₉ NO ₆₁	C ₁₇₆ H ₂₀₈ O ₅₈ Yb ₉	C ₁₇₆ H ₂₀₈ O ₅₈ Lu ₉
Formula weight	4738.88	4808.90	4826.24
Crystal system	Orthorhombic	Tetragonal	Tetragonal
Space group	<i>Pbcn</i>	<i>P4₂/n</i> (#86)	<i>P4₂/n</i> (#86)
<i>a</i> / Å	29.1572(7)	23.5449(3)	23.857(3)
<i>b</i> / Å	21.2906(5)	23.5449(3)	23.857(3)
<i>c</i> / Å	31.7940(7)	36.1157(7)	36.2570(10)
<i>α</i> / deg	90	90	90
<i>β</i> / deg	90	90	90
<i>γ</i> / deg	90	90	90
<i>V</i> / Å ³	19736.9(8)	20021.2(5)	20636(4)
<i>Z</i>	4	4	4
<i>D</i> _{calcd} / g cm ⁻³	1.595	1.595	1.553
<i>T</i> / K	123.15	93.15	173.15
<i>μ</i> (MoK _α) / cm ⁻¹	30.655	42.345	43.357
Max 2θ / deg	55.0	56.6	50.7
No. of measured reflections	183154	74859	120501
No. of unique reflections	22608	22456	18839
<i>R</i> ^a	0.1215	0.0696	0.1265
<i>wR</i> ₂ ^b	0.2134	0.1726	0.2115

^a $R = \frac{\sum ||F_o| - |F_c||}{\sum |F_o|}$

^b $wR_2 = [\sum w(F_o^2 - F_c^2)^2 / \sum w(F_o^2)^2]^{1/2}$

where Q_k is the vertices of an actual structure, Q_0 is the center of mass of an actual structure, P_k is the vertices of an ideal structure, and N is the number of vertices. The S value represents the degree of the deviation from a specified ideal coordination geometry. The smaller the value of S , the closer the structure is to a specified ideal geometry. For example, $S = 0$ means that the structure is fully identical with the ideal geometry. CShM were chosen over another method called “Shape Measure” (ShM)^[13] because it accounts for the distortion of the center metal ion from the center of mass (see 4.5.2.). The S values calculated for the clusters are summarized in Table 4.2. For the center Ln(III) ion (Figure 4.2d), the S values ranged from 0.077 to 0.105 when calculated for 8-coordinated square antiprism (8-SAP) geometry and 2.371 to 2.481 for 8-coordinated trigonal dodecahedron (8-TDH) geometry. Therefore, the coordination geometry of the center Ln(III) ions is attributed to the 8-SAP structure. There was no specific dependence on the ionic radii of Ln(III) ions on the S values calculated for the clusters as 8-SAP. On the other hand, the other Ln(III) ions (Figure 4.2e) showed smaller S values when calculated for 8-TDH than 8-SAP. Therefore, the coordination geometry of the

Table 4.2 Continuous Shape Measure calculation results for Gd₉-Bu, Yb₉-Bu, and Lu₉-Bu.

	Gd ₉ cluster		Yb ₉ cluster		Lu ₉ cluster	
	8-TDH	8-SAP	8-TDH	8-SAP	8-TDH	8-SAP
Ln1	2.976	4.725	2.573	4.578	2.565	4.455
Ln2	2.836	4.813	2.545	4.546	2.481	4.633
Ln3	2.704	4.588	2.413	4.776	2.447	4.622
Ln4	2.513	4.822	2.404	4.623	2.400	4.507
Ln5	2.976	4.725	2.573	4.578	2.565	4.455
Ln6	2.836	4.813	2.545	4.546	2.481	4.633
Ln7	2.704	4.588	2.413	4.776	2.447	4.622
Ln8	2.513	4.822	2.404	4.623	2.400	4.507
Ln9 ^a	2.481	0.082	2.396	0.077	2.371	0.105

a) Center Ln(III) ion.

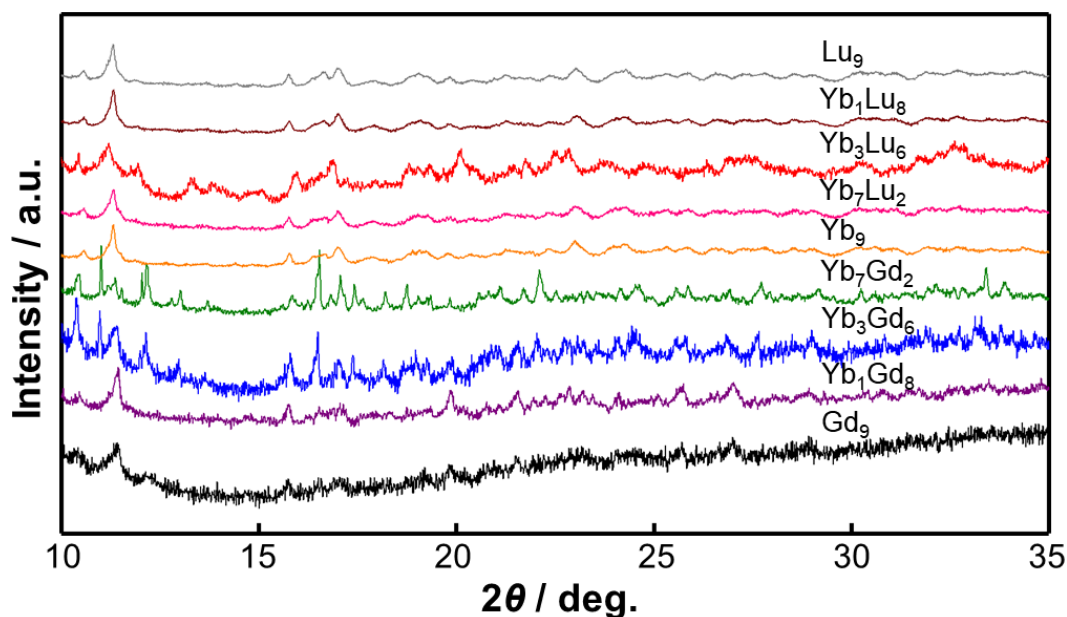


Figure 4.3 Powder XRD patterns of $\text{Yb}_n\text{Gd}_{9-n}\text{-Bu}$ and $\text{Yb}_n\text{Lu}_{9-n}\text{-Bu}$.

Ln(III) ions other than the center Ln(III) is attributed to the 8-TDH structure. Unlike the center Ln(III) ion calculated for 8-SAP, the other Ln(III) ions showed larger S values for Ln(III) ions with larger ionic radii when calculated for 8-TDH. However, the differences are still quite small, and these clusters can be considered to have the same structure. These structural results are similar to that of the previously reported $\text{Tb}_9\text{-Bu}$.^[9]

As a crystal, these three clusters have different crystal system with $\text{Yb}_9\text{-Bu}$ and $\text{Lu}_9\text{-Bu}$ being triclinic while $\text{Gd}_9\text{-Bu}$ being orthorhombic (Table 4.1). This may be due to the larger ionic radii of Gd(III) ions with minor influence on the microscopic level but is large on the larger scale. To compare the structure of the other clusters ($\text{Yb}_n\text{Gd}_{9-n}\text{-Bu}$ and $\text{Yb}_n\text{Lu}_{9-n}\text{-Bu}$, $n = 1, 3, \text{ and } 7$), XRD measurements were performed. The XRD patterns for the clusters shown in Figure 4.3 are similar, but the peaks shift to the lower angle with increasing number of Yb(III) and Lu(III) ions compared to $\text{Gd}_9\text{-Bu}$, and the peak heights are quite different among the clusters. The spectroscopic measurements were performed in methanol solution, and intermolecular interaction is minimized. Therefore, any spectroscopic differences of the clusters should arise from the structure of a single molecule. This will become important for the later discussion because a distortion of ligand alignment may affect both the ligand and Yb(III) emissions.

4.3.2. Photophysical Properties

The emission intensity of the fluorescence and phosphorescence from the ligands in $\text{Yb}_n\text{Gd}_{9-n}\text{-Bu}$ and $\text{Yb}_n\text{Lu}_{9-n}\text{-Bu}$ provides information on photophysical properties of the ligands (i.e., SOC) under the influence of the paramagnetic effect of Ln(III) ions. On the other hand, the emission intensity of Yb(III) emission implies the sensitization efficiency η_{sens} . The emission spectra of $\text{Yb}_n\text{Gd}_{9-n}\text{-Bu}$ and $\text{Yb}_n\text{Lu}_{9-n}\text{-Bu}$ in 1.0×10^{-4} M degassed methanol solution in the visible and NIR region excited at 371 nm are shown in Figure 4.4a. The peak at 410 nm corresponds to the fluorescence from the butyl salicylate ligands. The fluorescence intensity is the lowest for $\text{Yb}_9\text{-Bu}$ and increases with increasing number of Gd(III) or Lu(III) ions. Increasing number of Lu(III) ions showed greater enhancement in emission intensity compared to those with Gd(III) ions (Figure 4.4b). From these spectra, the strength of SOC in this cluster is in the order of Yb(III) > Gd(III) > Lu(III). A similar trend was reported by D. M. Guldi^[8]. The absolute quantum yield of the fluorescence of $\text{Lu}_9\text{-Bu}$ was below 1% (calculated as 0.2%). Phosphorescence was observed at low temperature (180 K) for $\text{Gd}_9\text{-Bu}$ and $\text{Yb}_9\text{-Bu}$ at around 465 nm (Figure 4.5). The intensity of the phosphorescence in relative to the fluorescence is significantly reduced for $\text{Yb}_9\text{-Bu}$ due to the presence of $T_1 \rightarrow \text{Ln}$ energy transfer. Phosphorescence was not observed for $\text{Lu}_9\text{-Bu}$ because of the high fluorescence intensity, and low $S_1 \rightarrow T_1$ ISC and $T_1 \rightarrow S_0$ relaxation rate compared to those of $\text{Gd}_9\text{-Bu}$.

Emission peak at 976 nm in Figure 4.4b originates from the ${}^2F_{5/2} \rightarrow {}^2F_{7/2}$ transition of Yb(III) ions. The spectral shape of the Yb(III) near-infrared (NIR) emission was identical for all compositions. The spectral shape of Ln(III) emission is known to be sensitive to the coordination geometry, thus the NIR emission spectra show that the coordination geometries around Yb(III) ions are identical for all clusters.^[14,15] The continuous shape measure calculations (see 4.5.2.) support this analysis. Therefore, the radiative rate constants of Yb(III) ions in these clusters are equal.

The NIR emission lifetimes monitored at 976 nm ($\lambda_{\text{EX}} = 371$ nm) were single-exponential for all compositions (Figure 4.6a). Emission lifetime values derived from single-exponential fitting showed that the lifetimes of the clusters gradually increased with decreasing number of Gd(III) ions and increasing number of Lu(III) ions (Figure 4.6b). In particular, the emission lifetimes of $\text{Yb}_1\text{Gd}_8\text{-Bu}$, $\text{Yb}_9\text{-Bu}$, and $\text{Yb}_1\text{Lu}_8\text{-Bu}$ were 568, 598, and 740 ns, respectively. The difference in the ionic radii of Gd(III), Yb(III), and Lu(III) ions may have contributed to the difference in the values of nonradiative rate constants of Yb(III) ions in the clusters.

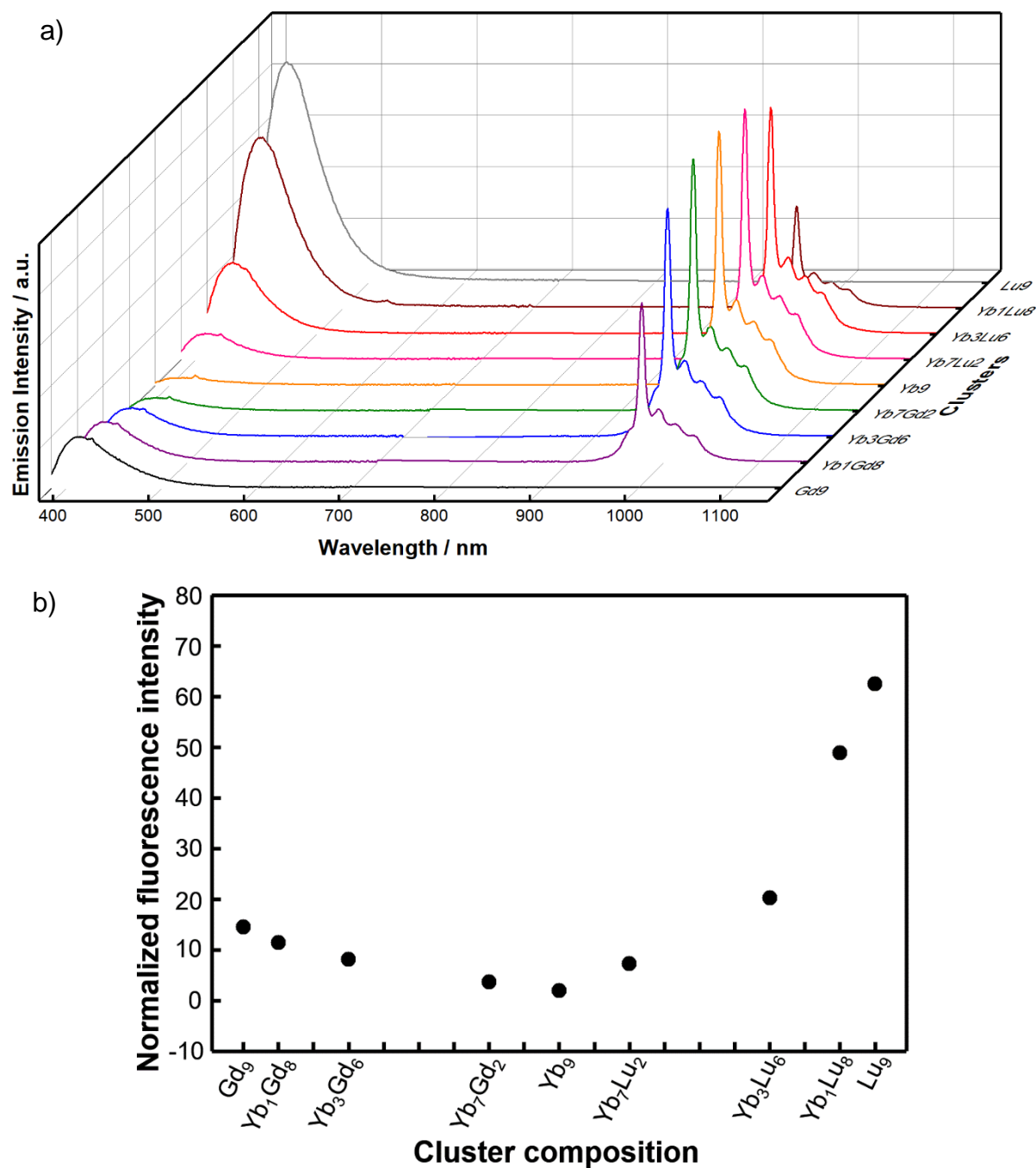


Figure 4.4 a) Emission spectra of $\text{Yb}_n\text{Gd}_{9-n}\text{-Bu}$ / $\text{Yb}_n\text{Lu}_{9-n}\text{-Bu}$ in 1.0×10^{-4} M methanol solution ($\lambda_{\text{EX}} = 371$ nm). The spectra for the UV-Vis and the NIR regions were measured separately, and connected by correcting the detectors with the previously reported $\text{Eu}(\text{hfa})_3(\text{TPPO})_2$ complex. b) Plot of the emission intensity ($\lambda_{\text{EM}} = 410$ nm) of the ligand fluorescence.

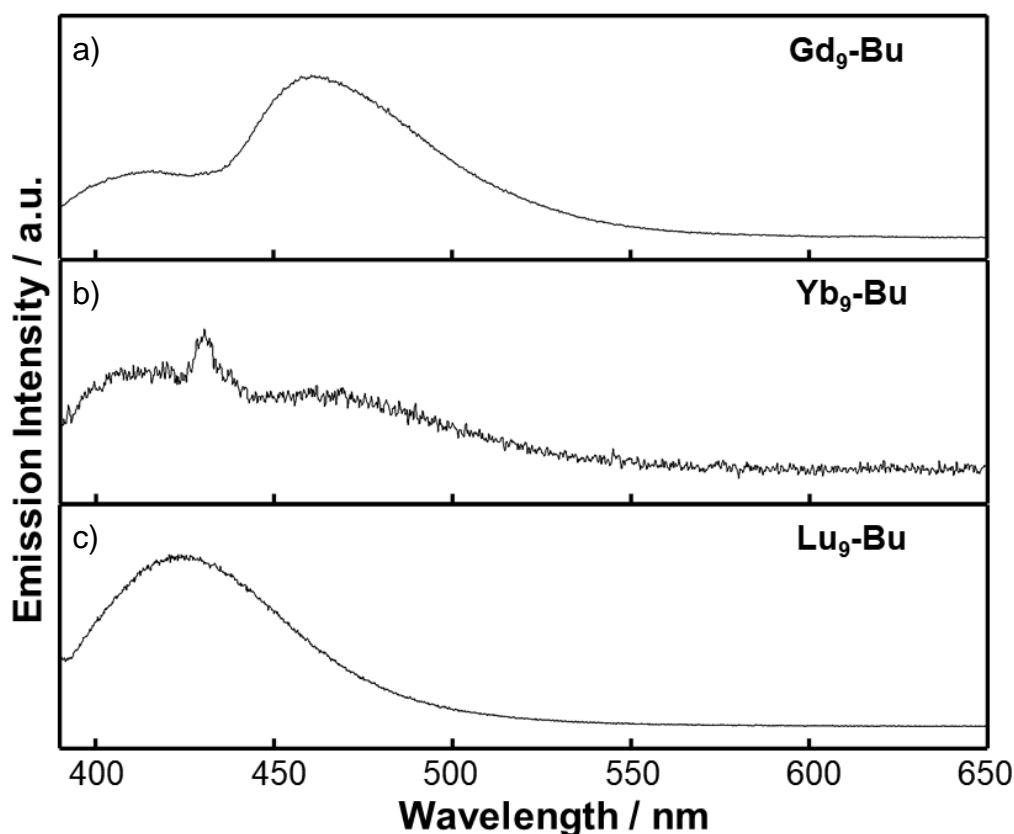


Figure 4.5 Emission spectra of a) $\text{Gd}_9\text{-Bu}$, b) $\text{Yb}_9\text{-Bu}$, and c) $\text{Lu}_9\text{-Bu}$ in 1.0×10^{-4} M methanol solution at 210 K ($\lambda_{\text{EX}} = 371$ nm). A Raman peak is observed at around 430 nm for $\text{Yb}_9\text{-Bu}$.

Figure 4.7a shows the plot of the NIR emission intensity of the clusters, normalized by the intensity of $\text{Yb}_9\text{-Bu}$. The emission intensities in the plot indirectly mean the sensitization efficiency. The emission intensity of $\text{Yb}_1\text{Gd}_8\text{-Bu}$ was 1.6 times higher than that of $\text{Yb}_1\text{Lu}_8\text{-Bu}$. For these two clusters, the main contributor to the sensitization efficiency is the $S_1 \rightarrow T_1$ ISC efficiency due to the SOC induced by Gd(III) or Lu(III) ions (region A). Stronger SOC by Gd(III) ions leads to more efficient $S_1 \rightarrow T_1$ ISC (Figure 4.7b, green arrow) in $\text{Yb}_1\text{Gd}_8\text{-Bu}$ compared to that of $\text{Yb}_1\text{Lu}_8\text{-Bu}$. On the other hand, $\text{Yb}_7\text{Gd}_2\text{-Bu}$, $\text{Yb}_9\text{-Bu}$, and $\text{Yb}_7\text{Lu}_2\text{-Bu}$ showed the same emission intensity. Normally, reduced number of emissive Ln(III) ions leads to a decrease in $T_1 \rightarrow \text{Ln}$ energy transfer efficiencies, but this phenomenon was not observed. Thus, for these three clusters, the $T_1 \rightarrow S_0$ relaxation is the main contributor to the sensitization efficiency (region B). Gd(III) and Lu(III) ions mitigated the fast $T_1 \rightarrow S_0$ relaxation induced by

the Yb(III) ions (Figure 4.7c, blue arrow) and thus the sensitization efficiency did not drop. These results suggest that there is an optimal strength of SOC for a high sensitization efficiency in Ln(III) complexes.

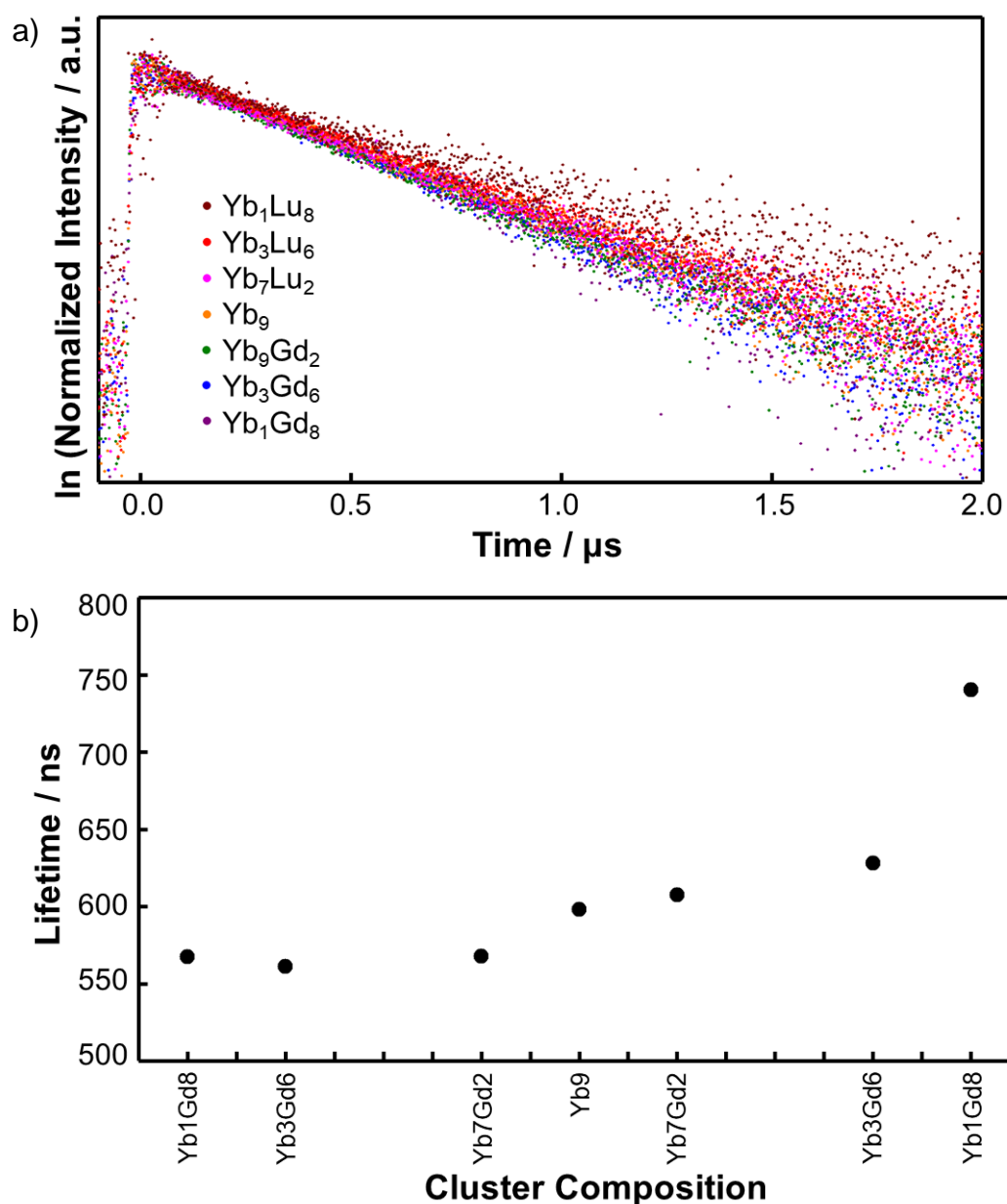


Figure 4.6 a) Emission decay profiles of Yb_nGd_{9-n}-Bu / Yb_nLu_{9-n}-Bu in 1.0×10⁻⁴ M methanol solution ($\lambda_{EX} = 371$ nm, $\lambda_{EM} = 976$ nm). b) Lifetime plot of the clusters.

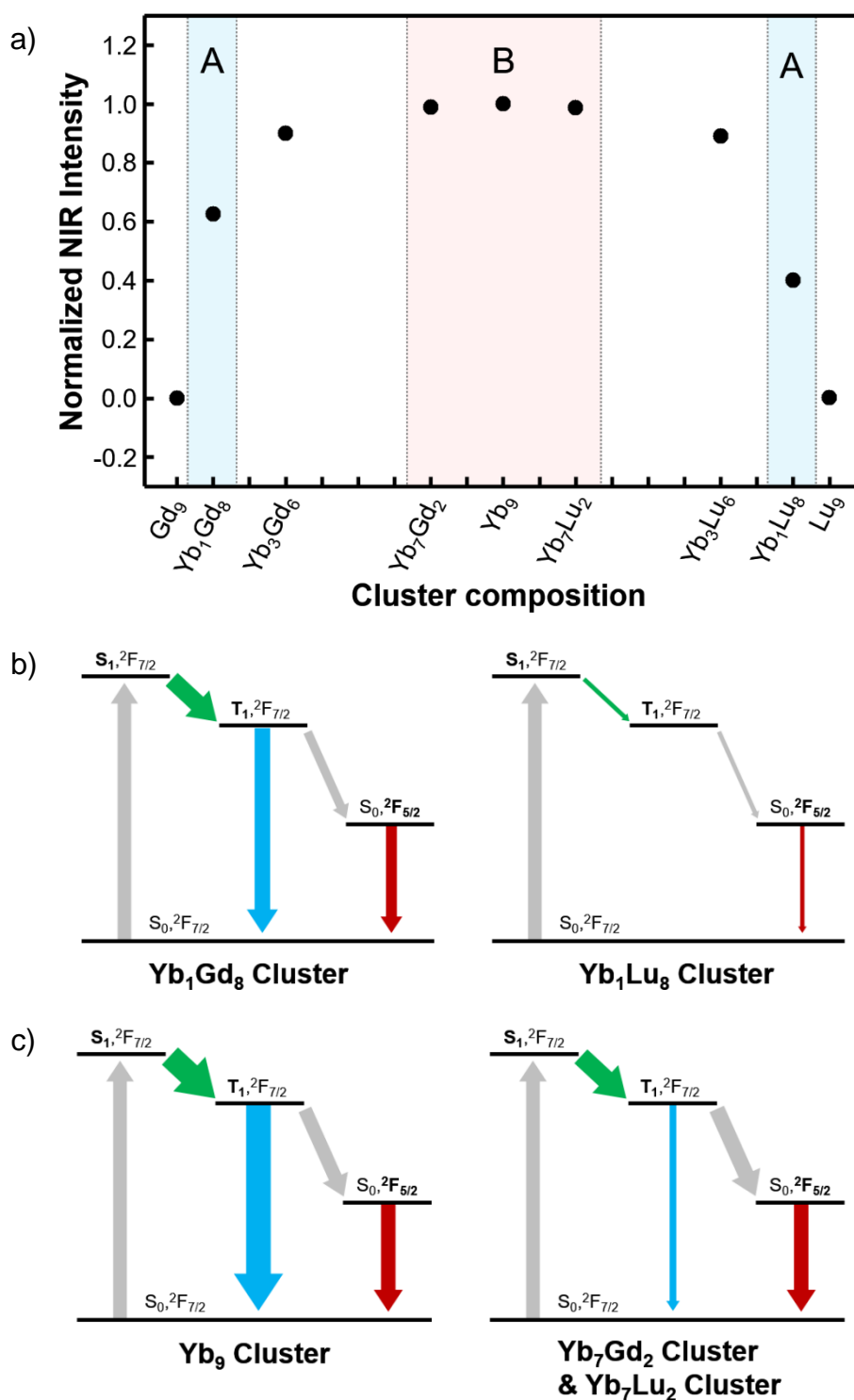
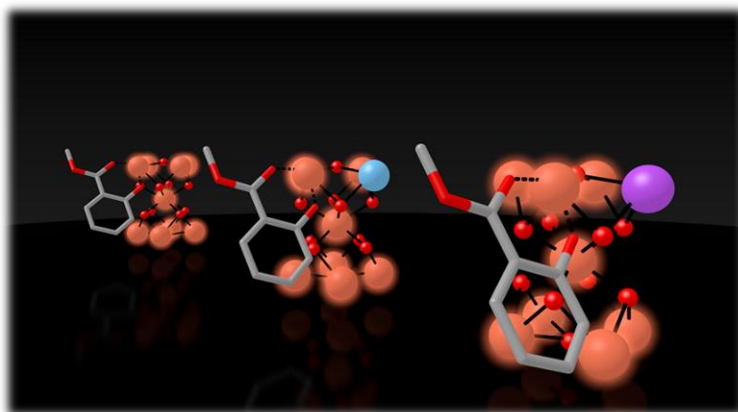


Figure 4.7 a) Plot of the NIR emission intensities normalized by the peak intensity of Yb₉-Bu. The shaded area represents the two different regions in which the dominating photophysical process differs. b) Comparison of the photophysical processes in Yb₁Gd₈-Bu and Yb₁Lu₈-Bu (region A) and c) Yb₉-Bu, Yb₇Lu₂-Bu, Yb₇Gd₂-Bu (region B). The thickness of the arrows represents the yield resulting from the process (not the rate constant of the process).

4.4. Conclusion

In this chapter, the effect of SOC strength induced by paramagnetic and diamagnetic Ln(III) ions on the sensitization efficiency in nonanuclear Ln(III) clusters was explored. Nonanuclear $\text{Yb}_n\text{Gd}_{9-n}\text{-Bu}$ and $\text{Yb}_n\text{Lu}_{9-n}\text{-Bu}$ ($[\text{Ln}_9(\mu\text{-OH})_{10}(\text{Bu})_{16}]^+\text{NO}_3^-$, $\text{Ln} = \text{Yb}_n\text{Gd}_{9-n} / \text{Yb}_n\text{Lu}_{9-n}$, $n = 0, 1, 3, 7, 9$) were synthesized and investigated their photophysical properties by emission spectra and lifetimes. The result implies that SOC affects sensitization efficiency both positively and negatively depending on the strength of SOC, and thus there is an optimal region in the SOC strength. It is also suggested that mixing Ln(III) ions with different SOC in Ln(III) clusters is an effective method to optimize sensitization efficiency. The findings are another step forward in understanding the fundamental photophysical processes in Ln(III) complexes, as well as providing a possible novel strategy to enhance the luminescence efficiency.



4.5. Appendix

4.5.1. Notes on Spin-Orbit Coupling

To be precise, spin-orbit coupling Hamiltonian H_{SO} does not always mix S_1 and T_1 state since this depends on the symmetry of the two states. In fact, spin-orbit coupling may mix higher singlet excited states S_n with another higher triplet excited states T_n . For example, mixing between singlet and triplet $n\pi^*$ state as well as singlet and triplet $\pi\pi^*$ states is not large. On the other hand, mixing of $n\pi^*$ and $\pi\pi^*$ state of different multiplicity is large (known as the El-Sayed rule).^[16] Nonetheless, the convention is that the intersystem crossing is written as a process that occurs between S_1 to T_1 for simplicity.^[17] Since this study focuses on nonanuclear $\text{Yb}_n\text{Gd}_{9-n}$ and $\text{Yb}_n\text{Lu}_{9-n}$ with the same butylsalicylate organic ligands (Bu), the mixing problem of S_1 and T_1 states can be neglected as long as the comparison is between these clusters.

4.5.2. Continuous Shape Measure and Shape Measure

Continuous shape measure (CShM) calculates the deviation of the vertices of an actual structure from the vertices of an ideal structure.^[10] The CShM criterion S_{CShM} is given by the following equation:

$$S_{\text{CShM}} = \min \frac{\sum_k^N |\mathbf{Q}_k - \mathbf{P}_k|^2}{\sum_k^N |\mathbf{Q}_k - \mathbf{Q}_0|^2} \times 100 \quad [4.2]$$

where \mathbf{Q}_k is the vertices of an actual structure, \mathbf{Q}_0 is the center of mass of an actual structure, \mathbf{P}_k is the vertices of an ideal structure, and N is the number of vertices. In the case of Gd₉-Bu, for each Gd(III) ion, N equals 9 (Gd(III) ion and eight oxygen atoms). CShM calculation takes accounts of the deviation of the metal atom from the center of mass.

On the other hand, shape measure (ShM)^[13] calculates the deviation of the dihedral angles of an actual structure from the dihedral angles of an ideal structure. The ShM criterion S_{ShM} is given by the following equation:

$$S_{\text{ShM}} = \min \sqrt{\frac{1}{M} \sum_i^M (\delta_i - \theta_i)^2} \times 100 \quad [4.3]$$

where δ_i is the angle of two planes of the ideal structure, θ_i is the angle of two planes of the actual structure, and M is the number of dihedral angles. In the case of Gd₉-Bu, for each Gd(III) ion, M equals 18. Since dihedral angles are independent of the effect of the distortion of the metal ion, ShM calculations do not take into consideration of the distortion of the metal ion.

Table A4.1 summarizes the difference in S_{CShM} values when the metal ion is taken into consideration to those of when the metal ion is not considered. The importance of considering the deviation of the metal atom from the center of mass of a structure lies in the fact that without such consideration, the S values were smaller. This indicates that when the metal ion is not considered, the actual structure is calculated to be closer to ideal. Therefore, the inclusion of the metal ion is indeed important to derive the more accurate result. It is essential to point out that the S_{CShM} value of Gd₉ (center Gd(III) ion) calculated with and without the metal ion was almost identical. This implies that the distortion of the structure of Gd₉ was purely due to the position of the oxygen atoms.

Table A4.1 Calculated S_{CShM} values for all Gd(III) ions with and without including metal ion.

Gd(III) ion	S_{SAP} (without)	S_{SAP} (with)	S_{TDH} (without)	S_{TDH} (with)
Gd1	4.670	4.725	2.920	2.976
Gd2	4.752	4.813	2.774	2.836
Gd3	4.532	4.588	2.646	2.704
Gd4	4.746	4.822	2.435	2.513
Gd5	4.670	4.725	2.920	2.976
Gd6	4.752	4.813	2.774	2.836
Gd7	4.532	4.588	2.646	2.704
Gd8	4.746	4.822	2.435	2.513
Gd9	0.082	0.082	2.481	2.481

S_{SAP} and S_{TDH} are S values calculated for an 8-coordinated square antiprism and an 8-coordinated trigonal dodecahedron, respectively. Label in parentheses indicates whether metal ion has been taken into consideration or not.

4.6. References

- [1] E. G. Moore, A. P. S. Samuel, K. N. Raymond, *Acc. Chem. Res.* **2009**, *42*, 542–552.
- [2] C. Huang, *Rare Earth Coordination Chemistry: Fundamentals and Applications*, John Wiley & Sons (Asia) Pte. Ltd., **2010**.
- [3] N. B. D. Lima, S. M. C. Gonçalves, S. A. Júnior, A. M. Simas, *Sci. Rep.* **2013**, *3*, 2395.
- [4] C. M. Marian, *WIREs Comput. Mol. Sci.* **2012**, *2*, 187–203.
- [5] L. S. Forster, *Coord. Chem. Rev.* **2006**, *250*, 2023–2033.
- [6] S. Tobita, M. Arakawa, I. Tanaka, *J. Phys. Chem.* **1985**, *89*, 5649–5654.
- [7] S. Tobita, M. Arakawa, I. Tanaka, *J. Phys. Chem.* **1984**, *88*, 2697–2702.
- [8] D. M. Guldi, T. D. Mody, N. N. Gerasimchuk, D. Magda, J. L. Sessler, *J. Am. Chem. Soc.* **2000**, *122*, 8289–8298.
- [9] T. Nakanishi, Y. Suzuki, Y. Doi, T. Seki, H. Koizumi, K. Fushimi, K. Fujita, Y. Hinatsu, H. Ito, K. Tanaka, Y. Hasegawa, *Inorg. Chem.* **2014**, *53*, 7635–7641.

- [10] D. Casanova, M. Llunell, P. Alemany, S. Alvarez, *Chem. Eur. J.* **2005**, *11*, 1479–1494.
- [11] M. Pinsky, D. Avnir, *Inorg. Chem.* **1998**, *37*, 5575–5582.
- [12] *SHAPE, version 2.1. Continuous shape measures calculations*. Electronic Structure Group, Universitat de Barcelona: Spain, **2010**.
- [13] J. Xu, E. Radkov, M. Ziegler, K. N. Raymond, *Inorg. Chem.* **2000**, *39*, 4156–4164.
- [14] Y. Hasegawa, T. Ohkubo, T. Nakanishi, A. Kobayashi, M. Kato, T. Seki, H. Ito, K. Fushimi, *Eur. J. Inorg. Chem.* **2013**, 5911–5918.
- [15] K. Miyata, T. Nakagawa, R. Kawakami, Y. Kita, K. Sugimoto, T. Nakashima, T. Harada, T. Kawai, Y. Hasegawa, *Chem. A Eur. J.* **2011**, *17*, 521–528.
- [16] M. A. El-Sayed, *J. Chem. Phys.* **1963**, *38*, 2834–2838.
- [17] J.-C. G. Bünzli, C. Piguet, *Chem. Soc. Rev.* **2005**, *34*, 1048–1077.

Chapter 5

***BACK ENERGY TRANSFER IN
NONANUCLEAR TERBIUM CLUSTERS***

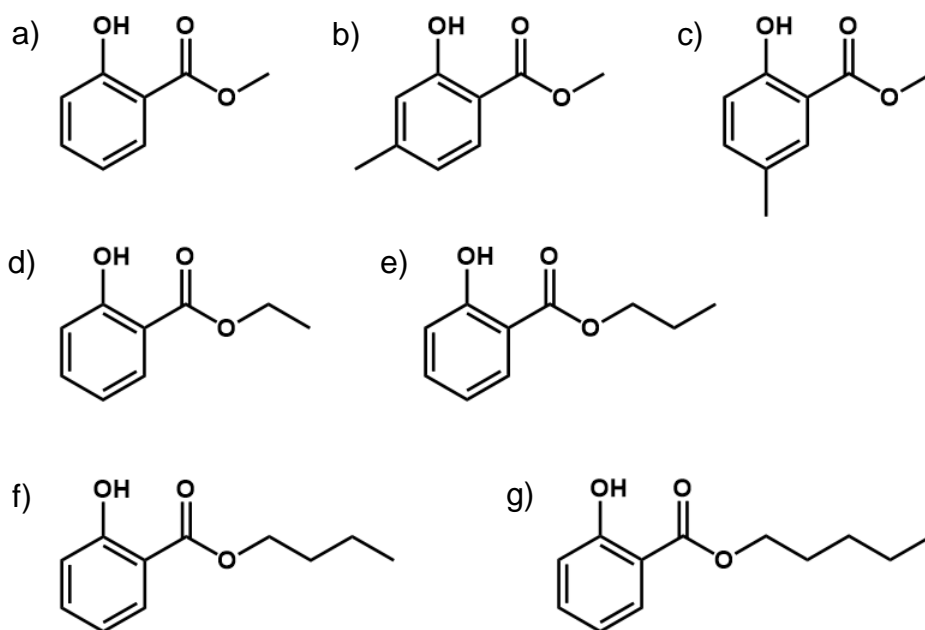
5.1. Introduction

Sensitization efficiency in Ln(III) complexes is one of the most critical factors that affect the quantum yield of Ln(III) complexes.^[1,2] Chapter 4 described the effect of SOC on the photophysical processes within the ligands of Ln(III) complexes that affects the sensitization efficiency. In this chapter, the FET process is the primary focus. FET efficiency is known to be dependent on the T_1 state energy in relative to the excited 4f-state of a Ln(III) ion.^[1,3] In particular, T_1 energy of Tb(III) complexes has a strong dependence on the quantum yield (and emission lifetimes) due to BET as shown in Figure 1.9.^[4] Within the region of the T_1 state energy below 1850 cm^{-1} , some Tb(III) complexes deviate from such trend (emission lifetimes as well). This is an important fact because it implies that there is a factor(s) other than the T_1 -Tb(5D_4) energy gap that affects the BET.

Herein, nonanuclear Tb(III) clusters were used for the investigation of the mechanism of BET.^[5] The main objective is to derive the parameters that affect the BET rate constant. By employing methyl salicylate with methyl substituent on the aromatic part as a ligand, the excited state energies of the ligand can be altered. Methyl is a weak electron-donating substituent with only of inductive effect (no resonance effect), allowing only a slight modification to the electronic structure and the excited state energies of the ligand. The reason for using nonanuclear Tb(III) clusters is similar to that explained in section 4.1. the structure of the cluster core is likely maintained. Since the luminescence property of Ln(III) ions is sensitive to the crystal field (see 1.2.2.),^[6-9] maintaining the core structure is necessary for direct comparison of the effects caused by the different ligands. However, there is a difference in the modifications mentioned in Chapter 4 and those in this chapter. In Chapter 4, different Ln(III) ions were mixed within the cluster whereas, in this chapter, different ligands are used. Therefore, the effect of the ligands on the luminescent properties of the cluster core must first be elucidated.

This chapter is composed of two parts: 1) elucidation of the effect of intramolecular interactions of the ligands on the photophysical properties of the clusters, and 2) investigation of the mechanism of BET and factors that determine the BET rate constants. The organic ligands used for this study are provided in Scheme 5.1. Alkylsalicylate ligands of different alkyl chain length, namely ethyl (Et), propyl (Pr), butyl (Bu), and hexyl (He), which changes the intramolecular interaction between ligands, were employed for 1). Methylsalicylate ligands (Me) with methyl substituent on the 4-position (4Me) and 5-position (5Me) of the aromatic part were used for 2). The synthesized nonanuclear Tb(III) clusters with these ligands above

($[\text{Tb}_9(\mu\text{-OH})_{10}(\text{L})_{16}]\text{NO}_3$, where $\text{L} = \text{Me}, 4\text{Me}, 5\text{Me}, \text{Et}, \text{Pr}, \text{Bu}, \text{or He}$) were identified by IR, mass spectroscopy, and elemental analysis. The photophysical properties were investigated by emission and absorption spectroscopy, absolute quantum yield measurements, and emission lifetimes.



Scheme 5.1 Organic ligands used for the study described in this chapter. a) Me, b) 4Me, c) 5Me, d) Et, e) Pr, f) Bu, g) He.

5.2. Experimental Section

5.2.1. Material

Salicylic acid ($\text{C}_6\text{H}_4(\text{OH})\text{COOH}$), methanol (CH_3OH), ethanol ($\text{C}_2\text{H}_5\text{OH}$), propanol ($\text{C}_3\text{H}_7\text{OH}$), *n*-butanol ($\text{C}_4\text{H}_9\text{OH}$), Tb(III) nitrate hexahydrate ($\text{Tb}(\text{NO}_3)_3 \cdot 6\text{H}_2\text{O}$) and triethylamine ($\text{C}_6\text{H}_{15}\text{N}$) were purchased from Kanto Chemical Co. Inc. Gd(III) nitrate hexahydrate ($\text{Gd}(\text{NO}_3)_3 \cdot 6\text{H}_2\text{O}$) were purchased from Sigma-Aldrich Co. Inc. *n*-hexanol ($\text{C}_6\text{H}_{13}\text{OH}$), 4-methyl-methylsalicylate ($\text{C}_{11}\text{H}_{14}\text{O}_3$) and 5-methyl-methylsalicylate ($\text{C}_{11}\text{H}_{14}\text{O}_3$) were purchased from Tokyo Chemical Industry Co., LTD. All other chemicals and solvents were reagent grade and were used without further purification.

5.2.2. Apparatus

Infrared spectra were recorded on a ThermoNicolet Avatar 320 FTIR spectrometer. XRD spectra were characterized by a RIGAKU X-ray diffractometer SmartLab. FAB-MS spectra were measured on a JEOL JMS-700TZ. Elemental analyses were performed by a MICRO CORDER JM10.

5.2.3. Synthesis

General synthetic procedures of Tb₉ Clusters with long alkyl chain: The general synthetic scheme is provided in Scheme 4.1 (4.2.3. Synthesis) and will be omitted in this section. Appropriate alkyl salicylate ligand (2.7 mmol) was dissolved in methanol, and triethylamine (0.44 mL, 4.40 mmol) was added to this solution while stirred at 40 °C. Tb(NO₃)₃·6H₂O (0.686 g, 1.52 mmol) dissolved in methanol was added dropwise to this solution and further stirred for 40 minutes. The resulting white precipitate (the target cluster) was vacuum filtered and dried in vacuum. The clusters were recrystallized by evaporation method from a concentrated methanol solution.

General synthetic procedures of Ln₉ clusters with methyl-methylsalicylate ligands: The synthetic procedures are the same as the procedures above but with a different scale. Appropriate methylsalicylate ligand (5.40 mmol) was dissolved in methanol, and triethylamine (1.22 ml, 8.80 mmol) was added to this solution while stirred at 40 °C. Ln(NO₃)₃·6H₂O (3.04 mmol) dissolved in methanol was added dropwise to this solution and further stirred for 40 minutes. The resulting white precipitate (the target cluster) was vacuum filtered and dried in vacuum.

Tb₉-Et ([Tb₉(μ-OH)₁₀(Et)₁₆]⁺NO₃⁻): Elemental analysis calculated for C₁₄₄H₁₅₄NO₆₁Tb₉: C, 40.17%, H, 3.61%, N, 0.33%. Found: C, 39.91%, H, 3.59%, N, 0.34%. FAB-MS: m/z = 4242.2 ([Tb₉(μ-OH)₁₀(Et)₁₆]⁺).

Tb₉-Pr ([Tb₉(μ-OH)₁₀(Pr)₁₆]⁺NO₃⁻): Elemental analysis calculated for C₁₆₀H₁₈₆NO₆₁Tb₉: C, 42.43%, H, 4.14%, N, 0.31%. Found: C, 42.12%, H, 4.10%, N, 0.34%. FAB-MS: m/z = 4466.6 ([Tb₉(μ-OH)₁₀(Pr)₁₆]⁺).

Tb₉-Bu ([Tb₉(μ-OH)₁₀(Bu)₁₆]⁺NO₃⁻): Elemental analysis calculated for C₁₇₆H₂₁₈NO₆₁Tb₉: C, 44.47%, H, 4.62%, N, 0.29%. Found: C, 44.16%, H, 4.57%, N, 0.51%. FAB-MS: m/z = 4691.3 ([Tb₉(μ-OH)₁₀(Bu)₁₆]⁺).

Tb₉-He ([Tb₉(μ-OH)₁₀(He)₁₆]⁺NO₃⁻): Elemental analysis calculated for C₂₀₈H₂₈₂NO₆₁Tb₉: C, 48.02%, H, 5.46%, N, 0.27%. Found: C, 47.8%, H, 5.28%, N, 0.31%. FAB-MS: m/z = 5140.0 ([Tb₉(μ-OH)₁₀(He)₁₆]⁺).

Tb₉-Me ([Tb₉(μ-OH)₁₀(Me)₁₆]⁺NO₃⁻): Selected IR (ATR, cm⁻¹): 3573 (w, O–H), 3235 (w, O–H), 2956 (m, C–H), 1319 (s, C–O). FAB-MS: m/z = 4018.8 ([Tb₉(μ-OH)₁₀(Me)₁₆]⁺).

Tb₉-4Me ([Tb₉(μ-OH)₁₀(4Me)₁₆]⁺NO₃⁻): Selected IR (ATR, cm⁻¹): 3573 (w, O–H), 3235 (w, O–H), 2956 (m, C–H), 1319 (s, C–O). FAB-MS: m/z = 4242.1 ([Tb₉(μ-OH)₁₀(4Me)₁₆]⁺). Elemental analysis calculated for C₁₄₈H₁₆₀NO₆₁Tb₉: C, 40.17%, H, 3.61%, N, 0.33%. Found: C, 39.45%, H, 3.66%, N, 0.31%.

Tb₉-5Me ([Tb₉(μ-OH)₁₀(5Me)₁₆]⁺NO₃⁻): Selected IR (ATR, cm⁻¹): 3573 (w, O–H), 3235 (w, O–H), 2956 (m, C–H), 1319 (s, C–O). FAB-MS: m/z = 4242.6 ([Tb₉(μ-OH)₁₀(5Me)₁₆]⁺). Elemental analysis calculated for C₁₄₈H₁₆₀NO₆₁Tb₉: C, 40.17%, H, 3.61%, N, 0.33%. Found: C, 39.40%, H, 3.69%, N, 0.35%.

Gd₉-Me ([Gd₉(μ-OH)₁₀(Me)₁₆]⁺NO₃⁻): Selected IR (ATR, cm⁻¹): 3573 (w, O–H), 3235 (w, O–H), 2956 (m, C–H), 1319 (s, C–O). FAB-MS: m/z = 4002.0 ([Gd₉(μ-OH)₁₀(Me)₁₆]⁺).

Gd₉-4Me ([Gd₉(μ-OH)₁₀(4Me)₁₆]⁺NO₃⁻): Selected IR (ATR, cm⁻¹): 3573 (w, O–H), 3235 (w, O–H), 2956 (m, C–H), 1319 (s, C–O). FAB-MS: m/z = 4228.2 ([Gd₉(μ-OH)₁₀(4Me)₁₆]⁺).

Gd₉-5Me ([Gd₉(μ-OH)₁₀(5Me)₁₆]⁺NO₃⁻): Selected IR (ATR, cm⁻¹): 3573 (w, O–H), 3235 (w, O–H), 2956 (m, C–H), 1319 (s, C–O). FAB-MS: m/z = 4229.6 ([Gd₉(μ-OH)₁₀(5Me)₁₆]⁺).

5.2.4. Spectroscopy

UV/Vis absorption spectra (1.0×10⁻⁴ M chloroform solution) and diffuse reflectance (powdered samples) were recorded using a JASCO V-670 spectrometer. Emission spectra were recorded using a Horiba FluoroLog-3ps. Emission lifetimes were measured using the third harmonics (355 nm) of a Q-switched Nd:YAG laser (Spectra Physics, INDI-50, FWHM = 5 ns, λ = 1064 nm) and a photomultiplier (Hamamatsu photonics, R928). The Nd:YAG laser response was monitored with a digital oscilloscope (Sony Tektronix, TDS3052, 500 MHz) synchronized to the single-pulse excitation. Emission lifetimes were determined from the slope of logarithmic plots of the decay profiles.

The absolute emission quantum yields were estimated using a JASCO FP-6600 spectrometer attached with a JASCO ILF-533 integrating sphere unit (φ = 100 mm). The wavelength dependences of the detector response and the beam intensity of Xe light source for each spectrum were calibrated using a standard light source. Quantum yield can be calculated

by $[\Phi = (E_c - E_a)/(L_a - L_c)]$ with E_c being the integrated emission spectrum of the sample, E_a the integrated “blank” emission spectrum, L_a the “blank” absorption, and L_c the sample absorption at the excitation wavelength.

5.2.5. Computational Details

DFT geometry optimizations and MO calculations of simplified clusters were performed with Gaussian 09 (Revision B.01) by employing the three-parameter hybrid functional of Becke based on the correlation functional of Lee, Yang, and Parr (B3LYP). The 6-31G(d) basis set was used for all atoms.

5.3. Results and Discussion

5.3.1. Structure

Identification of the Tb₉ clusters was performed by fast-atomic bombardment mass spectroscopy (FAB-MS). The *m/z* for Tb₉-Me, Tb₉-4Me, Tb₉-5Me, Tb₉-Et, Tb₉-Pr, Tb₉-Bu, and Tb₉-He were determined to be 4018.8, 4242.1, 4242.6, 4242.2, 4466.6, 4691.3, and 5140.0, respectively. The obtained *m/z* can be attributed to Tb₉ clusters without the NO₃⁻ counter-anion. The basic molecular structures of Ln₉ clusters are provided in Chapter 4 (see 4.3.1.). The single crystal X-ray analyses of the Tb₉-Me, Tb₉-Bu, and Tb₉-He, in particular, are already reported.^[5,10] Given the mass spectrometry results, the other clusters without single crystal X-ray analysis also have the same basic structure. In Chapter 4, it was mentioned that the Ln₉ clusters possess nine oxygen-bridged Ln(III) ions with an “hour-glass” structure surrounded by sixteen alkyl salicylate ligands (Figure 4.2). Focusing on the packing structure of the Tb₉ clusters (Tb₉-He as an example taken from ref [7]), a chain of intramolecular CH- π and π - π interactions between ligands can be seen (Figure 5.1). The π - π interactions are observed between two aromatic rings (center-to-center distance of ~ 4.25 Å) around the equator of the cluster. The CH- π interactions are also found between alkyl chain and aromatic ring (> 2.75 Å) near the top and bottom of the cluster. From the structure, the methyl substituent on the aromatic part of methylsalicylate ligands (4Me and 5Me) would face outside of the cluster with very small steric hindrance. This is likely the reason behind the retained structure of Tb₉-4Me and Tb₉-5Me as nonanuclear Ln(III) clusters.

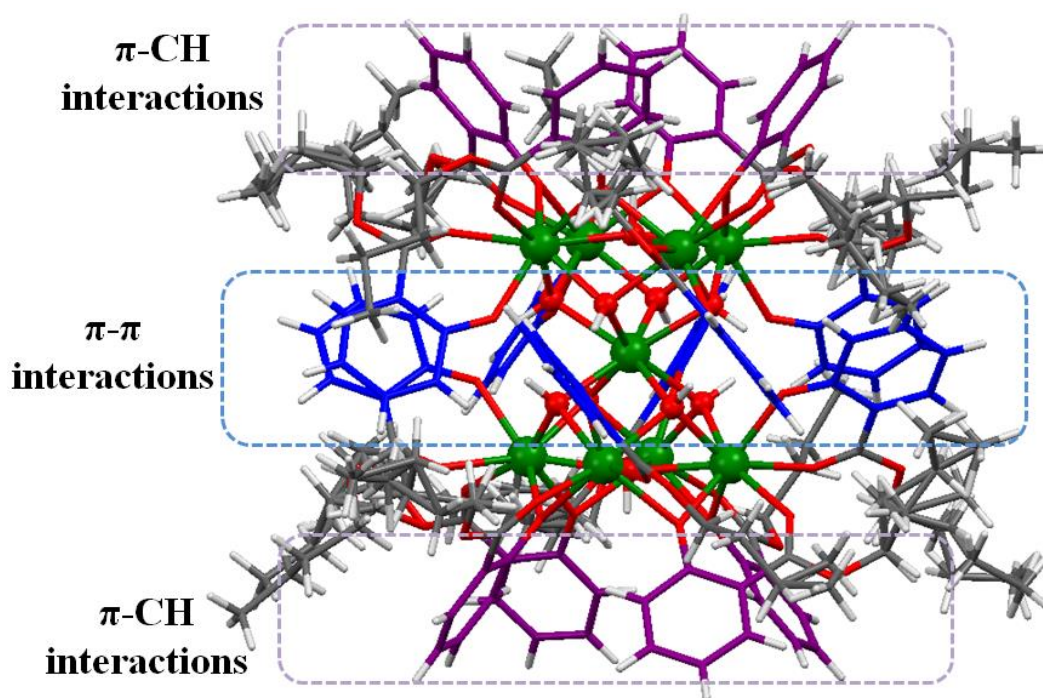


Figure 5.1 Intramolecular CH- π and π - π interactions between ligands in Tb₉-He. The crystal structure was redrawn from the CIF provided in ref [7].

5.3.2. Intramolecular Interactions and Photophysical Properties

In order to investigate the influence of intramolecular interaction on the photophysical properties of the organic ligands, absorption spectra of Et, Pr, Bu, He, and the Tb₉ clusters with these ligands in 1.0×10^{-5} M chloroform solution were measured. The spectra of the ligands and the clusters are shown in Figures 5.3a and 5.3b, respectively. All ligands showed a negligibly small difference in absorption spectra. Meanwhile, a difference in absorption coefficient ϵ is observed for the Tb₉ clusters with the different alkyl chain, although there is no proportional relationship between the length of alkyl chain and the absorption coefficient. Tb₉-Bu showed the largest absorption coefficient of $55508 \text{ M}^{-1} \text{ cm}^{-1}$ while Tb₉-Et showed the smallest absorption coefficient of $46432 \text{ M}^{-1} \text{ cm}^{-1}$. The change in the oscillator strength is suggested to be caused by changes in the intramolecular interactions. However, given the lack of proportional relationship between the length of alkyl chain and the absorption coefficient, the effect is complicated and is not easily predictable.

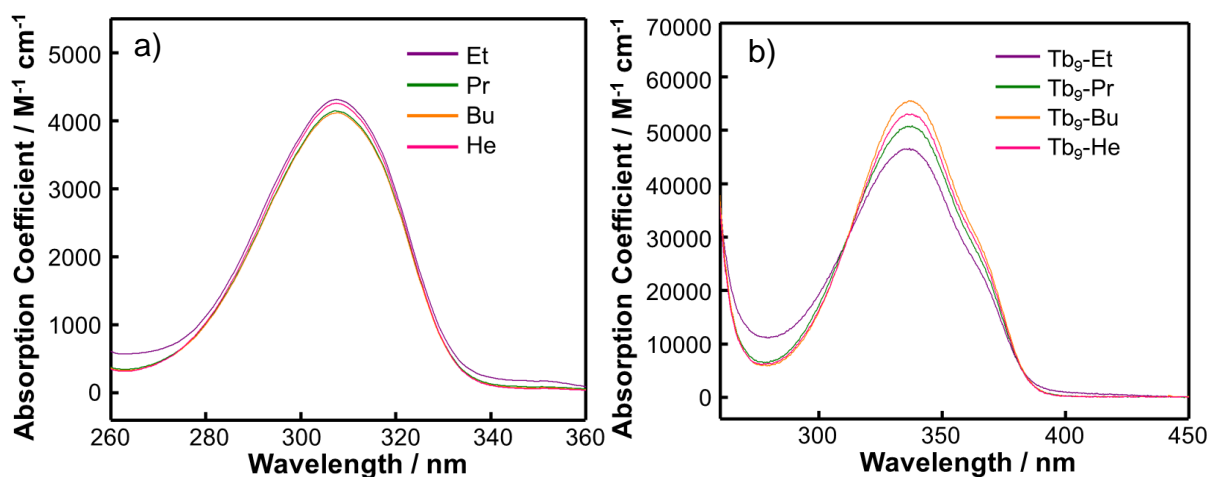


Figure 5.3 Absorption spectra of a) the ligands dissolved in 1.0×10^{-4} M chloroform solution, and b) the clusters in 1.0×10^{-5} M chloroform solution.

The influence of intramolecular interactions on the photophysical properties of the Tb(III) ions in the clusters was investigated by the emission spectra of the Tb₉ clusters. The emission of Ln(III) ions is known to be sensitive to the surrounding environment in terms of spectral shape (Stark-splitting) and radiative rate constant.^[6–8] The emission spectra of Tb₉-Et, Tb₉-Pr, Tb₉-Bu, and Tb₉-He in 1.0×10^{-4} M chloroform solution are shown in Figure 5.4a. The clusters were excited at 375 nm. The emission spectra were normalized at the $^5D_4 \rightarrow ^7F_5$ emission. The emission bands of the Tb₉ clusters were observed at approximately 487, 548, 582, 623, 651, and 681 nm, which are attributed to the typical 4f-4f transition of Tb(III) ions ($^5D_4 \rightarrow ^7F_J$, where $J = 6 - 1$). The spectral shape was identical for all the clusters, indicating that the clusters have identical coordination environment despite the difference in the intramolecular interactions. The identical spectral shapes also imply that the radiative rate constants are the same for these clusters.

The emission decay profiles and the emission lifetimes τ_{obs} of Tb₉-Et, Tb₉-Pr, Tb₉-Bu, and Tb₉-He in 1.0×10^{-4} M chloroform solution are shown in Figure 5.4b and Table 5.1, respectively. Tb₉-Et had the longest lifetime of 1.26 ms. Tb₉-Pr and Tb₉-Bu showed similar lifetime of 1.13 and 1.17 ms, respectively. Tb₉-He exhibited the shortest lifetime of 1.00 ms. Since the radiative rate constants of these clusters are likely the same, the difference in the lifetimes likely arose from the difference in the nonradiative rate constants. The quantum yields of the clusters by ligand excitation at 375 nm ($\Phi_{\pi\pi^*}$) are around 40% (Table 5.1). The emission lifetime and the

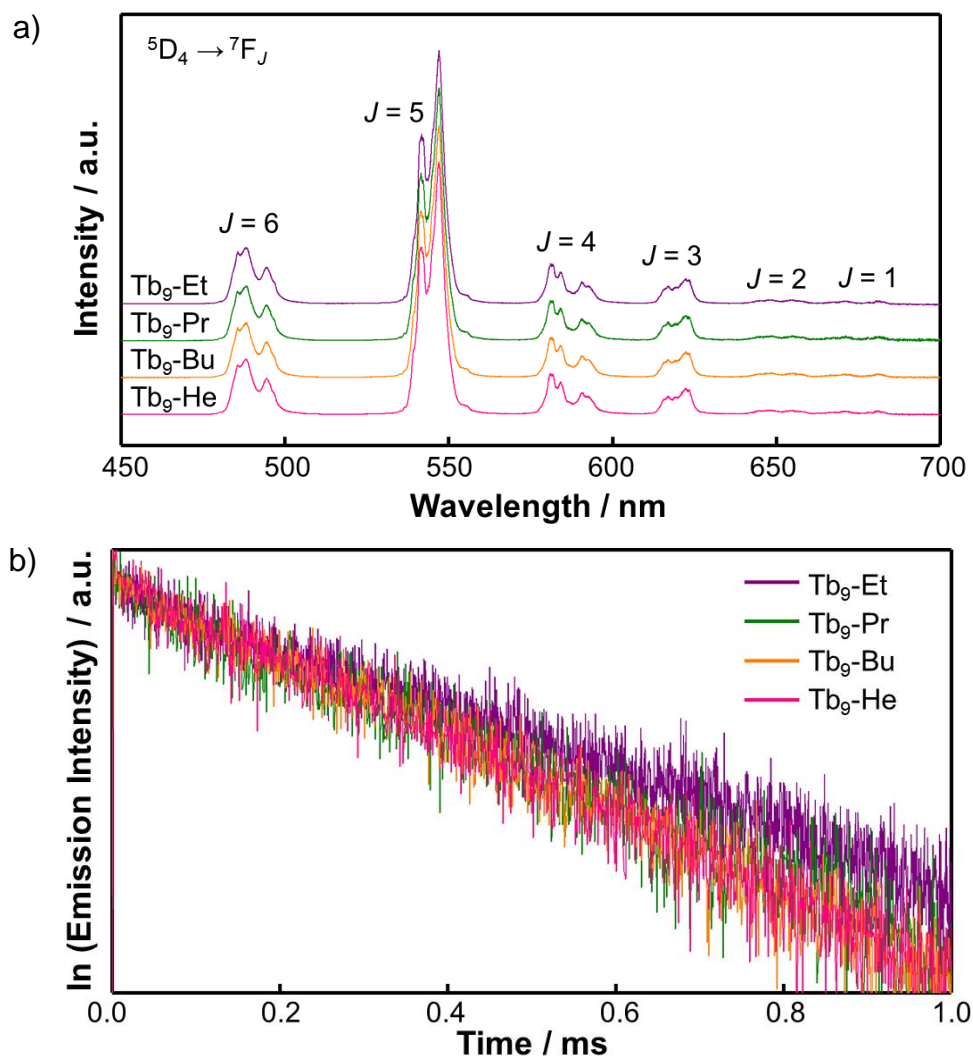


Figure 5.4 a) Emission spectra of Tb₉-Et, Tb₉-Pr, Tb₉-Bu, and Tb₉-He in 1.0×10⁻⁴ M chloroform solution ($\lambda_{\text{EX}} = 375$ nm). The emission spectra were normalized and given an offset. b) Emission decay profiles of the clusters in 1.0×10⁻⁴ M chloroform solution.

Table 5.1 Photophysical properties of Tb₉-Et, Tb₉-Pr, Tb₉-Bu, and Tb₉-He.

Cluster	$\epsilon / \text{M}^{-1} \text{cm}^{-1}$	$\Phi_{\pi\pi^*}$	$\Phi_{\text{ff}}^{\text{a}}$	$\eta_{\text{sens}}^{\text{a}}$	$\tau_{\text{obs}} / \text{ms}$	$\tau_{\text{rad}} / \text{ms}^{\text{a}}$	$k_{\text{r}} / \text{s}^{-1 \text{a}}$	$k_{\text{nr}} / \text{s}^{-1 \text{a}}$
Tb ₉ -Et	46432	0.42	0.69	0.61	1.26	1.82	548	246
Tb ₉ -Pr	50665	0.40	0.56	0.72	1.13	2.03	493	392
Tb ₉ -Bu	55508	0.39	0.42	0.93	1.17	2.79	358	497
Tb ₉ -He	52897	0.42	0.86	0.49	1.00	1.16	859	137

a) These values are unreliable due to the uncertainties in the measurement of Φ_{ff} .

quantum yield results altogether imply that the increase in the length of the alkyl chain leads to the increase in the nonradiative rate constant of Tb(III) ions, but also in the sensitization efficiency (η_{sens}) as well.

It should be noted here that the quantum yields of the clusters by Tb(III) ion excitation at 487 nm (Φ_{ff}) were also measured, which in principle allow the calculation of the radiative and nonradiative rate constants (kr and knr , respectively). The values are summarized in Table 5.1. However, the small absorption coefficient of the Tb(III) ions (approximately $10 \text{ M}^{-1} \text{ cm}^{-1}$ for a cluster containing nine Tb(III) ions) and thus the very low emission intensity observed in the absolute quantum yield measurement makes these values unreliable (see Figure A5.9 in 5.5.1.). Moreover, there exist two different coordination sites in the clusters as mentioned in 4.3.1. in these clusters. When ligands are excited first, the Tb(III) ions coordinated directly to the ligands will be excited first and then the center Tb(III) ion that is not coordinated to alkyl salicylate ligands. On the other hand, when Tb(III) ions are directly excited, all of the Tb(III) ions are excited at first. This fundamental difference in the initial excitation of Tb(III) ions renders the $\Phi_{\pi\pi^*}$ and Φ_{ff} to be a (directly) incompatible values. This will be explained in Chapter 6 in details.

Provided with the results above, it is suggested that the intramolecular interactions mainly affect the photophysical properties on the ligand side than the cluster core side. The effect of ionic radii of Ln(III) ions on the photophysical property of the clusters was also briefly mentioned in Chapter 4 where the Yb(III) emission was monitored when the cluster was mixed with Gd(III) and Lu(III) ions. It was found that ionic radii do not affect the radiative rate constant of Yb(III) ions, but only the nonradiative rate constant. Overall, the nonanuclear Ln(III) clusters contain a rigid core and maintain the fundamental photophysical properties of Ln(III) ions. Such property of the Tb₉ clusters sets the stage for the next step where the influence of using methyl salicylate derivatives on the energy transfer rate constant is investigated. It is preferred for such investigation that the fundamental properties of Tb(III) ions core is maintained as much as possible so that the effect arising from the ligands can be directly compared.

5.3.3. Mechanism of Back Energy Transfer

The effect of the methyl substituent on the photophysical properties of methyl salicylate ligands was investigated by quantum chemical calculations (DFT with B3LYP functional). The calculations were performed for Me, 4Me, and 5Me ligands bonded with Li(I) ion to

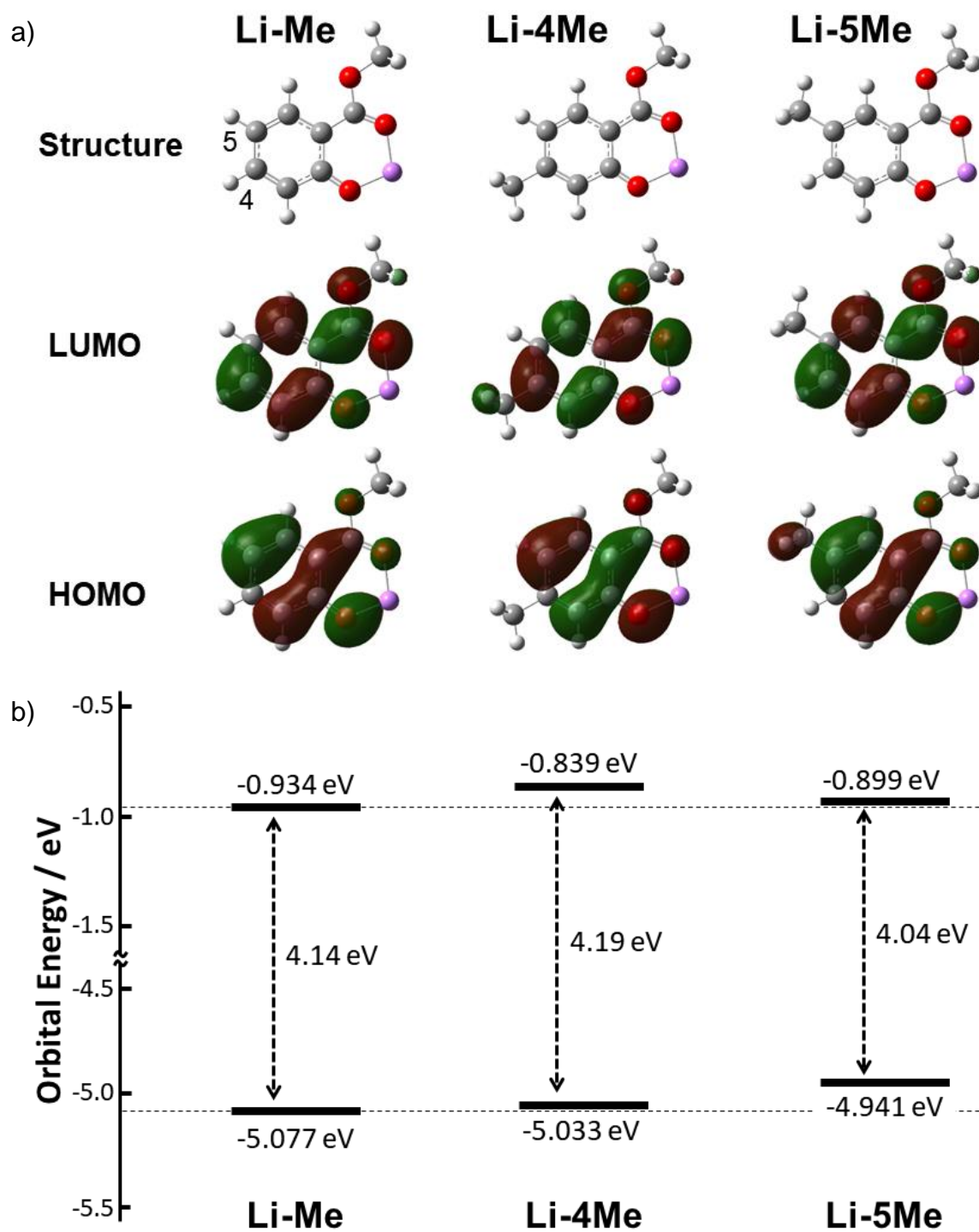


Figure 5.5 a) Molecular orbitals of Li-Me, Li-4Me, and Li-5Me calculated by DFT (B3LYP functional with 6-31G(d) basis set). b) Energy diagram of the orbital energy of HOMO and LUMO. Dotted horizontal lines are the HOMO and LUMO energy level of Li-Me.

simplify the discussion. These complexes will be referred to as Li-Me, Li-4Me, and Li-5Me. The highest-occupied and lowest-unoccupied molecular orbitals (HOMO and LUMO, respectively) of Li-Me, Li-4Me, and Li-5Me are depicted in Figure 5.5a, and their energies are summarized in Figure 5.5b. Focusing on Li-Me, both the HOMO and LUMO are distributed throughout the aromatic part of Me ligand including the carboxyl part of the ester group. The HOMO was poorly distributed on the 4-position carbon of the aromatic ring (opposite side of the ester group) while LUMO was poorly distributed on the 5-position. Li-4Me and Li-5Me did not show much difference in the distribution of the HOMO and LUMO compared to those of Li-Me, but the energies of these two orbitals were different. In Li-4Me, the LUMO energy was higher than that of Li-Me (0.095 eV) while the HOMO did not show much shift (0.044 eV). The opposite was observed for Li-5Me where the HOMO rose in energy (0.136 eV) while the LUMO only slightly shifted (0.035 eV). Li-4Me and Li-5Me showed the opposite effect regarding which orbital energy rises because of the distribution differences of HOMO and LUMO on 4- and 5-positions. The resulting HOMO-LUMO energy gaps of Li-Me, Li-4Me, and Li-5Me were 4.14, 4.19, and 4.04 eV, respectively.

The rise in the energy is caused by the methyl substituent, which donates the electron into HOMO or LUMO leading the rise in the electron density and thus the energy as well. Methyl substituent is a weak electron donor with only the inductive effect. This shows that using methyl substituent is an effective method for slightly modifying the HOMO-LUMO gap without significantly altering the electronic structure. The clusters are composed of 16 methylsalicylate ligands, and the result above is not necessarily accurate in predicting the effect of the methyl substituent because of the intramolecular interaction between the ligands as explained in 5.3.2. Nonetheless, the goal here is to slightly modify the energy gap between the T_1 and S_0 states so that the FET process is changed. The calculation results justify the use of these ligands to investigate the effect of electronic energy on the energy transfer processes.

The diffuse reflectance spectra of Tb_9 -Me, Tb_9 -4Me, and Tb_9 -5Me were carried out to compare the absorption edge of the ligands (Figure 5.6a). The clusters were measured as a powdered state because of the poor solubility. The absorption edge slightly shifted toward the longer wavelength in the order of Tb_9 -Me, Tb_9 -4Me, and Tb_9 -5Me. TD-DFT calculation of Li-Me, Li-4Me, and Li-5Me showed that the $S_0 - S_1$ transition of these molecules are of HOMO-to-LUMO origin ($\pi-\pi^*$ transition). The absorption of the clusters can be assigned to the $\pi-\pi^*$ transition of the methylsalicylate ligands.

Figure 5.6b shows the emission spectra of Gd_9 -Me, Gd_9 -4Me, and Gd_9 -5Me excited at 380 nm at 100 K. Gd(III) ions have excited states above 32000 cm^{-1} , which is well above of the

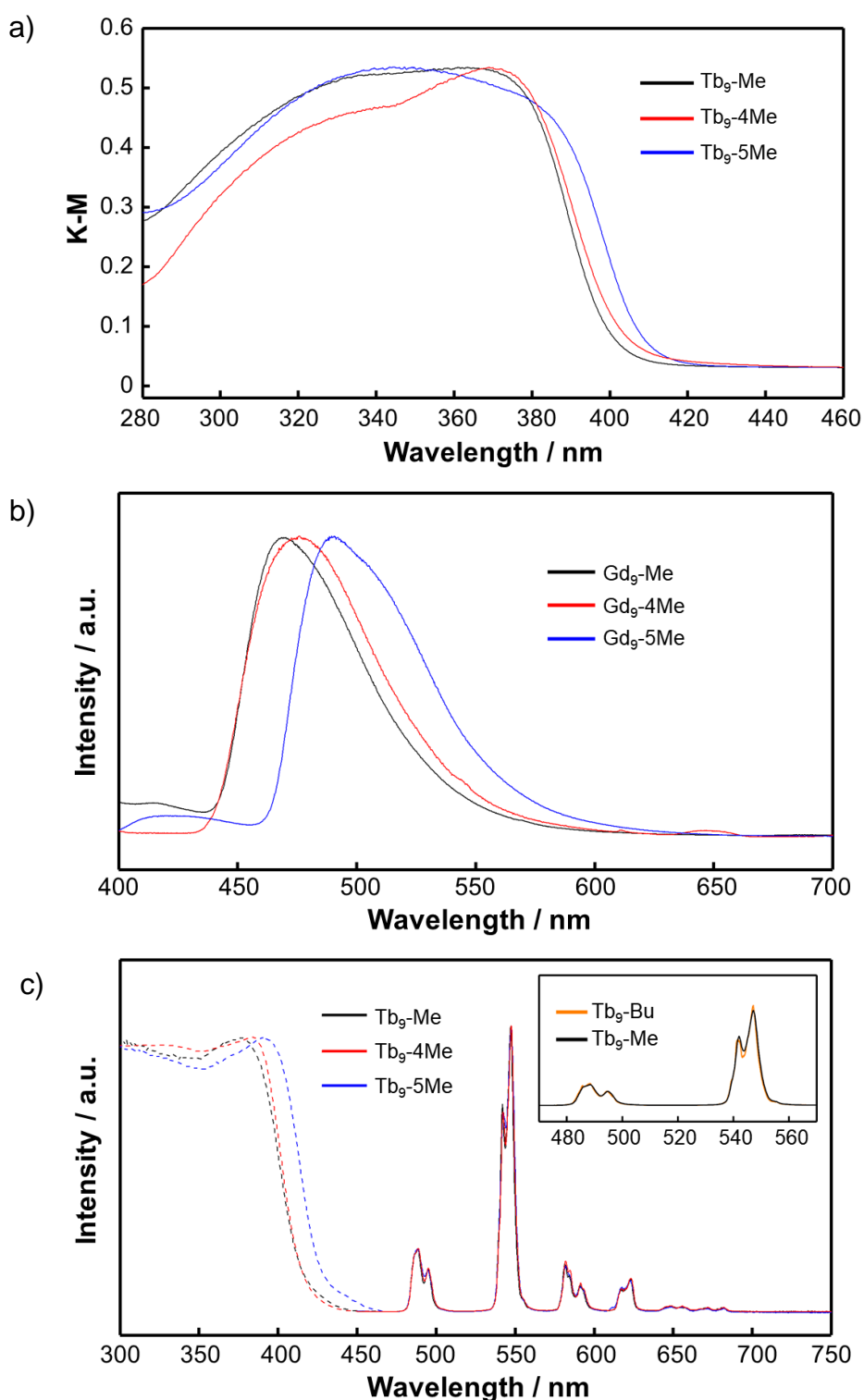


Figure 5.6 a) Diffuse reflectance spectra of Tb_9 -Me, Tb_9 -4Me, and Tb_9 -5Me. b) Emission spectra of Gd_9 -Me, Gd_9 -4Me, and Gd_9 -5Me at 100 K. c) Emission spectra of Tb_9 -Me, Tb_9 -4Me, and Tb_9 -5Me at room temperature. The inset shows the comparison of spectral shape between Tb_9 -Bu and Tb_9 -Me. The measurement was performed as powder, and the excitation wavelength was 380 nm for the emission spectra.

ligands and energy transfer do not proceed from the ligands to Gd(III) ions. As a result, emission from the ligands is observed, and at lower temperature phosphorescence from the triplet excited state. This is a common method to identify the T_1 state energy of Ln(III) complexes.^[3,4] These result clearly indicate a gradual shift to longer wavelength in the order of Gd₉-Me, Gd₉-4Me, and Gd₉-5Me, similar to the diffuse reflectance spectra results. The energy of the T_1 state (T_1-S_0 gap) of Gd₉-Me, Gd₉-4Me, and Gd₉-5Me were estimated to be 21277, 21053, and 20408 cm^{-1} , respectively. The combination of diffuse reflectance spectra of the Tb₉ clusters and emission spectra of the Gd₉ clusters confirms that the slight modification of the (singlet and triplet) excited states of the ligands using methyl substituents was successful. The steady-state emission spectra of Tb₉-Me, Tb₉-4Me, and Tb₉-5Me in solid-state excited at 380 nm are shown in Figure 5.6c. The clusters were poorly soluble in solvents and had to be performed in the solid state. The spectral shape of Tb(III) emission of these clusters was identical with those of Tb₉-Et, Tb₉-Pr, Tb₉-Bu, and Tb₉-He (Figure 5.6c inset). Therefore, coordination geometry of Tb(III) ions is once again similar among all of the clusters mentioned in this chapter. The excitation spectra of the clusters monitored at 548 nm also showed a shift to the longer wavelength region in the order of Tb₉-Me, Tb₉-4Me, and Tb₉-5Me, which are consistent with the diffuse reflection spectra (Figure 5.6a) and triplet excited state phosphorescence spectra (Figure 5.6b). The result further supports that Ln(III) ions core of the cluster is rigid and retains its core structure even with changes in the intramolecular interactions. From the emission spectra of Tb₉-Me, Tb₉-4Me, and Tb₉-5Me as well as their Gd(III) ion analogs, the energy gaps between the T_1 state and the 5D_4 state of the Tb(III) ions in the clusters $\Delta E (= E_{T_1} - E_{^5D_4})$ are summarized in Table 5.2. Tb₉-Me showed the largest ΔE of 740 cm^{-1} while Tb₉-5Me showed the smallest ΔE of -130 cm^{-1} . Generally, the sensitization efficiency is known to be proportional to ΔE especially when the value is less than 1850 cm^{-1} since BET is known to occur under this energy gap.^[4,11] The clusters therefore likely show the effect of BET.

Table 5.2 Photophysical properties of Tb₉-Me, Tb₉-4Me, and Tb₉-5Me.

Cluster	$\Delta E / \text{cm}^{-1}$	$\tau_{\text{obs}} / \mu\text{s}$	Ea / cm^{-1}	D / s^{-1}	$\Phi_{\pi\pi^*}$
Tb ₉ -Me	+740	284	1822	5.76×10^5	0.07
Tb ₉ -4Me	+520	815	2082	1.17×10^6	0.31
Tb ₉ -5Me	-130	190	1496	1.17×10^6	0.02

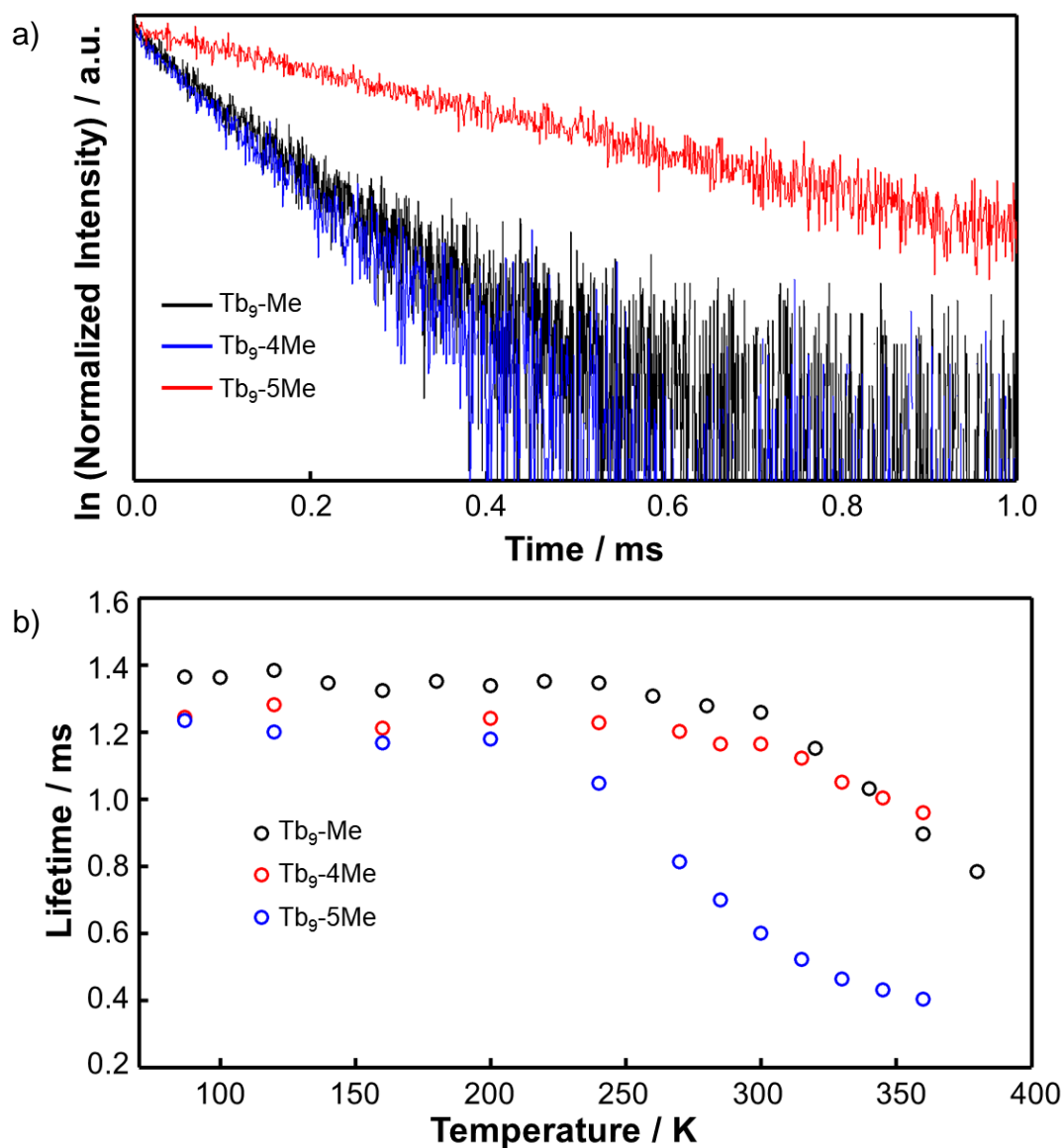


Figure 5.7 a) Emission decay profiles of Tb₉-Me, Tb₉-4Me, and Tb₉-5Me at room temperature. b) Temperature dependence of emission lifetimes of the clusters. All measurements were performed as powder and excited at 355 nm.

The emission decay profiles (excited at 355 nm) and the absolute quantum yields (excited at 380 nm) of the clusters were measured. The values are summarized in Table 5.2. The profiles and its value τ_{obs} of the clusters revealed single-exponential decays as shown in Figure 5.7a. The largest τ_{obs} was observed for Tb₉-4Me (815 μs), while the smallest was observed for Tb₉-5Me (190 μs). Tb₉-Me showed a value in the middle (264 μs). The emission quantum yields

showed a similar trend where the values were in the order from large to small Tb₉-4Me ($\Phi_{\pi\pi^*} = 31\%$), Tb₉-Me ($\Phi_{\pi\pi^*} = 6.7\%$), and Tb₉-5Me ($\Phi_{\pi\pi^*} = 2.4\%$). These results are inconsistent with the trend observed for the energy gap ΔE .

In order to explain this inconsistency, the focus is now primarily on the BET rate constant k_{BET} , which would directly provide information on the energy transfer processes. BET can be considered as a temperature dependent process because the process needs to be assisted by thermal energy to compensate for the energy difference between ⁵D₄ state and T₁ state. Ignoring temperature dependence of nonradiative rate constant of Tb(III) ions, at sufficiently low temperature, BET does not proceed. The BET rate constant k_{BET} can be expressed using emission lifetimes by:

$$k_{\text{BET}} = (kr + knr + k_{\text{BET}}) - (kr + knr) = \frac{1}{\tau(T)} - \frac{1}{\tau(87\text{K})} \quad , \quad [5.1]$$

where kr and knr are radiative and nonradiative rate constants, respectively. $\tau(T)$ is the emission lifetime at a given temperature T , and $\tau(87\text{K})$ is the emission lifetime at 87 K. Since this process is temperature dependent, Arrhenius plot can be applied^[12,13] (see 5.5.2. and 5.5.3. for details):

$$k_{\text{BET}} = D \exp\left(-\frac{Ea}{k_{\text{B}}T}\right) \quad , \quad [5.2]$$

where D is the frequency factor. By combining Equations [5.1] and [5.4], the following equation is derived:

$$k_{\text{BET}} = \frac{1}{\tau(T)} - \frac{1}{\tau(87\text{K})} = D \exp\left(-\frac{Ea}{k_{\text{B}}T}\right) \quad . \quad [5.3]$$

The equation implies that by plotting $\frac{1}{\tau(T)} - \frac{1}{\tau(87\text{K})}$ against temperature and fitting the right side of the equation leads to the derivation of the frequency factor D and the activation energy of BET Ea .

The temperature dependence (87 – 380 K) of emission lifetimes for Tb₉-Me, Tb₉-4Me, and Tb₉-5Me are provided in Figure 5.7b. The derived frequency factor D and the activation energy Ea are summarized in Table 5.2. The activation energy Ea for Tb₉-Me, Tb₉-4Me, and Tb₉-5Me were 1822 cm⁻¹, 2082 cm⁻¹, and 1496 cm⁻¹, respectively. The values were clearly larger than the energy gap ΔE by more than 1000 cm⁻¹. Furthermore, the frequency factor D for Tb₉-Me, Tb₉-4Me, and Tb₉-5Me were 5.76×10^5 , 1.17×10^6 , and 1.17×10^6 s⁻¹, respectively. These value of the frequency factors is proportional to the fundamental electronic correlation between the organic ligands and the Ln(III) ion in a Ln(III) complex ($|\langle S_0, {}^5D_4 | H_{\text{ET}} | T_1, {}^7F_6 \rangle|$), and has been the central discussion of the ET between ligand and Ln(III) ions. The values indicate that fundamentally, the T₁ state of 4Me and 5Me ligand interacts strong electronically with the ⁵D₄

level of Tb(III) ions compared to that of Me ligands. The results also imply that the FET and BET processes can be expressed by potential energy surface as shown in Figure 5.8. This argument on the existence of the activation energy in the ET process between ligands and Tb(III) ions is consistent with the previous report.^[14] On the other hand, the nature of the other constants has been overlooked. In the particular case of these clusters, the energy gap is inconsistent with the lifetime results, but now can be explained by the activation energy and frequency factor. All of these three parameters, i.e., the energy gap ΔE , the activation energy E_a , and the frequency factor were shown to be important in discussing BET in Ln(III) complexes.

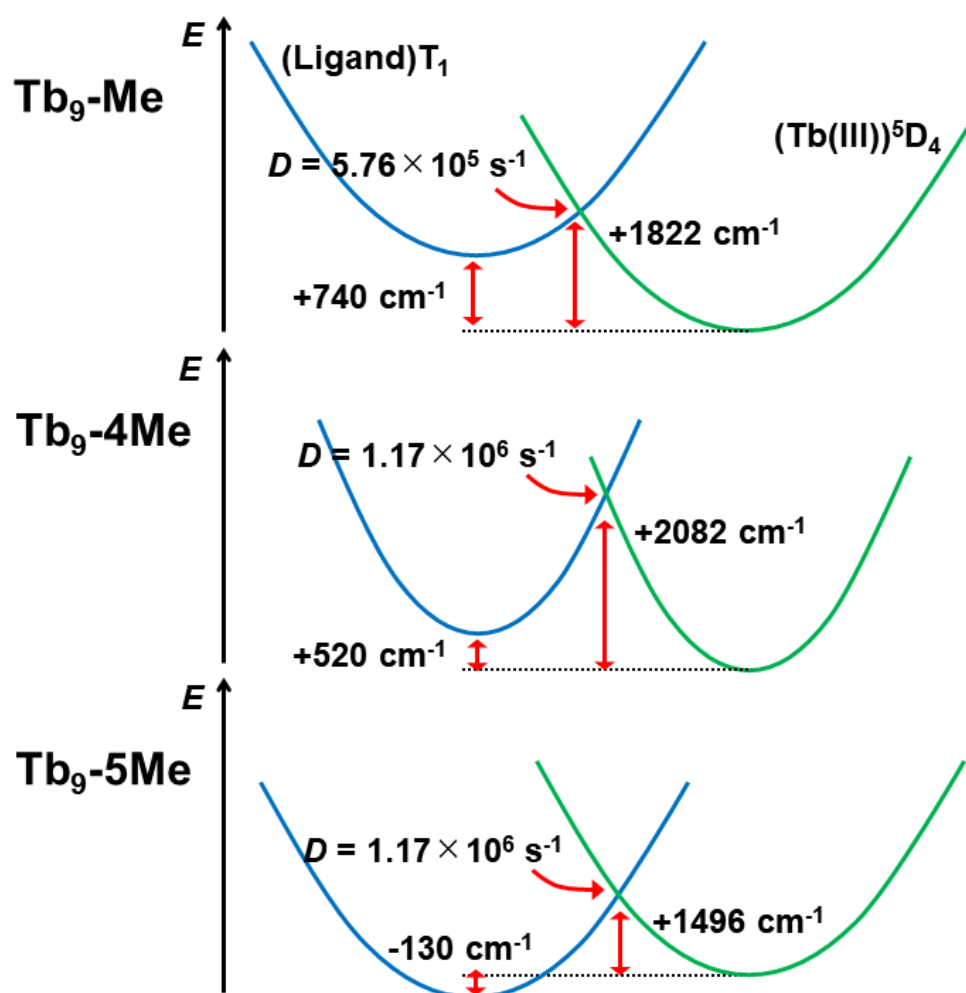
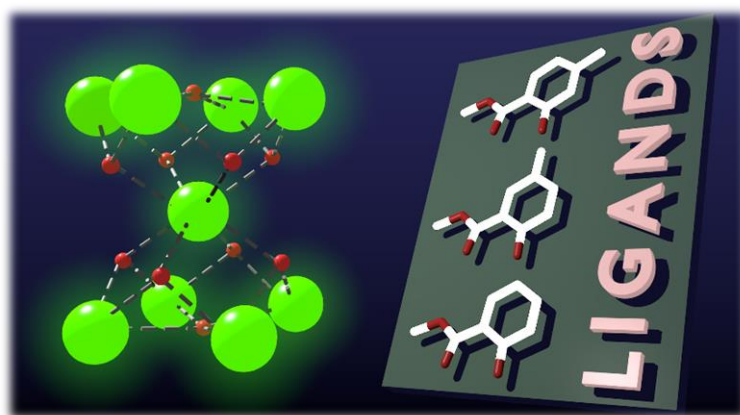


Figure 5.8 Schematic diagram of the potential energy curve of T_1 and 5D_4 states of the clusters.

5.4. Conclusion

A series of nonanuclear Tb(III) clusters with ester salicylate derivatives, Tb₉-Me, Tb₉-4Me, Tb₉-5Me, Tb₉-Et, Tb₉-Pr, Tb₉-Bu, and Tb₉-He has been synthesized and characterized by their photophysical properties. The difference in the photophysical properties arising from the ligands depended on the length of the alkyl chain of the ligands. Meanwhile, the emission spectra of Tb(III) emission showed that the photophysical properties arising from the core structure of the cluster remained unaffected. The length of the alkyl chain of the ligands affects the CH- π and π - π interactions, which systematically changes the packing structure of the clusters, but does not affect the core structure of the cluster. It is suggested that the core structure of the cluster is rigid.

The photophysical properties of Tb₉-Me, Tb₉-4Me, and Tb₉-5Me, where the ligands have the same alkyl chain length but the different position of the methyl substituent on the aromatic ring, were drastically different. Tb₉-4Me showed more than four times the increase in the lifetime compared to Tb₉-Me, and three times the increase compared to Tb₉-5Me. DFT calculations revealed that the position of the methyl group is directly linked to the HOMO and LUMO energy of the ligands. The introduction of the methyl group and its position on the aromatic ring also slightly altered the S₀-S₁ and S₀-T₁ energy gap. This affected the photophysical properties of the clusters significantly due to BET that is sensitive to the T₁-⁵D₄ energy gap ΔE . Meanwhile, the energy gaps and the emission lifetimes were not consistent: the energy gap was the largest for Tb₉-Me, but Tb₉-4Me showed the longest lifetime. The plot of emission lifetime temperature dependence was fitted with Arrhenius equation and lead to the conclusion that the activation energy E_a and the frequency factor D of the energy transfer was the main contributor to the lifetimes, not the energy gap ΔE , for these clusters. The results provide new insight into the BET and FET mechanism of Ln(III) complexes.



5.5. Appendix

5.5.1. Intrinsic Quantum Yield Measurements

Absolute quantum yield measurement uses integration sphere. The measurement monitors the emission intensity of blank sample and the cluster sample. This requires that the cluster sample is emitting enough for adequate quantitative detection. As shown in Figure A5.9, due to the low intensity of the emission observed for direct excitation of Tb(III) ions, the value obtained here, is still unreliable.

The intrinsic emission quantum yield Φ_{Ln} can also be calculated by Equation [1.4]:

$$\Phi_{Ln} = \frac{kr}{kr + knr} = \frac{\tau_{obs}}{\tau_{rad}}, \quad [1.4]$$

where τ_{rad} ($= 1/kr$) is the emission lifetime of Ln(III) in the ideal state where there are no quenching. Radiative rate constant kr is estimated as emission lifetime at 100 K under the assumption that lifetime at low temperature is purely radiative (non-radiative rate constant knr is negligible).^[15,16] This assumption is not accurate and also does not yield a very reliable values. The results are summarized in Table A5.1.

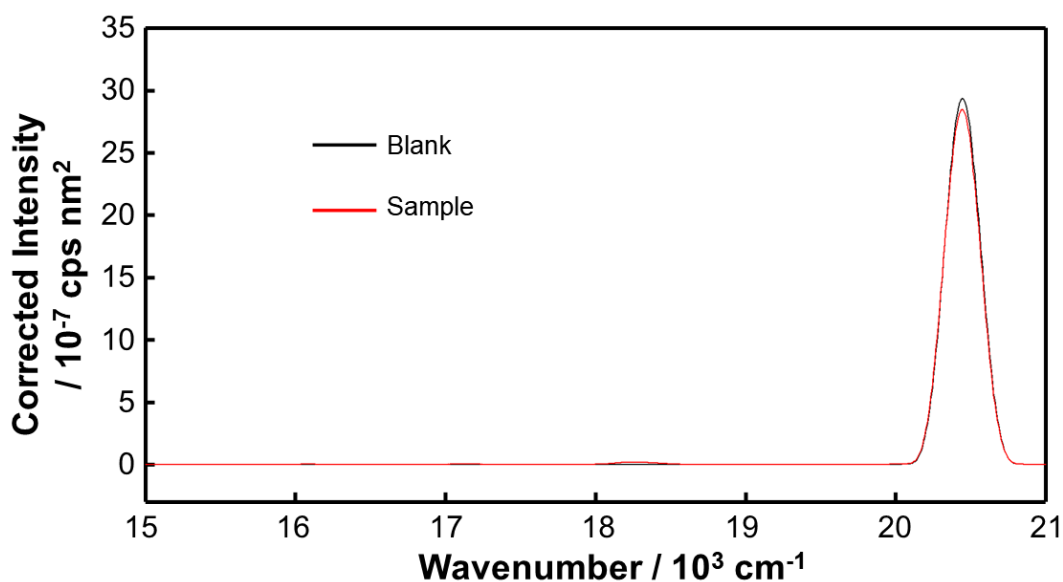


Figure A5.9 Emission spectra measured in integration sphere with corrections.

Table A5.1 Photophysical properties of Tb₉-Me, Tb₉-4Me, and Tb₉-5Me.

Cluster	$\Phi_{\pi\pi^*}$	Φ_{Ln}	η_{sens}	τ_{obs} / ms	τ_{rad} / ms	k_r / s ⁻¹	k_{nr} / s ⁻¹
Tb ₉ -Me	31%	57%	54%	0.815	1.44	696	531
Tb ₉ -4Me	2.4%	16%	15%	0.190	1.22	823	4430
Tb ₉ -5Me	6.7%	17%	39%	0.264	1.53	654	3127

5.5.2. BET Rate Constant

BET can be considered as a transition from ⁵D₄ state to T₁ state coupled by Coulomb interaction between electrons. Taking the Coulomb potential as a perturbation in a system (the cluster), the transition rate constant can be expressed by Fermi's Golden Rule. Applying the Marcus-type equation to ET rate constant under the assumption that the BET is a nonadiabatic process, k_{BET} can be expressed in the following equation:^[17–19]

$$k_{BET} = \frac{2\pi}{\hbar} |\langle S_0, {}^5D_4 | \mathbf{H}_{ET} | T_1, {}^7F_6 \rangle|^2 \frac{1}{\sqrt{4\pi\lambda k_B T}} \exp\left(-\frac{Ea}{k_B T}\right), \quad [5.4]$$

where \hbar , $\langle S_0, {}^5D_4 | \mathbf{H}_{ET} | T_1, {}^7F_6 \rangle$, λ , k_B , T , Ea , are Planck constant, matrix element of the ET from S₀,⁵D₄ to T₁,⁷F₆ states (BET), reorganization energy, Boltzmann constant, temperature, and activation energy of BET. Reorganization energy λ is given by:

$$\lambda = 2Ea \left(1 - \frac{\Delta E}{2Ea} + \sqrt{1 - \frac{\Delta E}{Ea}} \right). \quad [5.5]$$

By combining Equations [5.1] and [5.2], the following is derived:

$$k_{BET} = \frac{1}{\tau(T)} - \frac{1}{\tau(87K)} = \frac{2\pi}{\hbar} |\langle S_0, {}^5D_4 | \mathbf{H}_{ET} | T_1, {}^7F_6 \rangle|^2 \frac{1}{\sqrt{4\pi\lambda k_B T}} \exp\left(-\frac{Ea}{k_B T}\right). \quad [5.6]$$

Equation [5.4] is often simplified to Equation [5.2]:

$$k_{BET} = D \exp\left(-\frac{Ea}{k_B T}\right), \quad [5.2]$$

where D becomes the frequency factor that includes matrix element of the BET. $\frac{1}{\sqrt{4\pi\lambda k_B T}}$ is also temperature dependent in Equation [5.6] but will be neglected here. For example, $\frac{1}{\sqrt{4\pi\lambda k_B T}}$ changes by a factor of 0.48 when the temperature changes from 87 K to 380 K. Such temperature changes can be ignored as long as the clusters are considered at a same temperature.

The Arrhenius plot using Equation [5.2] is given in Figure A5.10.

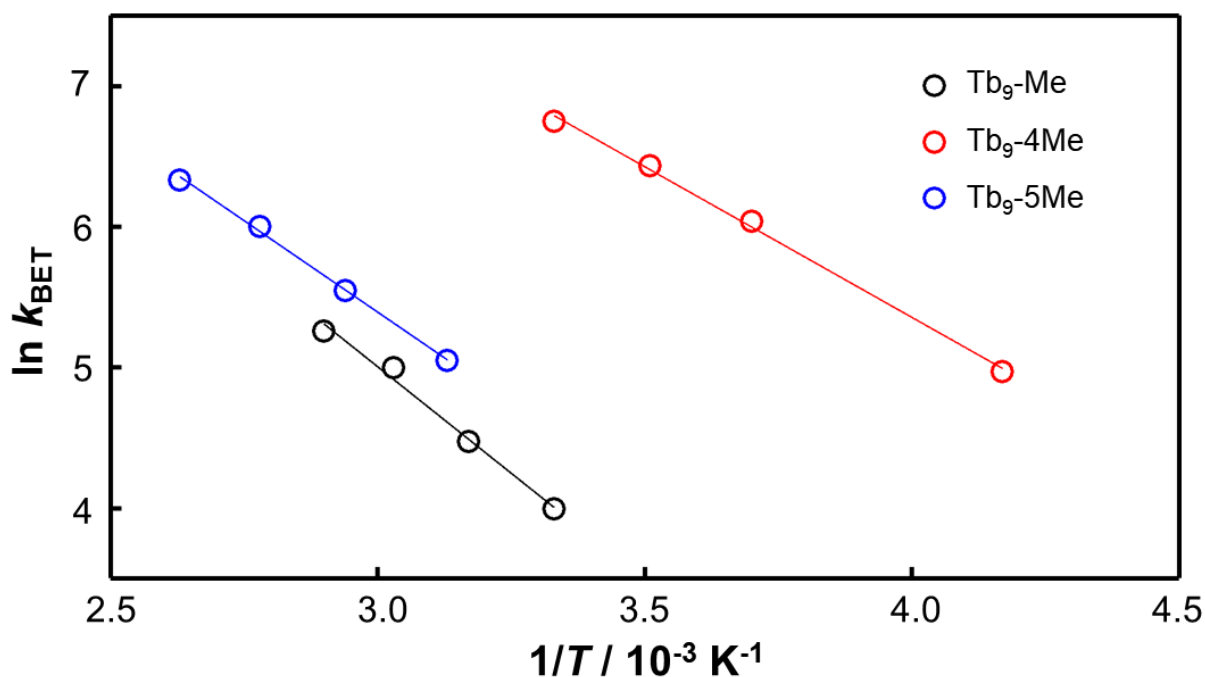


Figure A5.10 Arrhenius plots of the emission lifetimes temperature dependence of the clusters.

5.5.3. BET and T₁ Decay

As explained in 2.2.3., in the presence of BET, the emission lifetime is not precisely expressed simply by Equation [5.1]. Looking at Equation [2.57] and under the circumstance that in most cases, S₁ and T₁ states have very short lifetimes ($a_{11} \gg a_{22} \gg a_{33}$), the total relaxation rate constant for a Tb(III) ion $k_{Tb,actual}$ is expressed as:

$$k_{Tb,actual} = \frac{k_{T_1} + k_{T_b} + k_{FET} + k_{BET} - \sqrt{(k_{T_1} - k_{T_b})^2 + (k_{FET} + k_{BET})^2 + 2(k_{T_1} - k_{T_b})(k_{FET} + k_{BET})}}{2}, \quad [5.7]$$

where k_{T_1} and k_{T_b} are intrinsic relaxation rate of T₁ state and Ln excited state, respectively. Under the assumption that the T₁ state and the ⁵D₄ state of the clusters can be expressed with the potential energy diagrams shown in Figure 5.8, $k_{FET} = k_{BET} \frac{1}{\exp(\frac{\Delta E}{kT})}$ and the frequency factor can be assumed same for FET and BET near the intersection, and thus Equation [5.7] converts to:

$$k_{Tb,actual} = \frac{k_{T_1} + k_{T_b} + k_{BET} \left(\frac{1}{\exp(\frac{\Delta E}{kT})} + 1 \right) - \sqrt{(k_{T_1} - k_{T_b})^2 + k_{BET}^2 \left(\frac{1}{\exp(\frac{\Delta E}{kT})} + 1 \right)^2 + 2k_{BET}(k_{T_1} - k_{T_b}) \left(\frac{1}{\exp(\frac{\Delta E}{kT})} - 1 \right)}}{2}. \quad [5.8]$$

Equation [5.8] implies the decay rate of T_1 state also affect the emission lifetimes of 5D_4 state (not just BET rate constant).

Meanwhile, this study concerns comparison between three Tb_9 clusters with different ligands. As long as the k_{T_1} is identical between the ligands, the comparison can still be restricted to the BET rate and the energy gap between T_1 and 5D_4 states. TD-DFT calculation of the S_1 state of Li-Me, Li-4Me, and Li-5Me resulted in an $S_1 \rightarrow S_0$ oscillator strengths of $f = 0.1377$, 0.1368 , and 0.1363 , respectively (corresponding to a pure HOMO-LUMO transition). Along with the close structure of the ligands, we can assume that the k_{T_1} are nearly identical between these three clusters. Therefore, the comparison can still be restricted to the BET rate constants k_{BET} of the clusters.

5.6. References

- [1] L. Smentek and A. Kędziorowski, *J. Lumin.* **2010**, *130*, 1154–1159.
- [2] Y. Hasegawa, Y. Wada, S. Yanagida, *J. Photochem. Photobiol. C* **2004**, *5*, 183–202.
- [3] F. Gutierrez, C. Tedeschi, L. Maron, J.-P. Daudey, R. Poteau, J. Azema, P. Tisnès, C. Picard, *Dalton Trans.* **2004**, 1334–1347.
- [4] M. Latva, H. Takalo, V.-M. Mikkala, C. Matachescu, J. C. Rodríguez-Ubis, J. Kankare, *J. Lumin.* **1997**, *75*, 149–169.
- [5] T. Nakanishi, Y. Suzuki, Y. Doi, T. Seki, H. Koizumi, K. Fushimi, K. Fujita, Y. Hinatsu, H. Ito, K. Tanaka, Y. Hasegawa, *Inorg. Chem.* **2014**, *53*, 7635–7641.
- [6] N. B. D. Lima, S. M. C. Gonçalves, S. a Júnior, A. M. Simas, *Sci. Rep.* **2013**, *3*, 2395.
- [7] K. Miyata, T. Nakagawa, R. Kawakami, Y. Kita, K. Sugimoto, T. Nakashima, T. Harada, T. Kawai, Y. Hasegawa, *Chem. Eur. J.* **2011**, *17*, 521–528.
- [8] K. Yanagisawa, T. Nakanishi, Y. Kitagawa, T. Seki, T. Akama, M. Kobayashi, T. Taketsugu, H. Ito, K. Fushimi, Y. Hasegawa, *Eur. J. Inorg. Chem.* **2015**, 4769–4774.
- [9] Y. Hasegawa, T. Ohkubo, T. Nakanishi, A. Kobayashi, M. Kato, T. Seki, H. Ito, K. Fushimi, *Eur. J. Inorg. Chem.* **2013**, 5911–5918.
- [10] K. Manseki, Y. Hasegawa, Y. Wada, H. Ichida, Y. Kanematsu, T. Kushida, *J. Lumin.* **2007**, *122–123*, 262–264.
- [11] S. Katagiri, Y. Tsukahara, Y. Hasegawa, Y. Wada, *Bull. Chem. Soc. Jpn.* **2007**, *80*, 1492–1503.
- [12] K. Yanagisawa, Y. Kitagawa, T. Nakanishi, T. Akama, M. Kobayashi, T. Seki, K.

- Fushimi, H. Ito, T. Taketsugu, Y. Hasegawa, *Eur. J. Inorg. Chem.* **2017**, 3843–3848.
- [13] K. Miyata, Y. Konno, T. Nakanishi, A. Kobayashi, M. Kato, K. Fushimi, Y. Hasegawa, *Angew. Chem. Int. Ed.* **2013**, 52, 6413–6416.
- [14] M. Hatanaka, K. Morokuma, *J. Chem. Theory Comput.* **2014**, 10, 4184–4188.
- [15] I. Nasso, N. Geum, G. Bechara, B. Mestre-Voegtlé, C. Galaup, C. Picard, *J. Photochem. Photobiol. A* **2014**, 274, 124–132.
- [16] A. P. Bassett, S. W. Magennis, P. B. Glover, D. J. Lewis, N. Spencer, S. Parsons, R. M. Williams, L. De Cola, Z. Pikramenou, *J. Am. Chem. Soc.* **2004**, 126, 9413–9424.
- [17] R. A. Marcus and N. Sutin, *Biochim. Biophys. Acta* **1985**, 811, 265–322.
- [18] R. A. Marcus, *J. Chem. Phys.* **1984**, 81, 4494–4500.
- [19] L. Sudha Devi, M. K. Al-Suti, C. Dosche, M. S. Khan, R. H. Friend, A. Köhler, *Phys. Rev. B* **2008**, 78, 1–8.

Chapter 6

***SUPPRESSION OF BACK ENERGY TRANSFER BY
ENERGY TRANSFER BETWEEN TERBIUM IONS***

6.1. Introduction

So far, various factors that affect the ET processes in Ln(III) complexes have been discussed. In Chapter 3, the effect of YbYbET on the photophysical properties of Yb(III) coordination polymers was elucidated. Chapter 4 described the effect of SOC on the sensitization efficiency by using nonanuclear Yb(III)/Gd(III) and Yb(III)/Lu(III) clusters. The effect of BET and its mechanism in Chapter 5 were explored using nonanuclear Tb(III) clusters. These chapters provided new insights into LnLnET of polynuclear Ln(III) complexes as well as some fundamental properties of nonanuclear Ln(III) clusters and factors that affect sensitization efficiency. Now it is set to combine these insights and focus on LnLnET in nonanuclear Ln(III) clusters and its effect on the photophysical properties.

The hypothesis here is that the ET between Tb(III) ions (TbTbET) can suppress BET in Tb(III) complexes. Considering that both BET and TbTbET occur from the same 4f-excited state of Tb(III) ion (5D_4), these two processes are competitive. When TbTbET is adequately larger than BET, the overall contribution of BET could be suppressed. In this regard, nonanuclear Tb(III) clusters are a good candidate since the Ln-Ln distance is quite short at around 3.65 Å. The structural feature of nonanuclear Tb(III) cluster is also important. The center Tb(III) ion is coordinated only with OH⁻ ions (see section 4.3.1.) and thus the center Tb(III) ion is expected not to involve (or involve negligibly little) in FET and BET compared

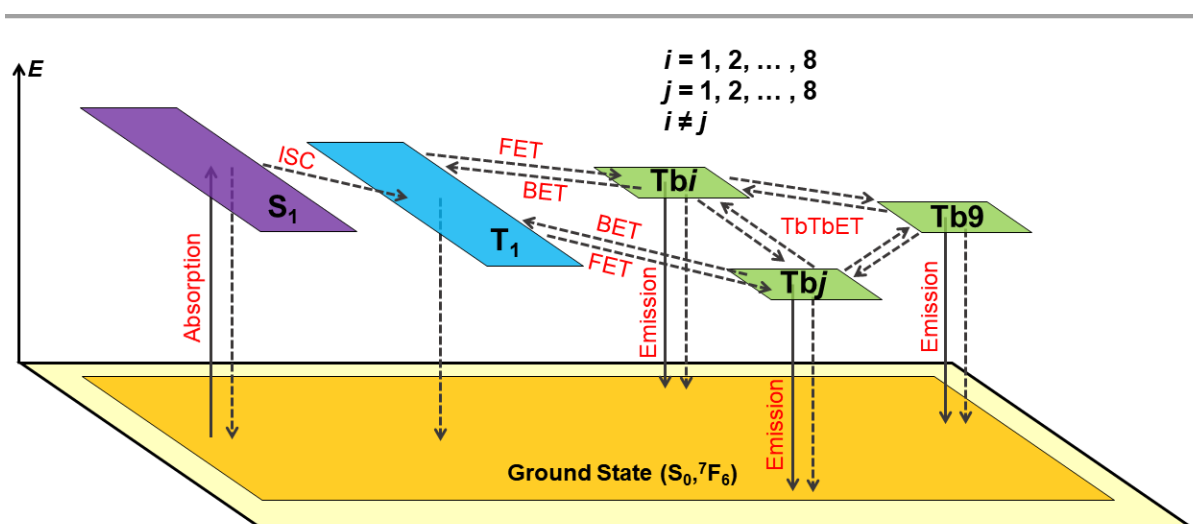


Figure 6.1 Schematic 3D energy diagram depicting the ET processes in nonanuclear Tb(III) clusters.

to those of the other Tb(III) ions (Figure 6.1). Therefore, TbTbET to this center Tb(III) ion overall raises the probability of the cluster emitting from the Tb(III) ions than BET to the ligands. The details of this concept are discussed in section 6.2 of this chapter. This new strategy implies that BET can be suppressed without changing T_1 state energy, which may become important for applications such as spectral converters where both the absorption and emission wavelength are specified.^[1-3] For example, two-color white LED consists of blue GaN-based LED chip with blue absorbing, yellow emitting Ce:YAG spectral converter. Fluorescent lamps use spectral converters that absorb in the UV region and emit in blue, green, and red.^[4]

In this study, Gd(III) ions were introduced to nonanuclear Tb(III) clusters to investigate the relationship between TbTbET and BET. Gd(III) ions were used as spacers between Tb(III) ions to modulate the TbTbET processes. Novel nonanuclear Ln(III) clusters containing Tb(III) and Gd(III) ions $[\text{Tb}_n\text{Gd}_{9-n}(\mu\text{-OH})_{10}(\text{Bu})_{16}\text{NO}_3]$ ($n = 0, 1, 2, 5, 8, 9$) (referred to as $\text{Tb}_n\text{Gd}_{9-n}\text{-Bu}$) were synthesized by complexation reaction of Tb(III)/Gd(III) nitrate salt and Bu ligands. Their characteristic structures were evaluated using mass spectroscopy and powder XRD. Emission spectroscopy, quantum yield, and emission lifetime measurements were performed for the clusters in a chloroform solution. Temperature dependence of emission lifetimes was also measured for the estimation of the activation energy of BET. The experimental results are compared with that of theoretical motivation (section 6.2.) to qualitatively see the suppression effect. The promising properties of Ln(III) clusters and their potential as a new class of highly efficient luminescent materials are presented in this chapter.

6.2. Theoretical Motivation

6.2.1. Theoretical Method

The importance of TbTbET and a Tb(III) ion site unaffected by BET and FET in suppressing BET has been briefly mentioned in 6.1. This section elaborates on this hypothesis by taking nonanuclear Tb(III) cluster as a model and qualitatively calculate the theoretical emission lifetimes and BET efficiencies by rate equation analysis.^[5]

First, the Tb(III) ions are labeled as “Tb1”, “Tb2”, ... , and “Tb9” (where 9 is the center Tb(III) ion) as shown in Figure 6.2 to distinguish between Tb(III) ions of a different site. The dynamics model of the energy transfer processes in $\text{Tb}_9\text{-Bu}$ is shown in Figure 6.3. Three assumptions are made here that does not affect the conclusion of the section in any way but

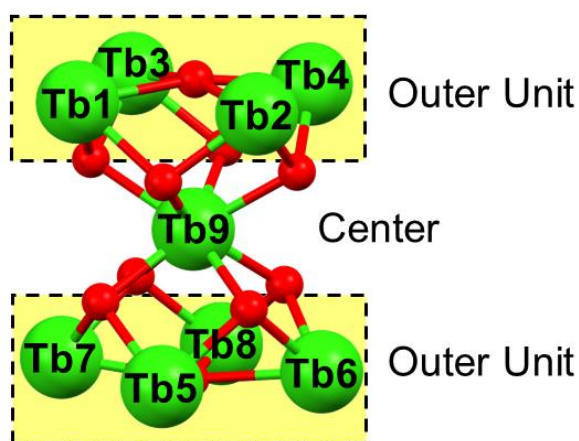


Figure 6.2 Labeling of the Tb(III) ions in Tb₉-Bu.

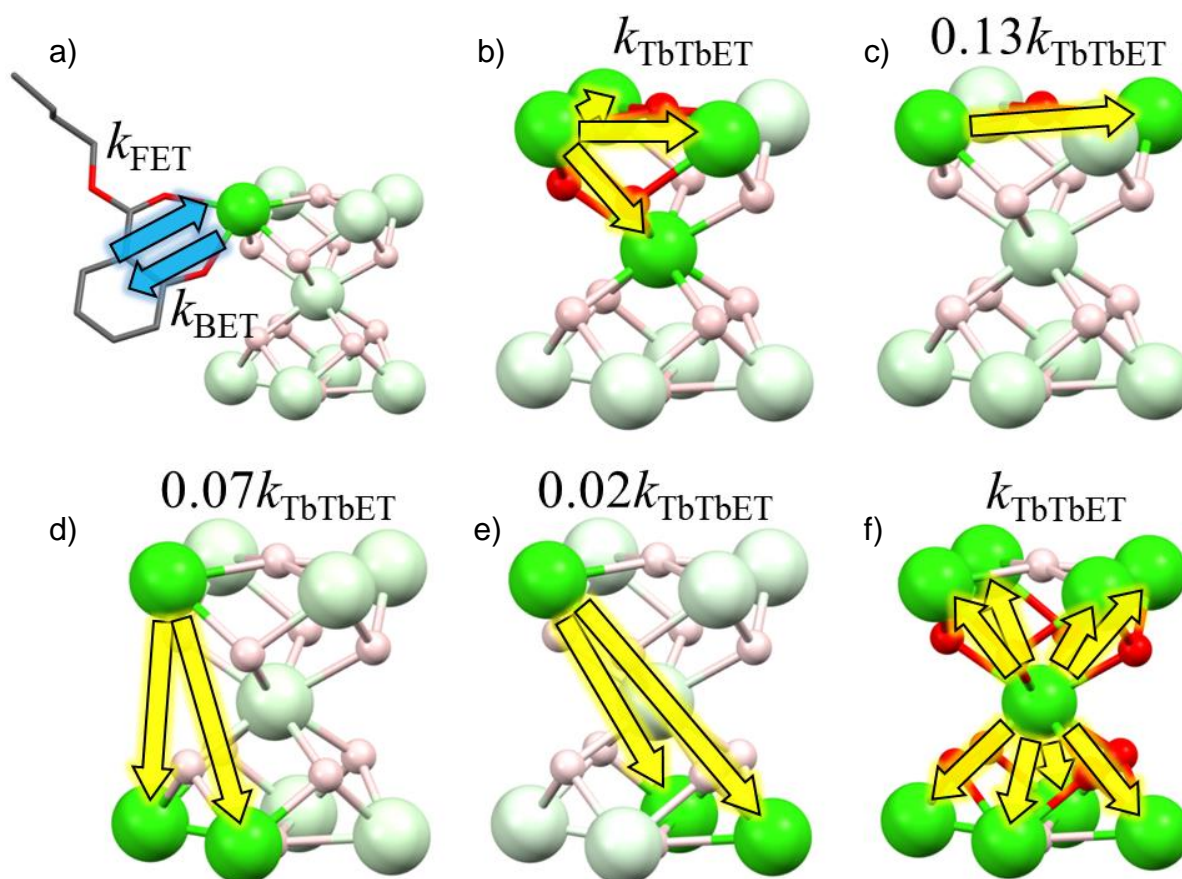


Figure 6.3 Excited state dynamics model of Tb₉-Bu. a) Between a Tb(III) ion and ligands, b) closest Tb(III) ion pair of the same outer unit, c) Tb(III) ion pair on the opposite of the same outer unit, d) closest Tb(III) ion pair of different outer unit, e) Tb(III) ion pair on the opposite of the different outer unit, and f) Tb9 and all the other Tb(III) ions.

are important in the calculations for the sake of discussion and simplicity. 1) Both FET and BET are ignored for Tb9 (the center Tb(III) ion). Tb9 is not directly coordinated with the Bu ligands. Due to the strong distance sensitivity of ET, the ET between Bu ligands and Tb9 is significantly more inefficient compared to the other Tb(III) ions that are coordinated directly with the Bu ligands ($m = 1, 2, \dots, 8$). This means that Tb9 can only be populated by TbTbET. 2) TbTbET is calculated based on the R^{-6} distance dependence (dipole-dipole interaction), and all the other interactions are neglected (i.e., exchange, dipole-quadrupole, and quadrupole-quadrupole interactions).^[6,7] While the Tb-Tb distance of 3.65 Å is close enough for all types of interactions, considering these interactions would only enhance TbTbET, thereby enhancing the BET suppression effect. Thus, for this qualitative investigation, calculating the dipole-dipole interaction is adequate. 3) The rate constants used for the calculations are based on the previous reports on different systems. The rate constants are arbitrary (as long as they are not zero), but to keep the rate constant within a reasonable scale, values previously reported were used.

The excited state dynamics can be expressed as a system of linear differential equations in the matrix form as introduced in 2.3.:

$$\frac{d\mathbf{X}(t)}{dt} = \mathbf{A}\mathbf{X}(t) + \mathbf{J}(t) , \quad [2.33]$$

where $\mathbf{X}(t)$ is the vector of population density of a specific state. In this case, there are 11 excited states, namely singlet excited state $S1(t)$, triplet excited state $T1(t)$, excited Tb(III) ions in the outer unit $Tbm(t)$ ($m = 1, 2, \dots, 8$), and the center Tb(III) ion ($Tb9(t)$):

$$\mathbf{X}(t) = \begin{pmatrix} S1(t) \\ T1(t) \\ Tb1(t) \\ \vdots \\ Tb8(t) \\ Tb9(t) \end{pmatrix} . \quad [6.1]$$

\mathbf{A} is the “interaction matrix” that models the system. With the assumptions above, the interaction matrix \mathbf{A} for Tb₉-Bu becomes:

$A =$

$$\begin{bmatrix}
 -\frac{1}{\tau_{S1}} & 0 & 0 & 0 & 0 & 0 & 0 & 0 & 0 & 0 & 0 \\
 k_{isc} & -\frac{1}{\tau_{T1}} & k_{BET} & 0 \\
 0 & k_{FET} & -\frac{1}{\tau_{Tbm}} & k_{TbTbET} & k_{TbTbET} & 0.13k_{TbTbET} & 0.07k_{TbTbET} & 0.02k_{TbTbET} & 0.07k_{TbTbET} & 0.02k_{TbTbET} & k_{TbTbET} \\
 0 & k_{FET} & k_{TbTbET} & -\frac{1}{\tau_{Tbm}} & 0.13k_{TbTbET} & k_{TbTbET} & 0.07k_{TbTbET} & 0.07k_{TbTbET} & 0.02k_{TbTbET} & 0.02k_{TbTbET} & k_{TbTbET} \\
 0 & k_{FET} & k_{TbTbET} & 0.13k_{TbTbET} & -\frac{1}{\tau_{Tbm}} & k_{TbTbET} & 0.02k_{TbTbET} & 0.07k_{TbTbET} & 0.02k_{TbTbET} & 0.07k_{TbTbET} & k_{TbTbET} \\
 0 & k_{FET} & 0.13k_{TbTbET} & k_{TbTbET} & k_{TbTbET} & -\frac{1}{\tau_{Tbm}} & 0.02k_{TbTbET} & 0.02k_{TbTbET} & 0.07k_{TbTbET} & 0.07k_{TbTbET} & k_{TbTbET} \\
 0 & k_{FET} & 0.07k_{TbTbET} & 0.07k_{TbTbET} & 0.02k_{TbTbET} & 0.02k_{TbTbET} & -\frac{1}{\tau_{Tbm}} & k_{TbTbET} & k_{TbTbET} & 0.13k_{TbTbET} & k_{TbTbET} \\
 0 & k_{FET} & 0.02k_{TbTbET} & 0.07k_{TbTbET} & 0.07k_{TbTbET} & 0.02k_{TbTbET} & k_{TbTbET} & -\frac{1}{\tau_{Tbm}} & 0.13k_{TbTbET} & k_{TbTbET} & k_{TbTbET} \\
 0 & k_{FET} & 0.07k_{TbTbET} & 0.02k_{TbTbET} & 0.02k_{TbTbET} & 0.07k_{TbTbET} & k_{TbTbET} & 0.13k_{TbTbET} & -\frac{1}{\tau_{Tbm}} & k_{TbTbET} & k_{TbTbET} \\
 0 & k_{FET} & 0.02k_{TbTbET} & 0.02k_{TbTbET} & 0.07k_{TbTbET} & 0.07k_{TbTbET} & 0.13k_{TbTbET} & k_{TbTbET} & k_{TbTbET} & -\frac{1}{\tau_{Tbm}} & k_{TbTbET} \\
 0 & 0 & k_{TbTbET} & -\frac{1}{\tau_{Tb9}}
 \end{bmatrix}, \quad [6.2]$$

where

$$\frac{1}{\tau_{S1}} = kr_{S1} + knr_{S1} + k_{isc}, \quad [6.3]$$

$$\frac{1}{\tau_{T1}} = kr_{T1} + knr_{T1} + 8k_{FET}, \quad [6.4]$$

$$\frac{1}{\tau_{Tbm}} = kr_{Tb} + knr_{Tb} + 3.31k_{TbTbET} + k_{BET}, \quad [6.5]$$

$$\frac{1}{\tau_{Tb9}} = kr_{Tb} + knr_{Tb} + 8k_{TbTbET}, \quad [6.6]$$

k_{isc} , kr , knr , k_{FET} , k_{BET} , and k_{TbTbET} are defined as intersystem-crossing, radiative, nonradiative, FET, BET, and TbTbET rate constants, respectively. The subscript indicates a species in Tb₉-Bu. Finally, vector $J(t)$ represents the input function of each species in Tb₉-Bu:

$$J(t) = \begin{pmatrix} J_{S1}(t) \\ J_{T1}(t) \\ J_{Tb1}(t) \\ \vdots \\ J_{Tb8}(t) \\ J_{Tb9}(t) \end{pmatrix}. \quad [6.7]$$

In Tb₉-Bu, the ligands are excited to the singlet excited state S₁, and all the other states are not directly excited by outside sources. Here, doubly excited states were ignored since excitation with reasonably low intensity (under 20 W mm⁻²) is considered.^[8] Thus, $J_{T1}(t) = J_{Tb1}(t) = \dots = J_{Tb8}(t) = J_{Tb9}(t) = 0$. $J_{S1}(t)$ depends on the purpose of the calculation. If the emission lifetimes are to be calculated, then laser pulse excitation is assumed and $J_{S1}(t)$ is expressed by an impulse function $\delta(t)$ (Dirac's delta function):

$$J(t) = \begin{pmatrix} \delta(t)K \\ 0 \\ 0 \\ \vdots \\ 0 \\ 0 \end{pmatrix} = j_1 \begin{pmatrix} \delta(t) \\ 0 \\ 0 \\ \vdots \\ 0 \\ 0 \end{pmatrix}, \quad [6.8]$$

where the constant j_1 is the amplitude of the excitation (the intensity of the excitation source). Since the intensity in terms of lifetimes are arbitrary, constant j_1 can be any value other than zero. For simplicity, $j_1 = 1$, which means that the excitation intensity is normalized. Calculation under this input function will lead to time-dependent population density, which is linearly proportional to emission lifetimes. If the quantum yields are to be calculated, then we are assuming steady excitation and $J_{S1}(t)$ is expressed by a constant K :

$$J(t) = \begin{pmatrix} K \\ 0 \\ 0 \\ \vdots \\ 0 \\ 0 \end{pmatrix} = j_1 \begin{pmatrix} 1 \\ 0 \\ 0 \\ \vdots \\ 0 \\ 0 \end{pmatrix}, \quad [6.9]$$

where the constant K , once again, is the amplitude of the excitation. If the excitation intensity is normalized ($K = 1$), then the efficiency of a process can be calculated. Here, the focus is the emission quantum yield $\Phi_{\pi\pi^*,\text{calc}}$ and the BET efficiency $\eta_{\text{BET,calc}}$. The BET efficiency $\eta_{\text{BET,calc}}$ is defined as the percentage of loss of population density of Tb(III) ions in the presence of BET to when BET is absent:

$$\eta_{\text{BET,calc}} = \frac{[\text{Tb1}(t)+\text{Tb2}(t)+\dots+\text{Tb9}(t)]_{k_{\text{BET}}=0} - [\text{Tb1}(t)+\text{Tb2}(t)+\dots+\text{Tb9}(t)]_{k_{\text{BET}}\neq 0}}{[\text{Tb1}(t)+\text{Tb2}(t)+\dots+\text{Tb9}(t)]_{k_{\text{BET}}=0}}. \quad [6.10]$$

The rate constants used for this calculation are summarized in Table 6.1.^[9,10] The values of k_{FET} and k_{BET} are arbitrary but 6000 and 3000 s⁻¹, respectively, were for clarity. Here, two cases are compared: 1) effect of TbTbET in the absence of BET, and 2) effect of TbTbET in the presence of BET on the photophysical properties of Tb₉-Bu. The calculations were performed on MATLAB, and the script (algorithm) is provided in 6.6.2.

Table 6.1 Rate constants used for the calculations.

Species	$kr + knr / s^{-1}$	k_{isc} / s^{-1}	k_{FET} / s^{-1}	k_{BET} / s^{-1}
S1	3.4×10^8 ^a	3.4×10^8 ^a	0	0
T1	1.5×10^4 ^a	0	6.0×10^3	0
Tb1 – Tb8	8.0×10^2 ^b	0	0	3.0×10^3 or 0
Tb9	8.0×10^2 ^b	0	0	0

a) From ref [9].

b) From ref [10].

6.2.2. Results

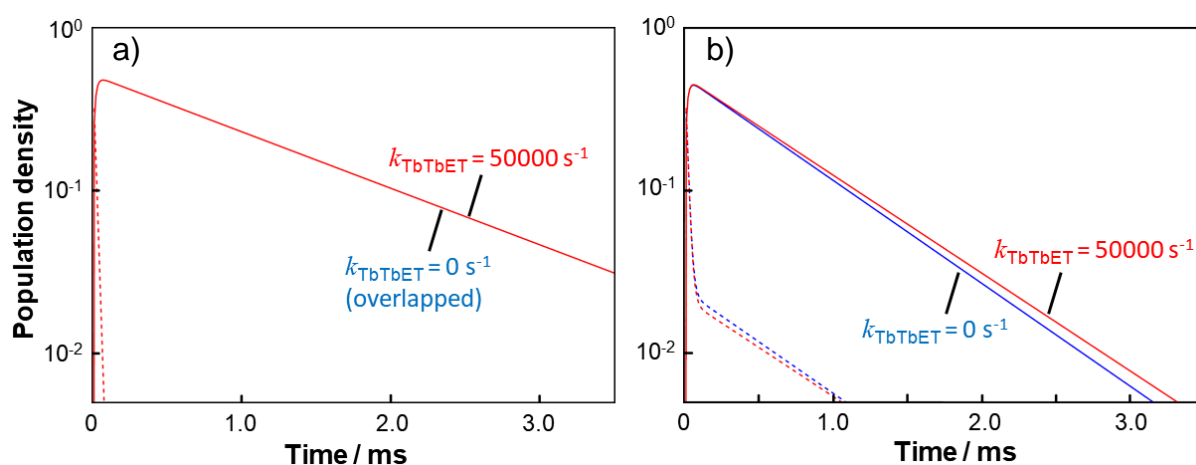

Figure 6.4 Calculated population density decay profiles a) in the absence of BET, and b) in the presence of BET. Solid lines: excited Tb(III) ions, dashed lines: the T_1 state. Blue lines: absence of FET, red lines: presence of FET.

Table 6.2 Calculated lifetimes, quantum yields and BET efficiencies of Tb₉ cluster in the presence of BET.

k_{TbET} / s^{-1}	$\tau_{calc} / \mu s$	$\Phi_{\pi\pi^*,calc}$	$\eta_{BET,calc}$
50000 (presence of TbET)	720	14.1%	44.3%
0 (absence of TbET)	685	13.4%	47.2%

Figure 6.4 shows the calculated population density decay profile of Tb₉-Bu after an impulse excitation. In the absence of BET (Figure 6.4a), the decay profile for $k_{\text{TbTbET}} = 0 \text{ s}^{-1}$ (absence of TbTbET: blue line) and $k_{\text{TbTbET}} = 50000 \text{ s}^{-1}$ (presence of TbTbET: red line) completely overlaps. The lifetime τ_{calc} was calculated to be 1.30 ms from the slope. The emission quantum yield $\Phi_{\pi\pi^*,\text{calc}}$ was also the same value of 25.3%. Calculating for $k_{\text{TbTbET}} = 0, 500, 5000, \text{ and } 50000 \text{ s}^{-1}$ still produced the same result (see Table A6.1). These results indicate that the TbTbET does not affect the observable photophysical properties of Tb₉-Bu. Meanwhile, in the presence of BET (Figure 6.4b), the decay profile for $k_{\text{TbTbET}} = 50000 \text{ s}^{-1}$ is longer compared to the case for $k_{\text{TbTbET}} = 0 \text{ s}^{-1}$. The lifetime was extended from $\tau_{\text{calc}} = 685 \text{ }\mu\text{s}$ to $720 \text{ }\mu\text{s}$. The emission quantum yield $\Phi_{\pi\pi^*,\text{calc}}$ increased from 13.4% to 14.1% and the BET efficiency $\eta_{\text{BET},\text{calc}}$ decreased from 47.2% to 44.3%. Furthermore, the population density of T₁ in the decay profile (dashed line in Figure 6.4) was lower when $k_{\text{TbTbET}} = 50000 \text{ s}^{-1}$. These results are summarized in Table 6.2. These results indicate that TbTbET can suppress BET in Tb₉-Bu.

To confirm the importance of Tb₉ in Tb₉-Bu, a hypothetical cluster where Tb₉ also involves in FET and BET the same way with other Tb(III) ions was also considered. The interaction matrix \mathbf{A}' for this cluster is:

$$\mathbf{A}' = \begin{bmatrix} -\frac{1}{\tau_{\text{S1}}} & 0 & 0 & 0 & 0 & 0 & 0 & 0 & 0 & 0 & 0 & 0 \\ k_{\text{isc}} & -\frac{1}{\tau_{\text{T1}}} & k_{\text{BET}} \\ 0 & k_{\text{FET}} & -\frac{1}{\tau_{\text{Tbm}}} & k_{\text{TbTbET}} & k_{\text{TbTbET}} & 0.13k_{\text{TbTbET}} & 0.07k_{\text{TbTbET}} & 0.02k_{\text{TbTbET}} & 0.07k_{\text{TbTbET}} & 0.02k_{\text{TbTbET}} & k_{\text{TbTbET}} & k_{\text{TbTbET}} \\ 0 & k_{\text{FET}} & k_{\text{TbTbET}} & -\frac{1}{\tau_{\text{Tbm}}} & 0.13k_{\text{TbTbET}} & k_{\text{TbTbET}} & 0.07k_{\text{TbTbET}} & 0.07k_{\text{TbTbET}} & 0.02k_{\text{TbTbET}} & 0.02k_{\text{TbTbET}} & k_{\text{TbTbET}} & k_{\text{TbTbET}} \\ 0 & k_{\text{FET}} & k_{\text{TbTbET}} & 0.13k_{\text{TbTbET}} & -\frac{1}{\tau_{\text{Tbm}}} & k_{\text{TbTbET}} & 0.02k_{\text{TbTbET}} & 0.07k_{\text{TbTbET}} & 0.02k_{\text{TbTbET}} & 0.07k_{\text{TbTbET}} & k_{\text{TbTbET}} & k_{\text{TbTbET}} \\ 0 & k_{\text{FET}} & 0.13k_{\text{TbTbET}} & k_{\text{TbTbET}} & k_{\text{TbTbET}} & -\frac{1}{\tau_{\text{Tbm}}} & 0.02k_{\text{TbTbET}} & 0.02k_{\text{TbTbET}} & 0.07k_{\text{TbTbET}} & 0.07k_{\text{TbTbET}} & k_{\text{TbTbET}} & k_{\text{TbTbET}} \\ 0 & k_{\text{FET}} & 0.07k_{\text{TbTbET}} & 0.07k_{\text{TbTbET}} & 0.02k_{\text{TbTbET}} & 0.02k_{\text{TbTbET}} & -\frac{1}{\tau_{\text{Tbm}}} & k_{\text{TbTbET}} & k_{\text{TbTbET}} & 0.13k_{\text{TbTbET}} & k_{\text{TbTbET}} & k_{\text{TbTbET}} \\ 0 & k_{\text{FET}} & 0.02k_{\text{TbTbET}} & 0.07k_{\text{TbTbET}} & 0.07k_{\text{TbTbET}} & 0.02k_{\text{TbTbET}} & k_{\text{TbTbET}} & -\frac{1}{\tau_{\text{Tbm}}} & 0.13k_{\text{TbTbET}} & k_{\text{TbTbET}} & k_{\text{TbTbET}} & k_{\text{TbTbET}} \\ 0 & k_{\text{FET}} & 0.07k_{\text{TbTbET}} & 0.02k_{\text{TbTbET}} & 0.02k_{\text{TbTbET}} & 0.07k_{\text{TbTbET}} & k_{\text{TbTbET}} & 0.13k_{\text{TbTbET}} & -\frac{1}{\tau_{\text{Tbm}}} & k_{\text{TbTbET}} & k_{\text{TbTbET}} & k_{\text{TbTbET}} \\ 0 & k_{\text{FET}} & 0.02k_{\text{TbTbET}} & 0.02k_{\text{TbTbET}} & 0.07k_{\text{TbTbET}} & 0.07k_{\text{TbTbET}} & 0.13k_{\text{TbTbET}} & k_{\text{TbTbET}} & k_{\text{TbTbET}} & -\frac{1}{\tau_{\text{Tbm}}} & k_{\text{TbTbET}} & k_{\text{TbTbET}} \\ 0 & k_{\text{FET}} & k_{\text{TbTbET}} & -\frac{1}{\tau_{\text{Tbm}}} & k_{\text{TbTbET}} \end{bmatrix} \quad . \quad [6.11]$$

The difference between Equations 6.11 and 6.2 is the 11th row and the 11th column, which express the interaction of Tb₉ with the others. The elements (11, 2) and (2, 11) contain k_{FET} and k_{BET} , respectively, for Equation 6.11. In the case of Equation 6.2, these elements are zero.

The element (11, 11) in Equation 6.11 is $-\frac{1}{\tau_{Tbm}}$ instead of $-\frac{1}{\tau_{Tb9}}$ as in Equation 6.2. The same calculation as done above was once again performed.

The results of the calculation of the lifetime, emission quantum yield, and BET efficiency of the hypothetical cluster are summarized in Table 6.3. No difference in the values was observed in the presence and the absence of TbTbET. Above results unambiguously indicate that the energy migration between Tb(III) ions and a Tb(III) ion site unaffected by BET is crucial in suppressing BET.

In 6.4.2., the temperature dependences of emission lifetimes of Tb₉-Bu and Tb₁Gd₈-Bu are compared. Tb₁Gd₈-Bu does not show any energy transfer between Tb(III) ions. As mentioned in Chapter 5, BET proceeds provided that there is enough thermal energy to compensate for the energy difference between the excited state of Tb(III) ions and Bu ligands. Complete suppression of BET can thus be achieved at low temperature. Therefore, the investigation of the lifetimes as done in this section can be performed experimentally by comparing the emission lifetimes of Tb₉-Bu and Tb₁Gd₈-Bu at room and low temperatures.

Table 6.3 Calculated quantum yield and BET efficiency of the hypothetical cluster with nine Tb(III) ions in direct contact with ligands.

k_{TbET} / s^{-1}	$\tau_{calc} / \mu s$	$\Phi_{\pi\pi^*,calc}$	$\eta_{BET,calc}$
50000 (presence of TbET)	713	14.31%	44.90%
0 (absence of TbET)	713	14.31%	44.90%

6.3. Experimental Section

6.3.1. Material

Terbium(III) nitrate hexahydrate (Tb(NO₃)₃·6H₂O) and triethylamine (C₆H₁₅N) were purchased from Kanto Chemical Co. Inc. Gadolinium(III) nitrate hexahydrate (Gd(NO₃)₃·6H₂O) was purchased from Sigma-Aldrich Co. Butylsalicylate (C₁₁H₁₄O₃) was purchased from Tokyo Chemical Industry Co., LTD. All other chemicals and solvents were of reagent grade and were used without further purification.

6.3.2. Apparatus

FAB-MS spectra were measured on a JEOL JMS-700TZ. Elemental analyses were performed by Exter Analytical CE440. Infrared spectra were recorded on a JASCO FT/IR-4600 spectrometer. XRD spectra were characterized by a RIGAKU X-ray diffractometer RINT 2200. Single crystal X-ray diffractions were made on a RIGAKU RAXIS RAPID imaging plate area detector.

6.3.3. Synthesis

General synthetic procedures of Tb_nGd_{9-n} -Bu: Butylsalicylate (Bu, 1.05 g, 5.40 mmol) was dissolved in methanol, and triethylamine (1.22 mL, 8.80 mmol) was added to the solution to be stirred at 40°C. A stoichiometric mixture of $Tb(NO_3)_3 \cdot 6H_2O$ and $Gd(NO_3)_3 \cdot 6H_2O$ (total of 3.04 mmol) in methanol was added dropwise to the solution. The solution stirred for 30 minutes and then cooled to room temperature. A white precipitate (target cluster) formed in the process. The precipitate was vacuum filtered and dried in vacuum.

Gd_9 -Bu ($[Gd_9(\mu-OH)_{10}(Bu)_{16}]^+NO_3^-$): Yield: 59%. Selected IR (ATR, cm^{-1}): 3573 (w, O–H), 3234 (w, O–H), 2956 (m, C–H), 1318 (s, C–O). FAB-MS: $m/z = 4676.8 [Gd_9(\mu-OH)_{10}(Bu)_{16}]^+$. Elemental analysis calculated for $C_{176}H_{218}NO_{61}Gd_9$: C, 44.61%, H, 4.64%, N, 0.30%. Found: C, 44.30%, H, 4.53%, N, 0.25%.

Tb_1Gd_8 -Bu ($[Tb_1Gd_8(\mu-OH)_{10}(Bu)_{16}]^+NO_3^-$): Yield: 82%. Selected IR (ATR, cm^{-1}): 3573 (w, O–H), 3234 (w, O–H), 2956 (m, C–H), 1318 (s, C–O). FAB-MS: $m/z = 4677.8 [Tb_1Gd_8(\mu-OH)_{10}(Bu)_{16}]^+$. Elemental analysis calculated for $C_{176}H_{218}NO_{61}Tb_1Gd_8$: C, 44.59%, H, 4.64%, N, 0.30%. Found: C, 43.95%, H, 4.53%, N, 0.29%.

Tb_2Gd_7 -Bu ($[Tb_2Gd_7(\mu-OH)_{10}(Bu)_{16}]^+NO_3^-$): Yield: 51%. Selected IR (ATR, cm^{-1}): 3573 (w, O–H), 3234 (w, O–H), 2956 (m, C–H), 1318 (s, C–O). FAB-MS: $m/z = 4679.8 [Tb_2Gd_7(\mu-OH)_{10}(Bu)_{16}]^+$. Elemental analysis calculated for $C_{176}H_{218}NO_{61}Tb_2Gd_7$: C, 44.58%, H, 4.63%, N, 0.30%. Found: C, 44.32%, H, 4.54%, N, 0.26%.

Tb_5Gd_4 -Bu ($[Tb_5Gd_4(\mu-OH)_{10}(Bu)_{16}]^+NO_3^-$): Yield: 41%. Selected IR (ATR, cm^{-1}): 3573 (w, O–H), 3234 (w, O–H), 2956 (m, C–H), 1318 (s, C–O). FAB-MS: $m/z = 4684.9 [Tb_5Gd_4(\mu-OH)_{10}(Bu)_{16}]^+$. Elemental analysis calculated for $C_{176}H_{218}NO_{61}Tb_5Gd_4$: C, 44.53%, H, 4.63%, N, 0.30%. Found: C, 44.23%, H, 4.52%, N, 0.24%.

Tb_8Gd_1 -Bu ($[Tb_8Gd_1(\mu-OH)_{10}(Bu)_{16}]^+NO_3^-$): Yield: 49%. Selected IR (ATR, cm^{-1}): 3573 (w, O–H), 3234 (w, O–H), 2956 (m, C–H), 1318 (s, C–O). FAB-MS: $m/z = 4689.8 [Tb_8Gd_1(\mu-$

$\text{OH})_{10}(\text{Bu})_{16}]^+$. Elemental analysis calculated for $\text{C}_{176}\text{H}_{218}\text{NO}_{61}\text{Tb}_8\text{Gd}_1$: C, 44.48%, H, 4.62%, N, 0.29%. Found: C, 44.24%, H, 4.53%, N, 0.24%.

Tb₉-Bu ($[\text{Tb}_9(\mu\text{-OH})_{10}(\text{Bu})_{16}]^+\text{NO}_3^-$): Yield: 52%. Selected IR (ATR, cm^{-1}): 3573 (w, O–H), 3234 (w, O–H), 2956 (m, C–H), 1318 (s, C–O). FAB-MS: $m/z = 4691.3$ $[\text{Tb}_9(\mu\text{-OH})_{10}(\text{Bu})_{16}]^+$. Elemental analysis calculated for $\text{C}_{176}\text{H}_{218}\text{NO}_{61}\text{Tb}_9$: C, 44.47%, H, 4.62%, N, 0.29%. Found: C, 44.20%, H, 4.57%, N, 0.27%.

6.3.4. Spectroscopy

Absorption spectra of $\text{Tb}_n\text{Gd}_{9-n}\text{-Bu}$ were obtained by using a JASCO V-670 spectrometer. Emission spectra were measured using a Horiba/Jobin-Yvon FluoroLog-3 spectrofluorometer and a JASCO FP-6600 spectrometer. The combination of an integration sphere and a JASCO FP-6600 spectrometer was used to measure emission quantum yields. Emission lifetimes were measured using the third harmonic (355 nm) of a Q-switched Nd:YAG laser. The temperature was controlled using an Oxford Instruments OptistatDN2 cryostat.

6.4. Results and Discussion

6.4.1. Structure and Identification

The molecular structure and coordination geometry of the nine Ln(III) ions in $\text{Tb}_n\text{Gd}_{9-n}\text{-Bu}$ were elucidated by X-ray single-crystal analysis of $\text{Gd}_9\text{-Bu}$ in Chapter 4 (see 4.3.1. Structure and Identification). Here, the structure is briefly reviewed (See Figure 4.2a). The analysis showed that the Gd(III) ions in the cluster form an “hour-glass” structure in which the upper four and lower four Gd(III) ions are connected to the center Gd(III) ion via oxygen. All Gd(III) ions have an 8-coordination structure. The center Gd(III) ion is coordinated only by oxygen atoms and not by Bu ligands. Each of the Gd(III) ions in the outer unit is coordinated by both Bu ligands and oxygen atoms. The distances between two Gd(III) ions for all combinations are summarized in Table 6.4. From Continuous Shape Measure (CShM)^[11,12] calculations, Gd(III) ion in the center and Gd(III) ions in the outer unit was attributed to 8-square antiprism (8-SAP) and 8-trigonal dodecahedron (8-TDH) coordination geometry, respectively.

The structures of the other $\text{Tb}_n\text{Gd}_{9-n}\text{-Bu}$ ($n = 1, 2, 5, 8$) were compared by the combination of powder XRD (Figure 6.5a) and FAB-MS (Figure 6.5b). In the XRD results, the diffraction angle is corrected on the Si powder peak at $2\theta = 28.43$ degrees for precise comparison of the

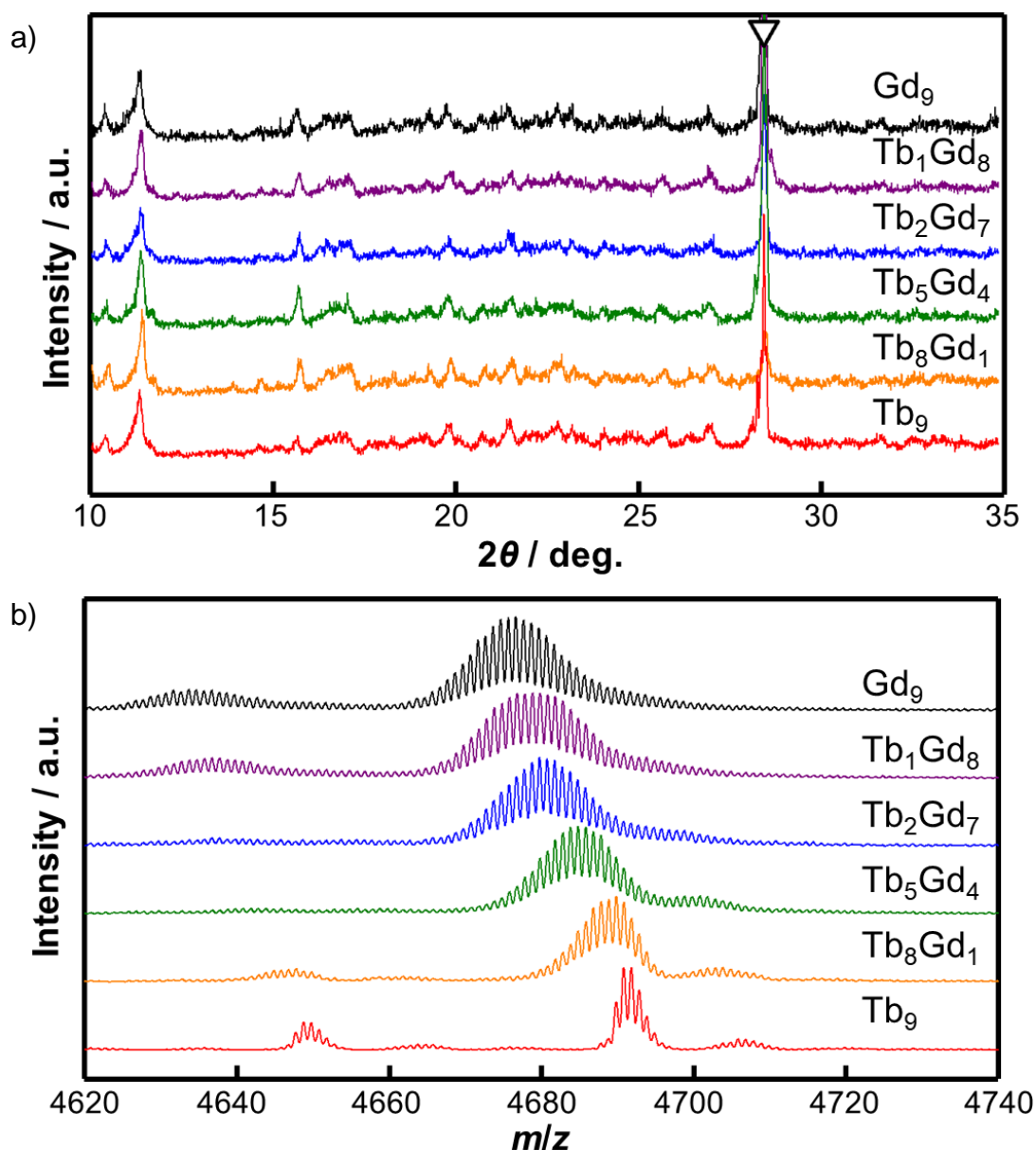


Figure 6.5 a) Powder XRD pattern of Tb_nGd_{9-n} -Bu. The inverse triangle represents the peak of Si power as a standard. b) FAB-MS results of Tb_nGd_{9-n} -Bu. The broadening of the peak with increasing number of Gd(III) ions is due to the stable isotopes.

peaks. Focusing on the three distinguished peaks ($2\theta_1 = 11.3$ degrees, $2\theta_2 = 15.6$ degrees, and $2\theta_3 = 19.8$ degrees), these peaks only showed shift within 0.02 degrees indicating that the mixed Tb/Gd clusters have the same structure as those of Tb_9 -Bu and Gd_9 -Bu. This is further supported by FAB-MS spectroscopy which showed m/z value of the Tb_nGd_{9-n} -Bu corresponding to their calculated molecular weight without the NO_3^- counter-anion. The results

presented above indicate that all the clusters were successfully synthesized with the identical structure.

Table 6.4 Distance between Gd(III) ions for all combinations (in Angstroms)

2 nd Gd	Gd1	Gd2	Gd3	Gd4	Gd5	Gd6	Gd7	Gd8	Gd9
Gd1	-	3.631	3.640	5.153	5.618	7.086	5.717	7.168	3.698
Gd2	3.631	-	5.128	3.638	5.749	5.622	7.168	7.070	3.691
Gd3	3.640	5.128	-	3.631	7.104	7.203	5.618	5.749	3.710
Gd4	5.153	3.638	3.631	-	7.203	5.764	7.086	5.622	3.709
Gd5	5.618	5.749	7.104	7.203	-	3.631	3.640	5.128	3.710
Gd6	7.086	5.622	7.203	5.764	3.631	-	5.153	3.638	3.709
Gd7	5.717	7.168	5.618	7.086	3.640	5.153	-	3.631	3.698
Gd8	7.168	7.070	5.749	5.622	5.128	3.638	3.631	-	3.691
Gd9	3.698	3.691	3.710	3.709	3.710	3.709	3.698	3.691	-

a) The labels of the Gd ions in this table are based on the labels used in the Theoretical Background section and not the labels in the CIF file for consistency with the main text.

6.4.2. Photophysical Properties

The measured (normalized) emission spectra of Tb_nGd_{9-n}-Bu ($n = 1, 2, 5, 8, 9$) in 1.0×10^{-4} M chloroform ($\lambda_{EX} = 380$ nm, ligand excitation) are shown in Figure 6.6a. The shape of the Ln(III) emission spectrum is known to be influenced by the coordination geometry. The spectral shape of the emission was identical in all Tb_nGd_{9-n}-Bu indicating that the local geometry of the Tb(III) ions is retained in all of the clusters. Furthermore, the spectral shape of Tb₉-Bu in powder form (Figure 6.6 inset) was also the same as that in the solution form, indicating that the coordination structure is maintained in solution.^[13–15] The emission of Tb_nGd_{9-n}-Bu exhibited the characteristic 4f-4f transition of the Tb(III) ion with each of the

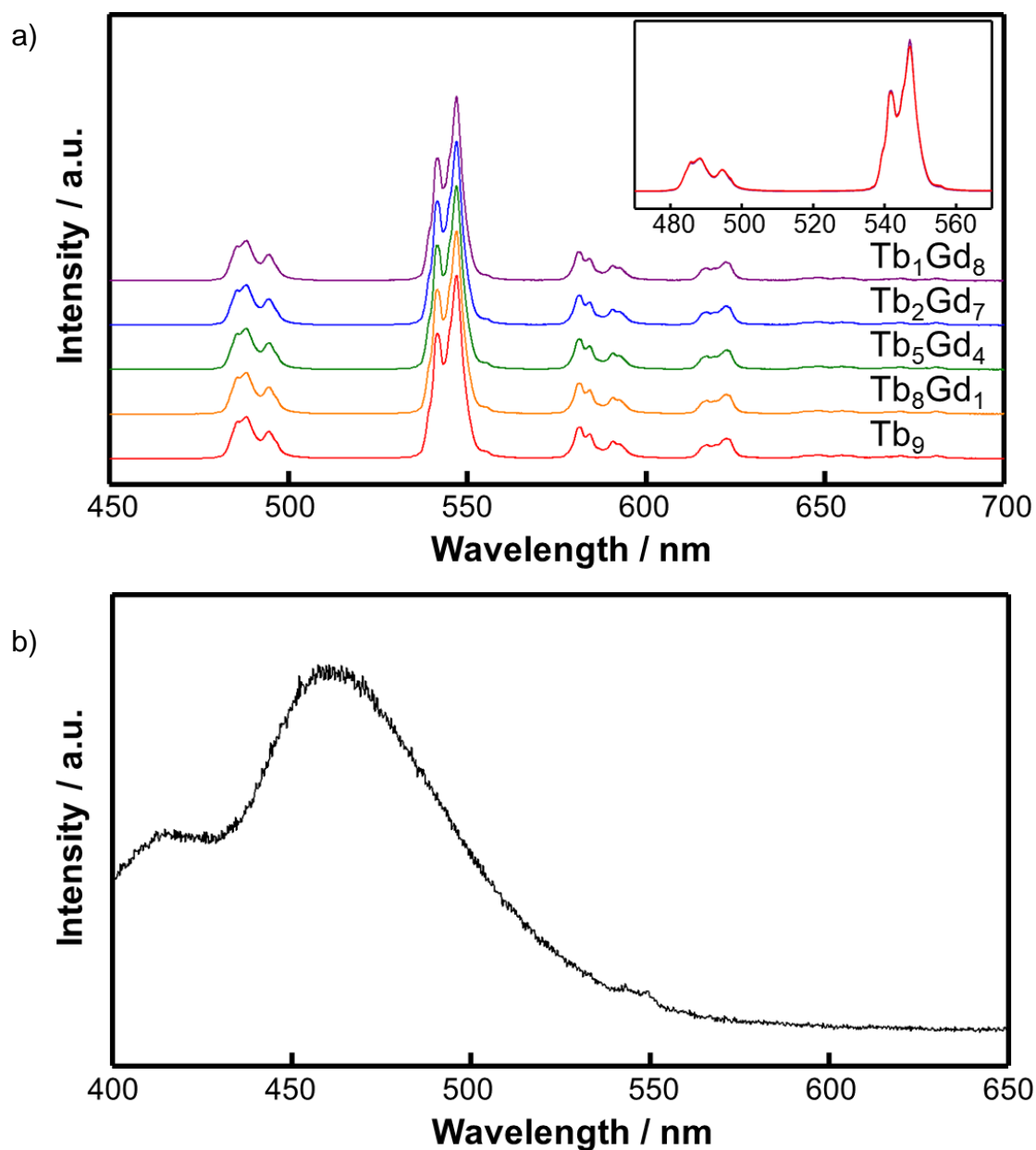


Figure 6.6 a) Emission spectra of Tb_nGd_{9-n}-Bu ($n = 1, 2, 5, 8, 9$) in 1.0×10^{-4} M chloroform solution ($\lambda_{\text{EX}} = 380$ nm). The spectra were normalized at the peak intensity and were applied an offset. Inset is the 470 – 570 nm region of the spectra ($^5\text{D}_4 \rightarrow ^7\text{F}_6$ and $^7\text{F}_5$ transitions) of Tb₁Gd₉-Bu in solution (red) and powder (black). The spectra completely overlap. b) Emission spectrum of Gd₉-Bu in 1.0×10^{-4} M chloroform solution ($\lambda_{\text{EX}} = 380$ nm).

peaks corresponding to its $^5D_4 \rightarrow ^7F_J$ ($J = 6 - 1$) transitions.^[16] The emission spectrum of Gd₉-Bu in 1.0×10^{-4} M chloroform solution at 210 K (Figure 6.6b) was measured to estimate the triplet excited state (T_1) energy level of the ligand. The excited state of Gd(III) ion is energetically higher than the excited states of the ligand, and thus the T_1 state is the lowest excited state. At sufficiently low temperature, the nonradiative process is suppressed, and the emission from the T_1 state was observed.^[17] An emission peak was observed at 461 nm (21690 cm^{-1}). Since the 5D_4 level of a Tb(III) ion is 20620 cm^{-1} as observed in the emission spectra (485 nm), the energy gap ΔE between T_1 and 5D_4 is 1070 cm^{-1} . This gap is well within the range for BET in Tb(III) complexes ($\Delta E < 1850 \text{ cm}^{-1}$) and thus BET is expected to take place in Tb_nGd_{9-n}-Bu.^[18]

The emission lifetimes were determined by using a nanosecond pulse laser ($\lambda_{\text{EX}} = 355 \text{ nm}$, $\lambda_{\text{EM}} = 550 \text{ nm}$) for the clusters in a 1.0×10^{-4} M chloroform solution. The emission decay profiles were single-exponential (Figure 6.7a) in all the clusters. As summarized in Table 6.5, the lifetimes τ_{obs} increased with increasing number of Tb(III) ions in the Tb_nGd_{9-n}-Bu. The effect of TbET with increasing number of Tb(III) ions in the clusters was investigated by measuring the temperature dependence of emission lifetimes (Figures 6.7b). A clear

Table 6.5 Photophysical properties of Tb_nGd_{9-n}-Bu.

Clusters	$\Phi_{\pi\pi^*}$ ^a	$\tau_{\text{obs}} / \text{ms}$ ^b	$\tau_{210\text{K}} / \text{ms}$ ^b	$D / 10^8 \text{ s}^{-1}$ ^c	$k_{\text{BET}} / \text{s}^{-1}$ ^c	$Ea_{\text{BET}} / \text{kJ mol}^{-1}$ ^d
Tb ₁ Gd ₈	14%	0.96	1.11	9.10	167	38.7
Tb ₂ Gd ₇	23%	1.06	1.12	*	*	*
Tb ₅ Gd ₄	33%	1.16	1.11	*	*	*
Tb ₈ Gd ₁	40%	1.17	1.13	*	*	*
Tb ₉	39%	1.16	1.14	*	*	*

a) Measured in 1.0×10^{-4} M chloroform solution ($\lambda_{\text{EX}} = 380 \text{ nm}$).

b) Measured in 1.0×10^{-4} M chloroform solution ($\lambda_{\text{EX}} = 355 \text{ nm}$).

c) Calculated from Equation [6.12]. D is the frequency factor.

d) Analyzed from an Arrhenius plot of Equation [6.12] using lifetime temperature dependency results.

k_{BET} and Ea_{BET} were only calculated for Tb₁Gd₈-Bu since other Tb_nGd_{9-n}-Bu ($n = 2, 5, 8, 9$) involve TbTbET, which contributes to the temperature dependency of lifetimes.

temperature dependence was observed above 270 K for Tb₁Gd₈-Bu and Tb₂Gd₇-Bu, while lifetimes remained fairly constant for Tb₅Gd₄-Bu, Tb₈Gd₁-Bu, and Tb₉-Bu. As mentioned in Chapter 5, the rate constant of BET k_{BET} can be estimated by the following equation:^[19,20]

$$k_{\text{BET}} = \frac{1}{\tau(T)} - \frac{1}{\tau(210\text{K})} = D \exp\left(-\frac{Ea}{k_{\text{B}}T}\right), \quad [6.12]$$

where τ is the measured emission lifetime at a given temperature, $\tau_{210\text{K}}$ is the emission lifetime at 210 K, D is the frequency factor, Ea_{BET} is the activation energy of BET, k_{B} is the Boltzmann constant, and T is the temperature. Ea_{BET} and k_{BET} can be calculated for Tb₁Gd₈-Bu by an Arrhenius plot within the range in which the temperature dependency was observed. These two values for the other clusters do not provide any meaningful result because other processes may play a factor in determining k_{BET} . The BET rate constant k_{BET} and activation energy Ea_{BET} for Tb₁Gd₈-Bu were calculated to be 167 s⁻¹ and 3235 cm⁻¹, respectively (Table 6.5).

Emission lifetime and its temperature dependence are in qualitative agreement with theoretical results presented in section 6.2. The theoretical lifetime of Tb₉-Bu in the absence of BET was constant regardless of TbTbET rate k_{TbTbET} (Table A6.1). As shown in Figure 6.7b and Table 6.5, the experimental emission lifetimes of Tb_nGd_{9-n}-Bu at 210 K are the same value of approximately 1.12 ms. Meanwhile, the theoretical lifetime of Tb₉-Bu in the presence of BET shows that the lifetime is longer in the presence of TbTbET than in the absence of TbTbET. Indeed, experimental emission lifetimes at above 270 K in Figure 6.7b clearly shows that the increase in number of Tb(III) ions (and thus faster TbTbET) leads to the increase in the emission lifetimes. Such agreement between the theoretical and experimental results qualitatively imply that the contribution of BET is suppressed in Tb₉-Bu because of the TbTbET and the existence of the center Tb(III) ion that is not in direct contact with the Bu ligands.

The obtained results provide new insight into a strategy to suppress BET in Ln(III) complexes. Formerly, the only strategy to suppress BET in Ln(III) complexes was to use ligands with high T₁ energy (> 1850 cm⁻¹ in relative to the excited state of Ln(III) ion relevant to the FET process). This study now suggests that utilizing fast LnLnET in polynuclear Ln(III) complexes with at least one Ln(III) site that does not involve in the FET and BET process leads to suppression of BET without changing the T₁ energy of the ligands. Furthermore, since LnLnET is distance sensitive, Ln(III) clusters, in general, are a promising candidate as a material with low BET efficiency.

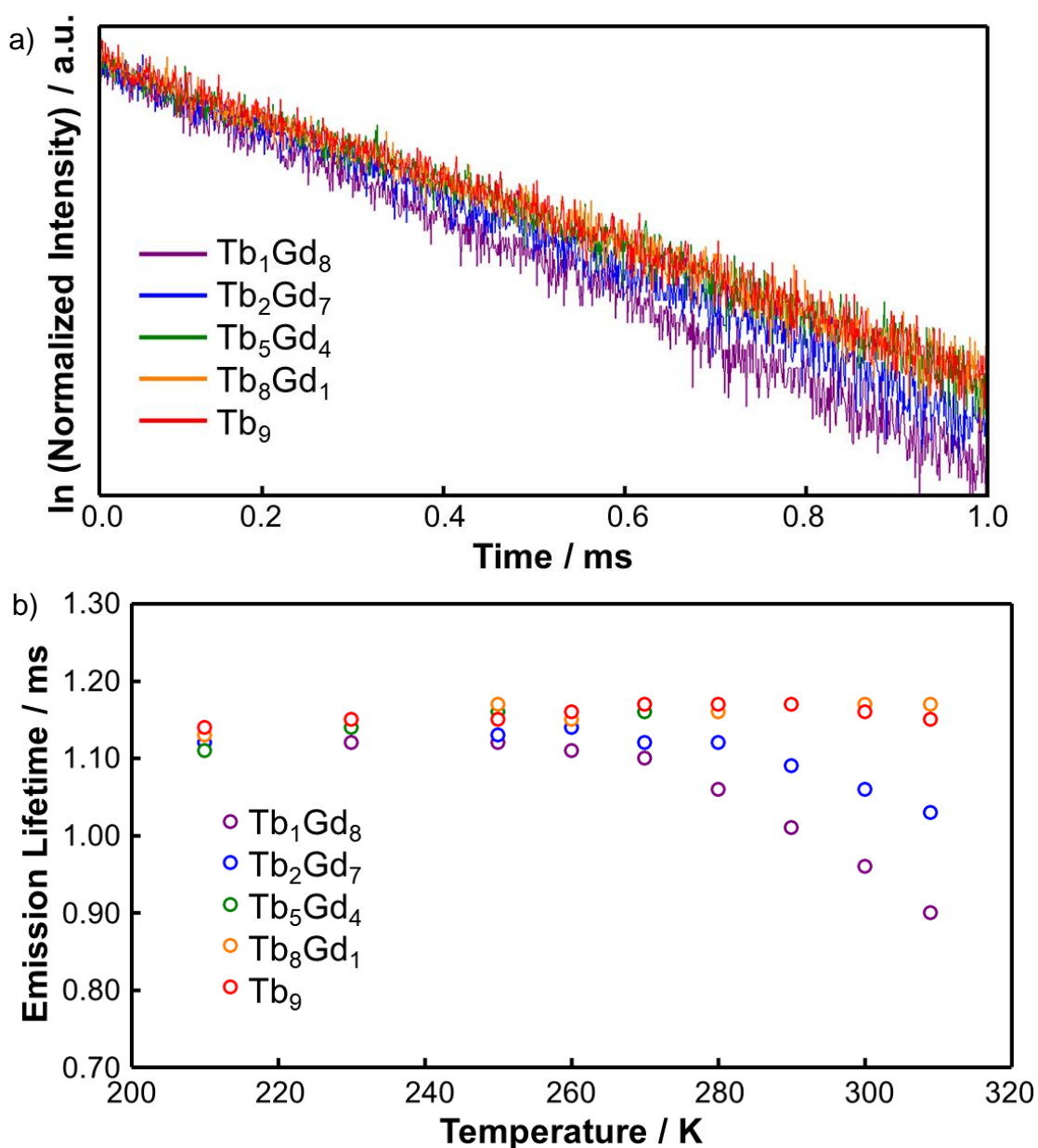
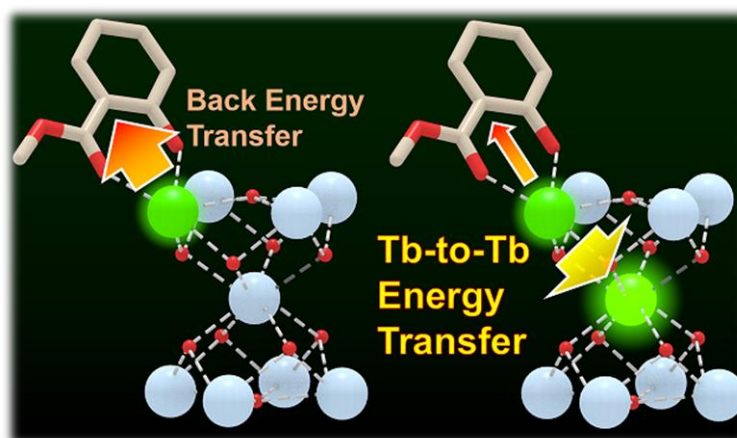


Figure 6.7 a) Emission decay profiles of Tb_nGd_{9-n}-Bu ($n = 1, 2, 5, 8,$ and 9) in 1.0×10^{-4} M chloroform solution ($\lambda_{\text{EX}} = 355$ nm, $\lambda_{\text{EM}} = 550$ nm). b) Plot of emission lifetime temperature dependence. The experimental uncertainties in the reported lifetimes are up to $\pm 1.5\%$.

6.5. Conclusion

The role of ET between Tb(III) ions (TbTbET) in luminescent nonanuclear Tb(III) clusters in the reduction of BET has been demonstrated both theoretically and experimentally using

$\text{Tb}_n\text{Gd}_{9-n}\text{-Bu}$ ($[\text{Tb}_n\text{Gd}_{9-n}(\mu\text{-OH})_{10}(\text{Bu})_{16}]^+\text{NO}_3^-$) as a model system. In the Theoretical Motivation section, it was demonstrated that the two features of $\text{Tb}_9\text{-Bu}$ were important for suppressing BET: 1) TbTbET by closely assembled Tb(III) ions and 2) the existence of center Tb(III) that is isolated from BET (and FET). Experimentally, the photophysical properties of nonanuclear $\text{Tb}_n\text{Gd}_{9-n}\text{-Bu}$ where $n = 0, 1, 2, 5, 8,$ and 9 were synthesized and investigated. The combination of X-ray single-crystal analysis, powder XRD, FAB-MS, and emission spectra revealed that these clusters have identical structures. Temperature dependence measurements of emission lifetime revealed that effect of BET becomes prominent in $\text{Tb}_n\text{Gd}_{9-n}\text{-Bu}$ at temperatures above 270 K. Below this temperature, the emission lifetime is constant for all clusters. Above 270 K, the decrease in emission lifetime is mitigated for clusters with over five Tb(III) ions. By comparing the trends observed in experimental results to those of theoretical results, it was found that the contribution of BET is indeed suppressed in clusters with a large number of Tb(III) ions. These findings provide new insight into the fundamental photophysics of Ln(III) complexes as well as an indication of a novel strategy to achieve higher luminescence efficiency in Ln(III) complexes.



6.6. Appendix

6.6.1. Dependence of TbTbET in Absence of BET

TbTbET rate constant dependence on the lifetime of $\text{Tb}_9\text{-Bu}$ in the absence of BET was evaluated by the same method presented in section 6.2., but with different values for TbTbET rate constant k_{TbTbET} ($= 0, 500, 5000,$ and 50000 s^{-1}). BET rate constant k_{BET} is 0 s^{-1} ,

representing the absence of BET. Calculated lifetime τ_{calc} , quantum yield $\Phi_{\pi\pi^*,\text{calc}}$, and BET efficiency $\eta_{\text{BET,calc}}$ are summarized in Table A6.1. No dependence of TbTbET rate constant on the lifetimes and quantum yields were observed, unambiguously indicating that TbTbET serves no role in changing the photophysical properties of Tb₉-Bu in the absence of BET.

Table A6.1 TbTbET rate constant dependency on the theoretical lifetime in the absence of BET.

$k_{\text{TbET}} / \text{s}^{-1}$	$\tau_{\text{calc}} / \mu\text{s}$	$\Phi_{\pi\pi^*,\text{calc}}$	$\eta_{\text{BET,calc}}$
0	1300	25.28%	0%
500	1300	25.28%	0%
5000	1300	25.28%	0%
50000	1300	25.28%	0%

6.6.2. MATLAB Script for Theoretical Calculation of Tb₉-Bu

Theoretical calculations were performed using MATLAB software. The procedures are explained in 6.2. Below is an example of the script for the calculation of lifetimes and quantum yield.

Theoretical lifetime ($k_{\text{TbET}} = 0 \text{ s}^{-1}$, $k_{\text{BET}} = 3000 \text{ s}^{-1}$):

```
syms t s j krS1 knrS1 kisc krT1 knrT1 kPSEnT kBEnT krTbt knrTbt krTbs knrTbs kTbEnT
X1(t) X2(t) X3(t) X4(t) X5(t) X6(t) X7(t) X8(t) X9(t) X10(t) X11(t)

krS1 = 40000000
knrS1 = 340000000
kisc = 750000000
krT1 = 5000
knrT1 = 10000
kPSEnT = 6000
kBEnT = 3000
kTbEnT = 0
```

```

krTbt = 400
knrTbt = 400
krTbs = 400
knrTbs = 400

j = 1
I = eye(11)

C = [j; 0; 0; 0; 0; 0; 0; 0; 0; 0; 0]
A = [-(krS1+knrS1+kisc) 0 0 0 0 0 0 0 0 0 0;
      kisc -(krT1+knrT1+8*kPSEnT) kBEnT kBEnT kBEnT kBEnT kBEnT kBEnT kBEnT kBEnT 0;
      0 kPSEnT -(krTbt+knrTbt+kBEnT+3.31*kTbEnT) kTbEnT kTbEnT 0.13*kTbEnT
0.07*kTbEnT 0.02*kTbEnT 0.07*kTbEnT 0.02*kTbEnT kTbEnT;
      0 kPSEnT kTbEnT -(krTbt+knrTbt+kBEnT+3.31*kTbEnT) 0.13*kTbEnT kTbEnT
0.07*kTbEnT 0.07*kTbEnT 0.02*kTbEnT 0.02*kTbEnT kTbEnT;
      0 kPSEnT kTbEnT 0.13*kTbEnT -(krTbt+knrTbt+kBEnT+3.31*kTbEnT) kTbEnT
0.02*kTbEnT 0.07*kTbEnT 0.02*kTbEnT 0.07*kTbEnT kTbEnT;
      0 kPSEnT 0.13*kTbEnT kTbEnT kTbEnT -(krTbt+knrTbt+kBEnT+3.31*kTbEnT)
0.02*kTbEnT 0.02*kTbEnT 0.07*kTbEnT 0.07*kTbEnT kTbEnT;
      0 kPSEnT 0.07*kTbEnT 0.07*kTbEnT 0.02*kTbEnT 0.02*kTbEnT -
(krTbt+knrTbt+kBEnT+3.31*kTbEnT) kTbEnT kTbEnT 0.13*kTbEnT kTbEnT;
      0 kPSEnT 0.02*kTbEnT 0.07*kTbEnT 0.07*kTbEnT 0.02*kTbEnT kTbEnT -
(krTbt+knrTbt+kBEnT+3.31*kTbEnT) 0.13*kTbEnT kTbEnT kTbEnT;
      0 kPSEnT 0.07*kTbEnT 0.02*kTbEnT 0.02*kTbEnT 0.07*kTbEnT kTbEnT 0.13*kTbEnT -
(krTbt+knrTbt+kBEnT+3.31*kTbEnT) kTbEnT kTbEnT;
      0 kPSEnT 0.02*kTbEnT 0.02*kTbEnT 0.07*kTbEnT 0.07*kTbEnT 0.13*kTbEnT kTbEnT
kTbEnT -(krTbt+knrTbt+kBEnT+3.31*kTbEnT) kTbEnT;
      0 0 kTbEnT kTbEnT kTbEnT kTbEnT kTbEnT kTbEnT kTbEnT kTbEnT -
(krTbs+knrTbs+8*kTbEnT)]
[P, D]=eig(A)
X = (P*expm(D*t)*P^-1)*C
X1(t) = X(1, 1)
X2(t) = X(2, 1)
X3(t) = X(3, 1)

```

```

X4(t) = X(4, 1)
X5(t) = X(5, 1)
X6(t) = X(6, 1)
X7(t) = X(7, 1)
X8(t) = X(8, 1)
X9(t) = X(9, 1)
X10(t) = X(10, 1)
X11(t) = X(11, 1)
X22(t) = X2
X29(t) = X3+X4+X5+X6+X7+X8+X9+X10+X11

hold on
X29plot = ezplot(X29, [0, 0.005])
set(X29plot, 'color', 'b', 'Linewidth', 2)
X22plot = ezplot(X22, [0, 0.005])
set(X22plot, 'LineStyle', '--', 'color', 'b', 'Linewidth', 2)
Title = title('Tb9 Cluster', 'FontSize', 15)
ylabel('Population Density', 'FontSize', 10)
xlabel('Time / s', 'FontSize', 10)
legend([X29plot X22plot], 'All Tb', 'T1')
axis([0 0.005 0 1])

double(1/((log(X29(0.5))-log(X29(1)))/(1-0.5)))

```

Quantum yield ($k_{\text{TbET}} = 50000 \text{ s}^{-1}$, $k_{\text{BET}} = 3000 \text{ s}^{-1}$):

```

syms t s j krS1 knrS1 kisc krT1 knrT1 kPSEnT kBEnT krTbt knrTbt krTbs knrTbs kTbEnT
X1(t) X2(t) X3(t) X4(t) X5(t) X6(t) X7(t) X8(t) X9(t) X10(t) X11(t)

krS1 = 40000000
knrS1 = 340000000
kisc = 750000000
krT1 = 5000
knrT1 = 10000
kPSEnT = 6000

```

```

kBEnT = 3000
kTbEnT = 50000
krTbt = 400
knrTbt = 400
krTbs = 400
knrTbs = 400

j = 1
I = eye(11)

C = [j; 0; 0; 0; 0; 0; 0; 0; 0; 0; 0]
A = [-(krS1+knrS1+kisc) 0 0 0 0 0 0 0 0 0; kisc -(krT1+knrT1+8*kPSEnT) kBEnT
kBEnT kBEnT kBEnT kBEnT kBEnT kBEnT kBEnT 0; 0 kPSEnT -
(krTbt+knrTbt+kBEnT+3.31*kTbEnT) kTbEnT kTbEnT 0.13*kTbEnT 0.07*kTbEnT 0.02*kTbEnT
0.07*kTbEnT 0.02*kTbEnT kTbEnT; 0 kPSEnT kTbEnT -(krTbt+knrTbt+kBEnT+3.31*kTbEnT)
0.13*kTbEnT kTbEnT 0.07*kTbEnT 0.07*kTbEnT 0.02*kTbEnT 0.02*kTbEnT kTbEnT; 0 kPSEnT
kTbEnT 0.13*kTbEnT -(krTbt+knrTbt+kBEnT+3.31*kTbEnT) kTbEnT 0.02*kTbEnT 0.07*kTbEnT
0.02*kTbEnT 0.07*kTbEnT kTbEnT; 0 kPSEnT 0.13*kTbEnT kTbEnT kTbEnT -
(krTbt+knrTbt+kBEnT+3.31*kTbEnT) 0.02*kTbEnT 0.02*kTbEnT 0.07*kTbEnT 0.07*kTbEnT
kTbEnT; 0 kPSEnT 0.07*kTbEnT 0.07*kTbEnT 0.02*kTbEnT 0.02*kTbEnT -
(krTbt+knrTbt+kBEnT+3.31*kTbEnT) kTbEnT kTbEnT 0.13*kTbEnT kTbEnT; 0 kPSEnT
0.02*kTbEnT 0.07*kTbEnT 0.07*kTbEnT 0.02*kTbEnT kTbEnT -
(krTbt+knrTbt+kBEnT+3.31*kTbEnT) 0.13*kTbEnT kTbEnT kTbEnT; 0 kPSEnT 0.07*kTbEnT
0.02*kTbEnT 0.02*kTbEnT 0.07*kTbEnT kTbEnT 0.13*kTbEnT -
(krTbt+knrTbt+kBEnT+3.31*kTbEnT) kTbEnT kTbEnT; 0 kPSEnT 0.02*kTbEnT 0.02*kTbEnT
0.07*kTbEnT 0.07*kTbEnT 0.13*kTbEnT kTbEnT kTbEnT -(krTbt+knrTbt+kBEnT+3.31*kTbEnT)
kTbEnT; 0 0 kTbEnT kTbEnT kTbEnT kTbEnT kTbEnT kTbEnT kTbEnT kTbEnT -
(krTbs+knrTbs+8*kTbEnT)]
[P, D]=eig(A)
X = (A^-1)*((P*expm(D*t)*P^-1)-I)*C
X1(t) = X(1, 1)
X2(t) = X(2, 1)
X3(t) = X(3, 1)
X4(t) = X(4, 1)

```

$$X5(t) = X(5, 1)$$

$$X6(t) = X(6, 1)$$

$$X7(t) = X(7, 1)$$

$$X8(t) = X(8, 1)$$

$$X9(t) = X(9, 1)$$

$$X10(t) = X(10, 1)$$

$$X11(t) = X(11, 1)$$

$$X_{tbqy1}(t) = k_{rTbt} * (X3 + X4 + X5 + X6 + X7 + X8 + X9 + X10) + k_{rTbs} * X11$$

$$\text{double}(X_{tbqy1}(\text{inf}))$$

$$X_{alltbdecay}(t) = (k_{rTbt} + k_{nrTbt}) * (X3 + X4 + X5 + X6 + X7 + X8 + X9 + X10) + (k_{rTbs} + k_{nrTbs}) * X11$$

$$\text{double}(X_{alltbdecay}(\text{inf}))$$

6.7. References

- [1] B. M. van der Ende, L. Aarts, A. Meijerink, *Phys. Chem. Chem. Phys.* **2009**, *11*, 11081–11095.
- [2] X. Huang, S. Han, W. Huang, X. Liu, *Chem. Soc. Rev.* **2013**, *42*, 173–201.
- [3] Y. Shang, S. Hao, C. Yang, G. Chen, *Nanomaterials* **2015**, *5*, 1782–1809.
- [4] R. Gautier, X. Li, Z. Xia, F. Massuyeau, *J. Am. Chem. Soc.* **2017**, *139*, 1436–1439.
- [5] M. E. Starzak, *Mathematical Methods in Chemistry and Physics*, Springer, **1989**.
- [6] O. L. Malta, *J. Non. Cryst. Solids* **2008**, *354*, 4770–4776.
- [7] T. Kushida, *J. Phys. Soc. Japan* **1973**, *34*, 1327–1333.
- [8] L. Aboshyan-Sorgho, H. Nozary, A. Aebischer, J.-C. G. Bünzli, P. Y. Morgantini, K. R. Kittilstved, A. Hauser, S. V. Eliseeva, S. Petoud, C. Piguet, *J. Am. Chem. Soc.* **2012**, *134*, 12675–12684.
- [9] S. Tobita, M. Arakawa, I. Tanaka, *J. Phys. Chem.* **1985**, *89*, 5649–5654.
- [10] Y. Yang, J. Li, X. Liu, S. Zhang, K. Driesen, P. Nockemann, K. Binnemans, *ChemPhysChem* **2008**, *9*, 600–606.
- [11] D. Casanova, M. Llunell, P. Alemany, S. Alvarez, *Chem. Eur. J.* **2005**, *11*, 1479–1494.
- [12] M. Pinsky, D. Avnir, *Inorg. Chem.* **1998**, *37*, 5575–5582.

- [13] N. B. D. Lima, S. M. C. Gonçalves, S. a Júnior, A. M. Simas, *Sci. Rep.* **2013**, *3*, 2395.
- [14] K. Miyata, T. Nakagawa, R. Kawakami, Y. Kita, K. Sugimoto, T. Nakashima, T. Harada, T. Kawai, Y. Hasegawa, *Chem. Eur. J.* **2011**, *17*, 521–528.
- [15] K. Yanagisawa, T. Nakanishi, Y. Kitagawa, T. Seki, T. Akama, M. Kobayashi, T. Taketsugu, H. Ito, K. Fushimi, Y. Hasegawa, *Eur. J. Inorg. Chem.* **2015**, 4769–4774.
- [16] J. V Beitz, *J. Alloys Compd.* **1994**, *207–208*, 41–50.
- [17] A. P. Bassett, S. W. Magennis, P. B. Glover, D. J. Lewis, N. Spencer, S. Parsons, R. M. Williams, L. De Cola, Z. Pikramenou, *J. Am. Chem. Soc.* **2004**, *126*, 9413–9424.
- [18] M. Latva, H. Takalo, V.-M. Mikkala, C. Matachescu, J. C. Rodríguez-Ubis, J. Kankare, *J. Lumin.* **1997**, *75*, 149–169.
- [19] K. Miyata, Y. Konno, T. Nakanishi, A. Kobayashi, M. Kato, K. Fushimi, Y. Hasegawa, *Angew. Chem. Int. Ed.* **2013**, *52*, 6413–6416.
- [20] K. Yanagisawa, Y. Kitagawa, T. Nakanishi, T. Akama, M. Kobayashi, T. Seki, K. Fushimi, H. Ito, T. Taketsugu, Y. Hasegawa, *Eur. J. Inorg. Chem.* **2017**, 3843–3848.

Chapter 7

SUMMARY AND OUTLOOK

7.1. Summary and Conclusion

The objective of this study is to uncover various factors that affect the luminescence efficiency of Ln(III) complexes and to provide new insight into the molecular design of the complexes for highly efficient and strongly luminescent material. These various factors are concentration quenching, spin-orbit coupling, and back energy transfer. We have also provided a means of suppressing back energy transfer by energy transfer between Ln(III) ions.

Chapter 1 was a background on luminescence in general and lanthanide complexes and introduced the concepts that are relevant to the studies shown in this thesis. Special emphasis was placed on the photophysical aspect of luminescent Ln(III) complexes and the photophysical processes that affect the quantum yield.

In Chapter 2, the theory behind lanthanide luminescence as well as kinetic analysis of complicated systems was explained. The former describes the Judd-Ofelt theory as well as the theory of energy transfer under the framework of the Judd-Ofelt theory and explains the derivation of the rate constant of luminescence and energy transfer. The latter describes the derivation of rate equations for a system of complicated excited state dynamics under an impulse and a constant excitation source.

The consequence of energy transfer between Ln(III) ions is the concentration quenching, and their effects in Yb(III) coordination polymer was described in Chapter 3. The emission spectra and lifetimes of Yb(III) emission of the polymer were recorded and compared to the theoretical lifetimes under different concentration quenching model. These models are no concentration quenching, killer-site, and phonon-assisted energy transfer relaxation models. The theories described in Chapter 2 was extensively used for the derivation of theoretical lifetimes. The experimental results were qualitatively consistent with the phonon-assisted energy transfer relaxation model, indicating that this is the concentration quenching mechanism in Yb(III) coordination polymers.

The central discussion described in Chapter 4 was the effect of spin-orbit coupling on the sensitization efficiency of Ln(III) complexes. Specifically, the sensitization efficiency of Yb(III)/Gd(III) or Yb(III)/Lu(III) mixed nonanuclear Ln(III) clusters was discussed. The sensitization efficiency is dependent on the spin-orbit coupling that enhances both the $S_1 \rightarrow T_1$ intersystem crossing and the $T_1 \rightarrow S_0$ relaxation, which the former and the latter affects positively and negatively, respectively, positively and negatively to the sensitization efficiency. The emission spectra of the clusters indicated that strong spin-orbit coupling does not necessarily lead to high sensitization efficiency because it promoted $T_1 \rightarrow S_0$ relaxation.

In Chapter 5, the factors contributing to the back energy transfer rate constant in nonanuclear Tb(III) clusters were reported. The chapter also reported the effect of intramolecular interaction between alkyl salicylate ligands on the photophysical properties of the clusters. The result shows that the core structure of the cluster is rigid, and maintains the luminescent property of Tb(III) ions that are sensitive to the coordination environment. Provided with these results, methyl salicylates with methyl substituent on the aromatic part were used as ligands with modified excited state energy levels. Temperature dependent emission lifetime measurement revealed that back energy transfer is not only dependent on the energy gaps between T_1 and 5D_4 state of Tb(III) ion but also the activation energies and frequency factors.

Finally, in Chapter 6, the effect of the energy transfer between Tb(III) ions on the back energy transfer was described. The theoretical motivation section explained, using kinetic analysis, the possibility of fast energy transfer between Tb(III) ions to suppress the contribution of back energy transfer in nonanuclear Tb(III) clusters by delivering the energy to a Tb(III) ion site that is not involved in forward and back energy transfers. Experimental results, particularly the temperature dependence of emission lifetimes of Tb/Gd mixed clusters, showed similar trend observed for the theoretical lifetimes, indicating that back energy transfer is indeed suppressed by energy transfer between Tb(III) ions.

Given the results explained in these chapters, new insights into the strategy of molecular design for the achievement of high quantum yield is provided here as a conclusion. A Ln(III) complex with high quantum yield can be achieved if:

- 1) High vibronic modes are eliminated to suppress phonon-assisted energy transfer relaxation.
- 2) Spin-orbit coupling strength is kept optimum so that $T_1 \rightarrow S_0$ relaxation will not overcome the enhancing effect of $S_1 \rightarrow T_1$ intersystem crossing have on sensitization efficiency.
- 3) Fast energy transfer proceeds between Ln(III) ions to deliver the obtained energy to a more efficiently emitting Ln(III) site to counter a quenching process.

Ln(III) clusters are particularly advantageous for achieving these criteria.

7.2. Outlook

Improving the quantum yield of Ln(III) complexes have been one of the extensively studied aspects in this field. Suppression of radiative and nonradiative processes of Ln(III) ions and optimization of excited state energy of ligands have been the central discussion. This thesis provides completely new concepts to improve the quantum yield, by focusing on energy

transfer between Ln(III) ions, spin-orbit coupling, the photophysical details of back energy transfer, and utilization of complicated dynamics.

The fundamental studies given here sets the stage for further research in the new quantum yield improvement strategies. The author believe that the research on these strategies can perfect the photophysical properties of Ln(III) complexes, and become the last piece that was required for practical applications. The numerous potential applications include, but not limited to, lighting, OLEDs, lasers, bioimaging, sensors, and spectral converters. The author hope that the introduction of such Ln(III) complexes to these applications leads to a breakthrough in technology; low power-consuming, environmental friendly, and efficient.

Acknowledgements

Throughout my five years that I have been in the Advanced Materials Chemistry Laboratory (AMC Lab), there were many great experiences that were unimaginable for me before joining the group. Such experiences are not limited to research, but social life, friendship, responsibility, hardships...as a matter of fact, everything. The people of the AMC Lab become the central part of my life and have influenced me in every way possible. It is thus inevitable that my Ph.D. degree had a tremendous contribution from the people around me. Below is my attempt at showing my greatest appreciation towards those that have contributed to my Ph.D. thesis (or dissertation).

First and foremost, I would like to express my sincere gratitude to my main advisors, **Prof. Yasuchika Hasegawa, Ph.D.** and **Prof. Takayuki Nakanishi, Ph.D.** of the AMC Lab. Prof. Nakanishi in particular, my primary advisor, has supervised me for the five years that I was in the lab. I am proud to be the first one to graduate the master's course under him, and now the Ph.D. course. In terms of research, he and I had a very different approach, and yet he still granted me the freedom to choose the style I feel I am good at. Prof. Hasegawa is the reason why I decided to join this lab in the first place. I thank him for granting me the place to do what I can do. My advisors were very supportive of my academic career and goals. They were also the ones that stopped me when I have gone too far with my curiosity, which was crucially important to produce meaningful results. This thesis would never have even begun without them.

I would also like to express my gratitude toward my other advisors, **Prof. Koji Fushimi, Ph.D.** and **Prof. Yuichi Kitagawa, Ph.D.** of the AMC Lab as well as **Prof. Noboru Kitamura, Ph.D.** of the Analytical Chemistry Laboratory. I thank the three for their academic discussions. It has greatly helped me approach science. Prof. Fushimi's guidance in academic writing was also crucial for polishing my works. Quantum chemical discussions of excited states with Prof. Kitagawa and Prof. Kitamura gave me a good sense of scientific understanding of various photophysical phenomena.

I wish to thoroughly thank from my deepest heart, **Prof. Andries Meijerink, Ph.D.** for letting me stay in his group for two months. I regret not being able to produce much results at the time, and to be honest, I am still feeling terrible about the liquid helium incident. Nonetheless, he was always with a smile and did not hesitate whatsoever to help me even if he was extremely busy.

I would also like to express my gratitude toward **Prof. Hajime Ito, Ph.D.** and **Prof. Tomohiro Seki, Ph.D.** They were very supportive of my research and even provided me the opportunity to collaborate.

Next, I would like to show my gratitude toward **Hisataka Kataoka, Ph.D.** of Bridgestone Corporation. The joint works we did also gave me an opportunity to understand research in a company, which is quite different from research in a university. I also greatly thank **Hiroyasu Sato, Ph.D.** of RIGAKU Corporation. He was quick to help when I need them the most in the crystallographic analysis.

I also deeply appreciate the support of the **Japan Society for the Promotion of Science (JSPS)** with their Research Fellowship for Young Scientists (DC1) program. The program helped me financially and allowed me to focus on my research.

I wish to thank my Ph.D. course colleagues of the same grade: **Satoshi Wada, Masanori Yamamoto,** and **Yudai Yamamoto** as well as my seniors: **Yuichi Hirai, Ph.D., Akira Kawashima, Ph.D., Jun Seob Lee, Ph.D., Yu Takabatake, Ph.D., Kei Yanagisawa, Ph.D.** The way we supported each other was one of the main reason for my intellectual improvements. I remember when I first came into this Lab, completely clueless about what we were doing, attempting to understand all these information that was suddenly forcing its way inside me. Fortunately, these people were there to help me. Satoshi, you despite being a very smart man, that airhead character was unexpected. I loved teasing you about it. Masanori, I know you since freshman in college, and you are one of the most benign personality I have ever seen in my life. Don't sacrifice yourself for the others too much, though. Yudai, you really are something else in...well, everything. For some reason, we know a lot of weird things most people aren't interested in. I hope you and I could keep it up. Hopefully, we will stay in touch even after we part ways. I wish you guys the best.

I would like to continue on with the list of those I wish to show my gratitude towards **Tsubasa, Ayako, Sho (H), Takafumi, Yuki (S),** and **Kenji,** who were closely associated with me in terms whom we worked with. Tsubasa was my first real kohai that I've ever had. His cheerful and playful personality really helped me at hard times. Ayako was my first girl kohai that I've had, and I've learned quite a lot from her as well. Sho, keep it up with making new words and phrases. I loved them! Yuki, for some reason, he and I were often in the Lab at midnight. Let's work overnight again. Kenji, master your whistling skills. It's crucial to be able to do this as my kohai. Other AMC Lab members that were important to my five years in the lab in which I also must thank are: **Masashi, Yuki, Kazune, Kazunori, Nao, Haruya, Misako, Shiori (T), Takeshi, Shiori (N), Hajime, Ryosuke, Masaaki, Yui, Tomomi, Ryuto, Nick, Natsumi, Katsumasa, Yuya, Ryogo, Pedro-Paulo, Marina, Koki, Takuya,** and **Kei (N).** The time with you people is unforgettable.

I shall never forget to thank those in the Condensed Matter and Interfaces (CMI) Group at Utrecht University (The Netherlands): **Prof. D. A. M. Vanmaekelbergh, Ph.D., Federico, Annalisa, Maryam, Mathijs, Elleke, Jaco, Ward, Joost, Joep, Chenghui, Winston, Jacobine, Robin, Tim.** Federico, you were one of the earliest members I met when I came to visit the CMI Group and man you were an awesome guy. The time with you in the FOM party, party at Ward's home, and in Tokyo was magnificent! Ward, you handsome looking dude, I really enjoyed the time with you at the FOM party, your home, and in Tokyo. Also, thank you for the thesis. Jaco, my neck hurts when I look up to you. You were a friendly guy, and I am glad we met. I had a great time with you in the FOM party and the party at Ward's home. Mathijs, you were a great, brilliant guy and helped me with measurements. I am a bit embarrassed to give you my thesis after reading yours. I thank you and Joep for the little trip in Amsterdam. I had a great time! Maryam, you were such as cheerful, and fun person to hang out with. Annalisa, you were also a great person and gave me a comfortable time in the group. Chenghui and Winston, you guys helped me a lot when I came to the group. Chenghui, thank you for the power adapter, you saved me from being unable to do anything on my computer! Joost, I am glad you were the roommate in FOM meeting and took me to the party. Your presentation was also spectacular. Elleke, Jacobine, Robin, and Tim, thanks for helping me with measurements. Daniel, thank you for your time when we ate lunch together. I certainly enjoyed the conversation with you, especially about tennis.

I thank Hokkaido University, the place where it all began. I spent eight years at this university, and I cannot imagine what would've happened if I went anywhere else. Eight years is actually the longest that I have ever lived in one place and thus I can say that Hokkaido University has now effectively become my home. This place has provided me with the most precious experience in all aspect and made me who I am.

Last but not least, I cannot forget to thank my mom and dad. I know I am not the most obedient child you have and we tend to have a different opinion on things (even today and probably forever). Nonetheless, your support was without a doubt important to get to this point of my life. I also thank my brother and sister who were with great talents. Your existence and your success motivate me in doing what I do. Who would have ever thought that all three of us will go for Ph.D.?

There were good times and hard times. The hard times strengthened me to withstand all the hardship in my life so far, whether I deal with it alone or with the support of others. The good times provided me a reason to live. I thank this world for the beautiful and the ugly things in my life.

Thus concludes the prologue of my life as a scientist. Although it may not be in the form of writing, more chapters are certain to come.

March 2018,
Shun Omagari